



University of HUDDERSFIELD

University of Huddersfield Repository

Brown, Lee

Fundamental Studies of Transition Metal Elements in Electron Self-Exchange and Cross-Coupling Mechanisms

Original Citation

Brown, Lee (2018) Fundamental Studies of Transition Metal Elements in Electron Self-Exchange and Cross-Coupling Mechanisms. Doctoral thesis, University of Huddersfield.

This version is available at <http://eprints.hud.ac.uk/id/eprint/34851/>

The University Repository is a digital collection of the research output of the University, available on Open Access. Copyright and Moral Rights for the items on this site are retained by the individual author and/or other copyright owners. Users may access full items free of charge; copies of full text items generally can be reproduced, displayed or performed and given to third parties in any format or medium for personal research or study, educational or not-for-profit purposes without prior permission or charge, provided:

- The authors, title and full bibliographic details is credited in any copy;
- A hyperlink and/or URL is included for the original metadata page; and
- The content is not changed in any way.

For more information, including our policy and submission procedure, please contact the Repository Team at: E.mailbox@hud.ac.uk.

<http://eprints.hud.ac.uk/>

Fundamental Studies of Transition Metal Elements in Electron Self- Exchange and Cross-Coupling Mechanisms.

Lee Brown

A thesis submitted to the University of Huddersfield in partial
fulfilment of the qualification of PhD.

13/12/2018

i. Acknowledgments.

First, I give thanks to all the teaching staff at University of Huddersfield who made my undergrad course so enjoyable and stimulating, inspiring me to pursue my PhD. Next to my supervisor, Nathan who has been a kind, patient and enthusiastic mentor throughout my Masters and PhD. To Luke for teaching me the practical skills required to perform my research, his constant words of encouragement and general infectious enthusiasm for all things Chemistry. To Kevin who brought many new ideas to lab during his tenure that made a lot of this work possible. To Ollie, Rayhaan and Becky who gave me the few months of time in the lab that were the most enjoyable and some of the most productive during a very stressful period of my life. Ollie is a particularly selfless person who despite his own enormous workload always makes time to help others. I wish him the best of luck with the rest of his PhD and the future.

To my collaborators Dr Sweeney and James for working alongside me in such an exciting, challenging and productive project. To my other good friends in the Sweeney group Julien and Jordan who are aaaaaaabsolutley the best people to go drinking with, if you have the constitution for it.

Finally, to my wife Paris for her constant support and my daughter Michelle, my daily source of inspiration.

ii. Publications

This work has been included in the following publications:

- 1) Adams K., Ball A.K., Birkett J., Brown L., Chappell B., Gill D.M., Lo P.K., Patmore N.J., Rice C.R., Ryan J., Raubo P. and Sweeney J.B. An iron-catalysed C-C bond-forming spirocyclization cascade providing sustainable access to new 3D heterocyclic frameworks. *Nat Chem.* **2017**, 9 (4), 396-401.

The following manuscripts are also in preparation:

- 2) Vincent K.B., Wilkinson L.A., Brown L., Meijer A.J.H.M., and Patmore N.J. Bridging ligand effects on stabilisation of the mixed-valence state in hydrogen bonded 'dimers of dimers'.
- 3) Birkett J.R., Brown L., Lo P.K., Patmore N.J., Rice C.R. and Sweeney J.B. In search of the mechanism of iron-catalyzed cross-couplings: structural and spectroscopic characterization of competing pre-catalysts for Kumada-like reactions.⁷

iii. Contents

| | |
|--|----|
| 1. Chapter 1. Electron Self-Exchange Reactions. | 2 |
| 1.1 Metal Paddlewheel Complexes as Redox Centres | 2 |
| 1.1.1 Electronic Structure of the Quadruple Bond | 3 |
| 1.2 Electron-Self Exchange Reactions | 6 |
| 1.2.1 Inner Sphere and Outer Sphere | 6 |
| 1.3 Mixed Valency | 8 |
| 1.4 Robin-Day Classification System | 9 |
| 1.4.1 Class I: Valence Trapped | 9 |
| 1.4.2 Class II: Mixed Valence | 10 |
| 1.4.3 Class III: Electron Delocalised | 11 |
| 1.4.4 Spectroscopic Methods | 13 |
| 1.4.4.1 UV-Vis & UV-Vis NIR spectroscopy. | 13 |
| 1.4.4.2 IR Spectroscopy | 14 |
| 1.4.4.3 Electron Paramagnetic Resonance | 14 |
| 1.4.5 Electrochemical Methods | 16 |
| 1.5 Literature Study of Mixed Valence Complexes | 18 |
| 1.6 Solvent and Temperature Effects on Rate of Exchange. | 18 |
| 1.6.1 Class II to Class II-III Transitions. | 19 |
| 1.6.2 Class II-III to Class III Transitions. | 20 |
| 1.7 Effect of Bridging and Ancillary Ligand Alterations on ET rates. | 21 |
| 1.8 Mixed Valency in Di-Metal Paddlewheel Complexes | 25 |
| 1.9 Proton Coupled Electron Transfer (PCET) | 31 |
| 1.9.1 PCET self-exchange reactions in Inorganic complexes. | 33 |
| 1.10 Mixed Valency Across Hydrogen Bonded Complexes | 36 |
| 1.11 Proton Coupled Mixed Valency | 48 |
| 1.12 Conclusion | 55 |
| 1.13 References | 56 |

| | | |
|---------|---|----|
| 2. | Chapter 2. Building Blocks for the Assembly of Hydrogen Bonded Molecular Assemblies. | 60 |
| 2.1 | Abstract | 60 |
| 2.2 | Mixed Valence Extended Assemblies. | 61 |
| 2.2.1 | Mixed Valence Oligomers | 61 |
| 2.2.1.1 | Covalent | 61 |
| 2.2.1.2 | H-bonded | 63 |
| 2.2.2 | Molecular Wires | 64 |
| 2.2.2.1 | Covalent | 64 |
| 2.2.2.2 | H-bonded | 65 |
| 2.3 | Aims | 67 |
| 2.4 | Discussion | 69 |
| 2.4.1 | Synthesis & Structural Characterisation. | 69 |
| 2.4.1.1 | ¹ H NMR spectra | 72 |
| 2.4.1.2 | X-ray Crystallography | 73 |
| 2.4.2 | Cyclic Voltammetry | 76 |
| 2.4.3 | UV-Vis Absorption Spectroscopy. | 77 |
| 2.4.4 | Substitution Chemistry | 79 |
| 2.5 | Conclusions | 82 |
| 2.6 | Experimental | 82 |
| 2.6.1 | Materials and Physical Methods | 82 |
| 2.6.2 | Synthesis of N,N'-di-p-tolylformamidinate (HDTolF) | 83 |
| 2.6.3 | Synthesis of Mo ₂ (OAc) ₄ (1) | 83 |
| 2.6.4 | Synthesis of Mo ₂ (DTolF) ₄ (2) | 84 |
| 2.6.5 | Synthesis of Mo ₂ (DTolF) ₃ (OAc) (3) | 84 |
| 2.6.6 | Synthesis of trans-Mo ₂ (DTolF) ₂ (OAc) ₂ (4) | 84 |
| 2.6.7 | Synthesis of cis-Mo ₂ (TolF) ₂ (OAc) ₂ (5) | 85 |
| 2.6.8 | Synthesis of cis-(Mo ₂ (DTolF) ₂ (NCMe) ₄ .(BF ₄) ₂ . 2NCMe) (6) | 85 |
| 2.7 | References | 87 |

| | |
|---|-----|
| 3. Chapter 3. “Dimers of Dimers” Bridged by the 3,6-Dihydroxypyridazine Ion. How do Electronic Changes in the Bridge Affect Stabilization of the Mixed Valence State? | 88 |
| 3.1 Abstract | 88 |
| 3.2 Proton Coupled Mixed Valency | 89 |
| 3.3 Aims | 91 |
| 3.4 Discussion | 91 |
| 3.4.1 Synthesis & Structural Characterisation | 91 |
| 3.4.1.1 ¹ H NMR Spectroscopy | 93 |
| 3.4.1.2 IR Spectroscopy | 95 |
| 3.4.2 Cyclic Voltammetry | 96 |
| 3.4.3 UV-Vis NIR SEC | 99 |
| 3.4.3.1 UV-Vis NIR SEC of Mo ₂ (TiPB) ₃ (4-ClHDOP) (7) | 100 |
| 3.4.3.2 UV-Vis NIR SEC of Mo ₂ (TiPB) ₃ (4-BrHDOP) (8) | 102 |
| 3.4.3.3 UV-Vis NIR SEC of Mo ₂ (TiPB) ₃ (4-MeHDOP) (10) | 104 |
| 3.4.3.4 UV-Vis NIR SEC of Mo ₂ (TiPB) ₃ (3-Me,4-MeDOP) (11) | 105 |
| 3.4.3.5 UV-Vis NIR SEC of Mo ₂ (TiPB) ₃ (Phth) (12) | 107 |
| 3.5 Conclusions | 107 |
| 3.6 Experimental | 108 |
| 3.6.1 Materials and Physical Methods | 108 |
| 3.6.2 Synthesis of Mo ₂ (TiPB) ₃ (4-Cl-HDOP) (7) | 109 |
| 3.6.3 Synthesis of Mo ₂ (TiPB) ₃ (4-Br-HDOP) (8) | 109 |
| 3.6.4 Synthesis of Mo ₂ (TiPB) ₃ (4-Me-HDOP) (10) | 110 |
| 3.6.5 Synthesis of Mo ₂ (TiPB) ₃ (4,5-Me ₂ -HDOP) (11) | 110 |
| 3.6.6 Synthesis of Mo ₂ (TiPB) ₃ (Phthal) (12) | 110 |
| 3.7 References | 111 |
| 4. Chapter 4. “Dimer of Dimers” Bridged by Thio-Lactams: 1,2-dihydropyridazine-3,6-dithione (HSDOP) and 1,4-dihydropyridazine-2,3-dithione (HDSOP). | 113 |
| 4.1 Abstract | 113 |
| 4.2 Effects of Coordinating Atom Alterations on Stabilisation of the Mixed Valence State | 114 |
| 4.3 Aims | 116 |

| | | |
|---------|---|-----|
| 4.4 | Discussion | 117 |
| 4.4.1 | Synthesis and Characterisation | 117 |
| 4.4.1.1 | ¹ H NMR Spectroscopy. | 120 |
| 4.4.2 | Cyclic Voltammetry | 121 |
| 4.4.3 | UV-Vis NIR SEC | 125 |
| 4.4.3.1 | UV-VIS NIR SEC of Mo ₂ (DAniF) ₃ (HDSOP) (13) in DCM | 125 |
| 4.4.3.2 | UV-VIS NIR SEC of Mo ₂ (DAniF) ₃ (HDSOP) (13) in THF | 128 |
| 4.4.3.3 | UV-VIS NIR SEC of Mo ₂ (DAniF) ₃ (HSDOP) (14) in DCM | 130 |
| 4.4.3.4 | UV-VIS NIR SEC of Mo ₂ (DAniF) ₃ (HSDOP) (14) in THF | 132 |
| 4.4.4 | IR SEC | 133 |
| 4.4.4.1 | IR SEC of Mo ₂ (DAniF) ₃ (DSOP) (13) in DCM | 134 |
| 4.4.4.2 | IR SEC of Mo ₂ (DAniF) ₃ (SDOP) (14) in DCM | 136 |
| 4.5 | Conclusions | 138 |
| 4.6 | Experimental | 139 |
| 4.6.1 | Materials and Physical Methods | 139 |
| 4.6.2 | Synthesis of N,N'-bis(4-methoxyphenyl)formimidamide | 139 |
| 4.6.3 | Synthesis of Mo ₂ (DAniF) ₃ (HDSOP) (13) | 140 |
| 4.6.4 | Synthesis of Mo ₂ (DAniF) ₃ (HSDOP) (14) | 140 |
| 4.7 | References | 141 |
| 5. | Chapter 5. Part 1 Conclusion | 143 |
| 5.1 | Summary | 143 |
| 5.2 | References | 145 |
| 6. | Chapter 6. Iron Catalysed Kumada Cross-Coupling Reactions. | 148 |
| 6.1 | General Introduction; Kumada Couplings and the Appeal of Iron. | 148 |
| 6.1.1 | Early Work. | 151 |
| 6.1.2 | Resurgence and the Modern Field. | 152 |
| 6.1.3 | Substrate Scope. | 153 |
| 6.2 | Mechanistic Studies | 154 |
| 6.2.1 | Single-Electron-Transfer (SET) Mechanisms. | 154 |

| | | |
|---------|---|-----|
| 6.2.1.1 | SET: Fe(II)/(III) catalytic cycles. | 156 |
| 6.2.1.2 | SET: Fe(I)/(III) catalytic cycles. | 158 |
| 6.2.2 | Low Valent Active Species | 160 |
| 6.2.2.1 | Fe(0)/(II) Cycle. | 160 |
| 6.2.2.2 | Fe(0)/(-II) "Inorganic Grignard" Cycle | 161 |
| 6.2.3 | "Super-ate" Complexes. | 163 |
| 6.2.4 | Conclusions | 170 |
| 6.3 | References | 172 |
| 7. | Chapter 7. The Reaction Products of Fe(acac) ₃ with One Equivalent of Grignard Reagents. | 176 |
| 7.1 | Abstract | 176 |
| 7.2 | Reduced Products of Fe(acac) ₃ | 177 |
| 7.3 | Aims | 179 |
| 7.4 | Discussion | 180 |
| 7.4.1 | The Reaction Products of Fe(acac) ₃ and One Equivalent 4-biphenyl-MgBr. | 180 |
| 7.4.2 | Experimental Observations: Isolation of the FeBr ₂ (μ-acac) ₂ Mg(THF) ₂ intermetallic (15). | 181 |
| 7.4.3 | Analysis of Reaction Filtrate | 182 |
| 7.4.3.1 | ¹ H NMR Spectroscopy | 182 |
| 7.4.3.2 | Infra-Red Spectroscopy. | 184 |
| 7.4.4 | An Alternate Grignard Free Route to Fe ⁻ Mg Intermetallic Pre-Catalysts. | 185 |
| 7.4.5 | Grignard Screening. | 186 |
| 7.4.6 | Characterisation. | 189 |
| 7.4.6.1 | ¹ H NMR Spectroscopy | 189 |
| 7.4.6.2 | Magnetic Susceptibility | 190 |
| 7.4.6.3 | X-Ray Crystallography | 191 |
| 7.4.6.4 | Infra-Red Spectroscopy. | 198 |
| 7.4.6.5 | Cyclic Voltammetry | 199 |
| 7.5 | Competing Pre-Catalysts? | 202 |
| 7.5.1 | Comparison of Pre-Catalyst Activity in Literature Reactions. | 202 |
| 7.6 | Conclusions | 208 |

| | | |
|-------|---|-----|
| 7.7 | Experimental | 209 |
| 7.7.1 | Materials and Methods | 209 |
| 7.7.2 | Sample Synthesis of $\text{FeBr}_2(\mu\text{-acac})_2\text{Mg}(\text{THF})_2$ (15) | 209 |
| 7.7.3 | Synthesis of $\text{FeX}_2(\mu\text{-acac})_2\text{Mg}(\text{THF})_2$ (X = Cl (16) or I (17)) via FeX_2 . | 210 |
| 7.7.4 | Synthesis of $\text{Fe}(\text{acac})_2$. | 210 |
| 7.8 | References | 211 |
| 8. | Chapter 8. Reaction of Iron Pre-catalysts With More Than One Equivalent of Grignard Reagent. | 214 |
| 8.1 | Abstract | 214 |
| 8.2 | Aims | 214 |
| 8.3 | Further Stoichiometric Reactions with Grignard Reagents. | 215 |
| 8.4 | Reaction Product(s) of 15 with RMgBr . | 216 |
| 8.4.1 | Reaction Product(s) of $\text{Fe}(\text{acac})_3$ with three Equivalents 4-biPhMgBr and one equivalent electrophile. | 216 |
| 8.4.2 | Reaction Product(s) of 15 with one or two equivalents of PhMgBr . | 224 |
| 8.5 | Reaction Products of $\text{Fe}(\text{acac})_2$ with RMgBr . | 227 |
| 8.5.1 | Reaction Product(s) of $\text{Fe}(\text{acac})_2$ with two equivalents PhMgBr . | 227 |
| 8.6 | Conclusions | 227 |
| 8.7 | Experimental | 231 |
| 8.7.1 | Materials and Physical Methods | 231 |
| 8.7.2 | Isolation of $\text{Fe}(\text{Br})(\text{I})(\mu\text{-acac})_2\text{Mg}(\text{THF})_2$ (18) | 231 |
| 8.7.3 | Isolation of $\text{FeBr}_2(\mu\text{-Br})(\mu\text{-acac})\text{Mg}(\text{THF})_2$ (19) from 15 | 232 |
| 8.7.4 | Isolation of $[\text{FeBr}_4.\text{Mg}(\text{THF})_6]$ (19) | 232 |
| 8.7.5 | Isolation of $\text{FeBr}_2(\mu\text{-Br})(\mu\text{-acac})\text{Mg}(\text{THF})_2$ (20) from $\text{Fe}(\text{acac})_2$ (20) | 232 |
| 8.8 | References | 233 |
| 9. | Chapter 9. Part Conclusion | 234 |
| 9.1 | Summary | 234 |
| 9.2 | References | 236 |

| | | |
|------|---|-----|
| 10. | Chapter 10. Closing Remarks | 238 |
| 10.1 | References | 242 |
| 11. | 11. Appendixes: X-ray Crystal Structure Data & Refinement Tables | 245 |
| 11.1 | <i>cis</i> -Mo ₂ (DTolF) ₂ (OAc) ₂ (5) | 245 |
| 11.3 | <i>cis</i> -Mo ₂ (DTolF) ₂ (NCMe) ₄ .2BF ₄ .2CH ₂ Cl ₂ (6) | 247 |
| 11.4 | FeBr ₂ (μ-acac) ₂ Mg(THF) ₂ (15) | 249 |
| 11.5 | FeCl ₂ (μ-acac) ₂ Mg(THF) ₂ (16) | 251 |
| 11.6 | FeI ₂ (μ-acac) ₂ Mg(THF) ₂ (17) | 253 |
| 11.7 | FeBr(I)(μ-Br)(μ-acac)Mg(THF) ₃ (18) | 255 |
| 11.8 | FeBr ₂ (μ-Br)(μ-acac)Mg(THF) ₃ (19) | 257 |
| 11.9 | FeBr ₄ .Mg(THF) ₆ (20) | 258 |

iv. List of Figures, Schemes & Tables

| | | |
|--------------|--|----|
| Figure 1.1. | Examples of some of the structural modifications that can be made upon the paddlewheel motif. | 2 |
| Figure 1.2. | The five d-orbitals. | 4 |
| Figure 1.3. | Molecular orbital diagram for a quadruple bond. | 5 |
| Figure 1.4. | Double-well PES's of the reactant (R) and product (P) in an electron-self change reaction. | 7 |
| Figure 1.5. | The Creutz-Taube Ion. | 8 |
| Figure 1.6. | M ⁿ -Bridge-M ⁿ motif when oxidised generates M ⁿ -Birdge-M ⁿ⁺¹ , an electron Donor-Bridge-Acceptor model. | 9 |
| Figure 1.7. | Potential energy diagram for a Class I "valence trapped" complex. | 10 |
| Figure 1.8. | Potential energy diagram for a Class II mixed valence complex. | 11 |
| Figure 1.9. | Potential energy diagram for a Class III "electron delocalised" mixed valence complex. | 12 |
| Figure 1.10. | X-Band EPR spectra of [Mo ₂ (DAniF) ₃](C ₆ H ₂ O ₄)[Mo ₂ (DAniF) ₃] ⁺ in DCM at room temperature (top) and [Mo ₂ (DAniF) ₃](PFT)-[Mo ₂ (DAniF) ₃] ⁺ in THF/DCM at room 210 K (bottom). | 16 |
| Figure 1.11. | CV of (DAniF) ₃ Mo ₂ -O ₂ CCO ₂ -Mo ₂ (DAniF) ₃ using 0.1 M tetrabutylammonium hexafluorophosphate (TBAPF) in DCM at 100 mVs ⁻¹ scan rate. | 17 |
| Figure 1.12. | Gradual spectral coalescence observed for {[Ru ₃ O(OAc) ₆ (CO)(L)] ₂ (μ-pz)} ⁺ as the solvent (NCMe) approaches freezing temperature. | 21 |

| | |
|--|----|
| Figure 1.13. A plot of K_c (logarithmic scale) vs. $1/R_{MM}$ where R_{MM} is the intranuclear separation between the ferrocene redox centres. | 22 |
| Figure 1.14. $[\text{Ru}_3\text{O}(\text{OAc})_6(\text{CO})(\text{dmap})]_2(\text{B})$ B = pz (top) and 4,4'-bpy (bottom) together with their corresponding CV's (left) and IR spectra (right). | 23 |
| Figure 1.15. Simplified electronic structures for a series of $[\text{Ru}_3\text{O}(\text{OAc})_6(\text{CO})(\text{L})]_2(\text{B})$ complexes 1) B = pz L = dmap 2) B = pz L = py 3) B = pz L = 4-CNpy and 4) B = 4,4'-bpy L = dmap and there observed $\nu(\text{CO})$ IR bands. | 25 |
| Figure 1.16. Possible orbital combinations for the $\text{M}_2\text{-O}_2\text{CCO}_2\text{-M}_2$ system. | 26 |
| Figure 1.17. Shift in CR resonance bands due to increased coupling as Mo is substituted for W in the following series; $(\text{Piv})_3\text{Mo}_2\text{-O}_2\text{CCO}_2\text{-Mo}_2(\text{piv})_3$ (red) $(\text{piv})_3\text{MoW-O}_2\text{CCO}_2\text{-MoW}(\text{piv})_3$ and $(\text{piv})_3\text{Mo}_2\text{-O}_2\text{CCO}_2\text{-Mo}_2(\text{piv})_3$. | 27 |
| Figure 1.18. Qualitative frontier MO diagram for the MV state dicarboxylate bridged dimer of dimers; $[\text{M}_2\text{-bridge-M}_2]^+$ labelled with the important electronic transitions observed. | 28 |
| Figure 1.19. $\text{E}_1\text{E}_2\text{-thi-E}_1\text{E}_2$ bridged Mo_4 complexes reported by Liu et al. | 29 |
| Figure 1.20. NIR spectra of $[\text{OO-thi-OO}]^+$ (A), $[\text{NS-thi-NS}]^+$ (B), $[\text{OS-thi-OS}]^+$ (C) and $[\text{SS-thi-SS}]^+$ (D) in DCM (black), THF (red) acetonitrile (blue). | 30 |
| Figure 1.22. The Z-Scheme. Light absorption in photosystems I and II used to drive the formation of ATP. Figure taken from an open access source. ⁴⁵ | 33 |
| Figure 1.23. Concerted PT and ET (CPET) vs. stepwise processes. | 33 |
| Figure 1.24. Experimental criteria relevant to concerted and stepwise PT and ET as related by Hess' Law. | 34 |
| Figure 1.25. Possible pathways for net hydrogen atom transfer ($\text{H}\bullet$) between $[\text{Fe}^{\text{III}}(\text{Hbim})(\text{H}_2\text{bim})_2]^{2+}$ to $[\text{Fe}^{\text{II}}(\text{H}_2\text{bim})_3]^{2+}$. | 35 |
| Figure 1.26. Assembly of $\text{Ru}^{\text{III}}(\text{Hbim})_3$ in the solid-state produces the polymeric honeycomb structure, $\{\text{Ru}^{\text{III}}\text{Ru}^{\text{III}}\}_n$. | 36 |
| Figure 1.27. Three mechanism that can account for stabilisation of the mixed state in a hydrogen bonded dimer; electron transfer, step-wise proton transfer + electron transfer or proton-coupled mixed valency (PCMV). | 37 |
| Figure 1.28. Four literature complexes represented in the MV state dimer state. The corresponding author of the publication and presence or absence of an IVCT in the NIR region is noted for each complex. | 38 |
| Figure 1.29. CV of a) monomeric complex, ii' and b) dimeric (ii) ₂ in DCM. For the latter two, stable MV states are observed. | 40 |

| | |
|--|----|
| Figure 1.31. CV showing formation of the (iii) ₂ dimer and oxidation to produce firstly the mixed valence (ii) ₂ ²⁻ state then the doubly oxidised dimer (ii) ₂ ²⁻ in DCM (red). In contrast the CV taken in DMSO (black) shows no dimerization nor formation of a mixed valence state. | 43 |
| Figure 1.32. IR (a) and UV-Vis NIR (b) for iii (black), (iii) ₂ ⁻ (green) and (iii) ₂ ²⁻ . | 44 |
| Figure 1.33. CV of (iv) ₂ in DCM. | 47 |
| Figure 1.34. EPR spectrum of (iv) ₂ ⁺ in frozen DCM (77 K). | 47 |
| Figure reproduced from reference with permission of the ACS. ⁶¹ | 47 |
| Figure 1.35. Self-complimentary hydrogen-bonding motifs in [Mo ₂ (TiPB ₃)(DOP)] ₂ (v) ₂ and in [Mo ₂ (TiPB ₃)(DOP)] ₂ (vi) ₂ . | 49 |
| Figure 1.36. CV's of a) Mo ₂ (TiPB) ₃ (HDON) (v) and b) Mo ₂ (TiPB) ₃ (HDOP) (vi) in DCM (solid line) a mixed valence state for the dimerised species (vi) ₂ ⁺ (vii) ₂ ⁺ is observed. | 50 |
| After addition of DMSO (dashed line) the dimer is disrupted. | 50 |
| Figure 1.37. EPR spectra of Mo ₂ (TiPB) ₄ ⁺ PF ₆ ⁻ (top) and [Mo ₂ (TiPB) ₃ (HDOP)] ⁺ PF ₆ ⁻ , (vii) ₂ ⁺ PF ₆ ⁻ (bottom). | 52 |
| Recorded in DCM at -90 °C. | 52 |
| Figure 1.38. Possible mechanisms for stabilisation of the mixed valence state relating two proton coordinates; double proton transfer DPT (top), single proton transfer 1 (middle) and single proton transfer 2 (bottom). | 53 |
| Figure 1.39. Calculated potential energy surface for concerted double proton transfer in (vi') ₂ ⁺ . Figure reproduced from reference with permission of the RSC. ⁶⁴ | 54 |
| Figure 1.40. Calculated potential energy surfaces for two single proton transfer models in (vi') ₂ ⁺ . Figure reproduced from reference with permission of the RSC. ⁶⁴ | 54 |
| Figure 2.1 Crystal structures of the perfluoro terephthalate bridged molecular square and triangles reported by Cotton et al. | 62 |
| Figure 2.2. Ureido pyrimidine-dione derived supramolecular junctions reported by Wan et al. Reproduced from reference with permission from Wiley & Sons. ⁵ | 63 |
| Figure 2.3. OTREP drawing of the {[Ru ^{II} Ru ^{III}](O ₂ CC ₂ H ₅) ₄ (phz)}.BF ₄ } unit cell. Reproduced from reference with permission from Wiley & Sons. | 65 |
| Figure 2.4. A series of ZnP-C ₆₀ molecular wires incorporating an amidinium-carboxylate hydrogen bonding interaction as reported by Martín <i>et al.</i> | 66 |
| Scheme 2.1. Synthetic strategy for the generation of Hydrogen bonded assemblies incorporating Mo ₂ redox centres. | 68 |
| Scheme 2.2. Synthesis of Mo ₂ (OAc) ₄ (1) and Mo ₂ (DTolF) ₄ (2). | 69 |
| Scheme 2.3. Synthesis of Mo ₂ (DTolF) ₃ (OAc) (3) and trans-Mo ₂ (DTolF) ₂ (OAc) ₂ (4). | 70 |
| Scheme 2.4. Synthesis of cis-Mo ₂ (DTolF) ₂ (OAc) ₂ (5). | 71 |

| | |
|--|----|
| Scheme 2.5. Comparison of synthetic routes required to generate trans-Mo ₂ (DTolF) ₂ (OAc) ₂ (4) top and trans-Mo ₂ (DTolF) ₂ (OAc) ₂ (5) bottom. | 72 |
| Figure 2.5. ¹ H NMR spectra of complexes 2 (green), 3 (blue), 4 (red) and 5 (black) in CDCl ₃ at approximately 10 mM. | 73 |
| Figure 2.6. Solid-state structure of cis-Mo ₂ (DTolF) ₂ (OAc) ₂ (5) as determined by single-crystal XRD. Thermal ellipsoids are shown at 50 % probability. Hydrogen atoms are omitted for clarity. | 74 |
| Figure 2.7. Solid-state structure of cis-Mo ₂ (DTolF) ₂ (NCMe) ₄ .2BF ₄ (6) as determined by single-crystal XRD. Thermal ellipsoids are shown at 50 % probability. Hydrogen atoms are omitted for clarity. | 75 |
| Figure 2.8. CV's of complexes 2 – 5 using 0.1 M TBAPF ₆ electrolyte 5 mM analyte concentration in DCM at 100 mVs ⁻¹ scan rate. | 77 |
| Table 2.1. Electrochemical data taken from CV's of complexes 2 – 5 (Figure 2.3) and comparison to DAniF analogues. | 77 |
| Figure 2.9. UV-Vis Absorption spectra of complexes 1 – 4 in DCM 1 cm pathlength analyte concentration 6 – 12 mM. | 79 |
| Table 2.2. Data taken from the UV-Vis spectra of complexes 1-4 for the Mo ₂ (δ) → DTolF π* MLCT transition. | 79 |
| Scheme 2.6. Attempted reactions of Mo ₂ (DTolF) _{4-n} (OAc) _n n= 1, 2 (cis-) or 2 (trans-) with various ligands capable of forming self-complimentary hydrogen bonds. | 81 |
| Figure 3.1. Self-complimentary hydrogen-bonding motifs in [Mo ₂ (TiPB ₃)(DOP)] ₂ and [Mo ₂ (TiPB ₃)(DOP)] ₂ [9] ₂ . The TiPB ligands are omitted for clarity. | 90 |
| Figure 3.2. DFT model of proton transfer from the unoxidized half of the dimer towards the oxidised side. A large dipole is generated that induces electron transfer. | 90 |
| Scheme 3.1. Synthesis of Mo ₂ (TiPB) ₃ (3-R',4-R''-HDOP) where R', R'' = Cl, H (7), Br, H (8), H, H (9) Me, H (10) and Me, Me (11) and Mo ₂ (TiPB) ₃ (Phth) (12). | 91 |
| Scheme 3.2. Two coordination isomers possible in the mono-substituted Mo ₂ (R',R''DOP) complexes 7 , 8 and 10 . | 93 |
| Figure 3.3. ¹ H NMR spectra of complexes 7 – 12 (top to bottom) in CDCl ₃ . | 95 |
| Figure 3.4. A portion of the IR spectra of complexes 7 (blue), 8 (green), 9 (black), 10 (red), 11 (brown) and 12 (purple). | 96 |
| Figure 3.5. CV (left) and DPV (right) for complexes 7 – 12 (top to bottom) collected in 0.1 M TBAPF ₆ at 100 mVs ⁻¹ scan rate referenced vs Fc/Fc ⁺ . | 98 |
| Table 3.1. Cyclic voltammetry data for compounds 7 - 12 recorded in 0.1 M TBAPF ₆ at 100 mVs ⁻¹ scan rate. Analyte concentration of 5 mM in DCM and 2.5 mM in THF. Potentials referenced vs the Fc/Fc ⁺ redox couple occurring at 0.00 V. | 99 |

| | |
|--|-----|
| Figure 3.6. UV-Vis NIR SEC of complex 9 0.1M TBAPF ₆ electrolyte in DCM. At -20 °C. Transition from neutral [9] ₂ (red) → [9] ₂ ⁺ top and from [9] ₂ ⁺ → [9] ₂ ²⁺ (blue) bottom. Reproduced from reference with permission of the ACS. ² | 100 |
| Figure 3.7. The UV-Vis NIR SEC on complex 7 in 0.1M TBAPF ₆ electrolyte in DCM. Neutral (black), 1 ⁺ (green) and 2 ⁺ (red). | 101 |
| Figure 3.8. An expanded portion of the UV-Vis region highlighting the changes observed in the Mo ₂ δ → DOP π* MLCT transition in the UV-Vis NIR SEC of complex 7 . | 102 |
| Figure 3.9. UV-Vis NIR SEC of complex 8 in 0.1M TBAPF ₆ electrolyte in DCM. Neutral (black), 1 ⁺ (green) and 2 ⁺ (red). | 103 |
| Figure 3.10. An expanded portion of the UV-Vis region highlighting the isosbestic points for the Mo ₂ δ → DOP π* MLCT transitions in the UV-Vis NIR SEC of complex 8 . | 103 |
| Figure 3.11. UV-Vis NIR SEC of complex 10 in 0.1M TBAPF ₆ electrolyte in DCM. Neutral (black), 1 ⁺ (green) and 2 ⁺ (red). | 104 |
| Figure 3.12. An expanded portion of the UV-Vis region highlighting the isosbestic points for the Mo ₂ δ → DOP π* MLCT transitions in the UV-Vis NIR SEC of complex 10 . | 105 |
| Figure 3.13. UV-Vis NIR SEC of complex 11 in 0.1M TBAPF ₆ electrolyte in DCM. Neutral (black), 1 ⁺ (green) and 2 ⁺ (red). | 106 |
| Figure 3.14. An expanded portion of the UV-Vis region highlighting the changes in the Mo ₂ δ → DOP π* MLCT transitions in the UV-Vis NIR SEC of complex 11 . | 106 |
| Figure 3.15. UV-Vis NIR SEC of complex 12 in 0.1M TBAPF ₆ electrolyte in DCM. Neutral (black), 1 ⁺ (green) and 2 ⁺ (red). | 107 |
| Figure 4.1. E ₁ E ₂ -thi-E ₁ E ₂ bridged [Mo ₂] ₂ complexes reported by Liu et al. Figure reproduced from reference with permission of the RSC. ⁴ The ancillary ligands are DANiF where Ar = p-anisyl. | 114 |
| Figure 4.2. Mo ₂ -bridge-Mo ₂ complexes reported by Liu et al. with accompanying electrochemical data (K _c) and IVCT band analysis data, energy (E _{IVCT}) and width at half-height (Δ _{v1/2}). | 115 |
| Scheme 4.1. Synthesis of Mo ₂ (DANiF) ₃ (DSOP) (13) and Mo ₂ (DANiF) ₃ (SDOP) (14). The aromatic backbone of the HL ligand is numbered by standard conventions. | 117 |
| Figure 4.3. ¹ H NMR of complexes 13 and 14 in CDCl ₃ . | 121 |
| Figure 4.4. CV of [Mo ₂ (DANiF) ₃ (DSOP)] ₂ dimer [13] ₂ DCM (red) and monomer [13] after addition of 0.1 mL DMSO (red). Measurement taken in 0.1M TBAPF ₆ electrolyte in 100 mVs ⁻¹ scan rate. | 123 |
| Figure 4.5. DPV of dimer [13] ₂ in DCM (red) and monomer [13] after addition of 0.1 mL DMSO. Measurement taken in 0.1M TBAPF ₆ electrolyte in 5 mVs ⁻¹ scan rate. | 123 |
| Figure 4.6. CV of [Mo ₂ (DANiF) ₃ (SDOP)] ₂ dimer [14] ₂ DCM (red) and monomer [13] after addition of 0.1 mL DMSO (red). Measurement taken in 0.1M TBAPF ₆ electrolyte in 100 mVs ⁻¹ scan rate. | 124 |

| | |
|---|-----|
| Table 4.1. Cyclic voltammetry data for compounds 13 and 14 recorded in DCM 0.1 M TBAPF ₆ at 100 mVs ⁻¹ scan rate and with addition of 0.1 mL DMSO. Analyte concentration of 5 mM. Potentials referenced vs the Fc/Fc ⁺ redox couple occurring at 0.00 V. | 124 |
| Figure 4.7. The UV-Vis NIR SEC of complex 13 in 0.1M TBAPF ₆ electrolyte in DCM. Neutral [13] ₂ (black), 1 ⁺ [13] ₂ ⁺ (green), 2 ⁺ [13] ₂ ²⁺ (red) and neutral [13] ₂ reversed (black, dashed). | 126 |
| Figure 4.8. An expanded portion of the UV-Vis region highlighting the isosbestic points observed in the Mo ₂ δ → DSOP π* MLCT transition (high energy end) in the UV-Vis NIR SEC of complex 13 . | 127 |
| Figure 4.9. An expanded portion of the UV-Vis region highlighting the isosbestic points observed in the DSOP π → Mo ₂ δ LNCT transition (low energy end) in the UV-Vis NIR SEC of complex 13 . | 127 |
| Figure 4.10. An expanded portion of the UV-Vis region highlighting the isosbestic points for the Mo ₂ δ → DAniF π* MLCT transition in the UV-Vis NIR SEC of complex 13 . | 128 |
| Figure 4.11. The UV-Vis NIR SEC of complex 13 in 0.1M TBAPF ₆ electrolyte in THF. Neutral [13] (black) and 1 ⁺ [13] ⁺ (green). | 129 |
| Figure 4.12. The UV-Vis NIR SEC of complex 14 in 0.1M TBAPF ₆ electrolyte in DCM. Neutral [14] ₂ (black), 1 ⁺ [14] ₂ ⁺ (green), 2 ⁺ [14] ₂ ²⁺ (red) and neutral [14] ₂ reversed (black, dashed). | 131 |
| Figure 4.13. An expanded portion of the UV-Vis region highlighting the isosbestic points for the Mo ₂ δ → SDOP π* MLCT transition (high energy end) in the UV-Vis NIR SEC of complex 14 . | 131 |
| Figure 4.14. An expanded portion of the UV-Vis region highlighting the isosbestic points for the Mo ₂ δ → SDOP π* MLCT transition (low energy end) in the UV-Vis NIR SEC of complex 14 . | 132 |
| Figure 4.15. The UV-Vis NIR SEC of complex 13 in 0.1M TBAPF ₆ electrolyte in THF. Neutral [13] (black) and 1 ⁺ [13] ⁺ (green). | 133 |
| Figure 4.16. A portion of the IR SEC of complex [8] ₂ red, [8] ₂ ⁺ green and [8] ₂ ²⁺ blue showing the lactam C=O stretches of the DOP ligand and ring expansion resonances of the TiPB ligands. Reproduced from reference with permission of the RSC. ¹ | 134 |
| Figure 4.17. IR SEC of complex 13 in 0.1M TBAPF ₆ electrolyte in DCM. Neutral (black), 1 ⁺ (green) and 2 ⁺ (red). | 135 |
| Figure 4.18. An expansion of the IR SEC showing the C=S stretches of the DSOP ligand and ring expansion resonances of the DAniF ligands. | 136 |
| Figure 4.19. IR SEC of complex 14 in 0.1M TBAPF ₆ electrolyte in DCM. Neutral (black), 1 ⁺ (green) and 2 ⁺ (red). | 137 |
| Figure 4.20. An expansion of the IR SEC showing the C=S stretches of the SDOP ligand and ring expansion resonances of the DAniF ligands. | 138 |
| Scheme 6.1. Summary of common name cross-coupling reactions. Where in M-R ² is an organometallic species and couples with an organic molecule having a suitably activated R-X bond. | 149 |

| | |
|---|-----|
| Scheme 6.2. Vinylation of alkyl Grignard's catalysed by FeCl ₃ . Tamura and Kochi 1971. ⁵ | 151 |
| Scheme 6.3. Reaction of MeMgBr with a mixture of 1-propenyl bromide and ethyl bromide catalysed by FeCl ₃ . | 152 |
| Scheme 6.4. A remarkable yield improvement observed in the coupling of a vinyl chloride and an alkyl Grignard with addition of NMP. NMP equivalences relative to vinyl halide. ¹⁴ | 153 |
| Scheme 6.5. Summary of the Fe catalysed Kumada cross-coupling scope based on organic substrate hybridisation. | 154 |
| Scheme 6.6. A proposed Fe(II)/(III) SET catalytic cycle employing an Fe(II) pre-catalyst. | 155 |
| Scheme 6.7. Stoichiometric reactions of FeCl ₂ (SciOPP) with x equivalents of MesMgBr, molar ratios of products. | 156 |
| Scheme 6.8. An Fe(II)/(III) catalytic cycle with a second divergent unselective Fe(II) and minor unreactive Fe(I) and Fe(0) side products presented by Neidig. Figure reproduced from reference with permission of the RSC. ³⁸ | 158 |
| Scheme 6.9. An Fe(I)/(III) catalytic cycle initiating from reduction of and Fe(II) species by Grignard reagents. | 159 |
| Scheme 6.10. An Fe(I)/(III) catalytic cycle initiated from bond homolysis in a Fe(II) species. | 159 |
| Scheme 6.11. The reactions of Fe(dppbz)Cl ₂ with two equivalents of tolylMgBr and BnMgCl produces the penta-coordinate Fe(I) complexes Fe(dppbz) ₂ tol and Fe(dppbz) ₂ Cl respectively. ³⁹ | 160 |
| Scheme 6.12. An Fe(0)/(II) active catalyst cycle proposed by Nakamura et al. ⁴¹ | 161 |
| Scheme 6.13. Generation of the "Inorganic Grignard reagent" and observed hydrocarbon products from the reaction of FeX ₂ X = Br or Cl with 4 equivalents of n-heptane. ⁴³ | 161 |
| Scheme 6.14. Contrasting reactivity of Me and EtMgBr with 4-chloromethylbenzoate. | 162 |
| Scheme 6.15. Proposed mechanistic differences between Grignard reagents without a β-hydride (left) and alkyl Grignard's with a β-hydride (right). | 163 |
| Scheme 6.16. Proposed catalytic cycle for cross coupling of 1-alkenyl bromides via [MeLi + 5 mol % FeCl ₃] as reported by Kauffmann. ⁴⁵ | 164 |
| Figure 6.1. Crystal structure of the "super-ate" complex [(Me ₄ Fe)(MeLi)][Li(OEt ₂) ₂] reported by Füstner et al. Reproduced from reference with permission of Wiley and sons. ⁴⁷ | 165 |
| Scheme 6.17. Catalytic cycle proposed by Nagahsima et al. for the coupling of 1-bromoocatane with MesMgBr by FeCl ₃ in the presence of TEMDA. ⁴⁹ | 166 |
| Scheme 6.18. Catalytic cycle for the coupling bromo octane with MesMgBr. A secondary, unselective pathway exists in the absence of TMEDA. Figure reproduced from reference with permission of John Wiley & Sons. ⁵⁰ | 167 |

| | |
|---|------------------|
| Scheme 6.19. Conditions affecting the equilibria between three- and four-coordinate “ate” complexes. Adapted from reference. | 168 |
| Scheme 6.20. Observations of the reactivity of FeCl ₃ with MeMgBr by Neidig and Kochi et al. Spin of the detected Fe species is reported as detected by EPR spectroscopy. ^{13,53} | 169 |
| Figure 6.2. Crystal structure of the mixed valence cluster MgCl(THF) ₅ [Fe ₈ Me ₁₂] as reported by Neidig et al. Hydrogen atoms are not shown for clarity. ⁵² | 169 |
| Scheme 6.21. Contrasting reactivity of MgCl(THF) ₅ [Fe ₈ Me ₁₂] with β-bromostyrene in the absence and presence of additional MeMgBr. ⁵² | 170 |
| Scheme 6.22. Three interconnected catalytic cycles as suggested by Fürstner et al. Figure adapted from reference. ⁴⁷ | 171 |
| Table 7.1. Reaction of one equivalent Fe(acac) ₃ with n equivalents PhMgCl. Transferred electrons based on biphenyl quantification by GC MS and Fe speciation by EXAFS/ XANES. Data collected from reference. ¹² | 178 |
| Scheme 7.1. The reaction products for the equimolar reaction of Fe(acac) ₃ and 4-biPhMgBr are not defined in the literature. | 180 |
| Figure 7.1. Solid-state structure of FeBr ₂ (μ-acac) ₂ Mg(THF) ₂ (15) as determined by single-crystal XRD. Thermal ellipsoids shown at 50 % probability level. Hydrogen atoms omitted for clarity. | 182 |
| Figure 7.2. Annotated ¹ H NMR spectra of the reaction filtrate following removal of 4-quaterphenyl in the reaction of Fe(acac) ₃ with one equivalent of 4-biPhMgBr. A portion of the diamagnetic region has been enlarged to show the peaks belonging to Mg(acac) ₂ . | 183 |
| Scheme 7.2. The equimolar reaction of Fe(acac) ₃ and 4-biPhMgBr. | 184 |
| Figure 7.3. Comparison of the IR spectra of the crude reaction mixture resulting from the equimolar reaction of Fe(acac) ₃ with 4-biPhMgBr (black, solid line), to genuine samples of 15 (orange, dashed line), Fe(acac) ₂ (blue, dashed line) and Fe(acac) ₃ (red, dashed line). | 185 |
| Scheme 7.3. The synthesis of X ₂ Fe(μ-acac) ₂ Mg(THF) ₂ X = Br, Cl or I (15 – 17) by reaction of ferrous halide salts FeX ₂ , X = Br, Cl or I with Mg(acac) ₂ . | 186_Toc532296778 |
| Scheme 7.4. Isolated yields of 15 based on choice of Grignard reagent. | 188 |
| Figure 7.5. ¹ H NMR spectra of the crude reaction mixtures resulting from treatment of Fe(acac) ₃ in THF treated with one equivalent PhMgBr (top), PhMgCl (middle) and PhMgI (bottom). | 189 |
| Figure 7.6. ¹ H NMR spectra of complexes 15 (orange), 16 (green) and 17 (purple). The diamagnetic region of the spectra containing only residual solvent peaks has been omitted. | 190 |
| Table 7.2. ¹ H NMR spectroscopy chemical shifts of FeX ₂ (μ-acac) ₂ Mg(THF) ₂ X = Br, Cl or I (15 – 17). | 190 |
| Table 7.3. Selected bond lengths for the series FeX ₂ (μ-acac) ₂ Mg(THF) ₂ X = Br (15), Cl (16) and I (17). | |
| Table 7.4. Selected bond angles (°) for the series FeX ₂ (μ-acac) ₂ Mg(THF) ₂ X = Br (15), Cl (16) and I (17). | |

| | |
|---|-----|
| Figure 7.7. Crystal structure of $\text{FeBr}_2(\mu\text{-acac})_2\text{Mg}(\text{THF})_2$ (15) determined by single crystal XRD. | 193 |
| Figure 7.8. Crystal structure of $\text{FeCl}_2(\mu\text{-acac})_2\text{Mg}(\text{THF})_2$ (16) determined by single crystal XRD. | 195 |
| Figure 7.9. Crystal structure of $\text{FeI}_2(\mu\text{-acac})_2\text{Mg}(\text{THF})_2$ (17) determined by single crystal XRD. | 197 |
| Figure 7.10. The IR spectra for complexes 15 (yellow), 16 (green) and 17 (purple) containing acac- C-O, C-C and C-H stretches. A portion of the spectra has been omitted as it contained a strong THF absorbance. | 199 |
| Figure 7.11. Cyclic Voltammograms of $\text{Fe}(\text{acac})_2$ (black) and $\text{FeX}_2(\mu\text{-acac})_2\text{Mg}(\text{THF})_2$ X = Br (15 , orange), X = Cl (16 , green) and X = I (17 , purple). | 200 |
| Table 7.5. Electrochemical data for $\text{Fe}(\text{acac})_2$ and $\text{FeX}_2(\mu\text{-acac})_2\text{Mg}(\text{THF})_2$ X = Br, Cl and I (15 – 17). | 201 |
| Table 7.6. Selected literature $\text{Fe}(\text{acac})_3$ catalyzed cross-coupling reactions were the catalysts is substituted for $\text{FeX}_2(\mu\text{-acac})_2\text{Mg}(\text{THF})_2$ X = Cl, Br or I (15 – 17), $\text{Fe}(\text{acac})_2$. The isolated yield reported for $\text{Fe}(\text{acac})_3$ in the original publication is noted in brackets. Entries 1- 9 by Lee Brown & James Birkett. Entries 10 – 17 by Dr Anthony Ball. | 204 |
| Scheme 8.1. Isolable products of the reaction of $\text{Fe}(\text{acac})_3$ with three equivalents of 4-biPhMgBr and one equivalent electrophile, 2-[(2-iodophenoxy)methyl]furan. Dashed double arrows indicate a reaction of unknown stoichiometry. The colour change from the starting reaction mixture to the final addition of Grignard is noted. | 216 |
| Figure 8.1. Solid-state structure of $\text{Fe}(\text{Br})(\text{I})(\mu\text{-Br})\text{Mg}(\text{acac})(\text{THF})_3$ (18) as determined by single-crystal XRD. | 218 |
| Table 8.1. Selected bond lengths (Å) of 15 and 18 . | 219 |
| Scheme 8.2. A proposed catalytic cycle for the cross-coupling of $\text{R}^1\text{-X}$ R^2MgBr by $\text{Fe}(\text{acac})_3$. Mg centres are octahedral, coordinately saturated by THF solvent molecules that are omitted for clarity. | 220 |
| Scheme 8.3. Isolable products of the reaction of $\text{Fe}(\text{acac})_3$ with three equivalents of 4-biPhMgBr and one equivalent electrophile, 4-iodo-4-biphenyl. Dashed double arrows indicate a reaction of unknown stoichiometry. The colour change from the starting reaction mixture to the final addition of Grignard is noted. | 221 |
| Figure 8.2. Solid-state structure of $[\text{FeBr}_4.\text{Mg}(\text{THF})_6]$ (19) as determined by single-crystal XRD. | 222 |
| Table 9.2. Average bond lengths found in complexes 15 , 18 and 19 . | 223 |
| Scheme 8.4. Isolable products of the reaction of 15 with one or two equivalents of PhMgBr. Dashed double arrows indicate a reaction of unknown stoichiometry. The colour change from the starting reaction mixture to the final addition of Grignard is noted. | 224 |
| Figure 8.3. Solid-state structure of $\text{FeBr}_2(\mu\text{-Br})(\mu\text{-acac})\text{Mg}(\text{acac})(\text{THF})_3$ (20) as determined by single-crystal XRD. | 225 |
| Table 8.2. Collected bond lengths (Å) for intermetallic complexes 15 , 18 and 20 . | 226 |

Scheme 8.5. Isolable products of the reaction of $\text{Fe}(\text{acac})_2$ with two equivalents of PhMgBr . Dashed double arrows indicate a reaction of unknown stoichiometry. The colour change from the starting reaction mixture to the final addition of Grignard is noted. 227

Scheme 8.6. Summary of isolable Fe species arranged by equivalents of Grignard reagent. 229

v. List of Abbreviations

| | |
|-------------------------|--|
| 4,4'-bpy | 4,4'-bipyridine |
| 4-CNpy | 4-cyanopyridine |
| ACN | acetonitrile |
| ACS | American Chemical Society publishing group |
| CPET | Concerted Proton Electron Transfer |
| CV | Cyclic Voltammetry |
| DBA | Donor-Bridge-Acceptor |
| DCM | dichloromethane |
| DFT | Density functional theory |
| DMAP | Dimethylaminopyridine |
| EDX | Energy Dispersive X-ray |
| EPR | Electron Paramagnetic Resonance |
| ESR | Electron Spin Resonance |
| ET | Electron Transfer |
| HAT | Hydrogen atom transfer |
| H₂DON | 2,7-dihydroxy-1,8-naphthyridine |
| H₂DOP | 3,6-dihydroxypyridazine |
| HDAniF | <i>N,N'</i> -bis(4-methoxyphenyl)formimidamide |
| HDTolF | <i>N,N'</i> -bis(4-methylphenyl)formimidamide |
| HOMO | Highest occupied molecular orbital |
| HTiPB | 2,4,6-tri-isopropylbenzoic acid |
| IR | Infra-red |
| MALDI | Matrix assisted laser desorption ionisation |
| MS | Mass spectrometry |
| MV | Mixed Valence |
| Naph | naphthalene |
| NIR | Near Infrared |
| NMR | Nuclear Magnetic Resonance |
| PCET | Proton Coupled Electron Transfer |
| PCMV | Proton Coupled Mixed Valency |
| PES | Potential Energy Surface |
| PT | Proton Transfer |

Py Pyridine

Pz Pyrazine

RSC Royal Society of Chemistry publishing group

SEC Spectroelectrochemistry

SOMO Singly occupied molecular orbital

TEM transmission electron microscopy

THF tetrahydrofuran

TOF time of flight

UV-Vis Ultra Violet Visible

XRD X-ray Diffraction

Part 1: Proton Coupled Mixed Valency.
Electron Self-Exchange in Hydrogen Bonded
di-Molybdenum Complexes.

Chapter 1. Electron Self-Exchange Reactions.

1.1 Metal Paddlewheel Complexes as Redox Centres

Metal coordination complexes are frequently employed in the study of electron transfer, arguably the single most fundamental process in the chemical sciences. A class of metal compounds that are well presented in the literature in this context are paddlewheel complexes containing metal-metal quadruple bonds (Figure 1.1). The di-metal core in these complexes has a particularly unique electronic structure (discussed below) that imparts many interesting photophysical and magnetic properties that can be exploited spectroscopically and are especially desirable for the reversibility of their oxidations.¹

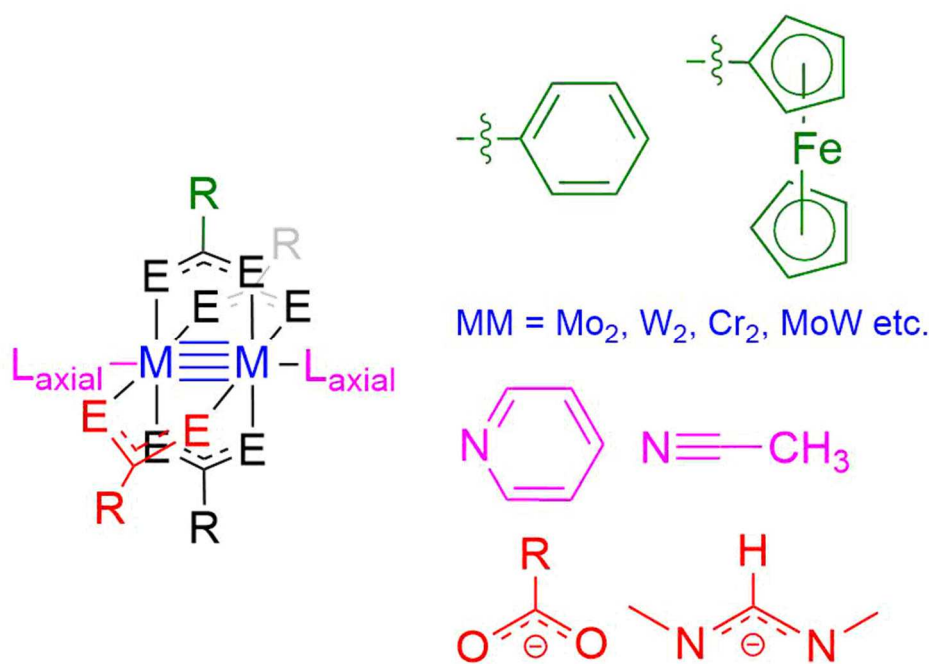


Figure 1.1. Examples of some of the structural modifications that can be made upon the paddlewheel motif.

An unimaginable degree of structural diversity can be observed in coordination complexes when we consider both the number of metal coordination centres and coordinating ligand motifs available. The underlying electronic structure of these complexes is equally fascinating to chemists as they govern a host of interesting properties that make them attractive for incorporation into functional materials.²

Di-molybdenum tetra acetate is perhaps the archetypical Mo_2 paddlewheel. The quadruple bond containing Mo_2^{4+} core is coordinated by four chelating anionic bidentate acetate ligands.³ This coordination mode usually produces a structurally rigid complex that makes paddlewheel complexes attractive synthons in the generation of molecular and supramolecular assemblies with interesting spectroscopic properties.^{4,5} Further structural diversity can be introduced by coordination into the axial coordination environments⁶ and though typically the quadruple bond is supported by π -donor ligands the periphery of these ligands can also be decorated in many ways, for instance to introduce further redox active centres.⁷

1.1.1 *Electronic Structure of the Quadruple Bond*

In organic compounds bonds are formed only from s- and p-orbitals, meaning two types of bond can be generated. An s-orbital has a single lobe and so lateral overlap generates a sigma bond. A p-orbital has two lobes and so in phase overlap generates a pi-bond. A maximum bond order of three can be thus achieved from one s and two perpendicular p-orbitals generating one sigma and two pi bonds (bonding electron configuration, $\sigma^2\pi^4$).

The formation of the quadruple bond is made possible by the additional occupancy of d-orbitals in the transition metal elements. There are five d-orbitals the d_{xy} , d_{yz} , d_{xz} , $d_{x^2-y^2}$ and d_{z^2} (Figure 1.2). Four of these orbitals, all but the d_{z^2} have four lobes, so given the correct orientation could theoretically produce what is known as a δ bond through face on constructive overlap.

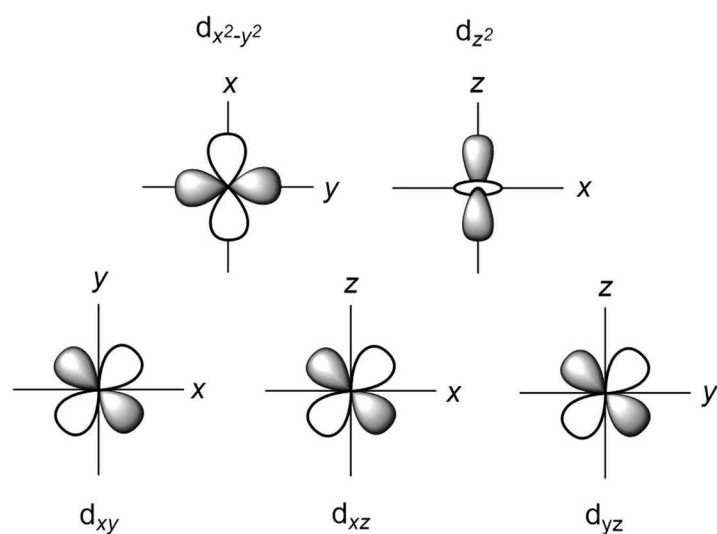


Figure 1.2. The five d-orbitals.

However, there are geometric constraints under which the quadruple bond can be formed. Figure 1.3 shows the molecular orbital diagram for a quadruple bond formed between two d^4 metal fragments. Each metal fragment is treated as having a square planar geometry, the energy levels of the atomic orbitals are as predicted by their crystal field and consider the two metal fragments being brought into bonding proximity with one another along the z-axis that runs directly through the centre of the square plane. Valence bond theory tells us the strongest bonds are those formed with the largest degree of orbital overlap. As such we can see the d_{z^2} orbitals, which are aligned head-to-head along this bonding axis will generate a strong σ bond. The next strongest bonds will be those formed from the orbitals that have some alignment along the z-axis, i.e. the d_{xz} and d_{yz} orbitals which will each form a π bond. The face-on-face alignment of the four lobes of the d_{xy} orbitals will then generate the comparatively weak δ bond. The $d_{x^2-y^2}$ orbitals of the metal are simply too high in energy to be involved in metal-metal bonding and instead are only involved metal-ligand bonding. The overall bonding electronic configuration for a formal quadruple bond is therefore $\sigma^2\pi^4\delta^2$.

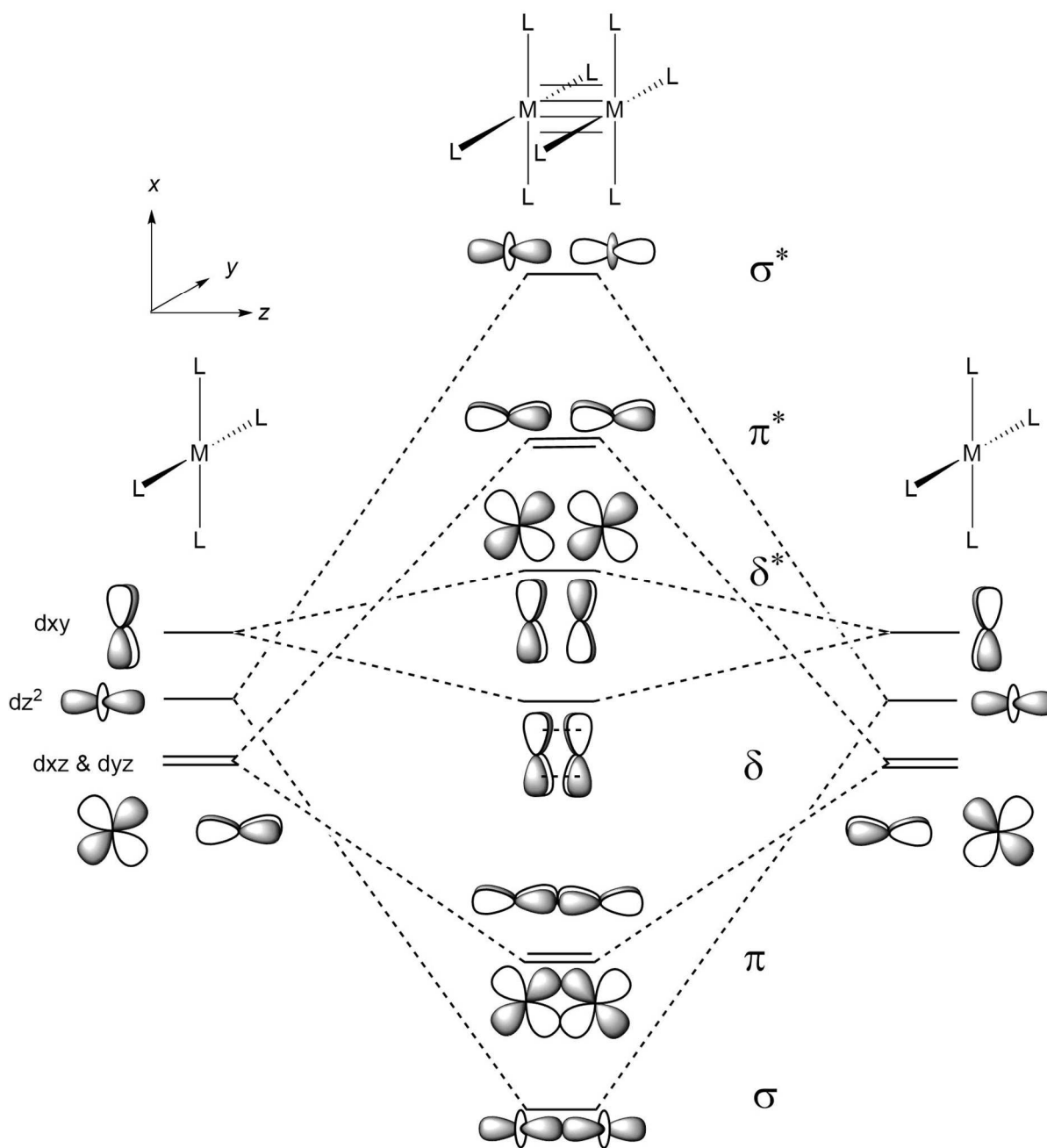


Figure 1.3. Molecular orbital diagram for a quadruple bond.

The molecular orbital diagram illustrates the propensity for quadruple bonded complexes to have their ancillary ligands in an eclipsed conformation. There is a large rotational barrier that exists for the δ bond whereas the σ and π bonds remain unaffected. Group theory allows us to relate the rotation about the z-axis to the extent of orbital overlap. The overlap is greatest, and hence bonding the strongest when there is no rotation. As the twist angle increases, orbital overlap and therefore bond

strength diminishes. Around 50 % of the bond strength is lost after a 30 ° rotation, with a much more rapid decrease in bond strength thereafter. This is merely a preference though as the strength of the δ -bond is just one thermodynamic contribution and ligand steric interactions can account for small twists of up to around 10 °.⁸

Molybdenum accounts for the highest proportion of known quadruple bonded di-metal complexes but they are also observed for Cr, W and Re.^{3,8} In a Mo_2 quadruple bond the HOMO is the fully occupied δ . Many of these complexes can produce stable often isolable one electron oxidation products ($\sigma^2\pi^4\delta^2 \rightarrow \sigma^2\pi^4\delta^1 \rightarrow \sigma^2\pi^4\delta^0$). This oxidation often displays excellent reversibility in electrochemical techniques making them ideal redox active moieties in the study of electron-self exchange mechanisms (discussed hereafter), namely through the synthesis and characterisation of mixed valence compounds (defined later).

1.2 Electron-Self Exchange Reactions

1.2.1 *Inner Sphere and Outer Sphere*

An electron self-exchange reaction is that in which electron transfer (ET) occurs between identical chemical species that differ only in their oxidation state. The reactant and products of the reaction are identical. The redox active moieties in the reaction could be metal atoms; in a coordination complexes or enzyme or they could be a simple organic fragment.

The ET between the two redox centres can occur via an outer- or inner-sphere mechanism. In an outer-sphere reaction separate chemical species come together by diffusion and the electron can tunnel from the orbitals of one redox centre to another. The Frank-Condon principle states that electron transfer is so fast that atoms are essentially stationary during the process.⁹ Because the product and reactants are equivalent, the energy of the exchanging electron before and after transfer will be identical. This forms the basis of Marcus Theory and means the reaction can be described by a symmetrical double well potential energy surface (Figure 1.4). Where the wells cross, the thermal vibrational motions have brought the two reactant parabolas to equal energy and ET can occur.¹⁰

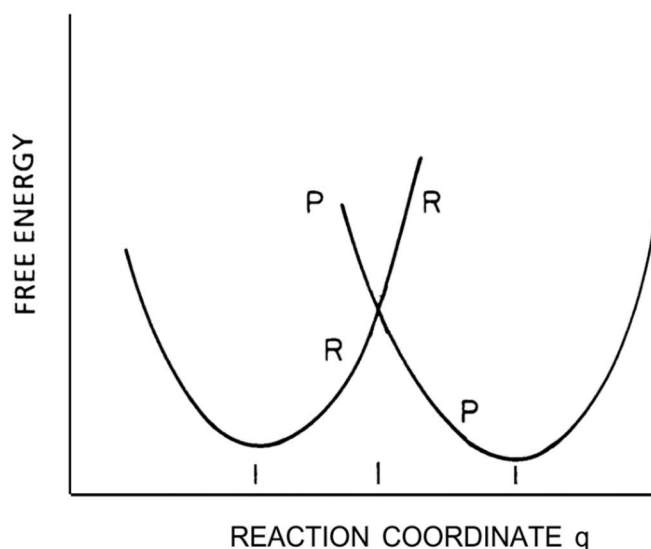


Figure 1.4. Double-well PES's of the reactant (R) and product (P) in an electron-self change reaction. Vertical lines on the reaction coordinate (q) denote from left to right, the energy minima of the reactants, transition state and products. Figure reproduced from reference with permission from Wiley & Sons.¹⁰

In an inner-sphere reaction the two redox centres are bridged covalently by some functionality capable of conveying electron motion. Typically, this bridge will be a ligand having lone pairs or a conjugated π -system. Where the redox centres are initially independent chemical species in a cross-exchange reaction this ligand must be labile and the formation of the bridge is implicit in a transition state. During her PhD supervision by Henry Taube, Carol Creutz synthesized a model complex for such bridged intermediates, $[(\text{NH}_3)_5\text{Ru-pz-Ru}(\text{NH}_3)_5]^{5+}$ (pz = pyrazine), dubbed the Creutz-Taube Ion (Figure 1.5) first reported in 1969.^{11,12} Here the bridging ligand is covalently bonded to both redox centres. This was the first deliberate synthesis of a mixed valence compound. The intuitive design of the Creutz-Taube ion highlights the intriguing nature of mixed valence compounds posing the fundamental question: how exactly is the 5+ oxidation state split across the two ruthenium centres?

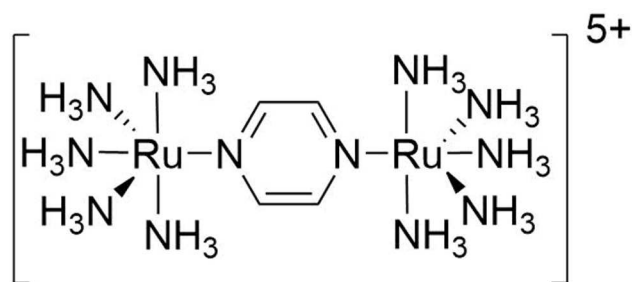


Figure 1.5. The Creutz-Taube Ion.

1.3 Mixed Valency

The simplest definition of a MV compound is a compound that contains two or more redox active centres having different oxidation states. More specifically it is used to describes complexes in which the redox active sites are in electronic communication as to allow electron delocalisation and stabilisation a MV state generated by a redox event. Spectroscopic analysis of these complexes allows us to monitor electron transfer, arguably the single most fundamental concepts in the chemical sciences. For this reason, there is much interest into the synthesis of MV compounds as it allows us to fully understand ET processes leading to advances in a wide variety of fields such as solar energy conversion and molecular electronics.¹³⁻¹⁵ To aid visualisation of the concept consider the metal-bridge-metal motif where the only redox active moieties are the metal sites. Upon single electron oxidation or reduction, the system can now be viewed as an electron donor-bridge-acceptor (Figure 1.6), a mixed valence complex. The identities of the metal, the metal coordination sphere and the bridge will all affect the extent of electronic communication between the donor and acceptor, and as such the extent to which the unpaired electron is delocalised. The two extremes and intermediary can easily be visualised and form the basis of the Robin-Day classification system.¹⁶

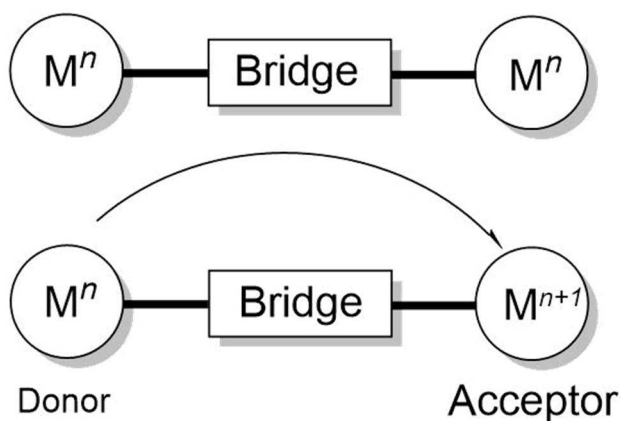


Figure 1.6. M^n -Bridge- M^n motif when oxidised generates M^n -Bridge- M^{n+1} , an electron Donor-Bridge-Acceptor model.

When there is no electronic communication, the odd electron remains entirely localised at one site, this is defined as Class I. When there is “poor” electronic communication, the electron is unevenly distributed across the two redox sites, this is Class II. When the communication is very strong, the odd electron is fully delocalised across the two redox centres and so each can be assigned an equal, non-integer oxidation state, this is Class III. The actual extent of electronic communication is determined by use of Marcus-Hush theory and will be discussed in relation to each class of compound below.

1.4 Robin-Day Classification System

1.4.1 Class I: Valence Trapped

In this class each redox centre in the molecule has a distinct integer oxidation state. The PES of the reactants; M^+ -bridge- M and M -bridge- M^+ are diabatic (non-interacting) as presented in Figure 1.7. There is no electronic communication between the two centres and as such they cannot be interconverted. Compounds in this class can potentially be distinguished crystallographically as the bond lengths associated with each metal centre will be slightly different.

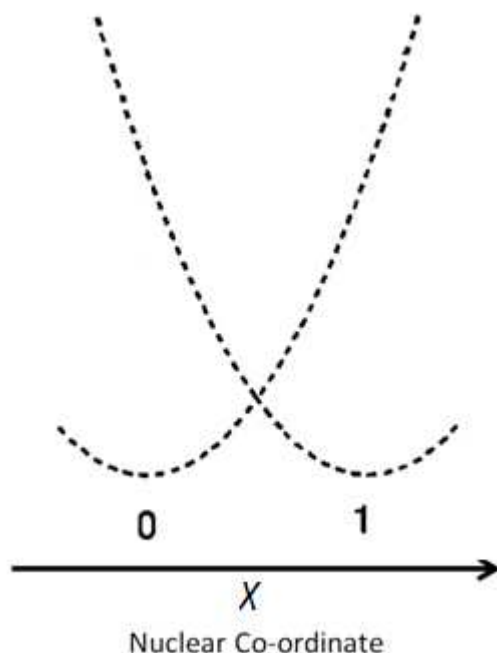


Figure 1.7. Potential energy diagram for a Class I “valence trapped” complex. Dotted lines are diabatic PES’s for the model complexes M^+ -bridge-M (centred at 0) and M-bridge- M^+ (centred at 1). Figure adapted from reference with permission from John Wiley & Sons. ¹⁷

1.4.2 Class II: Mixed Valence

Within this regime the extent of communication is such that there is partial delocalisation. Alternatively, we can view the charge as being localised until sufficient energy is provided to overcome ΔG^\ddagger , the Gibbs Free energy of the formation of the transition state (see Figure 1.8) allowing thermal transfer across the ground state PES. Optical excitation to the excited state PES can also result in ET.

In a Class II system the localisation of the odd electron is greater on one site than the other; M^{n+} -bridge- $M^{(1-n)+}$ where $0.5 < n < 1$. These systems can be described by a two-state potential energy diagram as in Figure 1.8 but sometimes a three-state model where the PES for the bridging ligand is included is more suitable. The dotted potential energy surfaces centred on the reaction coordinate at $\chi = 0$ and $\chi = 1$ represent the diabatic state of the two extremes of oxidation state; i.e. M^{n+} -bridge- $M^{(1-n)+}$ and $M^{(1-n)+}$ -bridge- M^{n+} . Unlike in the Class I system we now see mixing of these wave functions at $\chi = 0.5$ and the two resulting adiabatic surfaces are now degenerate. The energy difference between

these two states at $\chi = 0.5$ gives the electronic coupling parameter, H_{ab} (or just H) which is a direct measure of the overlap of donor and acceptor wavefunctions. In the Class II regime $2 H_{ab} < \lambda$, where λ is the reorganisation energy. This reorganisation energy is similar to the ν_{\max} of the Inter-Valence Charge Transfer (IVCT) transition that is observed in the near-IR (NIR). The relationship between the IVCT band and electronic coupling parameter (H_{ab}) will be discussed in further detail in section 1.4.1.1

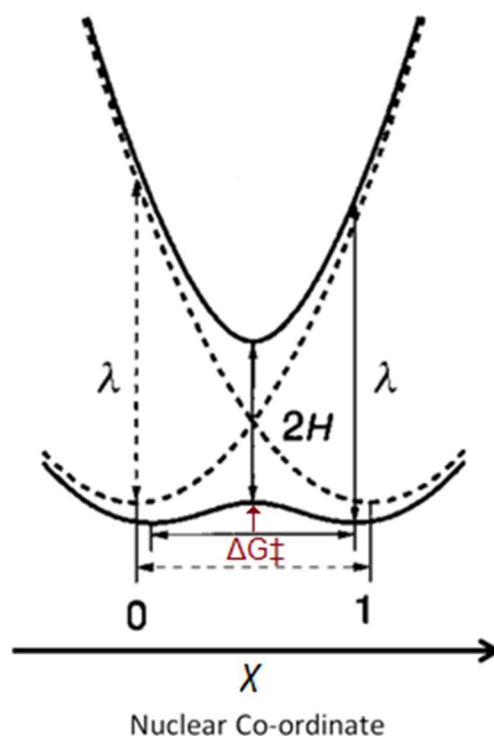


Figure 1.8. Potential energy diagram for a Class II mixed valence complex. Dotted lines are the diabatic PES's and solid lines the adiabatic PES's. H is the electronic coupling parameter and λ the reorganisation energy and is equal to the energy of the IVCT. Figure adapted from reference with permission from Wiley & Sons.¹⁷

A number of Creutz-Taube analogues¹⁸, for instance $[(\text{CN})_5\text{Ru}(\text{pz})\text{-Ru}(\text{CN})_5]]^{5+}$, Ru(II) 2,2'-bipyrimidine complexes¹⁹ i.e. $[(\text{bipy})_2\text{Ru}(\text{bipy})\text{Ru}(\text{bipy})_2]^{4+}$ and acetylene bridged tetra-ferrocene complexes²⁰ fall within the Class II regime.

1.4.3 Class III: Electron Delocalised

In this regime the extent of communication is so great that there is total delocalisation between the redox sites and no activation barrier to electron transfer exists so $\Delta G^\ddagger = 0$. The PES diagram for this

class is shown in Figure 1.9. Twice the electronic coupling parameter is now equal to or greater than the reorganisation energy, $2 H_{ab} \geq \lambda$.

A NIR transition is still observed but becomes sharper, less Gaussian in shape and more intense. It is now often referred to as a Charge Resonance band rather than an IVCT because there is no longer a change in net dipole. For this reason, the transition also no longer shows solvent dependence.

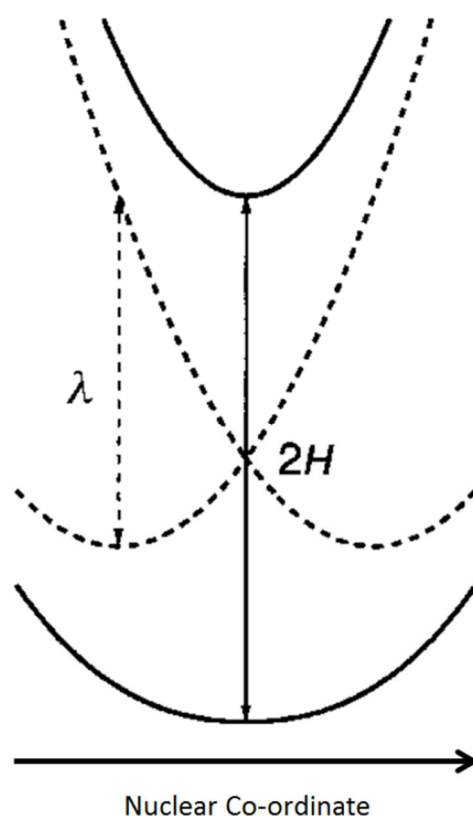


Figure 1.9. Potential energy diagram for a Class III “electron delocalised” mixed valence complex. Dotted lines are the diabatic PES’s. The solid lines are the adiabatic PES’s having a single energy minimum. H is the electronic coupling parameter and λ the reorganisation energy. Figure adapted from reference with permission from Wiley & Sons.¹⁷

The “carbon only” bridged half-sandwich complexes; $[\{\text{Cp}^*(\text{dppe})\text{Ru}\}(\mu\text{-C}\equiv\text{CC}\equiv\text{C})\{\text{Ru}(\text{dppe})\text{Cp}^*\}]^+$, $[\{\text{Cp}(\text{PPh}_3)_2\text{Ru}\}(\mu\text{-C}\equiv\text{CC}\equiv\text{C})\{\text{Ru}(\text{PPh}_3)_2\text{Cp}\}]^+$ and $[\{\text{Cp}^*(\text{NO})(\text{PPh}_3)\text{Re}\}(\mu\text{C}\equiv\text{CC}\equiv\text{C})\{\text{Re}(\text{PPh}_3)(\text{NO})\text{Cp}^*\}]^+$ are classic examples of Class III compounds originally reported in in the early 90’s by Laptine.²⁰ The Os analogue of the Creutz-Taube ion; $[(\text{NH}_3)_5\text{Os}(\text{-pz-})\text{Os}(\text{NH}_3)_5]^{5+}$ is similarly categorised as a Class III compound.^{21,22}

1.4.4 Spectroscopic Methods

Initial classification into the Robin-Day classification system in the 1960's was made possible using recent advances and availability of X-ray crystallography. But the utility of this technique varies largely from compound to compound. A wide range of spectroscopic methods have now superseded this. These methods are not only more convenient but a much more effective means of quantification for the stabilisation of the MV state. Most frequently employed is electronic absorption spectroscopy in the UV-Vis and NIR region which with application of Hush theory allows the degree of electronic coupling to be directly measured. Thermodynamic stabilisation of the MV state can also be quantified using electrochemistry, namely cyclic voltammetry.

1.4.4.1 UV-Vis & UV-Vis NIR spectroscopy.

Both the UV-Vis and NIR portion of the absorption spectra give information to the extent of electronic communication. For Class I systems the UV-Vis portion of the spectra shows transitions associated with the two-independent components. Class II systems not only show the transitions for the individual components but an additional IVCT transition in the NIR region. Class III systems the UV-Vis region shows transitions that are a mixture of the two components plus a charge resonance band in the NIR. Application of Marcus-Hush theory to these NIR transitions is arguably the ultimate means of quantifying electronic communication in mixed valence systems.

For a Class II system the energy of an IVCT band is approximately equal to that of the reorganisation energy (λ) between the ground and excited state. Analysis of the IVCT band can therefore be related to the electronic coupling parameter H_{ab} using equation 1.1, where d (Å) is the electron transfer distance, usually approximated to the internuclear separation of the redox centres, $\bar{\nu}_{max}$ (cm^{-1}) the absorption energy, $\Delta\bar{\nu}_{1/2}$ (cm^{-1}) the peak width at half height and ϵ_{max} ($\text{M}^{-1} \text{cm}^{-1}$) the absorption intensity.

$$H_{ab} = \left(\frac{0.0206}{d}\right) \cdot (\bar{\nu}_{max} \Delta\bar{\nu}_{1/2} \epsilon_{max})^{1/2} \quad \text{eqn. 1.1}$$

When coupling increases the reorganisation energy approaches zero as we enter the class III regime and the Charge Resonance band is now a direct measure of electronic coupling and can be related to H_{ab} using equation 1.2.

$$H_{ab} = \frac{\bar{\nu}_{max}}{2} \quad \text{eqn. 1.2}$$

1.4.4.2 IR Spectroscopy

Kubiak in collaboration with Ito also developed a novel spectroscopic method for estimating the rate of ET in MV complexes, provided that the rate is very fast (10^{10} - 10^{13} s⁻¹); IR spectroelectrochemistry (IRSEC) coalescence.²³ This method is essentially analogous to dynamic NMR spectroscopy (DNMR) commonly used to study fluxional processes such as Berry pseudo-rotations²⁴⁻²⁶ but occurring on a timescale 10^6 times faster. The principle behind a dynamic method is that the frequency shift between the two chemical shifts can be used to determine the dynamics of the chemical exchange process. For spectral coalescence to occur the rate of the dynamic process must be approximately the difference in frequency between the two spectral bands in the absence of exchange.

1.4.4.3 Electron Paramagnetic Resonance

Electron Paramagnetic Resonance (EPR) sometimes called Electron Spin Resonance ESR (ESR) is a method analogous to Nuclear Magnetic Resonance, where it is the spin state of electrons as opposed to atomic nuclei that are exploited spectroscopically.²⁷ It is used to study materials with unpaired electrons (those that are paramagnetic) commonly metal complexes or organic radicals.

The unpaired electron(s) in the analysed complex are not however disjointed from the complex itself, they are in fact subject to the magnetic fields of atomic nuclei, other paramagnetic species, the ligand field and electric quadrupoles. So just as atomic nuclei are shielded or de-shielded by neighbouring nuclei giving rise to chemical shift in NMR. The unpaired electrons are also influenced by their local environment in EPR and this is represented in changes in the observed g-factor.

Interaction with the magnetic field of local nuclei also gives rise to splitting of observed signals, known as hyperfine splitting. This is analogous to splitting observed in NMR and we can predict the number

of observed peaks, when coupling to a given nuclei in the same manner using the $2NI+1$ rule. Where N is the number of equivalent nuclei and I is the nuclear spin. This can give information regarding the number of atomic isotopes and the separation between a given atom and the measured electron. In the study of MV complexes this can be used to determine the degree of localisation of the odd electron in the MV state.

EPR is useful in the study of Mo_2 complexes because molybdenum has two spin active isotopes; ^{95}Mo and ^{97}Mo each with nuclear spin $I = 5/2$ and have a combined spin abundance of approximately 25 %. The remaining 75 % is $I = 0$ ^{96}Mo . We can therefore predict a single symmetric peak for the latter component with hyper fine splitting for the ^{95}Mo and ^{97}Mo isotopes. Various authors have demonstrated that in complexes of the form $[\text{Mo}_2(\text{DAniF})_3]-(\text{L})-[\text{Mo}_2(\text{DAniF})_3]^+$ the hyperfine coupling constants obtained can be related to the localisation of the odd electron and correlate well with the extent of electronic coupling as determined by UV-Vis NIR or stabilisation of the MV state by CV. Small hyperfine coupling constants (A) are typically observed in delocalised systems such as when $\text{L} = (\text{C}_6\text{H}_2\text{O}_4)$ ($A = 12$ G) (Figure 1.10, top). Larger hyperfine coupling constants are typically observed in localized systems, for instance in the weakly coupled $\text{L} =$ perfluoroterephthalate (PFT) system ($A = 27.2$ G) (Figure 1.10, bottom).

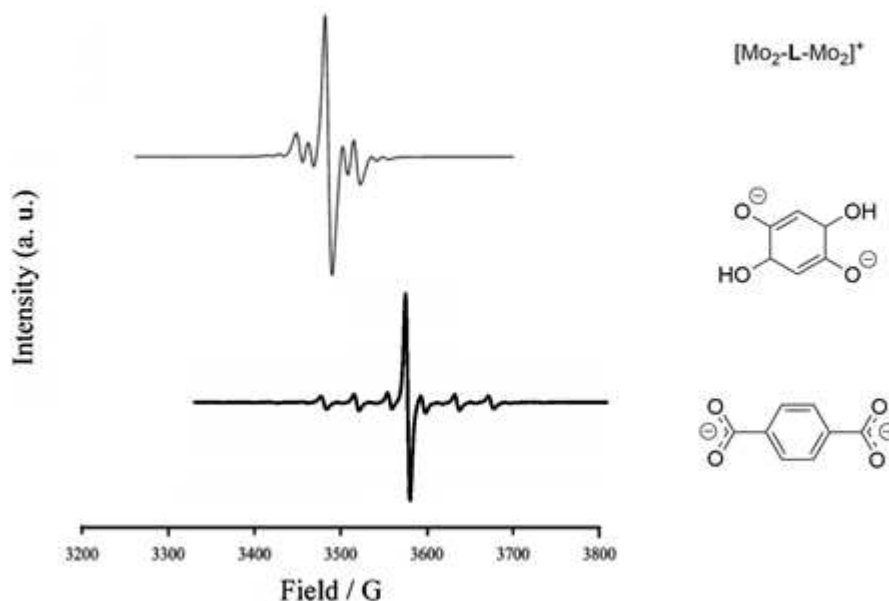


Figure 1.10. X-Band EPR spectra of $[\text{Mo}_2(\text{DAniF})_3]-(\text{C}_6\text{H}_2\text{O}_4)[\text{Mo}_2(\text{DAniF})_3]^+$ in DCM at room temperature (top) and $[\text{Mo}_2(\text{DAniF})_3]-(\text{PFT})-[\text{Mo}_2(\text{DAniF})_3]^+$ in THF/DCM at room 210 K (bottom). Figures adapted from reference with permission of the ACS and RSC respectively.^{28,29}

1.4.5 Electrochemical Methods

Using electrochemical techniques, the mixed valence state can be generated upon oxidation or reduction of the neutral complex by one electron. In cyclic voltammetry (CV) these redox processes will generate a current response at their associated potentials. Information on the reversibility of the redox events can be gathered from current response ratios and peak separation. Consider the cyclic voltammogram of $[(\text{DAniF})_3\text{Mo}_2\text{-O}_2\text{CCO}_2\text{-Mo}_2(\text{DAniF})_3]^{30}$ presented in Figure 1.11. The mixed valence state $[\text{Mo}_2]_2^+$ is generated upon oxidation. Where no electronic communication exists, the oxidation of the second metal centre or double oxidation of the same metal centre would be equally favoured and so only a single peak will be observed with twice the current response. When electronic communication exists between the two metal centres (as demonstrated below); after the first oxidation the second metal centre can effectively sense this change and becomes more difficult to oxidise again. This leads to a separation between the two oxidations. The potential of the individual redox events is denoted as $E_{1/2}$ and the separation, $\Delta E_{1/2}$.

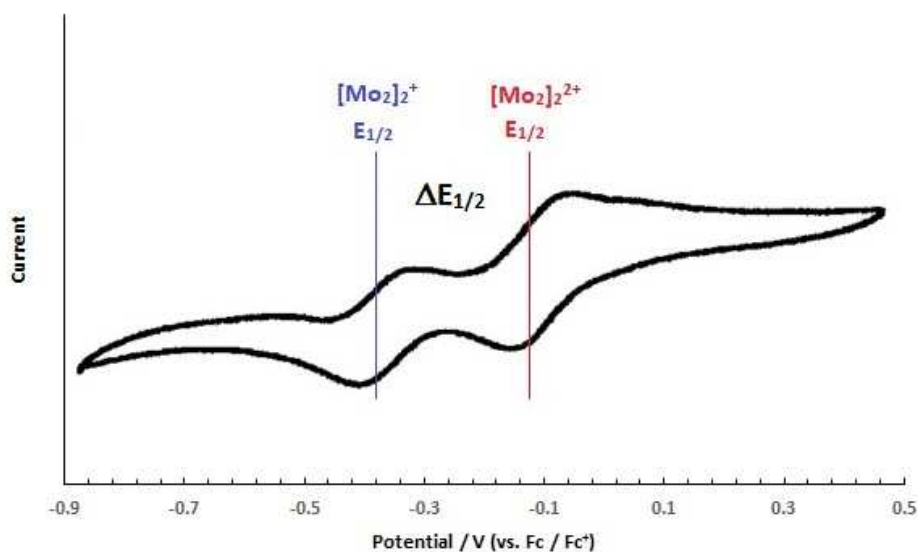


Figure 1.11. CV of (DAniF)₃Mo₂-O₂CCO₂-Mo₂(DAniF)₃ using 0.1 M tetrabutylammonium hexafluorophosphate (TBAPF) in DCM at 100 mVs⁻¹ scan rate. Referenced vs the Fc/ Fc⁺ redox couple with arbitrary current axis. Reproduced from reference with permission of the ACS.³⁰ Figure was annotated to show the generation of the [Mo₂]⁺ and [Mo₂]²⁺ states and the information that is required to determine K_c .

This separation is proportional to the stabilisation of the mixed valence state. This stabilisation can be expressed as an equilibrium with respect to disproportionation to the neutral and doubly oxidised species having the equilibrium constant K_c , as per equation 1.3. This can in turn be related to information that can be taken directly from the cyclic voltammograms by the Nernst Equation as per equation 1.4. $\Delta E_{1/2}$ is the splitting taken from the CV measurement in V, R is the gas constant ($\text{J mol}^{-1} \text{K}^{-1}$), T the temperature of the measurement in K, F is Faraday's constant and n_1 and n_2 the number of electrons involved in each redox process.

$$K_c = \frac{[(M-B-M)^+]^2}{[(M-B-M)][(M-B-M)^{2+}]} \quad \text{eqn. 1.3}$$

$$K_c = \exp\left(\frac{\Delta E_{1/2} n_1 n_2 F}{RT}\right) \quad \text{eqn. 1.4}$$

Being a thermodynamic property, K_c is an indirect measure of electronic coupling not a direct measure of orbital overlap as per H_{ab} . So, while the magnitude of K_c is a good approximation to electronic coupling cyclic voltammetry alone cannot be used to clearly distinguish between Class II and Class III systems, though typically K_c values greater than 10^6 are considered to be strongly coupled. The

electrochemical value can only be related to the electronic coupling H_{ab} reliably when the effects of exchange outweigh the electrostatic effects in the charged ions.³¹

1.5 Literature Study of Mixed Valence Complexes

Mixed Valence compounds have been a staple of inorganic chemistry journals for nearing 60 years since the publication of the Creutz-Taube ion and one would expect the theoretical underpinning of field to be well established. But in the words of Kubiak "...the most elementary questions about mixed valency have also been some of the most difficult to answer..."³² Many compounds since discovered do not fit into the rather rigid classical representation of the Robin Day system and continue to push the boundaries of our understanding.

Rather ironically, the Creutz-Taube ion is now thought to be a Class II-III borderline complex, meaning it appears to be Class II or Class III dependent upon the conditions in which it is studied and the rate of ET in the complex has yet to be defined. This fundamental measurement is important as it relates directly to the activation energy which in turn informs us of the ground state electronic potential energy surface.

The reason it was not initially defined is that it is in fact a very difficult experiment to perform. When we consider there is no net chemical change between reactant and product the dynamic process must instead be probed. Furthermore, when we consider the extremely fast ET rates associated with strongly coupled systems. There are a host of thermal and solvent motions to which ET can couple and it is for this reason that the ET process is so highly sensitive to the conditions in which it is studied.

1.6 Solvent and Temperature Effects on Rate of Exchange.

Meyer *et al.* first proposed how to distinguish between Class II, Class II-III and Class III systems based on three types of motion; solvent, vibrational and electronic and how they behave in an exchanging system.³³ In Class II, the solvent and exchanging electron are localised. In Class II-III the solvent is averaged, and the exchanging electron is localised. In Class III the solvent and vibrations are averaged, the exchanging electron is delocalised. The consequence being that the IVCT band appearance in Class

II-III systems is intermediate between that of Class II and the narrow bands found with solvent averaging for Class III.

There are two components to solvent reorientation each with an associated timescale for relaxation. Firstly, the slow diffusive motions being the collective reorientation of the local solvent molecules. Secondly, the ultra-fast single molecule rotations referred to as inertial motions. If the solvent is averaged (Class II-III or Class III) the ET rate is faster than even the ultra-fast solvent component, so a considerable fraction of the solvent polarization can couple to electron transfer on the sub-picosecond timescale.

The relaxation times of many common solvents have been determined using ultrafast laser flash photolysis. But the exact relationship between each component and solvent averaging by ET is not well understood.³⁴ The specific interactions of solvents and ligands, for example H-bonding appear to have major consequences. Some computational studies to this effect show that the timescale for these interacting solvent molecules would be considerably slower even than the bulk solvent diffusive motions. Ultimately, these details are beyond the scope of this work, and while most systems have to be judged on a case-by-case basis the information provided by such analysis is invaluable.

1.6.1 *Class II to Class II-III Transitions.*

The transition between Classes II and II-III is tied to the onset of dynamical coupling of solvent dipole reorientations to intramolecular ET. The complex to first inspire research into this area came from a non-traditional mixed valence complex; $[\text{cis}-(\text{bpy})_2(\text{Cl})\text{Os}(\text{pz})\text{Ru}-(\text{NH}_3)_5]^{4+}$.^{35,36} This complex can exist as two oxidation-state isomers: $\text{Os}^{\text{II}}-\text{Ru}^{\text{III}}$ or $\text{Os}^{\text{III}}-\text{Ru}^{\text{II}}$.

The $\text{Os}^{\text{II}}-\text{Ru}^{\text{III}}$ isomer is a Class II compound, favoured in strong Lewis basic solvents such as DMSO or DMF that hydrogen bond strongly to the ammonia ligands. Two overlapping, broad, solvent dependent IVCT bands are observed in the NIR. Changing the solvent from DMSO or DMF to CH_3CN or D_2O induces $\text{Os}(\text{III})$ to $\text{Ru}(\text{II})$ electron transfer.

The Os^{III}-Ru^{II} isomer is instead a Class II-III compound. The NIR IVCT band in CH₃CN is asymmetrical on the high energy side and still appears to be the convolution of two bands but an additional peak in the IR characteristic of $\nu(\text{bpy})\text{Os}^{\text{III}}$ indicates there is still electronic localisation.

The fact that a simple change of solvent was sufficient to induce electron transfer inspired research into how solvent would affect ET in traditional MV complexes where the redox active sites are identical.

1.6.2 Class II-III to Class III Transitions.

For a Class II-III complex the solvent modes are averaged but the intramolecular vibrations are not. So the complex should show properties of both a Class II and Class III complex if the rate constant for ET, k_{et} is intermediate between the solvent reorganisation frequency ($10^{11} - 10^{12} \text{ s}^{-1}$) and bond vibration frequencies ($10^{13} - 10^{14} \text{ s}^{-1}$).

In 1996 Meyer and Chen proposed that by using frozen solvents, solvent averaging can be totally decoupled from the ET leaving only the faster intramolecular vibrations. The electron transfer rate given by classical Marcus-Hush theory for a fluid system is given in equation 1.5. In a frozen, solid media the pre-exponential term, the transmission coefficient, ν_{ET} is expected to increase by at least an order of magnitude.³⁷ The result of which is that lowering the temperature of the solvent will in fact increase the rate of electron transfer, but only to the point at which the solvent freezes and no further.

$$k_{ET} = \nu_{ET} \exp[-\Delta G^* / RT] \quad \text{eqn. 1.5}$$

Indeed, Kubiak *et al.* provide experimental evidence to this effect for the series of complexes $\{[\text{Ru}_3\text{O}(\text{OAc})_6(\text{CO})(\text{L})_2(\text{pz})]\}^+$ where substitution of L = dimethylaminopyridine (dmap) for pyridine (py) for 4-cyanopyridine (4-CNpy) gives a gradual transition from Class II-III to Class III.³⁸ In all systems increased spectral coalescence (hence increased k_{ET}) is observed in the IR as the temperature approaches the freezing point of the solvent. As the solvent dependence of the system is removed, the faster internal vibrational modes dominate so the $\nu(\text{CO})$ band shape more strongly resembles that

of the Class III delocalised electronic structure. Coalescence of $\nu(\text{CO})$ bands for the 4-CNpy derivative in NCMe is shown in Figure 1.12

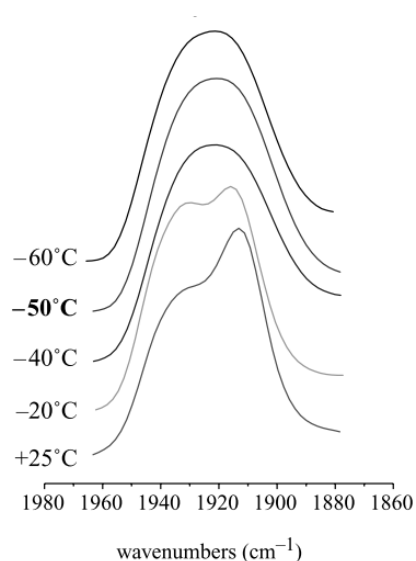


Figure 1.12. Gradual spectral coalescence observed for $\{[\text{Ru}_3\text{O}(\text{OAc})_6(\text{CO})(\text{L})]_2(\mu\text{-pz})\}$ as the solvent (NCMe) approaches freezing temperature. Figure adapted from reference. ³⁸

1.7 Effect of Bridging and Ancillary Ligand Alterations on ET rates.

From equation 1.2 we know the extent of electronic coupling in a system will be largely dependent on the intranuclear separation, r of the two redox centres. *Spangler et al.* report a series of diferrocenepolyenes of the form *trans*-Fc-(CH=CH) $_n$ -Fc where $n = 1$ to 6. A plot of $\log V_{ab}$ (equivalent to H_{ab}) vs. R_{MM} (Å) (equivalent to r) is shown in Figure 1.13. The slope is linear showing that electronic coupling decreases approximately exponentially with distance. The gradient of the solid slope shows that electronic communication decreases by a factor 2 for every 8 Å of separation.

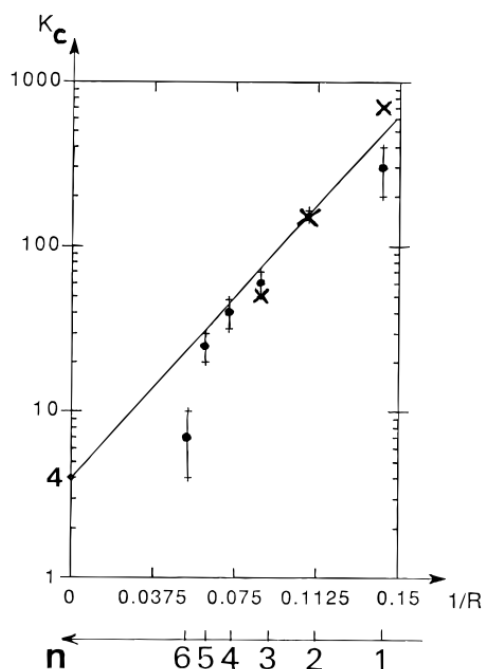


Figure 1.13. A plot of K_c (logarithmic scale) vs. $1/R_{MM}$ where R_{MM} is the intranuclear separation between the ferrocene redox centres.

A loss of conjugation however can account for much larger decreases in electronic coupling despite negligible changes in the internuclear separation. Consider the complexes $\{[Ru_3O(OAc)_6(CO)(dmap)]_2(\mu-B)\}^+$ where B is pyrazine (pz) or 4,4'-bipyridine (4,4'-bpy). The neutral complexes are $Ru_3^{III,III,II}$ where the carbonyl ligand is coordinated to the Ru^{II} centre. The reductive processes shown in the CV inform to inter-cluster mixed valence interactions which are of interest in the IRSEC study discussed hereafter. All reductions are one electron processes, where the neutral complex is first reduced to $[Ru_3^{III,III,II}-B-Ru_3^{III,II,II}]^+$ and then to $[Ru_3^{III,III,II}-B-Ru_3^{III,II,II}]^2+$. The splitting of these reductions corresponds to K_c values of 2.3×10^7 (B = pyrazine) and 1.1×10^2 (B = 4,4'-bpy). It is evident from these values the mixed valence state in the pyrazine derivative is much more thermodynamically stable.

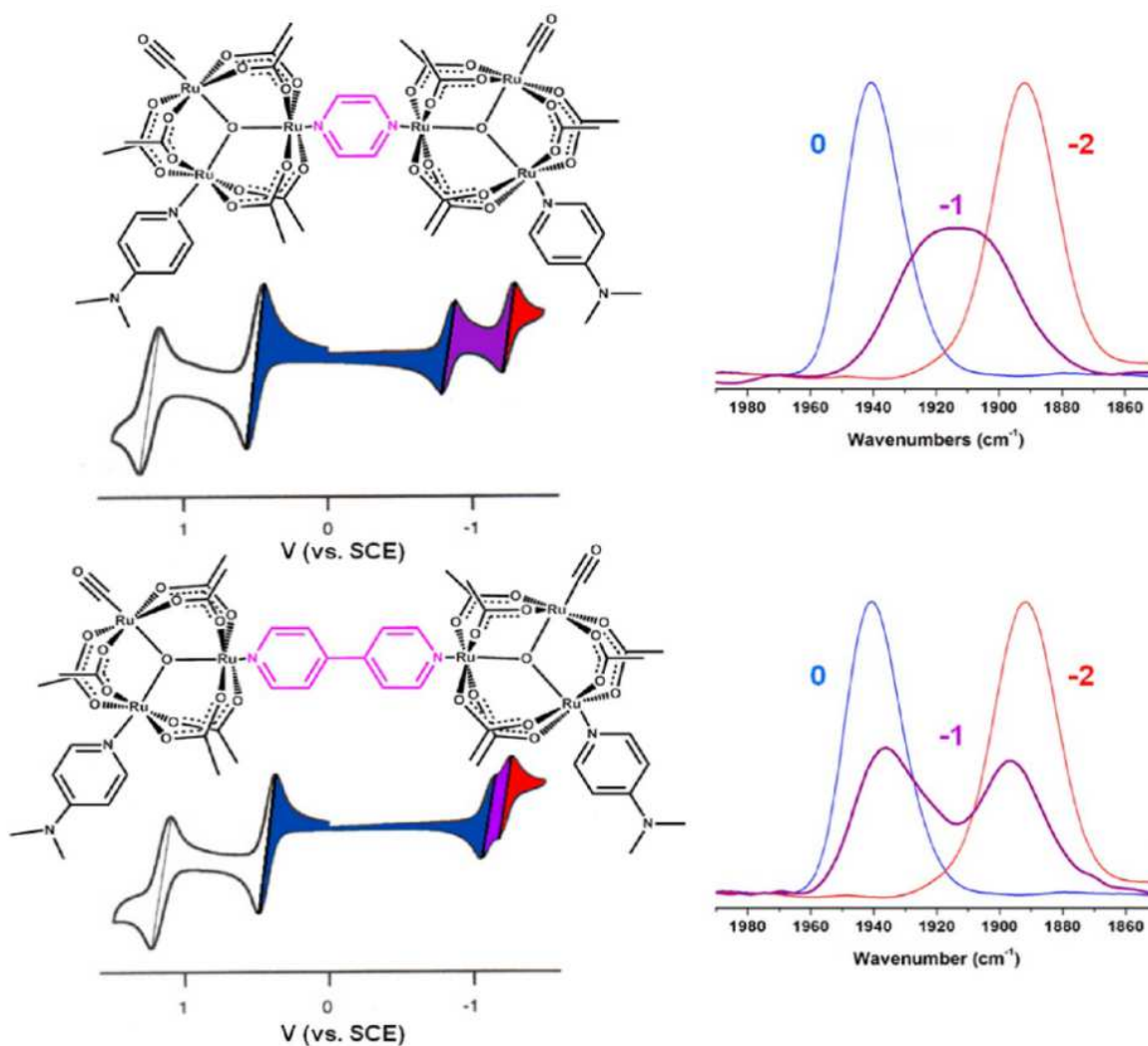


Figure 1.14. $[\text{Ru}_3\text{O}(\text{OAc})_6(\text{CO})(\text{dmap})]_2(\text{B})$ B = pz (top) and 4,4'-bpy (bottom) together with their corresponding CV's (left) and IR spectra (right). Coalescence of $\nu(\text{CO})$ bands is observed when B = pz but when B = 4,4'-bpy electronic communication is reduced resulting in localisation of the MV state on the IR timescale. Figure reproduced from reference with permission from the ASC.³²

The use of IRSEC allows the IR spectra of these individual oxidation states to be observed (Figure 1.14). The appearance of a single $\nu(\text{CO})$ at approximately 1940 and 1840 cm^{-1} for the neutral and doubly reduced species respectively is observed. This shows that changing the bridging ligand has very little effect on coordination environments of each half of the complexes in either the neutral or doubly reduced species.

By contrast, in the mixed valence state, the two complexes display drastically different IR spectra. A single Gaussian shaped IR band is observed for the pyrazine derivative. The coalesced line shape demonstrates that exchange in the mixed-valence state is delocalized on the IR time scale. The two observed peaks are separated by 50 cm^{-1} or $1.5 \times 10^{12}\text{ s}^{-1}$ in frequency so ET should occur on the picosecond timescale. By contrast, the 4,4'-bpy derivative shows two separate $\nu(\text{CO})$ bands having appearance composite of the bands in the neutral and doubly reduced species. This indicates that the mixed valence state in this complex is instead localised on the IR spectroscopy timescale. The decrease in π -conjugation thus produces a more rapid diminishing of electronic coupling compared to the purely an increase in internuclear separation as demonstrated in the works of Spangler *et al.* described previously.

The ET transfer rate is similarly affected by changes in the ancillary ligand (L). Substitution of L = dmap for pyridine (py) and 4-cyanopyridine (4-CNpy) in $[\text{Ru}_3\text{O}(\text{OAc})_6(\text{CO})(\text{L})_2(\mu\text{-B})]$ was investigated. The pyridine ring is substituted with a progressively stronger electron-withdrawing substituent, so in turn becomes a weaker donor ligand. Qualitative molecular orbital representations with corresponding simulated IR and calculated exchange rates are presented in Figure 1.15. We can see that the weaker the donor the less spectral coalescence is observed resulting in slower exchange rates. This is rationalised by the following electronic structural model; the energy of Ru $d\pi$ levels of the mixed valence ions lie just below the energy of the π^* bridging ligand. So as the energy of the Ru_3 clusters decreases as the dmap is substituted for a weaker donor ligand, the energy separation from the bridging ligand increases. The model also accounts for the difference in ET rates between the pyrazine and 4,4'-bpy derivatives where L = dmap in both cases, as the π^* system in the 4,4'-bpy bridge is simply much higher in energy because of the loss of conjugation.

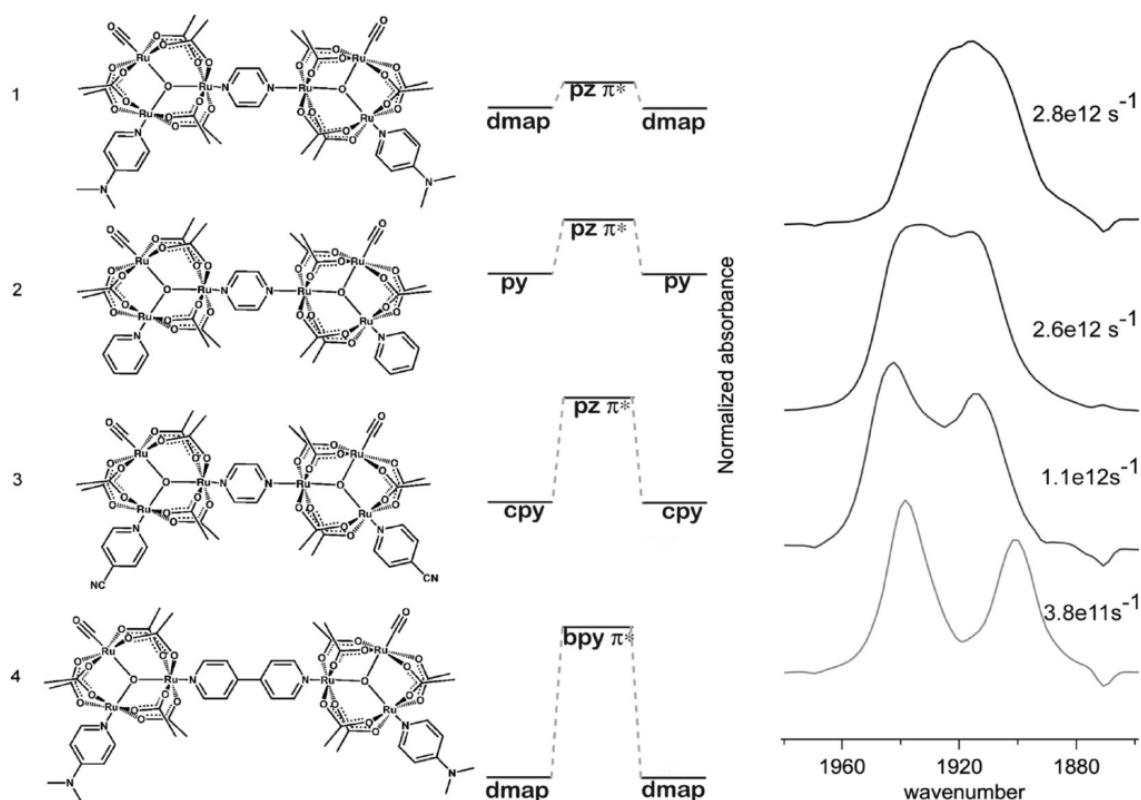


Figure 1.15. Simplified electronic structures for a series of $[\text{Ru}_3\text{O}(\text{OAc})_6(\text{CO})(\text{L})_2(\text{B})]$ complexes 1) $\text{B} = \text{pz}$ $\text{L} = \text{dmap}$ 2) $\text{B} = \text{pz}$ $\text{L} = \text{py}$ 3) $\text{B} = \text{pz}$ $\text{L} = 4\text{-CNpy}$ and 4) $\text{B} = 4,4'\text{-bpy}$ $\text{L} = \text{dmap}$ and their observed $\nu(\text{CO})$ IR bands. As the bridging ligand energy level is raised relative to the ML energy there is reduced communication and localisation on the IR timescale is observed. Figure reproduced from reference with permission from the ACS.³²

1.8 Mixed Valency in Di-Metal Paddlewheel Complexes

The quadruple bonded di-molybdenum and di-tungsten paddlewheels have been the primary redox active moieties of interest in our group for several years. The well-defined coordination geometry of the paddlewheel motif also allows for a range of structural derivatisations making them prime candidates for incorporation into coordination polymers and molecular electronic devices. This being the focus of our ongoing work in the group.

The electronic structure of the paddlewheel produces several interesting electronic transitions that are exploitable by several forms of spectroscopy and are informative of the mixed valence state. A

number of literature studies have been selected to highlight the specifics of spectroscopic analyses in these systems.

The simplest di-molybdenum MV complexes are the so called “dimer of dimers”. For instance, those reported by Chisholm *et al.* of the form $(\text{piv})_3\text{Mo}_2\text{-O}_2\text{CCO}_2\text{-Mo}_2(\text{piv})_3$ where piv = pivalate ion, $(^t\text{Bu})\text{CCO}_2^-$.^{4,39} The mixed valence state is strongly coupled (Class III) as there is extensive mixing of the $\text{M}_2\text{-}\delta$ with the $\text{C}_2\text{O}_4\text{-}\pi$ orbitals arising from both in- and out-of-phase orbitals combinations (Figure 1.16).^{40,41}

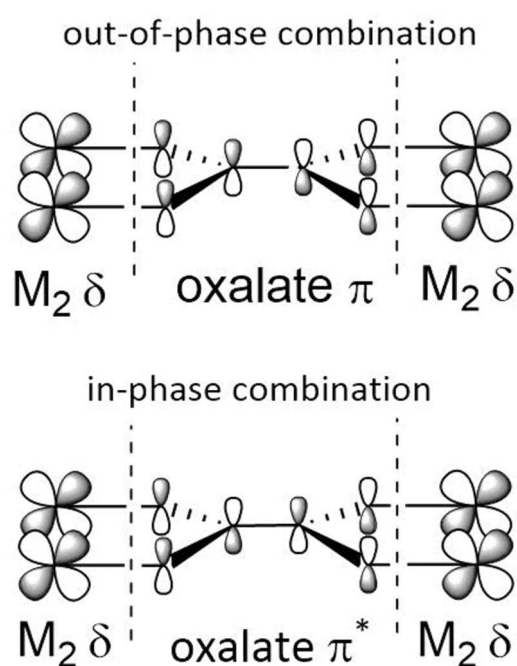


Figure 1.16. Possible orbital combinations for the $\text{M}_2\text{-O}_2\text{CCO}_2\text{-M}_2$ system.

The in-phase combination is the most important in terms of both energy and overlap considerations as the $\text{C}_2\text{O}_4\text{-}\pi^*$ it is closest to the $\text{M}_2\text{-}\delta$ orbitals. Consequently, when Mo atoms are substituted for W an increase in electronic coupling is observed, because despite a marginal decrease in the atomic radii (due to the lanthanide contraction) the energy levels of the W δ and oxalate π^* are more evenly matched. This is evident from the blue-shifting of the CR bands in the NIR region in Figure 1.17.

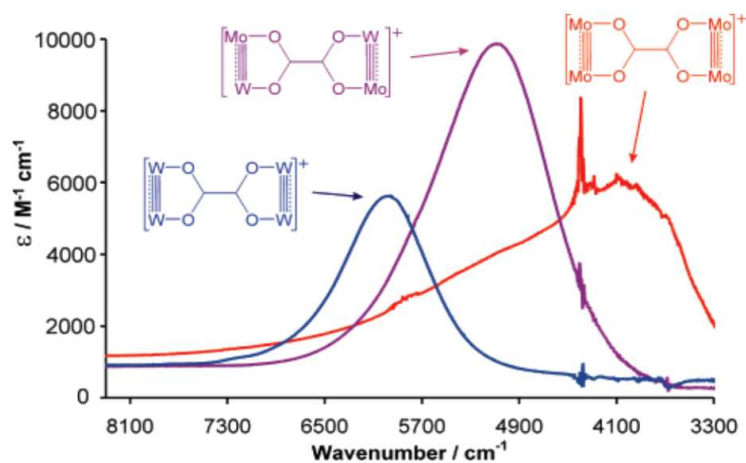


Figure 1.17. Shift in CR resonance bands due to increased coupling as Mo is substituted for W in the following series; $(\text{Piv})_3\text{Mo}_2\text{-O}_2\text{CCO}_2\text{-Mo}_2(\text{piv})_3$ (red) $(\text{piv})_3\text{MoW-O}_2\text{CCO}_2\text{-MoW}(\text{piv})_3$ and $(\text{piv})_3\text{Mo}_2\text{-O}_2\text{CCO}_2\text{-Mo}_2(\text{piv})_3$. Figure reproduced from reference with permission from the ACS.²⁷

A qualitative MO diagram for a strongly coupled $[\text{M}_2\text{-bridge-M}_2]^+$ species is presented in Figure 1.18 demonstrating the origin of the CR band and the other commonly observed electronic transitions observed for these species.

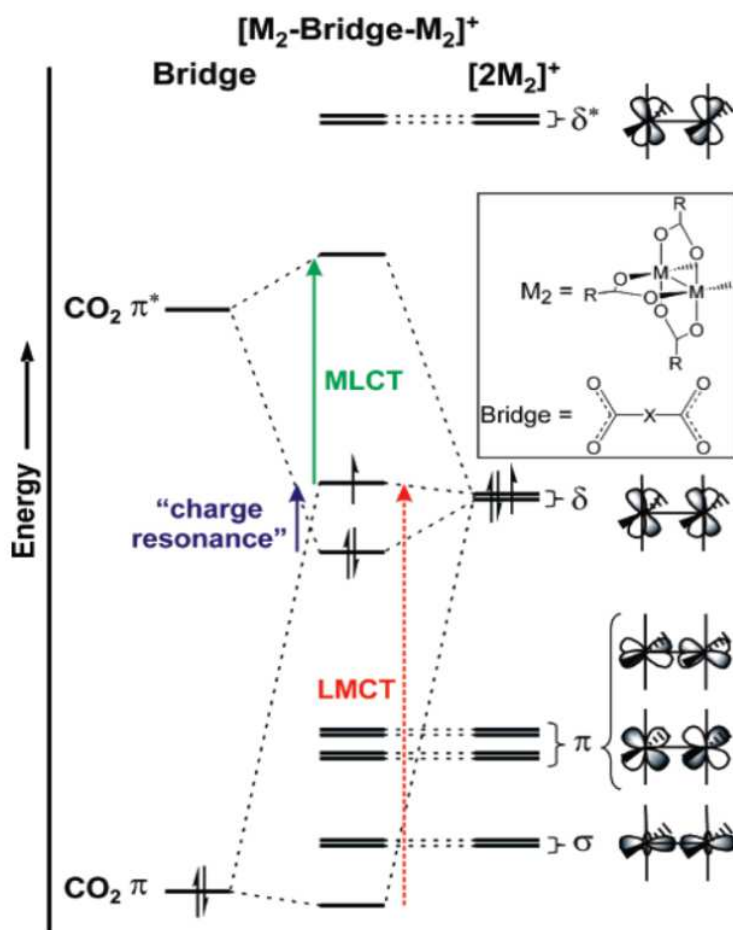


Figure 1.18. Qualitative frontier MO diagram for the MV state dicarboxylate bridged dimer of dimers; $[M_2\text{-bridge-M}_2]^+$ labelled with the important electronic transitions observed. Figure reproduced from reference with permission from the ACS.²⁷

A study by Liu *et al.* demonstrates rigorous analysis of the electronic absorption spectra for a range of thienylene bridged Mo₂(DAniF)₃ moieties.^{34,42} Where different coordinating atoms in the thiene bridging ligands; OO-thi-OO, NS-thi-NS, OS-thi-OS and SS-thi-SS (Figure 1.19) produce subtly different structures that demonstrate a systemic transition from Class II to the Class II-III borderline then into the Class III regime.

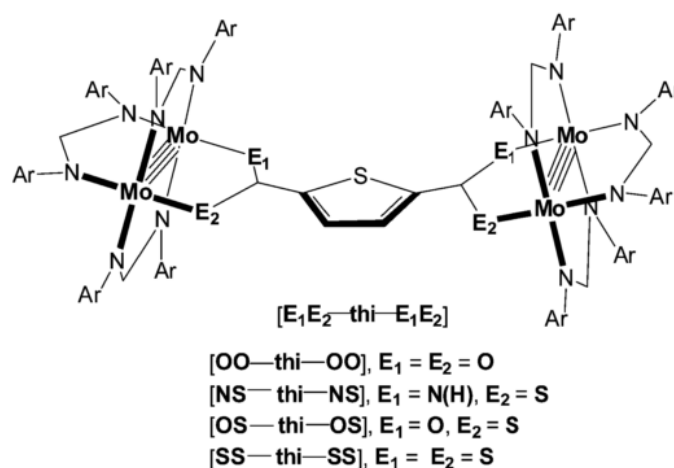


Figure 1.19. E₁E₂-thi-E₁E₂ bridged Mo₄ complexes reported by Liu et al. Figure reproduced from reference with permission of the RSC.³⁴ The ancillary ligands are DAniF where Ar = p-anisyl.

Consistent with work from the Patmore group substitution of N for O then for S coordinating atoms lowers the energy gap between the HOMO Mo₂-δ and LUMO π*. The decrease in HOMO-LUMO gap is observed in the UV-Vis spectra as lower energy, more intense MLCT transitions. An increase in electronic coupling is also evident from increasing ΔE_{1/2} values from cyclic voltammetry.⁴³ Upon oxidation these MLCT transitions will become shifted, but if the molecule is considered valence trapped it now formally contains a [Mo₂] and a [Mo₂]⁺ unit, so the latter should also demonstrate an LMCT. Indeed, for this series of complex both transitions are typically observed, albeit poorly resolved from one another in some cases. Generally, as electronic coupling increases the LMCT transition becomes more red shifted but is entirely absent in the very strong coupled [SS-thi-SS]⁺.

The IVCT bands observed in the NIR region for the oxidised species are similarly nuanced, and the most useful tool in characterisation of the Class II-III borderline systems. These transitions are shown in Figure 1.20. For the series [OO-thi-OO]⁺, [NS-thi-NS]⁺, [SO-thi-OS]⁺ a band energy reduction (4150, 2630 and 2254 cm⁻¹) and increase in intensity is observed as predicted. The IVCT for [SS-thi-SS]⁺ actually bucks this trend and occurs at 3290 cm⁻¹ but is extremely sharp and contrary to the other systems is solvent independent as expected for a Class III system. The authors state that with increasing electronic coupling [SO-thi-OS]⁺ enters the Class II-III regime. This can be determined by

measuring the cut-off area of the observed IVCT compared to the ideal calculated Gaussian band shape. As electronic coupling increases the cut-off area increases. Again the Class III [SS-thi-SS]⁺ defies this trend as a decrease in cut off area is observed. But this is not unexpected, as we have entered the Class III regime the physical transition that produces the IVCT band itself differs being more akin to standard CT event.

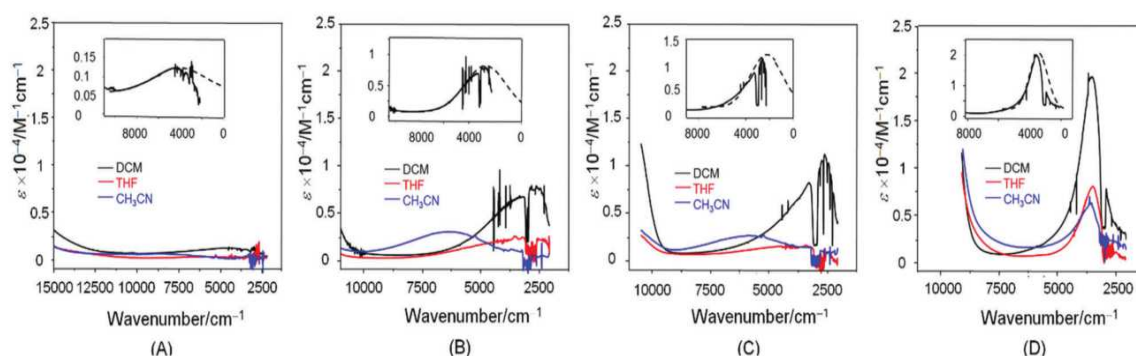


Figure 1.20. NIR spectra of [OO-thi-OO]⁺ (A), [NS-thi-NS]⁺ (B), [OS-thi-OS]⁺ (C) and [SS-thi-SS]⁺ (D) in DCM (black), THF (red) acetonitrile (blue). Insets show the cut-off of the observed IVCT versus the ideal Gaussian shaped simulated peaks. Reproduced from reference with permission from the RSC.³⁴

An interesting series of di-molybdenum complexes were presented by Cotton *et al.* where two [Mo₂] = Mo₂(DAniF)₃ moieties are bridged by [M(OMe)₄]²⁻ centres, where M = Co or Zn to give complexes of the form; [Mo₂]-[M(OMe)₄]-[Mo₂].⁴² As typical for covalently bridged Mo₂ units, two one electron oxidations can be observed by cyclic voltammetry indicating stabilisation of the MV state. But contrary to analogous carboxylate bridge systems, are much more easily oxidised, E_{1/2}¹ = -211 or -208 and E_{1/2}² = -4 or 4 mV for Co and Zn respectively, where E_{1/2}'s for [Mo₂]-O₂-C₂O₂-[Mo₂] are 294 and 506 mV. All potentials are references to the Fc / Fc⁺ redox couple.

The remarkable feature of this series of complexes is the accessibility of both the mono and bis-cationic species in crystalline form when the parent complex was chemically oxidised with one or two equivalences of ferrocenium hexafluorophosphate (Fc.PF₆). Both the Co and Zn neutral complexes are isostructural, upon oxidation the Mo-Mo bond length in one of the Mo₂ units is seen to lengthen

dramatically from 2.1113(8) to 2.151(1) Å when M = Zn and from 2.1142(9) Å to 2.1509(7) when M = Co. This is consistent with a bond order depletion from 4 to 3.5. In addition, two inequivalent pairs of Mo-O bond lengths are now observed. The Mo-O bonds corresponding to the portion of the complex containing the oxidised Mo-Mo unit become shorter while the other two are longer. In the doubly oxidised form lengthening of the previously unchanged Mo-Mo bond gives two identical [Mo₂] units and the Mo-O bonds similarly change in the predicted manner. This trend unequivocally supports the generation of a mixed valence state that is electronically localised (Class I) as only one Mo₂ undergoes change. A trend in the overall molecular size can also be observed, in the mono cation there is a slight decrease in the distance between the two [Mo₂] units as the reduction in the length of two Mo-O bonds exceeds the lengthening in the other two. In the doubly oxidised species an increase in the distance between the two [Mo₂] units is observed, likely due to increased electrostatic repulsion.

The odd electron generated upon oxidation is essentially a single unpaired δ electron and as such both the mono- and bis-oxidised complexes should be paramagnetic. This is confirmed by EPR measurements showing one dominant peak at around $g = 1.94$ for a single ⁹⁶Mo ($I = 0$) atom with hyperfine splitting pattern assignable to ^{95,97}Mo ($I = 5/2$) isotopes but poorly resolved for quantification. The doubly oxidised species contains two single unpaired electrons that are spatially separated but the EPR spectrum observed is nearly identical to that of the mono-oxidised species. This confirms that there is no coupling between the two electrons via ferromagnetic or antiferromagnetic coupling.

1.9 Proton Coupled Electron Transfer (PCET)

The term Proton Coupled Electron Transfer (PCET) was first used in 1981 to describe the concerted electron and hydrogen atom transfer observed in the comproportionation reaction between the Ru^{IV} and Ru^{II} complexes shown in Figure 1.21.

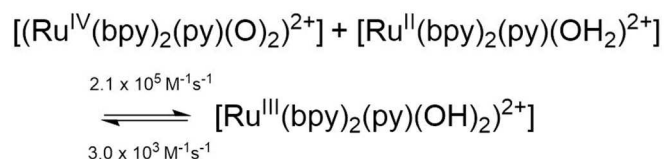


Figure 1.21. PCET in the comproportionation reaction of two Ru complexes.

It is now used more generally to describe any reaction in which both an electron and a hydrogen are transferred, regardless of mechanism, stepwise or concerted. Multi-electron and proton PCET reactions are ubiquitous in nature, fundamental in processes essential to life itself. Perhaps most famously the process by which plants convert light into chemical energy, photosynthesis. In photosynthesis light drives the chemical reduction of CO_2 by water which is then ultimately converted into carbohydrates (carbon fixation.) In the reverse process, cellular respiration, these carbohydrates are oxidised to produce carbon dioxide and water and the release of energy is used to drive metabolic processes. Photosynthesis is indeed one of the most remarkable cases of PCET in which 24 protons and 24 electrons are transferred. It annually accounts for the fixation of around 10^{11} tonnes of carbon storing approximately 10^{18} kJ of energy.⁴⁴

The specific mechanism of photosynthesis does vary from organism to organism but many PCET events occur in the electron transport chain called the Z-scheme (Figure 1.22). The photons that are captured by the light harvesting chlorophyll are raised to an excited state in Photosystem II. These excited electrons are shuttled along the electron transport chain to Photosystem I and excited again by harvested light. This energy used to pump protons across a membrane into the thylakoid space generating a chemiosmotic potential that is in turn used to drive the synthesis of ATP, the chemical energy feedstock of cells.

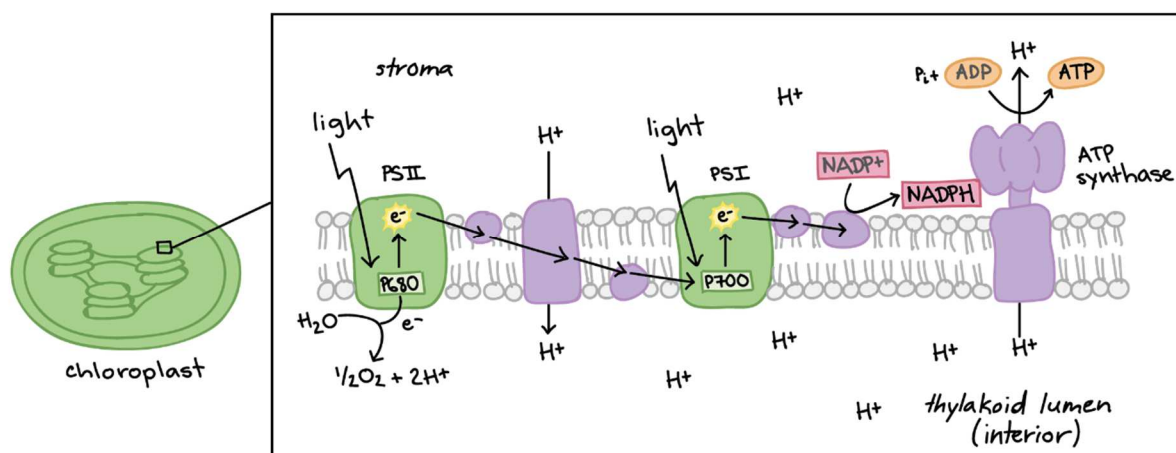


Figure 1.22. The Z-Scheme. Light absorption in photosystems I and II used to drive the formation of ATP. Figure taken from an open access source.⁴⁵

1.9.1 PCET self-exchange reactions in Inorganic complexes.

Figure 1.23 shows possible mechanisms for PCET which includes stepwise (ET and PT or PT then ET) or concerted (CPET) proton and electron transfer. It is usually straight forward to prove that ET and/ or PT has occurred, but far more complex to prove whether this has occurred in a stepwise or concerted manner.

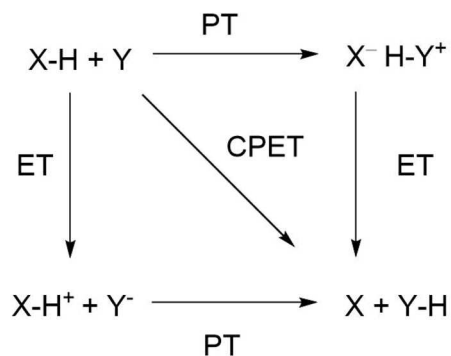


Figure 1.23. Concerted PT and ET (CPET) vs. stepwise processes.

The typical method when a concerted process is suspected is to prove that the activation energies (ΔG^\ddagger) of the individual step-wise processes are higher. This requires that the ground state ΔG° of each mechanism to be known which is in turn related to four parameters shown in Figure 1.24. The pK_a s of

the XH^{*+}/X^* and XH/X^- pairs, the reduction potentials of the protonated and deprotonated substrate, $E^\circ[XH^{*+}/XH]$ and $E^\circ[X^*/X^-]$ and the homolytic bond dissociation free energy (BDFE).

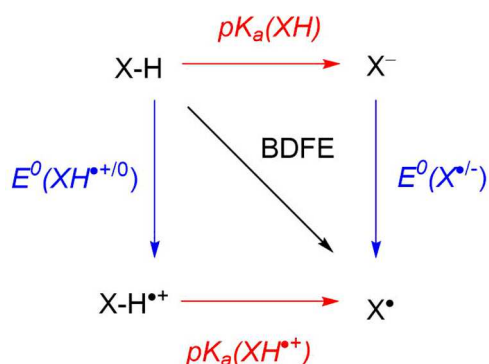


Figure 1.24. Experimental criteria relevant to concerted and stepwise PT and ET as related by Hess' Law.

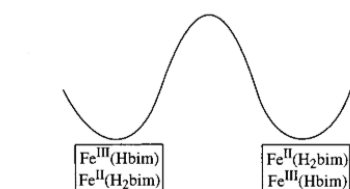
All these values are free energies so are interchangeable but are determined by different experimental procedures, titrations for pK_a s, and cyclic voltammetry for E° . BDFE's are calculated in turn from these values based on Hess' Law "regardless of the multiple stages or steps of a reaction, the total enthalpy change for the reaction is the sum of all changes".⁴⁶ To ensure the accuracy of the data the conditions for these experiments have to be kept as similar as possible. Hess' Law also states that the energy change around a closed system should be zero. This has some interesting and perhaps counter-intuitive ramifications. There are in fact only three independent parameters and in free energy terms, the change in pK_a upon oxidation will be equal to the change in redox potential upon deprotonation.

PCET occurs on the much slower NMR spectroscopy timescale (10^{-5} s) as opposed to the IR timescale (10^{-10} s) for electron-self exchange in strongly coupled MV complexes. So just as dynamic IR spectral coalescence can be used to study electron self-exchange rates in MV complexes, dynamic NMR line broadening can be used to study electron self-exchange in PCET.

Mayer *et al.* demonstrate that addition of $[Fe^{III}(H_2bim)_3]^{3+}$ to $[Fe^{II}(H_2bim)_3]^{2+}$ causes broadening of the ferric complex 1H NMR resonances indicative of electron self-exchange with an electron transfer rate of $k_{e^-} = 1.7 (\pm 0.2) \times 10^4 M^{-1} s^{-1}$ at 298 K in MeCN- d_3 .⁴⁷ The authors demonstrate similar broadening of the NMR resonances is observed for addition of $[Fe^{III}(Hbim)(H_2bim)_2]^{2+}$ to $[Fe^{II}(H_2bim)_3]^{2+}$. The self-

exchange reaction between these two species requires a net hydrogen atom transfer (H^\bullet , HAT). The mechanism of this transfer could be step-wise PT + ET or ET + PT or the concerted PCET mechanism. Kinetic and thermodynamic results preclude a step-wise mechanism as the individual PT and ET rates are slower than the observed rate in NMR line broadening, $k_{H^\bullet} = 5.8 (\pm 0.6) \times 10^3 \text{ M}^{-1} \text{ s}^{-1}$. The possible mechanisms with related kinetic and thermodynamic measurements are collected in Figure 1.25. The PCET rate is around three times slower than the related electron self-exchange reaction between $Fe^{III}(H_2bim)_3^{3+}$ to $[Fe^{II}(H_2bim)_3]^{2+}$.

a. Hydrogen atom transfer or proton-coupled electron transfer:
concerted transfer of H^\bullet and e^- without the presence of an intermediate.



b. and c. Stepwise transfer of (b) an electron followed by a proton, or (c) a proton followed by an electron. These pathways involve formation of $Fe^{II}(Hbim) + Fe^{III}(H_2bim)$ as an intermediate.

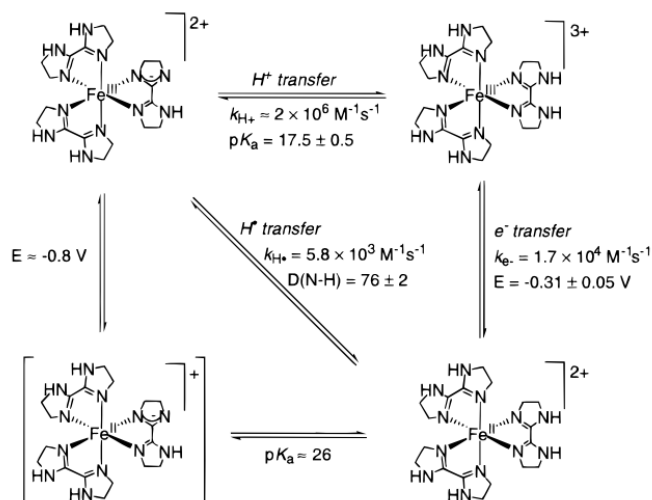
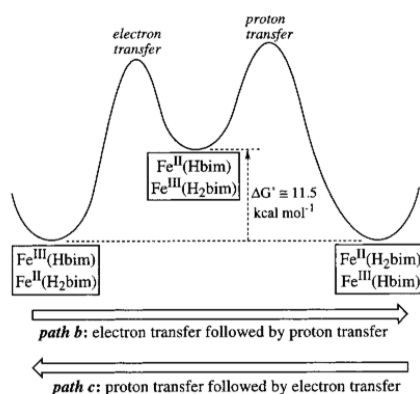


Figure 1.25. Possible pathways for net hydrogen atom transfer (H^\bullet) between $[Fe^{III}(Hbim)(H_2bim)_2]^{2+}$ to $[Fe^{II}(H_2bim)_3]^{2+}$. Path a) PCET, path b) ET + PT and path c) PT + ET. The accompanying kinetic and thermodynamic data supports the PCET mechanism. Figure adapted from reference with permission of the ACS.⁴⁷

Tadokoro *Et al.* report that crystallisation of analogous $[Ru^{III}(Hbim)_3]^-$ produces an H-bonded coordination polymer $\{Ru^{III}Ru^{III}\}_n$.⁴⁸ Through solid-state CV the authors demonstrate that proton-assisted electron transfer in the solid state produces a $\{Ru^{II}Ru^{III}\}$ mixed valence polymer. The first case

of solid-state PCET. The polymeric morphology can be described as a honey-comb pattern which in the MV state has alternating arrays of Ru^{II} and Ru^{III} (Figure 1.26).

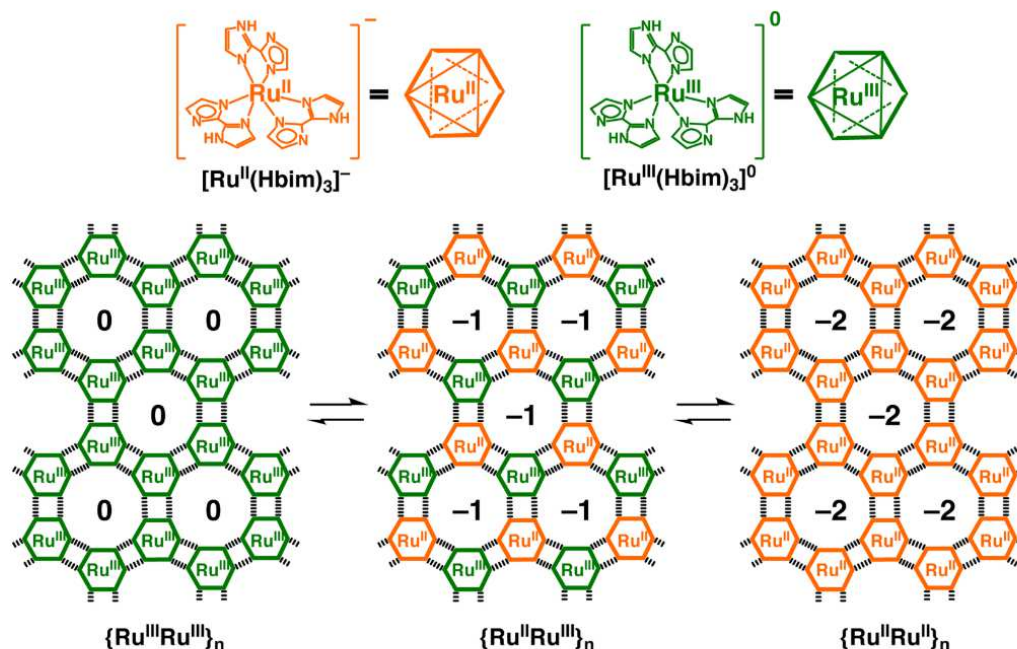


Figure 1.26. Assembly of Ru^{III}(Hbim)₃ in the solid-state produces the polymeric honeycomb structure, {Ru^{III}Ru^{III}}_n. Two multi-electron reductions are observed in solid-state CV producing firstly the {Ru^{II}Ru^{III}}_n MV polymer stabilised by solid state PCET and the {Ru^{II}Ru^{II}}_n polymer. Figure reproduced from reference with permission of the ACS.⁴⁸

1.10 Mixed Valency Across Hydrogen Bonded Complexes

When dimerization of the redox active species is generated through a self-complementary hydrogen bond, the mixed valence state must be stabilised by a mechanism distinct from PCET as there is no proton hole (Figure 1.27). But the exact mechanism through which these hydrogen bonds stabilize the mixed valence state is not well understood. We can envisage at least three potential mechanisms. Simple ET could account for the stabilisation, where electronic communication is very strong and there is direct overlap between the donor, bridge and acceptor. In such a case the hydrogen bonded dimers would be similar to a standard covalently bridged MV complex. Alternatively, it could be simply due to PT with no ET. Finally, it could be accounted by a concerted PT + ET mechanism where ET is somehow dependent on the proton coordinate. This mechanism is dubbed, Proton Couple Mixed Valency (PCMV). Recent results from the Patmore group provide the clearest evidence for MV

complexes stabilised by such a mechanism distinct from those published previously in the literature. But our understanding of this mechanism is built upon previous literature models (Figure 1.28) that mostly precedes our work and as such warrants in depth analysis.

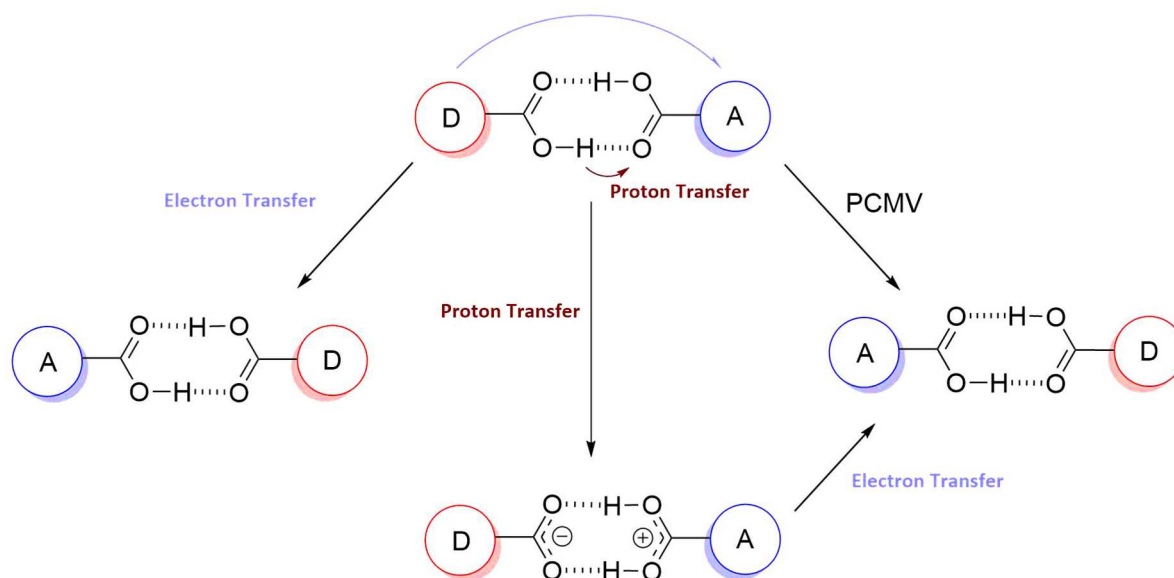


Figure 1.27. Three mechanism that can account for stabilisation of the mixed state in a hydrogen bonded dimer; electron transfer, step-wise proton transfer + electron transfer or proton-coupled mixed valency (PCMV).

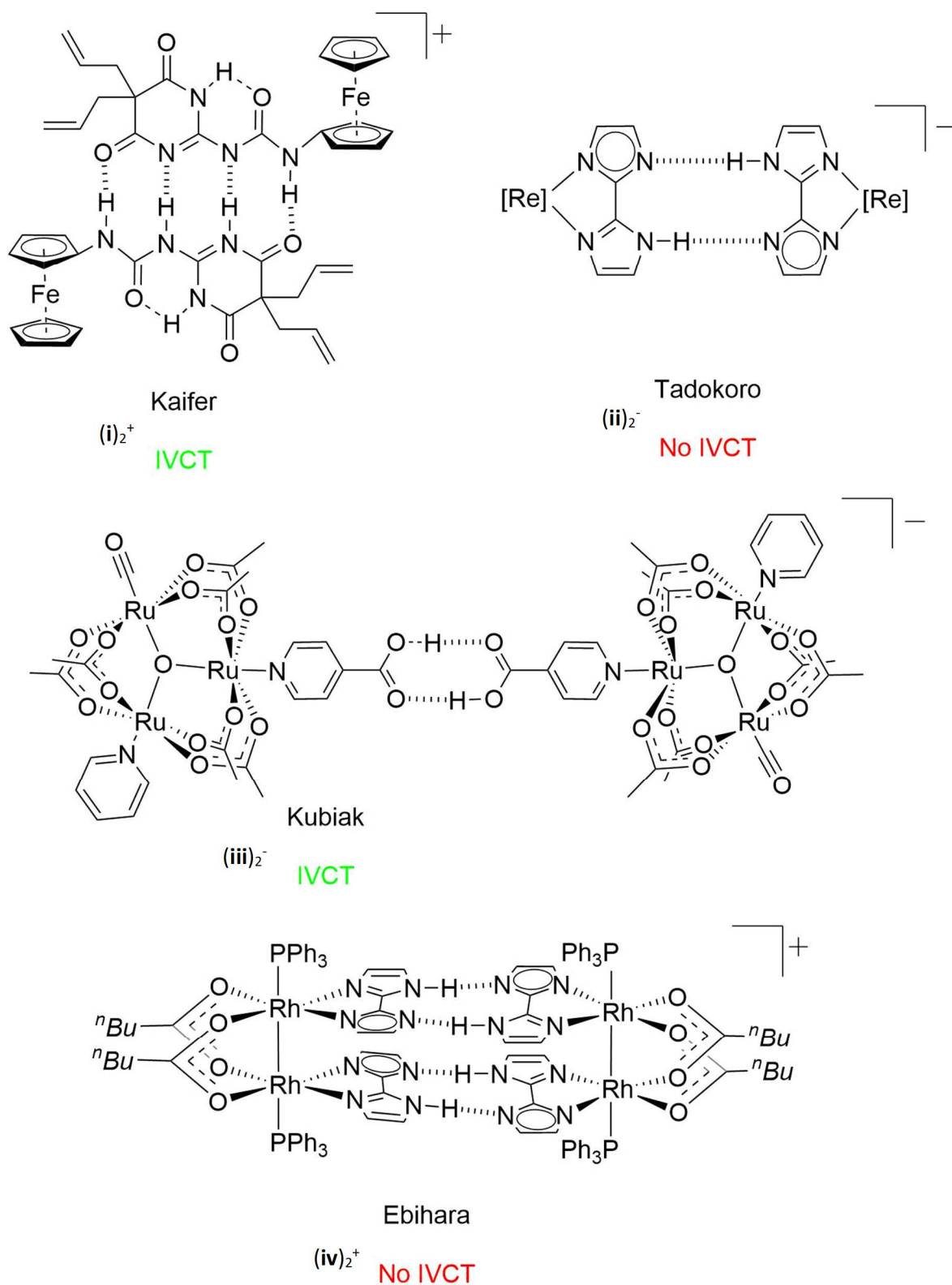


Figure 1.28. Four literature complexes represented in the MV state dimer state. The corresponding author of the publication and presence or absence of an IVCT in the NIR region is noted for each complex.

The first example of a mixed valence state stabilised over a self-complimentary hydrogen bond(s) was displayed in 2006 by Kaifer et al.⁴⁹ Ferrocene redox centres are bridged by coordinated ureidopyrimidine derived moieties forming a donor-donor-acceptor-acceptor (DDAA) hydrogen bonding motif (i)₂. The formation of the dimer can be confirmed by fast atom bombardment (FAB) MS and ¹H NMR spectroscopy showed a high association constant, $K_{dim} > 10^6 \text{ M}^{-1}$ in solution

The CV of (i)₂ in DCM shows two reversible one electron oxidations with a separation $\Delta E_{1/2}$ of ~390 mV accounting for a K_c of 3.9×10^6 . This suggest that the MV state is strongly stabilised. In the NIR an IVCT band is observed in DCM appearing at $\bar{\nu}_{max} = 8368 \text{ cm}^{-1}$, consistent with the strongly coupled dinuclear (covalent) ferrocene complexes; bis(ferrocenyl)acetylene and trans-bis(ferrocenyl)ethylene. Application of Marcus-Hush theory predicts a half-height bandwidth ($\Delta\bar{\nu}_{1/2}$) of 4397 cm^{-1} considerably larger than the experimentally observed value 560 cm^{-1} . Marcus-Hush theory is most applicable to weakly coupled systems. This overestimation is consistent with the large K_c value and indicates that electronic communication in this system is very strong. This is very surprising given the intranuclear distance between the two ferrocene centres is at least 1 nm. By contrast biferrocene has a $\Delta E_{1/2}$ of 350 mV and introduction of covalent spacers in bis(ferrocenyl)acetylene and trans-bis(ferrocenyl)ethylene reduces this to 130 and 120 mV respectively.

Tadokoro *et al.* report a rhenium dimer bridged by biimidazolate ligands, $[\{\text{Re}^{\text{III}}\text{Cl}_2(\text{P}n\text{Bu}_3)_2(\text{Hbim})\}]_2$ (ii)₂.⁵⁰ The dimeric complex is isolated by crystallisation from solutions of the monomer in MeOH by addition of NH₃ gas. The hydrogen bonding interaction in the dimer is clear in the crystal structure. The ¹H NMR spectra of the dimer in *d*₈-toluene also displays an upfield shift for the 4- and 5- position Hbim protons relative to the monomer. This demonstrates the increased shielding as the ligand environment is in proximity to two paramagnetic Re centres upon dimerization. In CD₂Cl₂ at -80 °C an association constant of $K = 1.4 \times 10^4 \text{ M}^{-1}$ is obtained.

The CVs of the protonated monomeric complex $\text{Re}^{\text{III}}\text{Cl}_2(\text{P}n\text{Bu}_3)_2(\text{H}_2\text{bim})$ (ii') and the hydrogen bonded dimer (ii)₂ can be taken individually in DCM, Figure 1.29. Two single electron reversible redox events

are observed for the monomeric complex, corresponding to a $\text{Re}^{\text{III/II}}$ reduction and a $\text{Re}^{\text{III/IV}}$ oxidation. In the dimer both the reduction and oxidation are now double wave processes showing the generation of two separate mixed valence states; $\text{Re}^{\text{II}}\text{Re}^{\text{III}}$ and $\text{Re}^{\text{III}}\text{Re}^{\text{IV}}$.

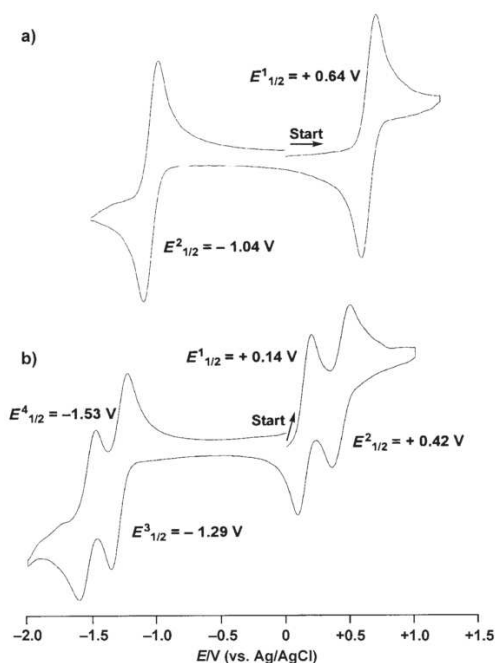


Figure 1.29. CV of a) monomeric complex, **ii'** and b) dimeric (**ii**)₂ in DCM. For the latter two, stable MV states are observed. Figure reproduced from reference with permission from John Wiley & Sons.⁵⁰

No IVCT band is observed for either mixed valence state. This supports the conclusion that no electronic communication exists between the two metal centres as the hydrogen bond prevents π -conjugation between the ligands.

The authors propose that the two hydrogen atoms in the H-bond would initially undergo a double concerted proton transfer through a symmetrical double-well potential surface having equivalent energies when both are Re^{III} centres. When one centre is oxidised or reduced the potential energy surface is no longer symmetrical and the two protons will be localised on the side of the dimer having the lower oxidation state. The mixed valence states $\text{Re}^{\text{II}}\text{Re}^{\text{III}}$ and $\text{Re}^{\text{III}}\text{Re}^{\text{IV}}$ thus produce two different proton transfer complexes; $[\{\text{Re}^{\text{II}}\text{Cl}_2(\text{L})_2(\text{H}_2\text{bim})\}\cdots\{\text{Re}^{\text{III}}\text{Cl}_2(\text{L})_2(\text{bim})\}]^-$ and $[\{\text{Re}^{\text{III}}\text{Cl}_2(\text{L})_2(\text{H}_2\text{bim})\}\cdots\{\text{Re}^{\text{IV}}\text{Cl}_2(\text{L})_2(\text{bim})\}]^+$. The lowest reduction wave in CV corresponds to the generation of $[\{\text{Re}^{\text{II}}\text{Cl}_2(\text{L})_2(\text{Hbim})\}]_2^{2-}$ while the highest to the generation of $[\{\text{Re}^{\text{IV}}\text{Cl}_2(\text{L})_2(\text{Hbim})\}]_2^{2+}$. In the former

process only the deprotonated $\{\text{Re}^{\text{III}}\text{Cl}_2(\text{L})_2(\text{bim})\}^-$ unit in the dimer is reduced, and in the latter case only the protonated $\{\text{Re}^{\text{III}}\text{Cl}_2(\text{L})_2(\text{H}_2\text{bim})\}^+$ is reduced so it is reasoned that the reversibility of the redox processes will correlate with the PT. To this effect, the authors determine the rate determining PT in the redox events by performing CV measurements at high scan rates (up to 10 V s^{-1}) at low temperature ($-60 \text{ }^\circ\text{C}$). Large shape deviations were observed consistent with the influence of a chemical reaction having slow rate limiting PT relative to ET in organic compounds.^{44,51}

Two potential models to account for the stabilisation of the mixed valence state were modelled computationally using density functional theory (DFT). Figure 1.30A shows the $\text{Re}^{3.5+}/\text{Re}^{3.5+}$ model complex $[\{\text{Re}^{3.5+}\text{Cl}_2(\text{PH}_3)_2(\text{Hbim})\}_2]^+$ and **B**) the $\text{Re}^{\text{III}}/\text{Re}^{\text{IV}}$ complex $[\{\text{Re}^{\text{III}}\text{Cl}_2(\text{PH}_3)_2(\text{H}_2\text{bim})\} \cdots \{\text{Re}^{\text{IV}}\text{Cl}_2(\text{PH}_3)_2(\text{bim})\}]^+$.

In **A** the two H-bonding atoms are symmetrically split across the two monomer units having equal, non-integer oxidation state, 3.5+. In **B**, the hydrogens are localised on Re^{III} monomer unit and the opposite Re centre is oxidised to the 4+ oxidation state. The mixed valence state of the models and by extension $(\text{iii})_2^+$ can be described by a double well potential energy surface and is calculated for both models and **B** is found to be more stable by $3.96 \text{ kcal mol}^{-1}$. In model **B**, the Re^{III} centre has a charge of +0.764 and the Re^{IV} centre +0.236 so there is a polarisation across the dimer and hence an unsymmetrical double well potential. If we envisage proton transfer from model complex **A** to **B** over the $6.15 \text{ kcal mol}^{-1}$ energy barrier a proton is transferred from a N-H group on one side of the complex and forms a new bond with a N atom lone pair on the other side of the complex. By contrast, there is no such driving force for proton transfer in the opposite direction **B** to **A** and the symmetrical double well potential.

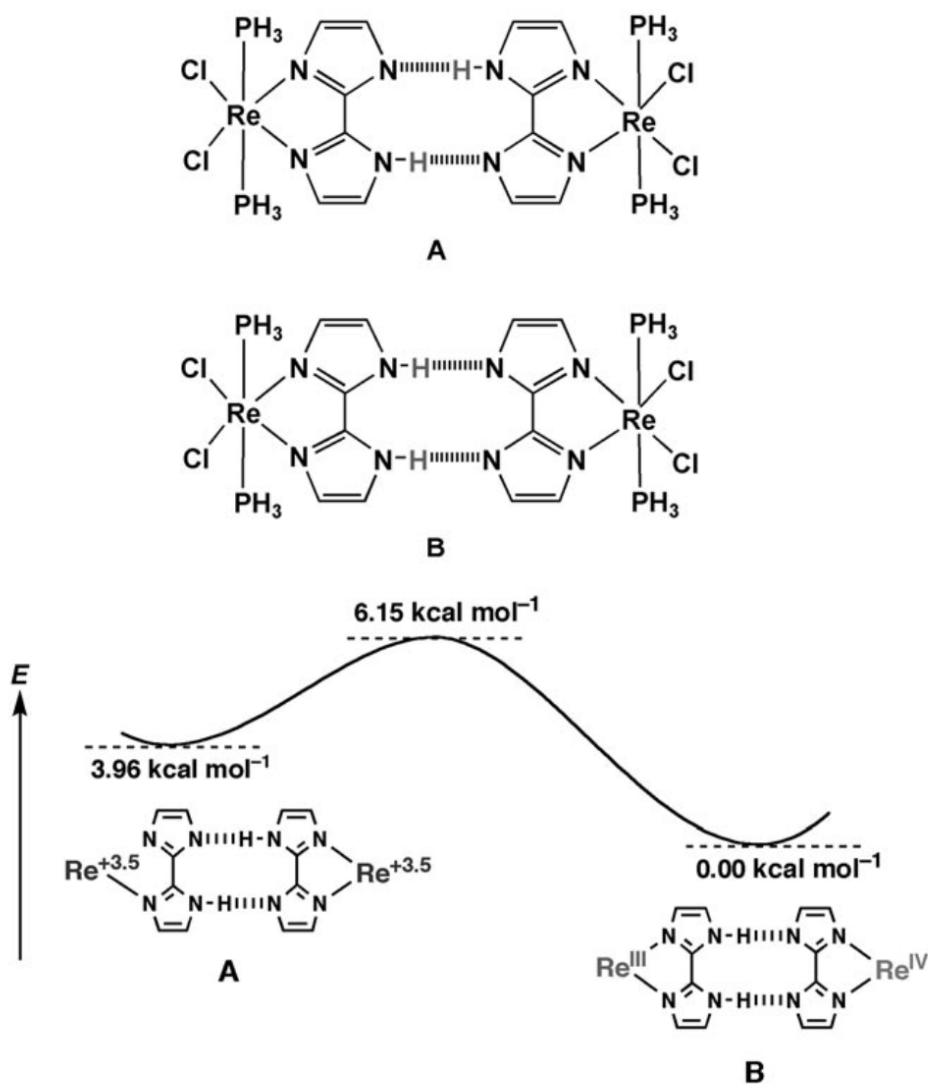


Figure 1.30. Two modelled proton transfer products A and B and their relative calculated potential energy's. Figure reproduced from reference with permission from John Wiley & Sons.⁵⁰

Kubiak presents an example where his commonly employed triruthenium oxolate centres are coordinated with isonicotinic acid (iii).⁵² Previous work predicted that communication in the mixed valence state of the covalently bridged dimers occurs through the pyridine π^* . This is likewise predicted for the hydrogen bonded, mixed valence dimer (iii)₂.

The oxidative processes observed in the CV of the covalent and hydrogen bonded dimers are identical and are one electron oxidations in all cases. But the reductive processes observed in the hydrogen bonded dimer are different. For the covalent system two one electron, reversible reductions are observed. The cathodic region for ii is much more nuanced, as shown in Figure 1.31. In DCM the two

waves for the initial reduction have a smaller splitting than the two re-oxidation waves. This is attributed to an ECE mechanism, where E is a one electron reduction and C, a reversible dimerization. The neutral complex (**iii**) is reduced to generate (**ii**)⁻ which dimerises with neutral **iii** forming a mixed valence dimer (**iii**)₂⁻. Which is further reduced to generate a double reduced dimer (**iii**)₂²⁻. This dimer is re-oxidised in two one-electron processes that are split symmetrically about the half-wave potential of the reduced monomer **iii**⁻ of the re-oxidation waves accounts for a $K_c \approx 10^7$ indicating a highly stable mixed valence state. In DMSO, a solvent capable of disrupting the hydrogen bond a single reversible reduction is observed. Furthermore, the use of Diffusion Ordered Spectroscopy (DOSY NMR) also confirms the presence of neutral monomer (**iii**) and reduced dimer (**iii**)₂⁻.

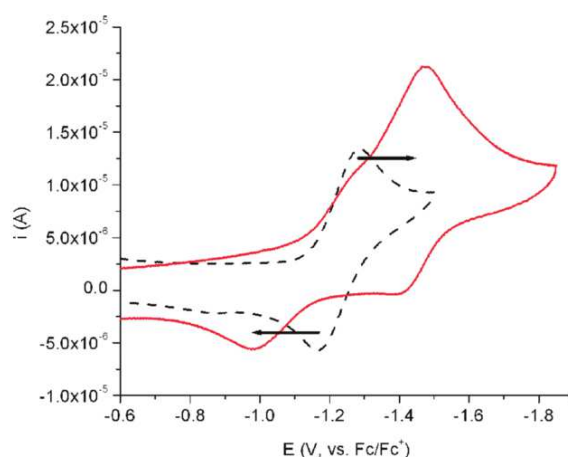


Figure 1.31. CV showing formation of the (**iii**)₂ dimer and oxidation to produce firstly the mixed valence (**ii**)₂²⁻ state then the doubly oxidised dimer (**ii**)₂²⁻ in DCM (red). In contrast the CV taken in DMSO (black) shows no dimerization nor formation of a mixed valence state. Figure reproduced from reference with permission from the ACS.⁵²

The use of UV/Vis/NIR SEC reveals the individual electronic structures of the neutral monomer **iii**, mixed valence, (**iii**)₂⁻ and doubly reduced dimer (**iii**)₂²⁻. The $\nu(\text{CO})$ bands in the IR region are shown in Figure 1.32 (a). The neutral black monomer (**iii**) shows a single band at 1940 cm^{-1} and the doubly reduced dimer a band at 1900 cm^{-1} (**iii**)₂²⁻ consistent with the covalently bridged analogues $[\text{Ru}_3\text{O}(\text{OAc})_6(\text{CO})(\text{L})_2(\text{pz})]$ where $\text{L} = \text{py}$ or dmap . The mono-reduced (**iii**)₂⁻ dimer spectrum is a

combination of the neutral and doubly oxidised species showing a localised mixed valence state (Class II), therefore there is an upper electron transfer rate limit of $\sim 10^{10} \text{ s}^{-1}$.

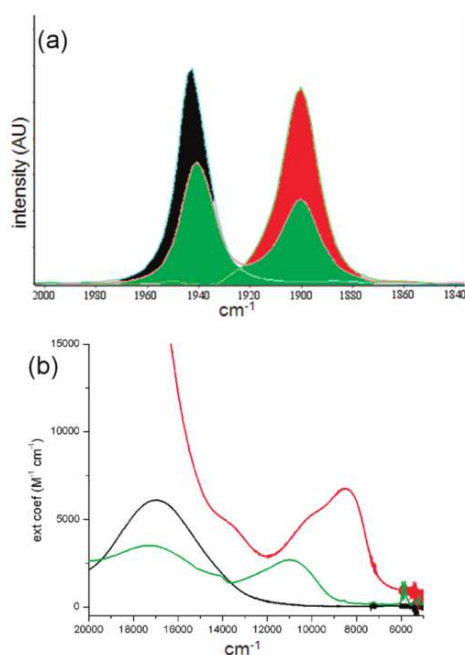


Figure 1.32. IR (a) and UV-Vis NIR (b) for **iii** (black), **(iii)₂⁻** (green) and **(iii)₂²⁻**. Figure adapted from reference with permission from the ACS.⁵²

The UV-Vis NIR response as **(iii)** (black) is stepped through two one electron reductions to produce **(iii)₂⁻** (green) and **(iii)₂²⁻** (red) is shown in Figure 1.32(b). The spectral response of the doubly reduced species (red) is no dissimilar to that of the doubly reduced form of the covalently bridged analogues. Several bands appear between 7000-12 000 cm^{-1} and there is a slight blue shifting of the intra-cluster band observed at 17 000 cm^{-1} (528 nm) that also displays an increase in intensity. The spectrum for the singly reduced species is interesting because unlike the IR it is not just a superposition of the individual neutral and doubly reduced spectra. The intra-cluster absorption band decreases in intensity from the neutral species just as in the covalent systems but the NIR band in the doubly reduced species, $\nu_{\text{max}} = 8500 \text{ cm}^{-1}$ occurs at a much lower energy in the mixed valence dimer $\nu_{\text{max}} = 11 000 \text{ cm}^{-1}$. The authors offer several potential explanations for the mixed valence electronic structure to support this observation; orbital destabilisation due to electron-electron repulsion, a non-Gaussian

IVCT band⁵³⁻⁵⁶ or a red-shifting of the cluster-to-ligand CT (CLCT) due to stabilisation of the ground state.⁵⁷

In related trispyridyl ruthenium clusters red shift for sequential reductions in CLCT transitions has been observed.⁵⁷ It is attributed to increasing electron-electron repulsions and destabilisation of an increasingly occupied cluster excited state. But this cannot be the case for $(\text{ii})_2^-$ as this would require sequential population of a SOMO and an electron delocalised excited state (Class III) which has already been ruled out by the use of IR-SEC.

An exciton shift, while plausible as $(\text{iii})_2^-$ is a dimer of chromophoric oxalate clusters could not account for such a large shift $\sim 2500 \text{ cm}^{-1}$ as is observed. The extent of exciton shifts is inversely proportional to the cube of the distance between the dipole moment centres, around 14 \AA in this dimer, so could account only for a shift in the region of 50 cm^{-1} .

If we assume $(\text{iii})_2^-$ lies firmly with the Class II regime as predicted by IR-SEC. The band at approximately $\nu_{\text{max}} = 8500 \text{ cm}^{-1}$ can be treated as a single, non-Gaussian IVCT. The electronic coupling parameter, H_{ab} and total reorganisation energy, λ can be determined through a combination of Marcus-Hush theory and measuring the transition dipole moment. The values determined are $H_{ab} = 370 \text{ cm}^{-1}$ and $\lambda = 11\,000 \text{ cm}^{-1}$. The reorganisation energy is in good agreement the thermodynamic estimates for the covalent analogues. The peak shape however shows poor agreement with what is predicted. This could be accounted for if the electron transfer distance, r is shorter than the Ru-Ru inter-cluster distance which would increase H_{ab} . But if this is indeed an IVCT this model does not account for that fact that a CLCT transition to the ancillary pyridine and bridging isonicotinic acid ligands has disappeared.

If the NIR transition is attributed to the overlapping of CLCT transitions, then the red shift can be explained as stabilisation of the ground state by the hydrogen bond and / or ion pairing, not unprecedented in the literature.⁵⁸ The combined effect of hydrogen bonding and the mixed valence state would account for a stabilisation of $\sim 2500 \text{ cm}^{-1}$ or $7.1 \text{ kcal mol}^{-1}$ in the ground state of $(\text{iii})_2^-$ with the effect not being fully observed in the doubly reduced dimer $(\text{iii})_2^{2-}$.

At this stage the identity of NIR transition was inconclusive. But Kubiak dubbed (iii)₂⁻ “the best example of proton-dependent or proton coupled mixed valency where in the latter case the electron transfer depends explicitly on the proton coordinate.” The first use of the term PCMV.

The issue was later revisited and resolved by describing the system using a three-state model. In the three state model, developed by Brunschwig, Sutin and Creutz (often BSC model)⁵⁹ the two-state classic Marcus-Hush theory is expanded to include a PES for the interacting bridging ligand. Both NIR transitions for (iii)₂⁻ (Figure 32(b), green) can be assigned as IVCTs. The lower energy transition being a traditional metal-to-metal CT (MMCT) type IVCT and the higher energy absorption a metal-to-bridge acceptor CT (MBCT) being an IVCT from the metal donor onto the bridge on the acceptor half of the dimer.⁶⁰

Ebihara *et al.* report a bis(biimidazolate)dirhodium dimer complex; [Rh₂(O₂CBu)₂(Hbim)₂(PPh₃)₂]₂ (iv)₂.⁶¹ A quadruple hydrogen bonding motif dimerises the dirhodium paddlewheel monomer complexes generating a four redox centre dimer. The dimerization in the isolable structure is confirmed by XRD crystallography. The ¹H NMR spectra of (iv)₂ remains unchanged upon dilution from 3.0 mM to 0.3 mM suggest a relatively high association constant for the dimerization. However, some spectral changes are observed in temperature dependent ¹H NMR spectroscopy suggesting some small structural changes such as shortening of the H-bond distances.

The CV of (iv)₂ in DCM (Figure 1.33) shows from left to right two reversible one electron redox waves indicating the formation of a mixed valences state and two quasi-reversible redox waves. The first oxidation can be assigned to the generation of the mixed valence state Rh₂⁴⁺ Rh₂⁴⁺ / Rh₂⁴⁺ Rh₂⁵⁺ (E_{1/2} = -0.325 V) and the second oxidation to the subsequent oxidation to Rh₂⁴⁺ Rh₂⁵⁺ / Rh₂⁵⁺ Rh₂⁵⁺ (E_{1/2} = -0.186 V). The K_c = 224 is comparable to the dimolybdenum “dimer of dimers” published by the Patmore group discussed hereafter. The two quasi-reversible oxidations produce Rh₂⁵⁺ Rh₂⁶⁺ / Rh₂⁵⁺ Rh₂⁵⁺ and Rh₂⁵⁺ Rh₂⁶⁺ / Rh₂⁵⁺ Rh₂⁶⁺ respectively.

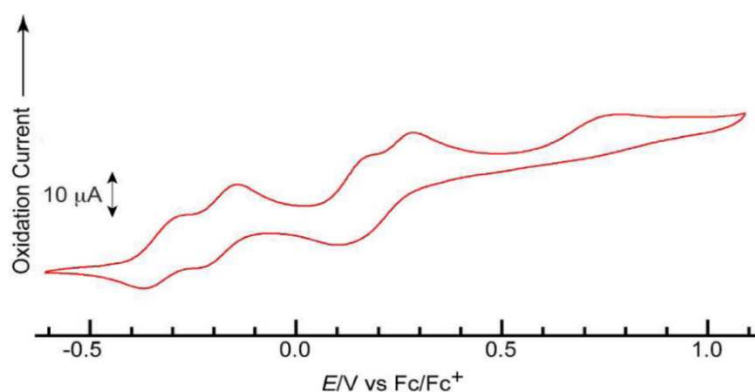


Figure 1.33. CV of $(iv)_2$ in DCM. Figure adapted from reference with permission from the ACS.⁶¹

Assignment of the oxidations can be confirmed by the use of EPR, bulk electrolysis of $(iv)_2$ at -0.29 V causes a colour change from red to bluish green and the EPR spectrum obtained is shown in Figure 1.34. The observed spectrum has $g_{\perp} = 2.14$ and $g_{\parallel} = 2.00$ and hyperfine coupling constants of $A_{\perp}(P) = 14.9$ mT, $A_{\parallel}(P) = 19.8$ mT, and $A_{\parallel}(Rh) = 1.54$ mT. It closely resembles the spectrum of the monomeric Rh_2^{5+} complex, $[Rh_2(O_2CR)_4(PPh_3)_2]_2^+$ confirming that the first two oxidations are sequential one electron oxidation to generate $Rh_2^{4+}Rh_2^{5+}$ and $Rh_2^{5+}Rh_2^{5+}$ respectively. The g values and hyperfine coupling constants indicate that the odd electron in the MV state is localised in a singly occupied (SOMO) Rh-Rh σ orbital having partial Rh-P σ^* character on one dirhodium unit. The doubly oxidised, $Rh_2^{5+}Rh_2^{5+}$ was too unstable to be measured via EPR.

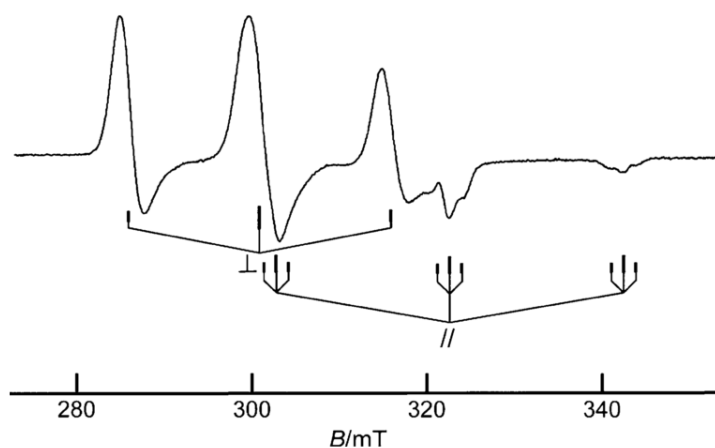


Figure 1.34. EPR spectrum of $(iv)_2^+$ in frozen DCM (77 K). Figure reproduced from reference with permission of the ACS.⁶¹

No IVCT was observed for the $\text{Rh}_2^{4+} \text{Rh}_2^{5+}$ species this attributed to the fact that the Rh-Rh σ HOMOs cannot interact with one another through the perpendicular plane of biimidazolate π -system and consistent with the localisation of the SOMO in the EPR spectrum.

The ultimate mechanistic conclusion for this system was “that the proton-coupled mixed-valence complex may be stabilized by the motion of dirhodium complexes along with the transfer of an electron and protons.”

Looking at the current literature in the field there are three possible mechanisms by which the MV states could be stabilised over a self-complimentary hydrogen bond.

Firstly, when the hydrogen bonding interaction is so strong that there is direct orbital overlap between the donor, bridge and acceptor, ET is sufficient to stabilise the MV state and these complexes are not unlike standard covalently bridged MV complexes. This mechanism is evident in the appearance of an IVCT in the NIR. Kubiak’s and Kaifer’s systems fall into this category. Secondly, proton transfer without electron transfer could stabilise the MV state, as per Tadokoro’s system. Finally, the electron transfer can in some way be related to the proton coordinate, but there is no electronic communication between the donor and acceptor so no IVCT band in the NIR. Ebihara’s example, inconclusively can be categorise to follow this mechanism, dubbed proton coupled mixed valency (PCMV).

Recent results from the Patmore group provide the clearest examples of complexes stabilised by the PCMV mechanism together with the most detailed mechanistic studies towards its understanding.⁶²⁻

64

1.11 Proton Coupled Mixed Valency

We reported initially a series of paddlewheel complexes bearing pendant lactam functionalities; $\text{Mo}_2(\text{TiPB})_3(\text{HDON})$ (**v**) or $\text{Mo}_2(\text{TiPB})_3(\text{HDOP})$ (**vi**) where HTiPB = 2,4,6-triisopropyl benzoic acid, H_2DON = 2,7-dihydroxy-1,8-naphthyridine and H_2DOP = 3,6-dihydroxypyridazine.⁶² These complexes generate a self-complimentary hydrogen bonding motif generating a “dimer of dimers” motif (Figure 1.35).

Primary evidence for solution state dimerization comes from ^1H NMR and DOSY where the hydrodynamic volume is seen to half when DMSO is added to DCM solutions of the dimer.

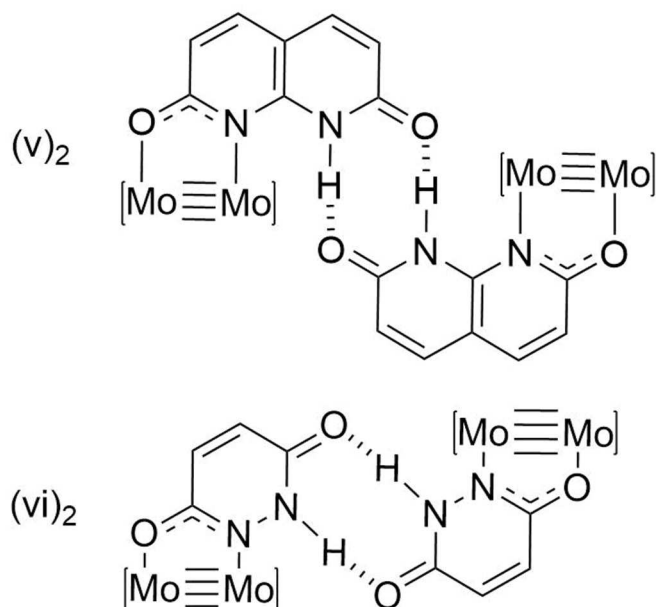


Figure 1.35. Self-complementary hydrogen-bonding motifs in $[\text{Mo}_2(\text{TiPB}_3)(\text{DOP})]_2$ (**v**)₂ and in $[\text{Mo}_2(\text{TiPB}_3)(\text{DOP})]_2$ (**vi**)₂. The TiPB ligands are omitted for clarity.

The CV of these complexes is also consistent with the formation of a mixed valence state; showing two consecutive one-electron reversible oxidations in DCM, $[\text{Mo}_2]_2 \rightarrow [\text{Mo}_2]_2^+ \rightarrow [\text{Mo}_2]_2^{2+}$ (solid line, Figure 1.36). Addition of DMSO disrupts the hydrogen bond and only a single reversible oxidation of approx twice the current intensity is observed $[\text{Mo}_2]_2 \rightarrow 2[\text{Mo}_2]^+$. A large cathodic shift is observed for the DOP derivative due to axial DMSO coordination upon breaking apart of the dimer. The values of K_c for these complexes are 233 (**v**) and 487 (**vi**). Typically, K_c 's of the order of 10^5 and greater suggest strong coupling (Class III regime) but it has been demonstrated for related di-metal complexes, complexes that have modest K_c values, as low as 510, can still display strong coupling simply due to the more diffuse nature of charge in the Mo_2^{5+} radical cation.

Direct comparison of the HDON and HDOP complexes reveals the most mechanistic details. Potentially a through-space columbic interaction could account for stabilisation of the mixed valence state, but this cannot be the case when we compare the K_c values to the internuclear $\text{Mo}_2 \cdots \text{Mo}_2$ separation. The

DOP derivative (**vi**)₂, despite having a greater intranuclear separation (8.38 Å) displays the higher K_c than (**v**)₂ (7.29 Å). Stabilisation must therefore be a result of the hydrogen bonding interaction but the absence of an IVCT in the NIR region also precludes electronic coupling, supporting the PCMV mechanism.

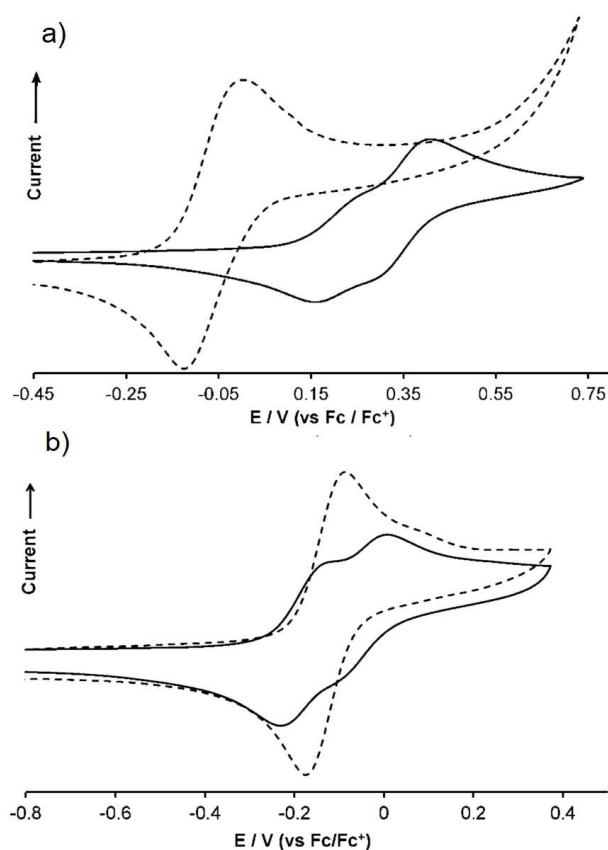


Figure 1.36. CV's of a) Mo₂(TIPB)₃(HDON) (**v**) and b) Mo₂(TIPB)₃(HDOP) (**vi**) in DCM (solid line) a mixed valence state for the dimerised species (**vi**)₂⁺ (**vii**)₂⁺ is observed. After addition of DMSO (dashed line) the dimer is disrupted. Recorded in 0.1 M TBAPF electrolyte.

Further evidence for ruling out standard electronic coupling came from synthesis of W₂(TiPB)₃(HDON), having $K_c = 111$. In covalent system substitution of Mo₂ for W₂ accounts for orders of magnitude increases in K_c as W₂- δ orbitals are around 0.5 eV higher in energy than for molybdenum and thus overlap more effectively with bridge π -orbitals. Consider this example [M₂(O₂C^tBu)₃](μ -2,5-dihydroxyterephthalate)⁺ where K_c is 21 for Mo, but increases to 2600 for M = W. The fact that we see

a slight decrease in K_c for **vi** surely precludes the standard super exchange via direct donor-bridge-acceptor orbital overlap.

At this stage sufficient evidence was gathered to show that these “dimer of dimer” structures clearly operate by a mechanism distinct from those in the previous literature. Now the focus of our group for the last few years has been to gain a more rigorous understanding of the exact nature of this stabilisation (our ongoing effort in this regard is discussed in Chapters 3 and 4). First, we sought to establish a timescale for ET in the $[\text{Mo}_2(\text{TiPB})_3(\text{HDOP})]_2^+$ MV state. If the ET rate is very fast, $>10^{10} \text{ s}^{-1}$ coalescence of vibrational bands is observed. The bridging HDOP ligand contains two suitable IR handles, C=O and N-H stretches. In both cases, no spectral coalescence was observed indicating the ET rate is slower than 10^{10} s^{-1} .

The EPR spectrum of $[\text{Mo}_2(\text{TiPB})_3(\text{HDOP})]^+$ in contrast to $[\text{Mo}_2(\text{TiPB})_4]^+$ is shown in Figure 1.37. It is well established in the literature for a complex of the form $[\text{Mo}_2\text{-B-Mo}_2]$ when the odd electron is delocalised over both Mo_2 units a hyperfine-couplings of $\sim 14 \text{ G}$ are observed. When the electron is instead localised on only one of the Mo_2 units a hyperfine coupling of $\sim 28 \text{ G}$ is observed. The $^{95/97}\text{Mo}$ hyperfine splitting for $\text{Mo}_2(\text{TiPB})_4$ though poorly resolved is 27.3 G as expected. For $[\text{Mo}_2(\text{TiPB})_3(\text{HDOP})]^+$ the Mo_2^+ is polarised as one Mo is coordinated to the N of the DOP ligand while the other is coordinated to an O atom. Thus, two sets of hyperfine splitting are observed, 25.3 and 32.8 G , but the magnitude of the measured values suggest the odd electron is still localised on one Mo_2 unit. Thus, the system is electron localised on the EPR timescale suggesting the ET rate is less than 10^9 s^{-1} . This is in the order of PCET self-exchange reaction of $[\text{Fe}^{\text{II}}(\text{H}_2\text{bim})_2(\text{Hbim})]^{2+} + [\text{Fe}^{\text{III}}(\text{H}_2\text{bim})_3]^{2+}$ discussed earlier where $k_{\text{PCET}} = (5.8 \pm 0.6) \times 10^3 \text{ M}^{-1} \text{ s}^{-1}$. Thus the ET rate for $[\text{Mo}_2(\text{TiPB})_3(\text{HDOP})]^+$ is expected to be somewhere between the electrochemical and EPR timescale. To test this theorem the deuterated derivative of **vi** was synthesised but the CV of two complexes showed no difference indicating the ET rate is certainly faster than $\sim 10^{-1} \text{ s}^{-1}$.

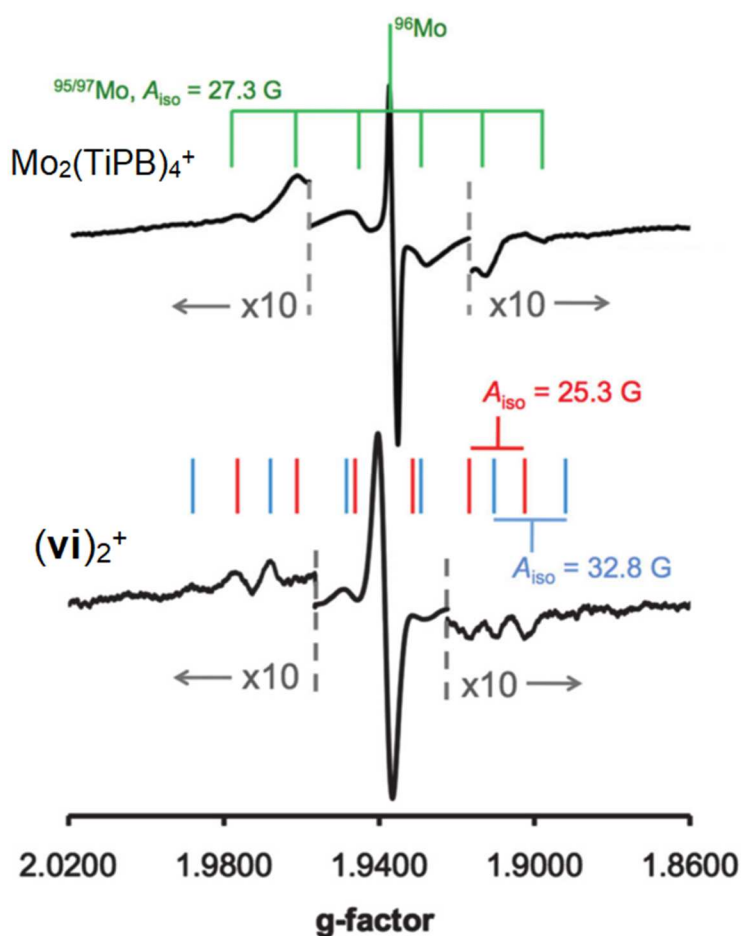


Figure 1.37. EPR spectra of $\text{Mo}_2(\text{TiPB})_4^+ \text{PF}_6^-$ (top) and $[\text{Mo}_2(\text{TiPB})_3(\text{HDOP})]^+ \text{PF}_6^-$, $(\text{vi})_2^+ \text{PF}_6^-$ (bottom). Recorded in DCM at -90°C . Regions of the spectra have been magnified to highlight hyperfine coupling. Figure reproduced from reference with permission of the RSC.⁶⁴

To determine the exact nature of the stabilisation DFT calculations were used to model the effects of proton coordinate motion (Figure 1.38). The model compound used substituted TiPB ligands for formate ligands to reduce calculation time; $[(\text{HCO}_2)_3\text{Mo}_2(\text{HDOP})]_2^+ [\text{vi}']_2^+$. The PES associated with three proton motions were modelled; double proton transfer (DPT) and two asymmetric single proton transfers SPT1/2. The N-H bond was constrained whilst allowing full geometry optimisation for the rest of the molecule.

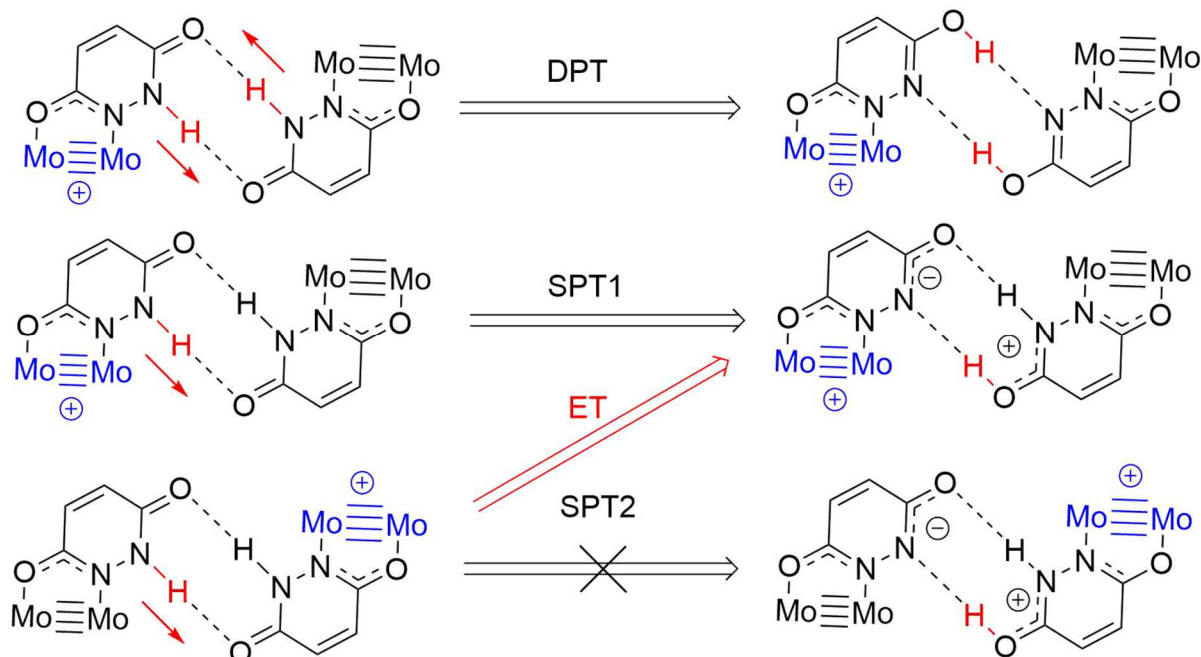


Figure 1.38. Possible mechanisms for stabilisation of the mixed valence state relating two proton coordinates; double proton transfer DPT (top), single proton transfer 1 (middle) and single proton transfer 2 (bottom).

For DPT the barrier to proton transfer is around 10 kcal mol^{-1} and the reaction product is 4 kcal mol^{-1} higher in energy than the ground state, thus not feasible (Figure 1.39). In SPT1 the proton on the oxidised side of the dimer is moved towards the unoxidized. While the ET barrier is lightly lower, the proton transfer product is higher in energy at $6.8 \text{ kcal mol}^{-1}$ (Figure 1.40. top). In both cases the proton transfer product is higher in energy than the ground state so supports the fact that simple proton transfer would not account for stabilisation of the mixed valence state. It also does not however account for why electron transfer is still related to the proton coordinate.

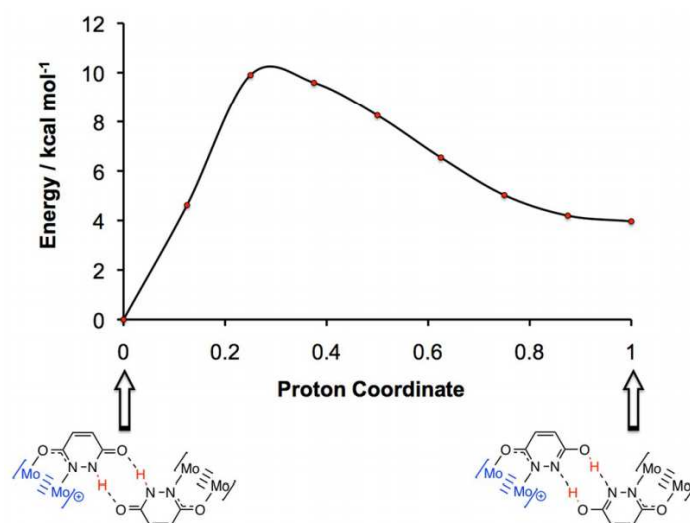


Figure 1.39. Calculated potential energy surface for concerted double proton transfer in $(vi)_2^+$. Figure reproduced from reference with permission of the RSC.⁶⁴

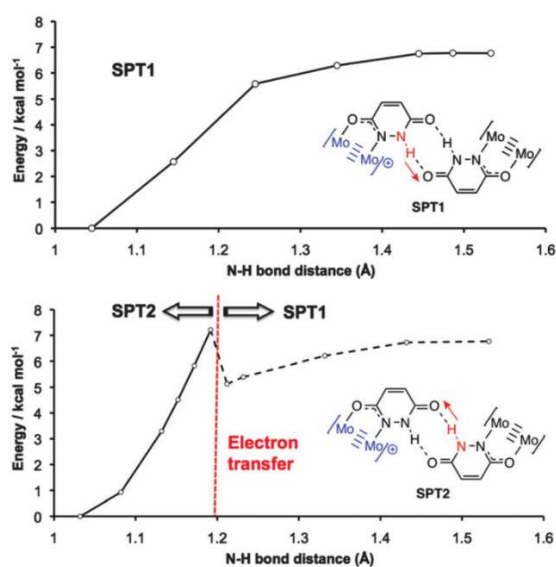


Figure 1.40. Calculated potential energy surfaces for two single proton transfer models in $(vi)_2^+$. Figure reproduced from reference with permission of the RSC.⁶⁴

This insight comes from the SPT2 mechanism (Figure 1.40, bottom) In the SPT2 model the proton on the neutral side of the model is moved towards the oxidised side producing a large dipole. The calculations reveal however that after only partial motion of the proton spontaneous ET occurs in the geometry optimisation at which point the SPT 2 PES can no longer be modelled and the product of

optimisation is identical to the SPT1 PES. The modelled PCMV mechanism can thus be described as being a “dipole induced self-exchange reaction”. The fact that only partial proton transfer is required to generate the dipole sufficient to induce electron transfer suggests that it is a concerted process.

1.12 Conclusion

There are still many questions remaining surrounding the PCMV mechanism primarily the ET transfer rate. Our current models fall somewhere between the NMR (10^{-5} s) and the EPR (10^{-9} s) timescale. In covalent systems reducing the electron transfer distance by reducing the bridge length^{65,66} or increasing mixing of $\text{Mo}_2(\delta)$ -bridge(π) can both increase electronic communication.³⁴ How the same alterations would affect the stabilisation of the MV state via the PCMV mechanism is not clear. Furthermore, when incorporated into larger assemblies for instance molecular wires would hydrogen-bonds interactions mediate electron transfer as effectively as covalent π -systems? Some of our efforts to resolve these questions are discussed in the following chapters.

In Chapter 2 the synthesis of new precursor paddlewheels and attempted synthesis of extended assemblies is discussed.

In Chapter 3 the introduction of electron-donating and -withdrawing substituents into the bridging ligand and the effects upon the stabilisation of the MV state is discussed.

In Chapter 4 two new “dimer of dimers” structures analogous to $[\text{Mo}_2(\text{TiPB})_3(\text{HDOP})]_2$ now coordinated by N and S atoms and bridged by thio-lactam functionalities are reported.

1.13 References

- (1) Brown-Xu, S. E.; Chisholm, M. H.; Durr, C. B.; Gustafson, T. L.; Spilker, T. F. *J. Am. Chem. Soc.* **2014**, *136*, 11428.
- (2) Nippe, M.; Goodman, S. M.; Fry, C. G.; Berry, J. F. *J. Am. Chem. Soc.* **2011**, *133*, 2856.
- (3) Cotton F A, B. W. K. *J. Am. Chem. Soc.* **1965**, *87*, 921.
- (4) Cayton, R. H.; Chisholm, M. H.; Huffman, J. C.; Lobkovsky, E. B. *J. Am. Chem. Soc.* **1991**, *113*, 8709.
- (5) Ongari, D.; Tiana, D.; Stoneburner, S. J.; Gagliardi, L.; Smit, B. *J. Phys. Chem. C* **2017**, *121*, 15135.
- (6) Miyasaka, H.; Clérac, R.; Campos-Fernández, C. S.; Dunbar, K. R. *J. Chem. Soc. Dalton. Trans.* **2001**, *2*, 858.
- (7) Brown-Xu, S. E.; Chisholm, M. H.; Durr, C. B.; Lewis, S. A.; Spilker, T. F.; Young, P. J. *Inorg. Chem.* **2014**, *53*, 637.
- (8) Walton, F. A. C. and R. A. *Multiple Bonds Between Metal Atoms Oxford Univ. Press. New York*, **1993**.
- (9) Franck, P. J. *Trans. Faraday Soc.*, **1926**, *21*, 536.
- (10) Marcus, R. *Rev. Mod. Phys.* **1992**, No. 2, 599.
- (11) Creutz, C. H.; Taube, H. *J. Am. Chem. Soc.* **1969**, *91*, 3988.
- (12) Creutz, C. Taube, H. *J. Am. Chem. Soc.* **1973**, *320*, 1086–109.
- (13) Wang, Y.; Lai, W.; Wang, N.; Jiang, Z.; Wang, X.; Zou, P.; Lin, Z.; Fan, H. J.; Kang, F.; Wong, C.-P.; Yang, C. *Energy Environ. Sci.* **2017**.
- (14) Smoleński, P.; Kłak, J.; Nesterov, D. S.; Kirillov, A. M. *Cryst. Growth Des.* **2012**, *12*, 5852
- (15) Huang, X.-C.; Zhang, J.-P.; Lin, Y.-Y.; Yu, X.-L.; Chen, X.-M. *Chem. Comm.* **2004**, 1100.

- (16) Robin, M. B.; Day, P. *Adv. Inorg. Chem. Radiochem.* **1968**, *10*, 247.
- (17) Stephen F. Nelsen. *Chem. Eur. J.* **2000**, *6*, 581.
- (18) Haga, M. aki; Matsumura-inoue, T.; Yamabe, S. *Inorg. Chem.* **1987**, *26*, 4148.
- (19) Hunziker, M.; Ludi, A. *J. Am. Chem. Soc.* **1977**, *99*, 7370.
- (20) Le Narvor, N.; Lapinte, C. *J. Chem. Soc. Chem. Commun.* **1993**, *8*, 357.
- (21) Dubicki, L.; Ferguson, J.; Krausz, E. R.; Lay, P. A.; Maeder, M.; Taube, H. *J. Phys. Chem.* **1984**, *88*, 3940.
- (22) Lay, P. A.; Magnuson, R. H.; Taube, H. *Inorg. Chem.* **1988**, *27*, 2364.
- (23) Ito, T.; Hamaguchi, T.; Nagino, H.; Yamaguchi, T.; Washington, J.; Kubiak, C. P. *Science*. **1997**, *277*.
- (24) Gutowsky, H. S.; Holm, C. H. *J. Chem. Phys.* **1956**, *25*, 1228.
- (25) Gutowsky, H. S.; McCall, D. W.; Slichter, C. P. *J. Chem. Phys.* **1953**, *21*, 279.
- (26) Bennett, M. J.; Cotton, F. A.; Davison, A.; Faller, J. W.; Morehouse, S. M. *J. Am. Chem. Soc.*, **1966**, *4371*.
- (27) Zavoisky, E. *Fiz. Zhurnal* **1945**, *9*, 211–245.
- (28) Cotton, F. A.; Murillo, C. A.; Villagrán, D.; Yu, R. *J. Am. Chem. Soc.* **2006**, *128*, 3281–3290.
- (29) Chisholm, M. H.; Pate, B. D.; Wilson, P. J.; Zaleski, J. M. *Chem. Commun.* **2002**, *2*, 1084–1085.
- (30) Cotton, F. A.; Donahue, J. P.; Lin, C.; Murillo, C. A. *Inorg. Chem.* **2001**, *40*, 1234–1244.
- (31) Winter, R. F. *Organometallics* **2014**, *1*, 4517.
- (32) Kubiak, C. P. *Inorg. Chem.* **2013**, *52*, 5633.
- (33) Demadis, K. D.; Hartshorn, C. M.; Meyer, T. J. *Chem. Rev.* **2001**, *101*, 2655.

- (34) Yang Wu, Y.; Meng, M.; Yi Wang, G.; Feng, P.; Liu, C. Y. *Chem. Commun.* **2017**, 3030.
- (35) Hupp, J. T.; Neyhart, G. A.; Meyer, T. J. *J. Am. Chem. Soc.* **1986**, *108*, 5349.
- (36) Neyhart G.A.; Hupp J.T.; Curtis J.C.; Timpson C.J.; Meyer T.J.; *J. Am. Chem. Soc.* **1196**, *118*, 3724.
- (37) Chen, P.; Meyer, T. J. *Inorg. Chem.* **1996**, *35*, 5520.
- (38) Glover, S. D.; Lear, B. J.; Salsman, J. C.; Londergan, C. H.; Kubiak, C. P. *Phil. Trans. R. Soc. A.* **2008** *366*, 177.
- (39) Roger H. Cayton and Malcolm H. Chisholm. *J. Am. Chem. Soc.* **1989**, *111*, 8921.
- (40) Chisholm, M. H. *Philos. Trans. R. Soc. A Math. Phys. Eng. Sci.* **2008**, *366*, 101
- (41) Chisholm, M. H.; Patmore, N. J. *Acc. Chem. Res.* **2007**, *40*, 19.
- (42) Cotton, F. A.; Dalal, N. S.; Liu, C. Y.; Murillo, C. A.; North, J. M.; Wang, X. *J. Am. Chem. Soc.* **2003**.
- (43) Hicks, J.; Ring, S. P.; Patmore, N. J. *Dalton. Trans.* **2012**, *41*, 6641.
- (44) Huynh, M. H. V.; Meyer, T. J. *Chem. Rev.* **2007**, *107*, 6961.
- (45) Hou, H. *Int. Environ. Res. J* **2011**, *6*, 50.
- (46) Mayer, J. M. *Annu. Rev. Phys. Chem.* **2004**, *55*, 363.
- (47) Roth, J. P.; Lovell, S.; Mayer, J. M. *J. Am. Chem. Soc.* **2000**, *122*, 5486.
- (48) Tadokoro, M.; Hosoda, H.; Inoue, T.; Murayama, A.; Noguchi, K.; Iioka, A.; Nishimura, R.; Itoh, M.; Sugaya, T.; Kamebuchi, H.; Haga, M. A. *Inorg. Chem.* **2017**, *56*, 8513.
- (49) Sun, H.; Steeb, J.; Kaifer, A. E. *J. Am. Chem. Soc.* **2006**, *128*, 2820.
- (50) Tadokoro, M.; Inoue, T.; Tamaki, S.; Fujii, K.; Isogai, K.; Nakazawa, H.; Takeda, S.; Isobe, K.; Koga, N.; Ichimura, A.; Nakasuji, K. *Angew. Chem. Int. Ed.* **2007**, *46*, 5938.
- (51) Markle, T. F.; Rhile, I. J.; Dipasquale, A. G.; Mayer, J. M. P. *Proc. Natl. Acad. Sci.* **2008**, *24*, 8185.

- (52) Goeltz, J. C.; Kubiak, C. P. *J. Am. Chem. Soc.* **2010**, *132*, 17390.
- (53) Waskasi, M. M.; Newton, M. D.; Matyushov, D. V. *J. Phys. Chem. B* **2017**, *121*, 2655.
- (54) Dinpajooh, M.; Matyushov, D. V. *J. Phys. Chem. B* **2014**, *118*, 7925.
- (55) Small, D. W.; Matyushov, D. V.; Voth, G. A. *J. Am. Chem. Soc.* **2003**, *125*, 7470.
- (56) Matyushov, D. V.; Voth, G. a. *J. Chem. Phys.* **2000**, *113*, 5413.
- (57) Baumann, J. a.; Salmon, D. J.; Wilson, S. T.; Meyer, T. J.; Hatfield, W. E. *Inorg. Chem.* **1978**, *17*, 3342.
- (58) Piotrowiak, P.; Kobetic, R.; Schatz, T.; Strati, G. *J. Phys. Chem.* **1995**, 2250.
- (59) Brunschwig, B. S.; Creutz, C.; Sutin, N. *Chem. Soc. Rev.* **2002**, *31*, 168.
- (60) Canzi, G.; Goeltz, J. C.; Henderson, J. S.; Park, R. E.; Maruggi, C.; Kubiak, C. P. *J. Am. Chem. Soc.* **2014**, *136*, 1710.
- (61) Jin-Long Y.; Matsuda, Y.; Uemura, K.; Ebihara, M. *Inorg. Chem.* **2015**, *54*, 2331.
- (62) Wilkinson, L. A.; McNeill, L.; Meijer, A. J. H. M.; Patmore, N. J. *J. Am. Chem. Soc.* **2013**, *135*, 1723.
- (63) Wilkinson, L. A.; McNeill, L.; Scattergood, P. A.; Patmore, N. J. *Inorg. Chem.* **2013**, *52*, 9683.
- (64) Wilkinson, L. A.; Vincent, K. B.; Meijer, A. J. H. M.; Patmore, N. J. *Chem. Commun.* **2016**, *52*, 100.
- (65) Lancaster, K.; Odom, S. A.; Jones, S. C.; Thayumanavan, S.; Marder, S. R.; Brédas, J.-L.; Coropceanu, V.; Barlow, S. J. *Am. Chem. Soc.* **2009**, *131*, 1717.
- (66) Shen, J. J.; Zhong, Y. W. *Sci. Rep.* **2015**, *5*, 1.

Chapter 2. Building Blocks for the Assembly of Hydrogen Bonded Molecular Assemblies.

2.1 Abstract

A series of di-molybdenum paddlewheel complexes of the form $\text{Mo}_2(\text{DTolF})_{4-n}(\text{OAc})_n$ where DTolF = *N,N'*-bis(4-methylphenyl)formimidate and OAc = acetate ($n = 0, 1, 2$ *cis-* or *trans-*) complexes **2** – **5** respectively, have been synthesized. The complexes were structurally characterised by ^1H NMR and IR spectroscopy and single-crystal x-ray diffraction.

Cyclic Voltammetry was also performed where oxidation potentials were seen to cathodically shift with substitution of DTolF ligand for OAc ligands ranging between -0.238 V (**2** and **3**) and -0.375 V (**5**). Data was also collected for the analogous $\text{Mo}_2(\text{DAniF})_{4-n}(\text{OAc})_n$ series where DAniF = *N,N'*-bis(4-methoxyphenyl)formimidate. The oxidation potentials did not follow the same pattern and the differences observed were much smaller ranging between -0.220 V with *trans*- $\text{Mo}_2\text{DAniF}_3(\text{OAc})$ and -0.272 V with *cis*- $\text{Mo}_2\text{DAniF}_3(\text{OAc})$ vs. the ferrocene/ferrocenium Fc/Fc^+ redox couple ($E_{1/2} = 0.00\text{V}$).

The attempted substitution of the acetate ligands for ligands capable of self-complimentary hydrogen bonds was explored in a range of conditions including but generally found to be unsuccessful. The synthetic insights gained were however useful informing the work described in following chapters.

2.2 Mixed Valence Extended Assemblies.

Owing to their interesting optical, electronic and magnetic properties there is much interest in the incorporation of metal paddlewheels into functional materials. Discussed below are a few examples of oligomeric molecular shapes and molecular wires formed through covalent bonding interactions that incorporate di-molybdenum paddlewheels where the MV state has been investigated.

To the authors knowledge there are no related hydrogen bonded assemblies incorporating di-molybdenum redox centres in the literature beyond the $[\text{Mo}_2(\text{TiPB})_3(\text{HDON})]_2$ and $[\text{Mo}_2(\text{TiPB})_3(\text{HDOP})]_2$ “dimer of dimers” reported by the Patmore group discussed in detail in Chapter 1. The latter complex was also revisited for a new series of mechanistic studies discussed in Chapter 3. For the specific mechanism by which the MV state can be stabilised over a hydrogen-bond turn to those chapters.

There are also two further examples of assemblies generated through hydrogen-bonding interactions, a “supramolecular junction” and a molecular wire type structure both generated through dimerization through a hydrogen bond. Though not structurally related to the complexes discussed in this body of this chapter they have been shown to display excellent conductivity, often comparable with covalent systems and so are perhaps the best proofs of concept for the targeted complexes of our own work.

2.2.1 Mixed Valence Oligomers

2.2.1.1 Covalent

Cotton *et al.* first demonstrated the synthesis of molecular triangles and squares having Mo_2 paddlewheels as molecular vertexes as per the synthetic strategy illustrated in Scheme 2.1. When $\text{Mo}_2(\text{DAniF})_2(\text{NCMe})_6(\text{BF}_4)_2$ is reacted with the tetraethyl ammonium salt of the perfluoroterephthalate dianion, $[\text{Et}_4\text{N}]_2[\text{O}_2\text{CC}_6\text{F}_4\text{CO}_2]$ a dynamic equilibrium exists between the molecular square, $[\text{cis-Mo}_2(\text{DAniF})_4(\text{O}_2\text{CC}_6\text{F}_4\text{CO}_2)_4]$ and the molecular triangle, $[\text{cis-Mo}_2(\text{DAniF})_3(\text{O}_2\text{CC}_6\text{F}_4\text{CO}_2)_3]$ (Figure 2.1).¹⁻³

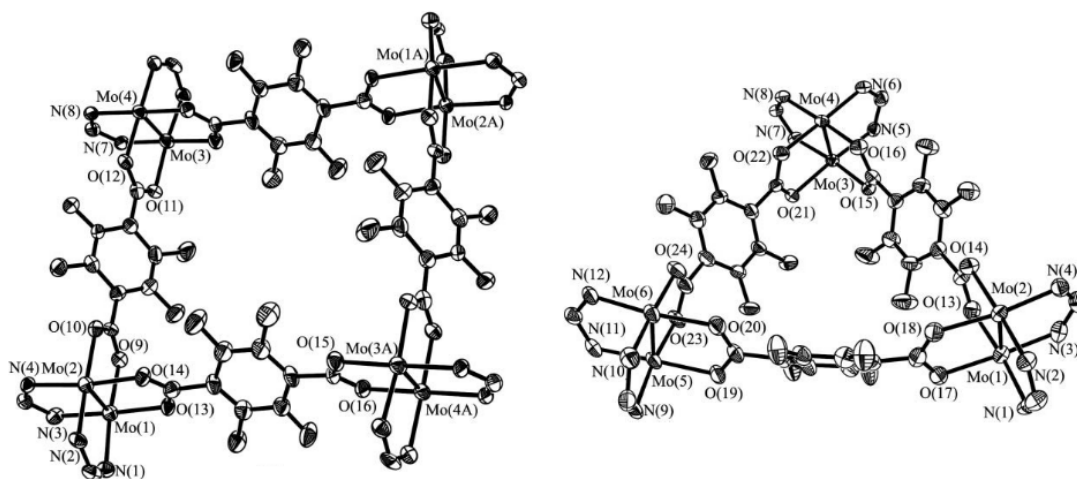


Figure 2.1 Crystal structures of the perfluoro terephthalate bridged molecular square and triangles reported by Cotton *et al.* The redox active vertices are the *cis*-Mo₂(DAniF)₃ moieties. Figure adapted from reference with permission of the RSC. ¹

The interconversion of the two can be observed by NMR spectroscopy. At room temperature a mixture of the two species is observed in the ¹H NMR but at -70°C only the square is observed and as the sample is allowed to equilibrate to room temperature again the peaks corresponding to the triangle grow in and the square is depleted. The signals do somewhat overlap though so the use of ¹⁹F NMR wherein the peaks are more separated allows the determination of the molar fractions of each component at equilibrium as both a function of the total concentration and temperature. From these experiments the authors determine for the conversion of 3 moles of the square to 4 moles of the triangle; $\Delta G^0 = 21.0 \text{ kJ mol}^{-1}$, $\Delta H^0 = 23.5 \text{ kJ mol}^{-1}$ and $\Delta S^0 = 8.2 \text{ J mol}^{-1} \text{ K}^{-1}$. These values indicate that there is very little strain in the triangular form, consistent with only small buckling of the bond angles between the Mo₂ units and perfluoroterephthalate bridge bond angles and would be easily offset by the increase in entropy.

The group of Chisholm *et al.* were the first to report on the electronic structure and perform spectroscopic analysis on the MV state in an analogous system.⁴ They report two molecular triangles [L₂Mo₂(O₂CCO₂)₃] where L = DAniF or DPhF generated by reaction of the bis cationic precursor (as above) with [ⁿBu₄]₂[O₂CCO₂]. In contrast to those reported Cotton *et al.* above the square and triangle are formed competitively and do not enter an equilibrium. When 0.75 equivalents of [ⁿBu₄][O₂CCO₂]

are used, the triangle is the exclusive product. Both triangles display IVCT transitions in the NIR with Hush analysis indicating delocalised (Class III) behaviour. Identical behaviour was proposed to the squares but was not discussed in detail due to synthetic limitations. The EPR spectra of the mixed valence state in both triangles shows a single peak at $g = 1.95$ indicating a metal centred radical. But the absence of hyperfine splitting for the $^{95/97}\text{Mo}$ spin isotope coupling means no comment on the extent of delocalisation on the EPR timescale could be made. This is reasoned to be a consequence of the Mo-N bonding as the $\text{Mo}_2(\text{DAniF})_4^+$ cation similarly shows no hyperfine splitting.⁴

2.2.1.2 H-bonded

Wan *et al.* report a supramolecular junction formed by the self-complimentary quadruple hydrogen bonding interaction between ureido pyrimidine-dione derivatives shown in Figure 2.2.⁵

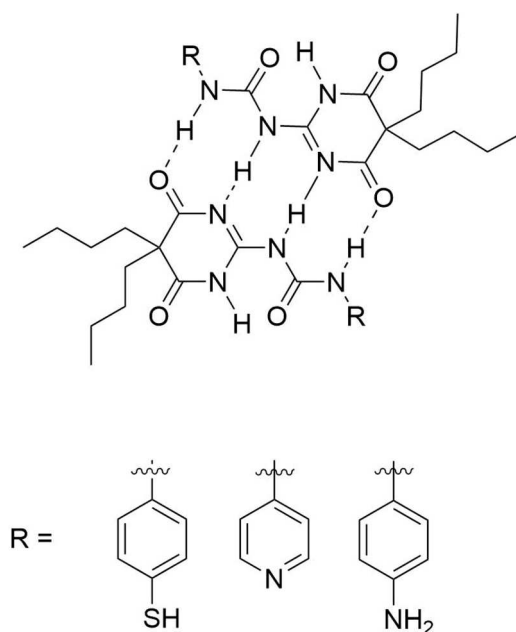


Figure 2.2. Ureido pyrimidine-dione derived supramolecular junctions reported by Wan *et al.* Reproduced from reference with permission from Wiley & Sons.⁵

The electron transport properties of the junctions are studied using scanning tunnelling microscopy, break junction (STM-BJ) methodology.⁶ The principle of this method is repeatedly to form and break contacts with the conductive gold STM tip and the substrate and to generate a conductance histogram.

Where no self-assembly of the dimer is observed there is exponential decay of the conductance. When self-assembly occurs, a plateau in the conductance histogram is observed and the dimer conductance can be determined. The thiol derivative shows the highest conductance approaching $10^{-3} G_0$. This is key, as it is comparable with that of fully-conjugated single molecular devices.

This means that supramolecular assemblies generated through hydrogen bonds could be equally suited to the design of molecular electronic devices and is perhaps the best proof of concept for our own research goals.

2.2.2 Molecular Wires

2.2.2.1 Covalent

There are many examples of polymeric assemblies incorporating di-metal paddlewheels, Chisholm *et al.* have published a comprehensive review on the topic.⁷ But to this authors knowledge most examples therein are discussed purely in interest of their structural diversity and there are few reports of characterisation of their electronic structure. One series of complexes where this is discussed is published by Cotton *et al.* They report mixed valence complexes of the form $\{[\text{Ru}_2(\text{O}_2\text{CC}_2\text{H}_5)_4(\text{axL})]\cdot\text{BF}_4\}_\infty$ where $\text{axL} = \text{Cl}, \text{Br}$ or phenazine (phz) where polymeric assembly occurs through axial coordination environment (Figure 2.3).⁸ The halogen bridged analogues are linear polymers whereas the phz bridged system forms a kinked chain. The kink occurs in the bond angles about either side of the phz ligand. Each Ru-Ru-N bond angle is approximately 180° but is not co-linear with the next. Magnetic susceptibilities of the complexes were determined using a superconducting quantum interference device (SQUID). The halogen bridged analogues show only slight temperature dependence and so despite the polymeric form can essentially be treated as a series of individual $S = 3/2$ centres. On the contrary, the phz analogue shows a temperature dependence profile suggesting antiferromagnetic coupling between the $[\text{Ru}_2]^+$ centres. The authors believe given the separation of the parallel chains the crystal packing due to the intervening BF_4^- ions the coupling should occur via an intrachain mechanism.⁸ The polymer can thus be described as a one-directional antiferromagnetic (ODAFM) system.

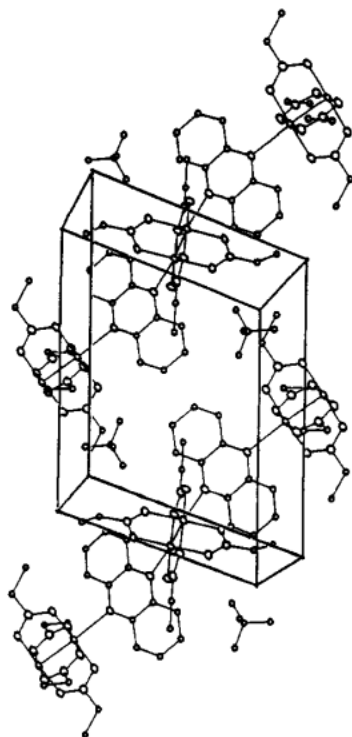


Figure 2.3. ORTEP drawing of the $\{[\text{Ru}^{\text{II}}\text{Ru}^{\text{III}}(\text{O}_2\text{CC}_2\text{H}_5)_4(\text{phz})], \text{BF}_4\}$ unit cell. Reproduced from reference with permission from Wiley & Sons.⁸

2.2.2.2 *H-bonded*

Martín *et al.* report a series of molecular wires where a *p*-(2-fulleropyrrolidinyl)benzoate (C_{60}) and zinc porphyrin (ZnP) redox moieties are connected by a hybrid of covalent π -conjugation and a hydrogen bonding interaction between carboxylate and amidinium termini (Figure 2.4).⁹ Photoexcitation of the zinc porphyrin induces intramolecular electron transfer to produce a radical-ion pair, $(\text{ZnP})^{\cdot+} \cdot (\text{C}_{60})^{\cdot-}$. The attenuation factor (β) is used to determine the magnitude of the electronic coupling between the redox sites in these systems and is related to the rates of charge separation and recombination vs. intramolecular separation of redox centres. In this series $\beta = 0.07 \pm 0.01 \text{ \AA}^{-1}$, amongst the lowest reported for any molecular wire so again shows that hydrogen bonding interactions can be comparable with covalently interactions in terms of charge transfer properties.

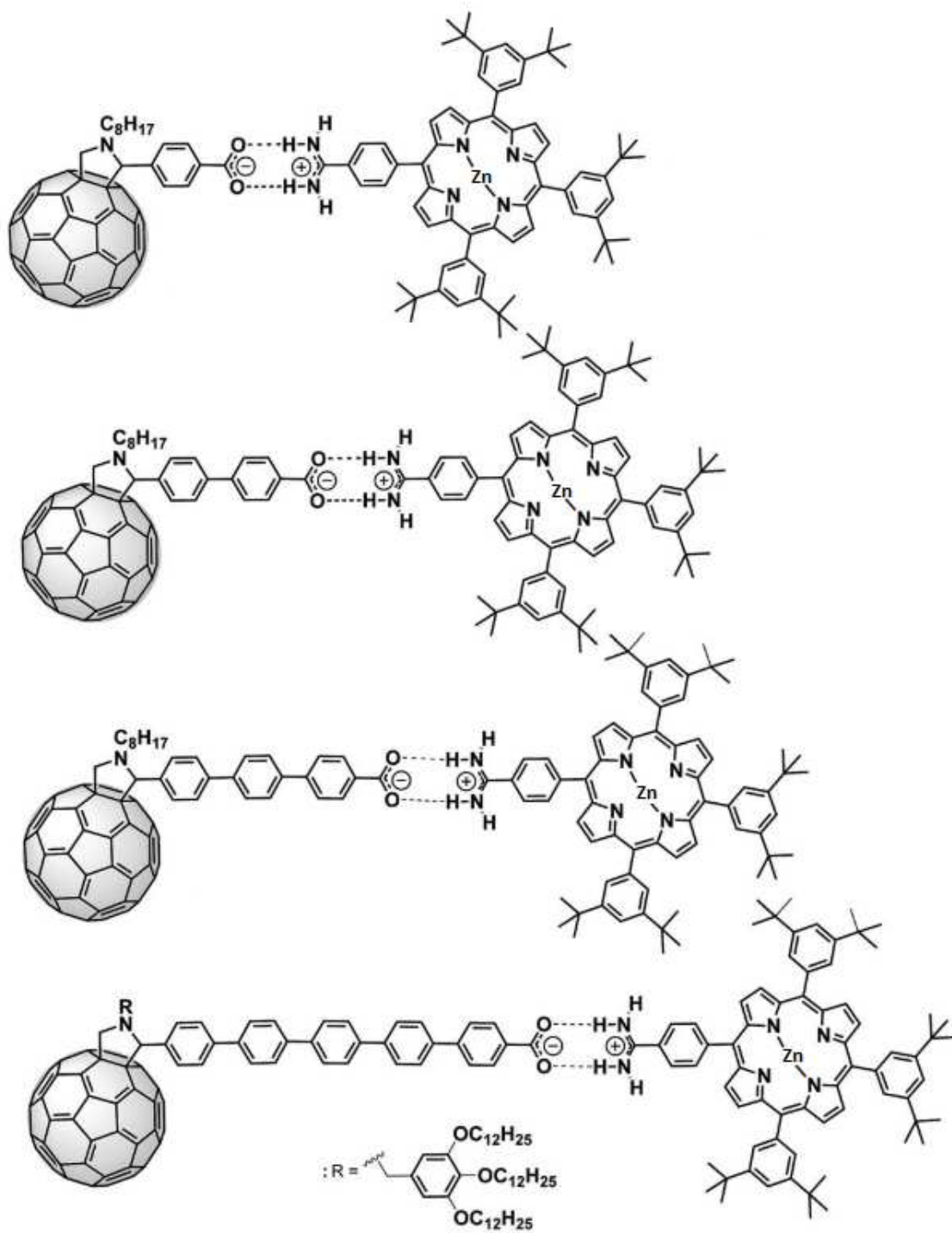
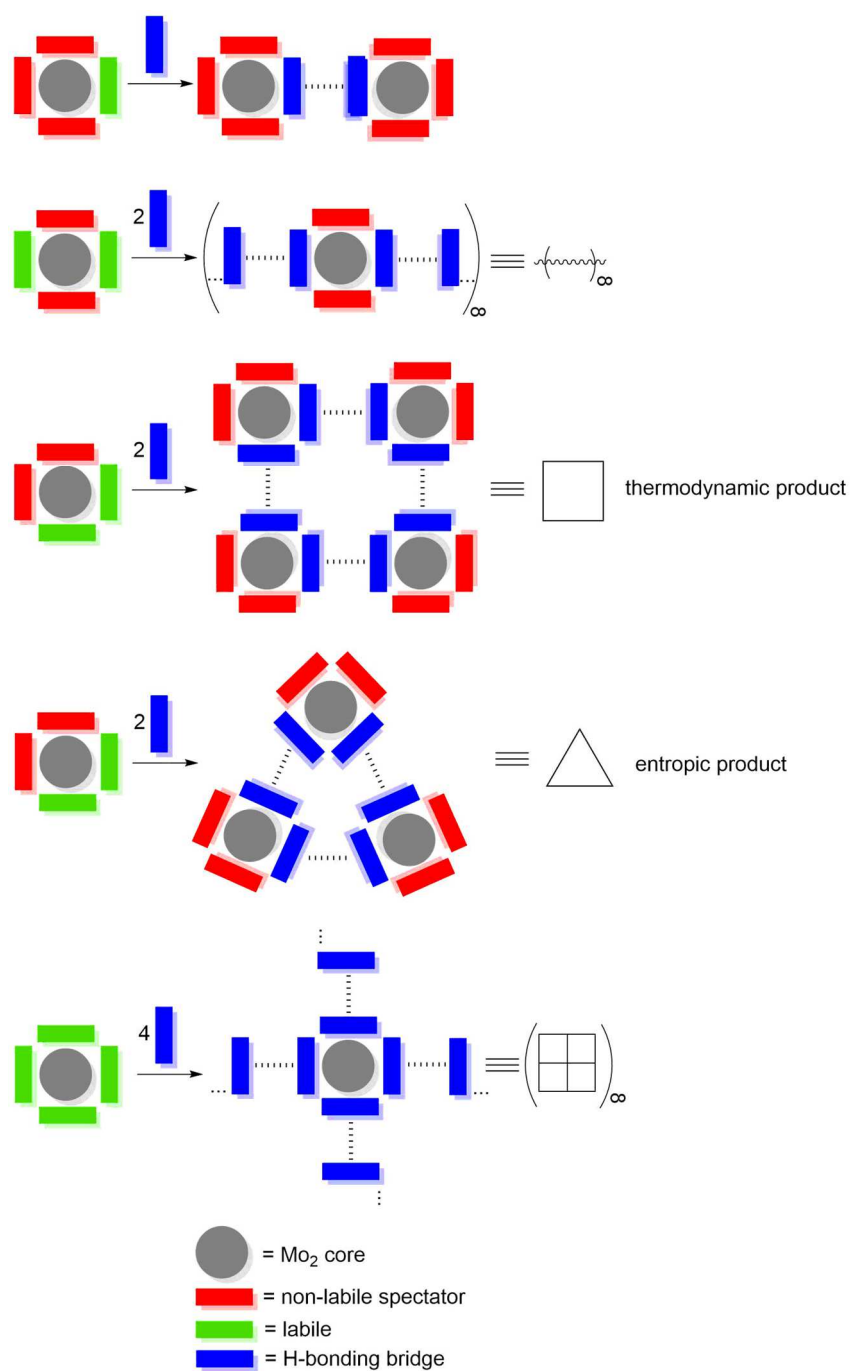


Figure 2.4. A series of ZnP-C₆₀ molecular wires incorporating an amidinium–carboxylate hydrogen bonding interaction as reported by Martín *et al.* Figure adapted from reference with permission of Wiley & Sons.⁹

2.3 Aims

The series of complexes $\text{Mo}_2(\text{DTolF})_{4-n}(\text{OAc})_n$ ($n = 0, 1, 2$ *cis*- and *trans*-) will be synthesised. These complexes have rigid molecular geometries due to the chelating ligands. It is proposed that upon substitution of the labile acetate ligands the presence of the non-labile sterically demanding spectator DTolF ligands maintains this structural rigidity thereby directing assembly of polymeric and oligomeric species. A schematic approach to this strategy is presented in Scheme 2.1. where the hydrogen bonded bridge is a ligand capable of forming self-complimentary hydrogen-bonds.

The redox properties and characterisation of the MV state in assemblies of this form beyond the simplest “dimer of dimer” has not been previously reported. Conductance measurements have been recorded for a supramolecular junction and a molecular wire type architecture that incorporates a H-bond. In these systems the H-bonding interaction can mediate charge transfer as effectively as a conjugated π -system.^{5,9} The successful synthesis of these target systems could therefore have important ramifications in the design of new molecular electronic devices.

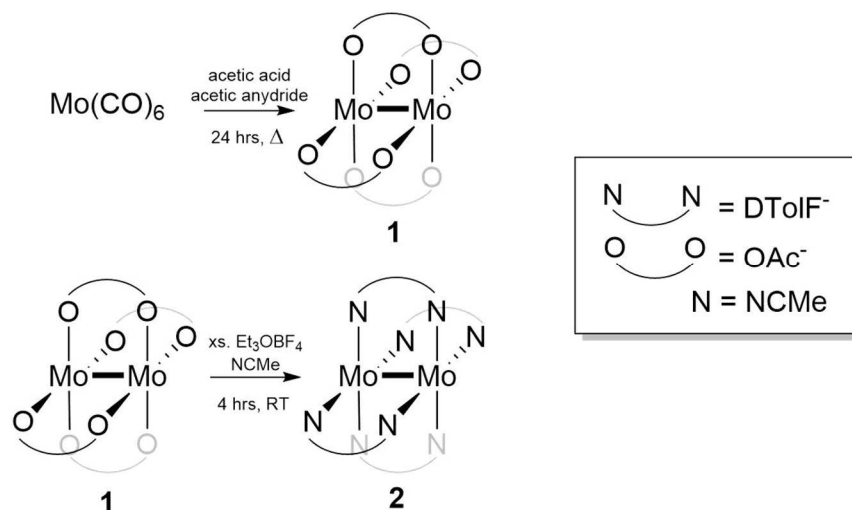


Scheme 2.1. Synthetic strategy for the generation of Hydrogen bonded assemblies incorporating Mo₂ redox centres.

2.4 Discussion

2.4.1 Synthesis & Structural Characterisation.

Synthesis of mixed formamidinate-carboxylate complexes first requires the synthesis of the homoleptic parent complexes; $\text{Mo}_2(\text{OAc})_4$ (**1**) and $\text{Mo}_2(\text{DTolF})_4$ (**2**) (Scheme 2.2).

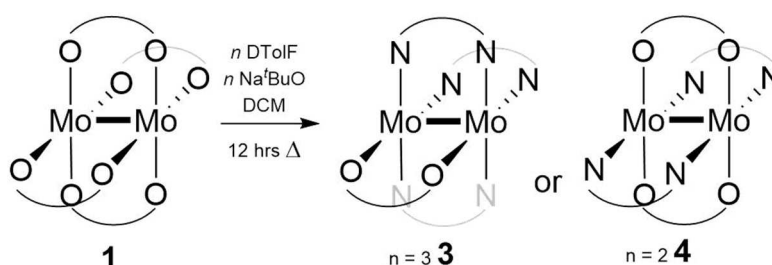


Scheme 2.2. Synthesis of $\text{Mo}_2(\text{OAc})_4$ (**1**) and $\text{Mo}_2(\text{DTolF})_4$ (**2**).

Complex **1** is synthesized by refluxing $\text{Mo}(\text{CO})_6$ in a mixture of acetic anhydride in acetic acid (40 % v/v). The CO ligands being strong π -acceptors, form progressively stronger metal-ligand bonds after their stepwise reduction as they receive a larger portion of the metal electron density. This necessitates a high reaction temperature allowed by the acetic acid / anhydride mixture. Due to the constant sublimation of $\text{Mo}(\text{CO})_6$ it is also necessary to add a small amount of a much lower boiling point solvent such as hexane (< 5% v/v) to wash the subliming material that collects on the reflux condenser. The reaction is also inhibited by water, the addition of acetic anhydride ensures any inadvertent exposure to water will produce further equivalences of acetic acid. Upon successful reaction, yellow crystalline $\text{Mo}_2(\text{OAc})_4$ is precipitated. Complex **2** is synthesised by refluxing $\text{Mo}(\text{CO})_6$ with excess HDTolF in 1,2-DCB. Alternatively, refluxing of **1** in the presence of excess HDTolF will also

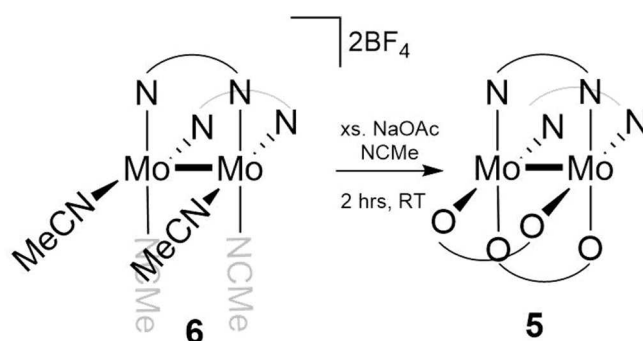
yield **2** owing to the increased thermodynamic stability going from the acetate ligands to the more basic N-donor DTOLF ligands.

The lability of the acetate ligands is key to the synthesis of the heteroleptic complexes $\text{Mo}_2(\text{NN})_4-n(\text{OAc})_n$ where $n = 1, 2$ and 3 . Cotton *et al.* had first exploited the following hierarchy of lability $\text{NCMe} > \text{OAc} > \text{NN}$ to generate the $\text{NN} = \text{DAnF}$ series of complexes. The use of DTOLF is desirable as they should impart increased solubility in solvents such as DCM that favour the formation of hydrogen bonding interactions upon substitution of the labile acetate ligands. While the general synthetic strategy Cotton developed is still applied here, the reactivity and solubility of the materials necessitated the development of different synthetic conditions. For instance, under the original conditions (NaOMe, THF at RT) synthesis of $\text{Mo}_2(\text{DTOLF})_3(\text{OAc})$ (**3**) and *trans*- $\text{Mo}_2(\text{DTOLF})_2(\text{OAc})_2$ (**4**) had proven problematic being prone to under-substitution. To drive the reaction to completion the solvent system was changed to DCM, a stronger base, Na^tBuO used and the reaction was performed under reflux conditions (Scheme 2.3.). The change in solvent can be explained by a stark difference in solubility in THF observed between **3** (soluble) and **4** (insoluble) where the DAniF analogues are soluble in both cases. Though the starting material in each case $\text{Mo}_2(\text{OAc})_4$ is even less soluble in DCM it becomes solubilised as it reacts with the base. Both product complexes **3** and **4** are soluble in DCM at reflux providing an entropic driving force. On cooling **4** being sparingly soluble in DCM is precipitated while **3** is isolated by precipitation upon addition of EtOH.



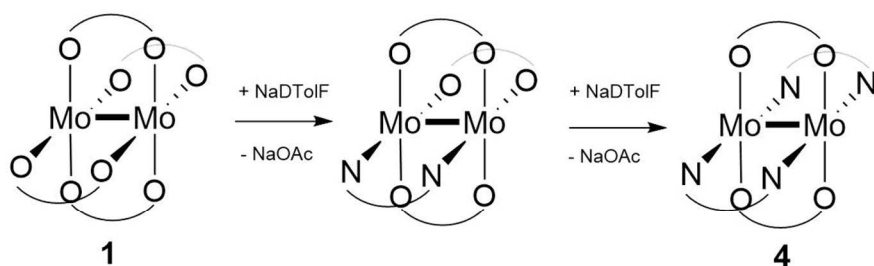
Scheme 2.3. Synthesis of $\text{Mo}_2(\text{DTOLF})_3(\text{OAc})$ (**3**) and *trans*- $\text{Mo}_2(\text{DTOLF})_2(\text{OAc})_2$ (**4**).

Note that in Scheme 2.3 when $n = 2$ the *trans* substituted complex **4** is produced, the *trans* isomerism is due to the large steric bulk of the formamidinate ligands. Synthesis of the *cis*- isomer, complex **5** is achieved by a different synthetic method. This first requires the synthesis of the precursor complex *cis*-Mo₂(DTolF)₂(NCMe)₄·(BF₄)₂ (**6**). Complex **6** is prepared by treating **1** with excess Et₃OBF₄ and a few drops of water in NCMe. This removes two *cis*-orientated DTolF ligands and coordinates NCMe solvent molecules in their place. The *cis*-geometry is attributed to the *trans* effect of the DTolF ligands. Complex **5** is yielded by reaction of the bis-cationic complex with excess NaOAc in NCMe (Scheme 2.2). The contrasting synthetic routes and the governing thermodynamic properties to generate the *cis*- and *trans*-isomers are further highlighted in Scheme 2.3

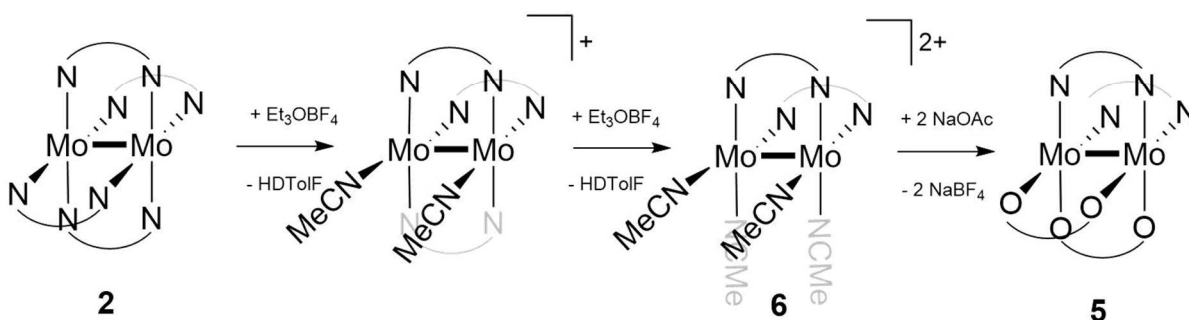


Scheme 2.4. Synthesis of *cis*-Mo₂(DTolF)₂(OAc)₂ (**5**).

Sterically directed ligand addition



Trans effect directed ligand loss



Scheme 2.5. Comparison of synthetic routes required to generate trans-Mo₂(DTolF)₂(OAc)₂ (**4**) top and trans-Mo₂(DTolF)₂(OAc)₂ (**5**) bottom.

2.4.1.1 ¹H NMR spectra

The ¹H NMR spectra of complexes **2** – **5** are shown below in Figure 2.5. In the tetra-substituted complex **2** a single DTolF ligand environment exists. The most characteristic change in the ¹H NMR response for the free ligand upon coordination to the Mo₂ core is a large downfield shift of the formamidine backbone (-N-CH-N-) proton from 8.07 ppm to 8.42 ppm in **2**. The aromatic protons are observed as doublets in all the complexes with coupling constant, *J* > 8 Hz. Upon substitution of one DTolF ligand for OAc, in complex **4**, there are now two DTolF ligand environments, two cis and one trans to the OAc ligand so each of the Ar-H the signals are a split in a 2:1 ration giving a total integration pattern of 8:8:4:4. Symmetry in the DTolF ligands is restored again upon second substitution in **5** and **6**. The cis and trans geometries can be distinguished by their chemical shifts.

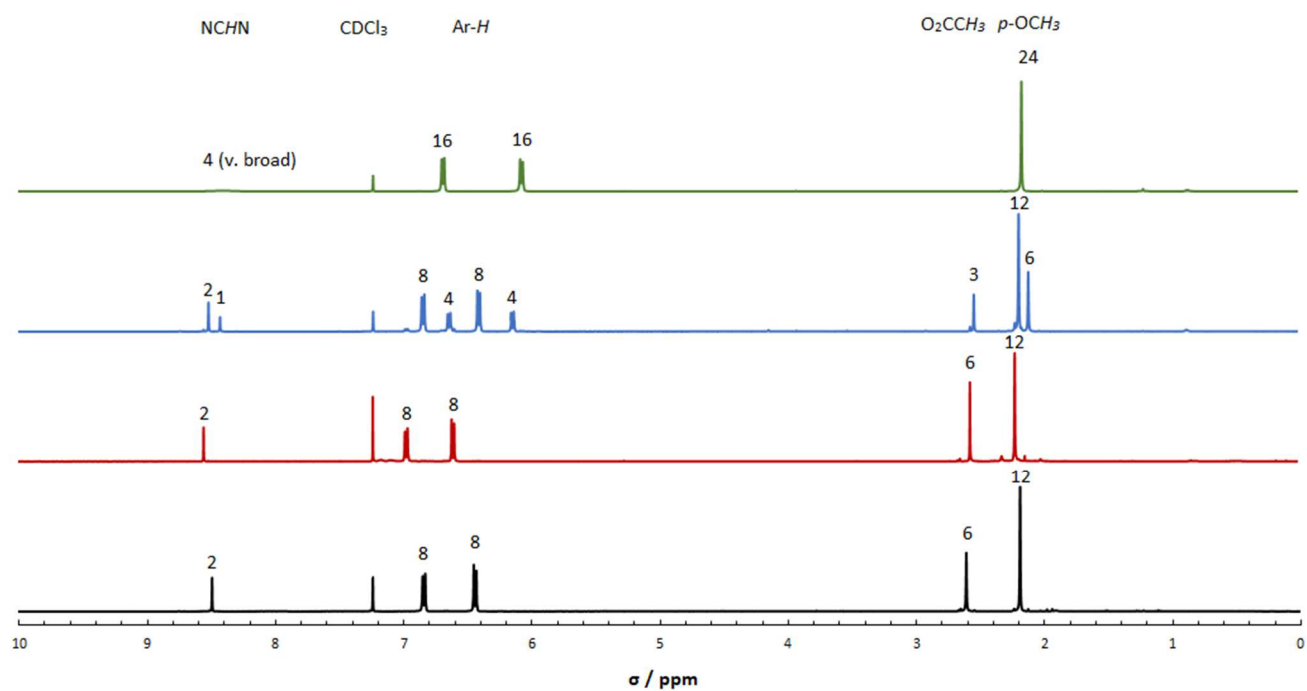


Figure 2.5. ¹H NMR spectra of complexes **2** (green), **3** (blue), **4** (red) and **5** (black) in CDCl₃ at approximately 10 mM.

2.4.1.2 X-ray Crystallography

The crystal structures of complexes **3** – **6** have not been previously reported, the structures of *cis*-Mo₂(DTolF)₂(OAc)₂ **5** and *cis*-Mo₂(DTolF)₂(NCMe)₄.2BF₄ **6** as determined by single-crystal x-ray diffraction are described herein.

Crystals of **5** were isolated by slow diffusion of hexanes into DCM solutions of **2** at 4 °C. The solid-state structure is presented in Figure 2.6.

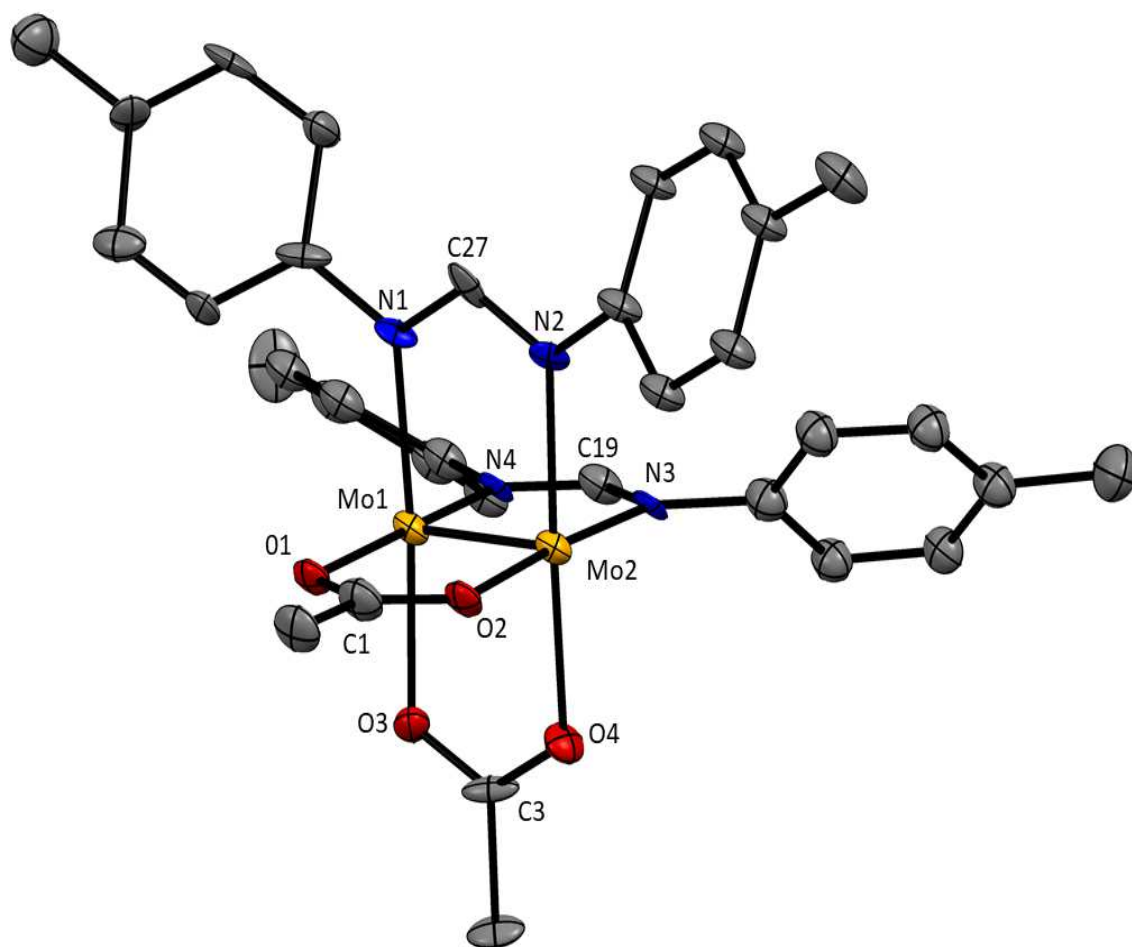


Figure 2.6. Solid-state structure of *cis*-Mo₂(DTolF)₂(OAc)₂ (**5**) as determined by single-crystal XRD. Thermal ellipsoids are shown at 50 % probability. Hydrogen atoms are omitted for clarity.

The X-ray crystal data obtained for **5** was of pure quality, indicated by a poor *R* index [$I > 2\sigma(I)$] $R_1 = 0.1300$ following refinement. As such it is not appropriate to discuss exact bond lengths but the determined structure is sufficient to confirm the overall structural connectivity of the complex.

Crystals of **6** were obtained by slow diffusion Et₂O into NCMe solutions of **6** at 4 °C. The solid-state structure determined by single crystal X-ray Diffraction is presented in Figure 2.7.

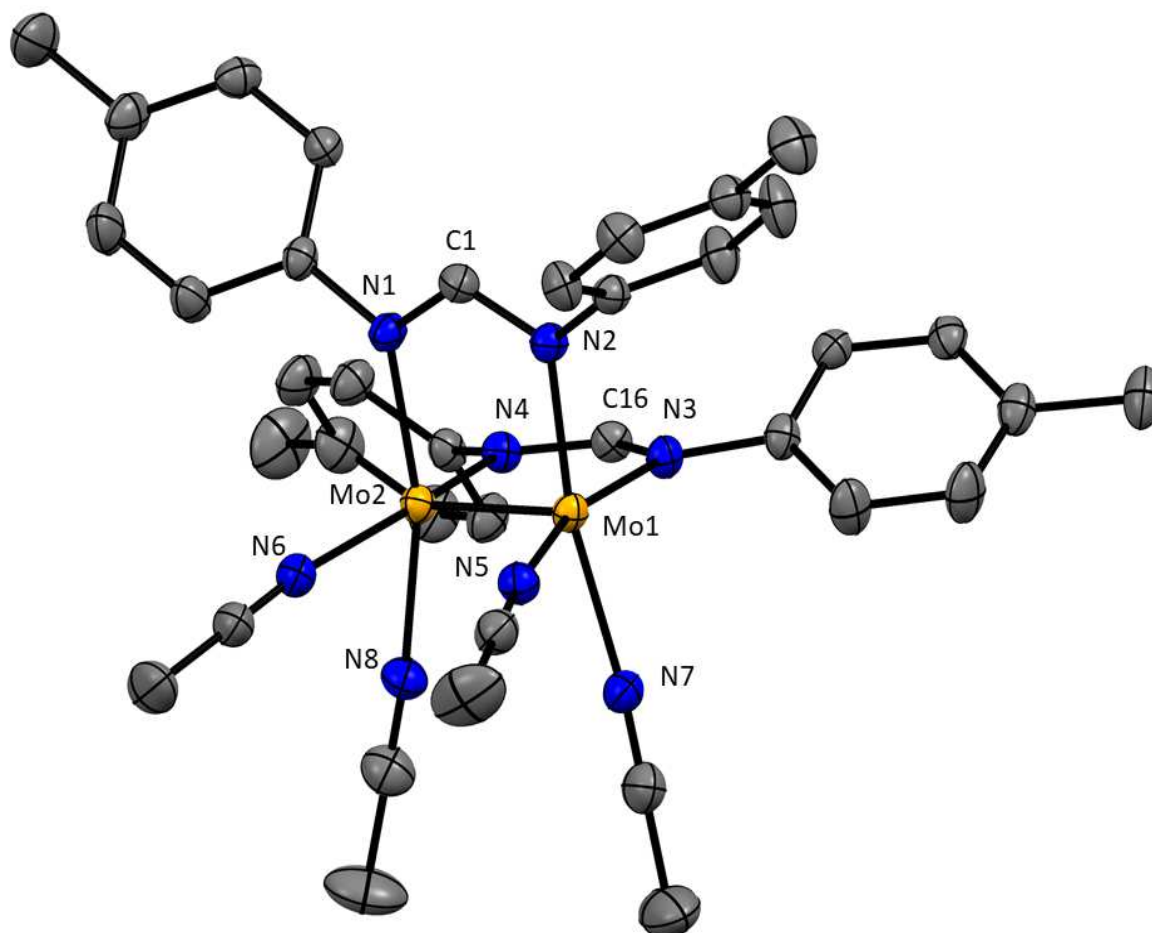


Figure 2.7. Solid-state structure of *cis*-Mo₂(DTolF)₂(NCMe)₄.2BF₄ (**6**) as determined by single-crystal XRD. Thermal ellipsoids are shown at 50 % probability. Hydrogen atoms are omitted for clarity. Selected bond lengths (Å): Mo1-Mo2 = 2.1235(3), Mo1-N1 = 2.095(3), Mo2-N2 = 2.094(2), Mo1-N3 = 2.100(2), Mo2-N4 = 2.093(3), Mo1-N5 = 2.162(3), Mo2-N6 = 2.182(3), Mo1-N7 = 2.169(3), Mo2-N8 = 2.169(3). Selected bond angles (°): N1-Mo1-Mo2 = 92.89(7), N3-Mo1-Mo2 = 92.23(7), N1-Mo1-N5 = 88.89(10), N3-Mo1-N5 = 163.70(10), N1-Mo1-N7 = 165.04(10), N2-Mo2-N8 = 164.60(10), N5-Mo1-N7 = 83.72(10), N8-Mo2-N6 = 82.63(11).

In complex **6** the two *cis*-orientated OAc⁻ ligands of **5** are replaced each with two monodentate acetonitrile ligands. The effect of substituting chelating ligands for monodentate ligands is reflected in the Mo-Mo bond which lengthens significantly to 2.1235(4) Å compared to 2.085(4) Å in the tetraformamidinate parent complex **1**, previously reported by Cotton *et al.*⁵⁴

The average Mo-N bond length for the DTolF ligands (N1-4) is 2.0955(6) Å compared to 2.1705(6) Å in the acetonitrile ligands (N5-8). This shows the effect of increased basicity and chelate effect which produces stronger, shorter bonds.

The DTolF N-Mo-N bond angles N1-Mo1-N3 and N2-Mo2-N4 are 94.59(10)° and 94.39(11)° versus acetonitrile N-Mo-N angles N5-Mo1-N7 and N6-Mo2-N8 at 83.73(11)° and 82.63 (11)°. The acetonitrile ligands in **6** are less sterically demanding than the OAc⁻ ligands in **5** so can be pushed close together providing further steric relief to the DTolF ligands.

2.4.2 Cyclic Voltammetry

Cyclic Voltammetry was performed on complexes **2** – **5** using 0.1 M TBAPF₆ electrolyte in DCM. Complex **6** is omitted due to its high instability with regards to oxygen making it unsuitable in this experimental set up. The results obtained at 100 mV s⁻¹ scan rate are shown in Figure 2.8. DCM was selected as the hydrogen bonded assemblies generated upon substitution of the labile acetate must have DCM solubility and comparison to the precursor complexes is informative of their stability as well as being useful to rule out their presence as impurities.

The CV's of complexes **3** – **6** all show single electron oxidations accounting to removal of an electron from the HOMO δ (Mo₂⁴⁺ → Mo₂⁵⁺). The peak separations of the oxidation and reverse reduction, E_v are rather large suggesting quasi-reversible behaviour. However, this expected to be in part a result of large internal resistance within the cell rather than solely as a property of the complexes as similar behaviour is observed for the Fc/ Fc⁺ reference in the experimental set up. Current response increases linearly as a function of the square root of the scan rate which confirms reversibility.

Both complexes **3** and **4** have $E_{1/2} = -0.238$ V so no change is observed after substitution of one DTolF ligand for an OAc ligand. The second substitution does produce a moderate cathodic shift to -0.344 V in **5** and -0.375 V **6**.

The CV data for substituted DAniF analogues have not been previously reported so these complexes were also synthesised, and their CV's collected for comparison. The data taken from these experiments is also collated in Table 2.1. The $E_{1/2}$ value of **1** and the DAniF analogue are very similar. Where moderate cathodic shifts are observed for the DTolF analogues as they are substituted for OAc ligands there is not an obvious trend in the DAniF analogues and the $E_{1/2}$ shifts are much smaller.

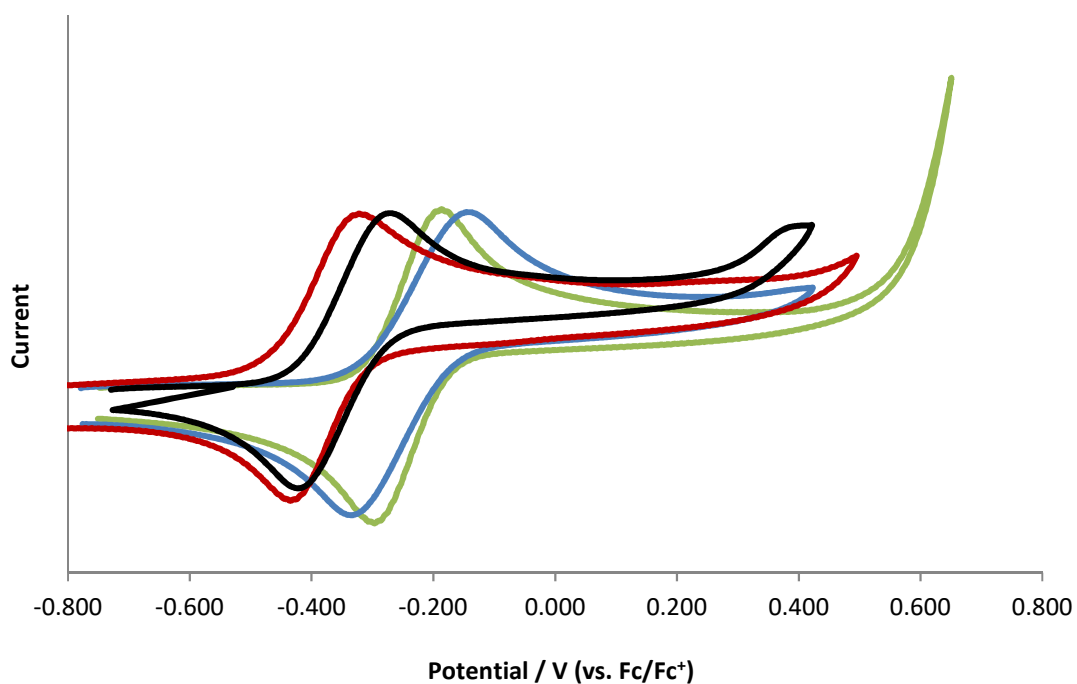


Figure 2.8. CV's of complexes **2** – **5** using 0.1 M TBAPF₆ electrolyte 5 mM analyte concentration in DCM at 100 mVs⁻¹ scan rate.

Table 2.1. Electrochemical data taken from CV's of complexes **2** – **5** (Figure 2.3) and comparison to DAniF analogues.

| Complex | $E_{1/2}$ | ΔE_v | $E_{1/2}$ DAniF |
|---|-----------|--------------|-----------------|
| Mo ₂ (DTolF) ₄ (2) | -0.238 | 0.110 | -0.242 |
| Mo ₂ (DTolF) ₃ (OAc) (3) | -0.238 | 0.195 | -0.222 |
| <i>trans</i> - Mo ₂ (DTolF) ₂ (OAc) ₂ (4) | -0.344 | 0.153 | -0.220 |
| <i>cis</i> - Mo ₂ (DTolF) ₂ (OAc) ₂ (5) | -0.375 | 0.112 | -0.272 |

2.4.3 UV-Vis Absorption Spectroscopy.

The UV-Vis Absorption spectra for complexes **2** - **5** are shown in Figure 2.9. As the DTolF ligand is a chromophore it is expected to have intense UV absorption properties, indeed the symmetry allowed

$\pi \rightarrow \pi^*$ transitions for the DTolF ligands in these complexes are intense and high energy appearing below 250 nm ($40\,000\text{ cm}^{-1}$). The OAc $\pi \rightarrow \pi^*$ should similarly appear in this region but are masked by the much more intense DTolF transitions.

The metal to ligand charge transfer (MLCT) are of greater interest as they are more distinct between the complexes. These result from the $\delta^* \rightarrow \pi^*$ transitions and are also symmetry allowed. They are observed for both the DTolF and OAc ligands where applicable. The DTolF MLCTs appear in UV-Vis region shown in Figure 2.9. the intensity of the transition is proportional to the number of ligands in the complex. Complex **2** having four DTolF ligands has the largest extinction coefficient. As DTolF ligands are substituted for OAc the intensity decreases, but doesn't decrease in a linear fashion as complex **3** shows only a slightly more intense MLCT compared to complexes **4** and **5**. This can be rationalised in part by the appearance of a second distinct MLCT transitions in complex **3** where there are two DTolF environments, one trans to an OAc ligand (265 nm) and two cis (295 nm). The latter being similar in intensity compared to the single transition observed **3** (348 nm) and **4** (352 nm).

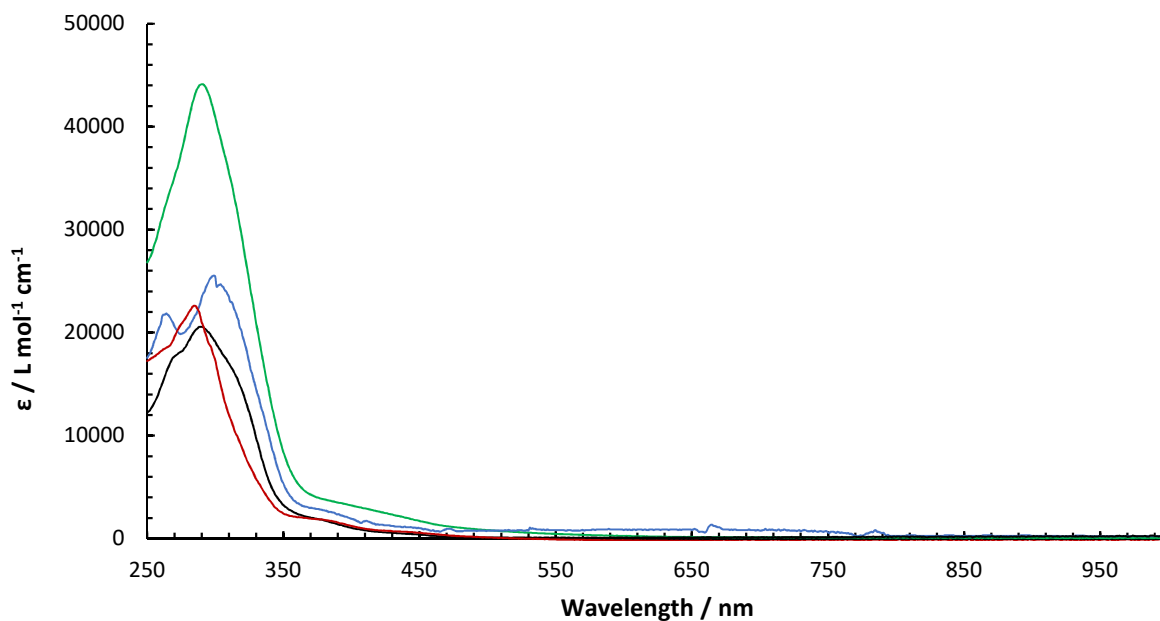


Figure 2.9. UV-Vis Absorption spectra of complexes **1** – **4** in DCM 1 cm pathlength analyte concentration 6 – 12 mM.

Table 2.2. Data taken from the UV-Vis spectra of complexes **1-4** for the $\text{Mo}_2(\delta) \rightarrow \text{DTolF } \pi^* \text{ MLCT}$ transition.

| | $\lambda_{\text{max}} / \text{nm}$ | $\epsilon / \text{L mol}^{-1} \text{cm}^{-1}$ |
|--|------------------------------------|---|
| $\text{Mo}_2(\text{DTolF})_4$ (2) | 345 | 44112 |
| $\text{Mo}_2(\text{DTolF})_3(\text{OAc})$ (3) | 333 | 29866 |
| <i>trans</i>- $\text{Mo}_2(\text{DTolF})_2(\text{OAc})_2$ (4) | 348 | 20706 |
| <i>cis</i>- $\text{Mo}_2(\text{DTolF})_2(\text{OAc})_2$ (5) | 352 | 22617 |

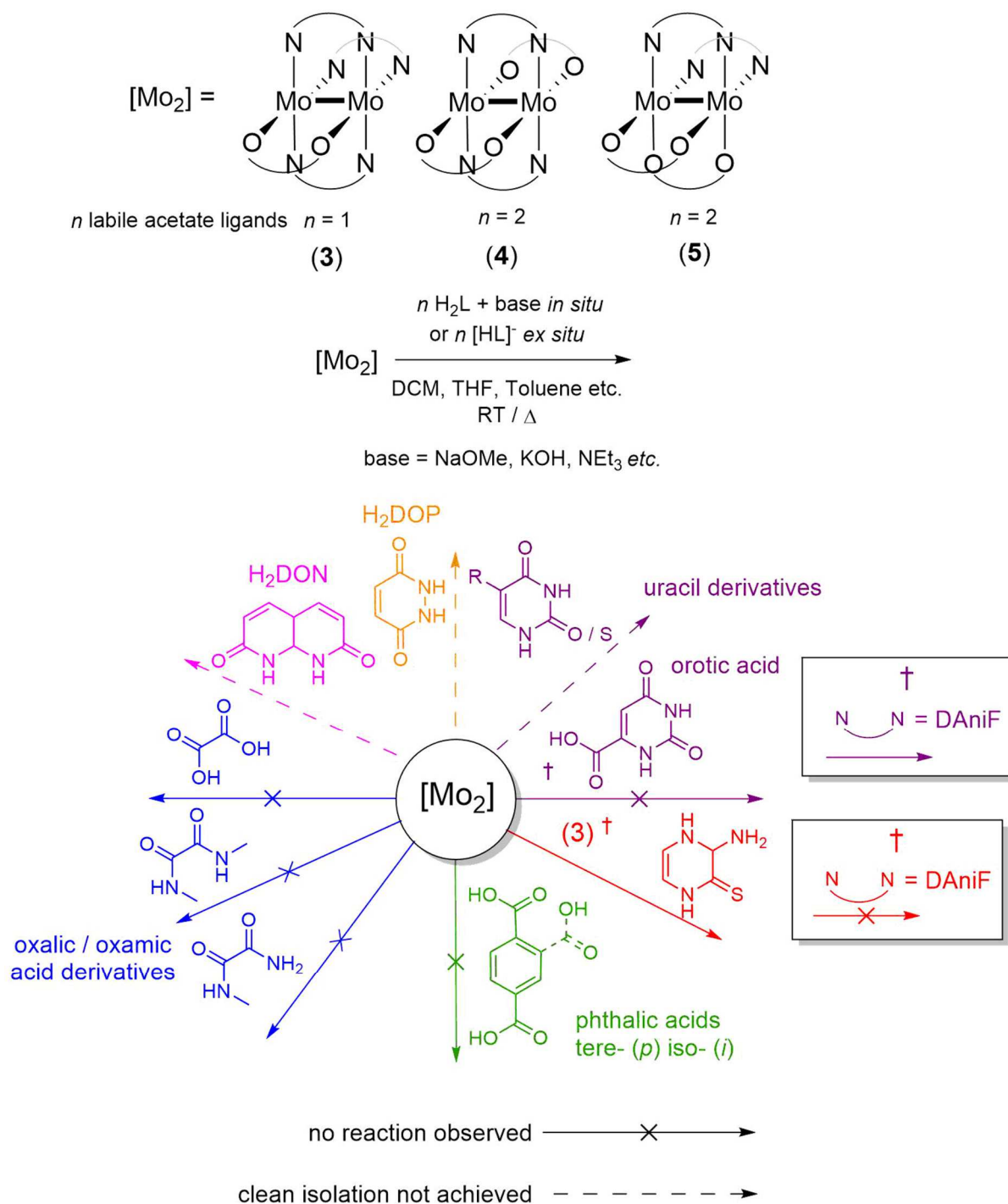
2.4.4 Substitution Chemistry

The substitution of the OAc ligands in these complexes has proven much less favourable than anticipated and little success was found despite much effort. Rationalising this has proven quite difficult but does explain the frequency of which the DAniF ligand is employed in the literature with little interest shown in alternatively substituted formamidinate ligands.

While both formamidinate ligands are substituted with electron donating groups, the *p*-OMe group does donate more strongly through resonance than the inductive effects of the methyl groups. The electrochemical data collected by cyclic voltammetry does reveal some difference in the redox chemistry of the two series, but only minor differences are observed. Solubility likely plays a bigger factor than electronics. Whereas the introduction of the methyl groups was expected to produce complexes that would be more soluble in DCM and thus favour formation of the hydrogen bonding assembly in many cases the result was only to produce complexes that are generally less soluble. Most being only sparingly soluble in DCM at best but often even poorly soluble in THF and DMSO. This is not only counterproductive to the formation of the dimer but extremely limiting in purification.

Scheme 2.5 demonstrates a not comprehensive range of ligands and conditions that were employed in attempted substitution of hydrogen bonded assemblies. Most effort was dedicated to the H₂DON and H₂DOP ligands, phthalic acids, oxalic / oxamic acids and uracil derivatives. The conditions explored including choice of solvent, choice of base with deprotonation of the H₂L both *in-situ* or *ex-situ*, temperature and reaction time. In most cases a total lack of reactivity of was observed. For instance, with oxalic acid, surprisingly when oxalic does react readily in a two to one stoichiometry with Mo₂(DAniF)₃(OAc) to produce a covalent dimer.¹⁰ In other cases, it was clean isolation which proved problematic, usually attributed to a general lack of solubility as discussed above. One of the rare successes was the reaction of 3-amino-3,4-dihydropyrazine-2-thione (red, Scheme 2.5) which reacted readily and could be purified by silica column-chromatography but unfortunately no stabilisation of the MV state was observed in the CV.

A few general observations were taken this work that would inform the synthesis discussed in latter chapters. Firstly, colour change indicative of successful reactions were more frequently observed in coordinating THF solvent. Secondly, the use of NEt₃ base as an alternative based to NaOMe prominent in the literature was both effective and more practical. Finally, the stability of the materials allowed purification via silica column chromatography under inert conditions.



Scheme 2.6. Attempted reactions of Mo₂(DTolF)_{4-n}(OAc)_n $n = 1, 2$ (*cis*-) or 2 (*trans*-) with various ligands capable of forming self-complementary hydrogen bonds. The reactions of the DAniF analogue derivative is noted when it differs.

2.5 Conclusions

A series of di-molybdenum paddlewheel complexes of the form $\text{Mo}_2(\text{DTolF})_{4-n}(\text{OAc})_n$ where DTolF = *N,N'*-bis(4-methylphenyl)formimidanate and OAc = acetate ($n = 0, 1, 2$ *cis*- or *trans*-) complexes **2** – **5** respectively, have been synthesized. The complexes were characterised by ^1H NMR, IR spectroscopy, single-crystal X-ray diffraction, mass spectrometry and cyclic voltammetry.

The electrochemical measurements revealed that the substitution of DTolF ligands for OAc ligands produces a cathodic shift from -0.238 V (**2** and **3**) to -0.375 V (**5**). Data was also collected for the analogous $\text{Mo}_2(\text{DAniF})_{4-n}(\text{OAc})_n$ series ($n = 0, 1, 2$ *cis*- or *trans*-), where DAniF = *N,N'*-bis(4-methoxyphenyl)formimidanate. The oxidation potentials did not observe the same pattern and the differences observed were much smaller ranging between just -0.220 V in *trans*- $\text{Mo}_2\text{DAniF}_3(\text{OAc})$ and -0.272 V in *cis*- $\text{Mo}_2\text{DAniF}_3(\text{OAc})$.

The attempted substitution of the acetate ligands for ligands capable of self-complimentary hydrogen bonds was explored in a range of conditions including; stoichiometry, temperature, choice of base *etc.* but generally found to be unsuccessful. This was largely accounted to solubility as the while the DTolF ligands we anticipated to produce increased solubility in non-coordinating solvents such as DCM that are required to stabilise the formation of a hydrogen bond, the resultant materials were largely insoluble in all common solvents. This observation supports the common use of the DAniF analogues in the literature where other derivatives are very rare and the successful reaction of $\text{Mo}_2(\text{DAniF})_3(\text{OAc})$ with the thio-lactam ligands reported in Chapter 4.

2.6 Experimental

2.6.1 *Materials and Physical Methods*

All manipulations of air sensitive materials were carried out under inert conditions using standard Schlenk-line and Glovebox techniques using argon gas. Chemicals were used as supplied unless specified. Reaction solvents were dried over CaH_2 for several hours and distilled under argon using a vertical still head apparatus. Deuterated solvents for NMR spectroscopy were dried over a potassium mirror and distilled under reduced pressure using short path distillation apparatus.

Single crystal x-ray diffraction data was collected at 150(2) K on a Bruker Apex Duo diffractometer using a graphite monochromated Cu (K_{α}) radiation source and cold stream of N_2 gas. Crystals were mounted onto a $X \mu\text{m}$ MiTeGen nylon loop using degassed Fomblin Y oil dried over Na metal. IR spectra were obtained on a JASCO 4100 FT-IR using a solution state cell 0.5 mm path length using sample concentrations of 20 mM at room temperature. ^1H NMR spectra were obtained on a Brucker Avance 400 MHz at room temperature and referenced versus the residual solvent peaks of the solvent. UV-Vis spectra were obtained on a Cary 60 UV-Vis spectrometer with a 0.05 cm path length. Matrix assisted laser desorption ionisation- time of flight (MALDI-TOF) mass spectrometry was collected on a Bruker Reflex III mass spectrometer using a dithranol matrix.

2.6.2 Synthesis of *N,N'*-di-*p*-tolylformamidinate (HDTolF)

Modified from literature procedure.¹¹ *p*-Toluidine (4.38 g, 35 mmol) and triethyl orthoformate (3.5 mL, 27 mmol) were added to a round bottom flask and refluxed for 2 hours (170 °C). The ethanol formed was then removed by distillation. A grey solid was obtained on cooling and recrystallized from warm toluene and washed with hexane (3 x 10 mL) to obtain off-white, needle-like crystals (3.67 g, 97 %). ^1H NMR (400 MHz) CDCl_3 : δ_{H} 9.95 (s, 1H, NH) 8.07 (s, 1H, N=CH-N) 6.98 (d, 4H, J_{H} , 8.5Hz, *o* Ar-H) 6.81 (d, 4H *m* Ar-H) 2.21 (s, 6H, Ar- CH_3). FTIR diamond tip: $\bar{\nu}$ (cm^{-1}) 2917 (med, broad) 1663 (strong) 1606 (med) 1586 (med, shoulder) 1520 (med, shoulder) 1504 (str, Ar C=C) 1407 (weak, shoulder) 1310, 1300 (strong, split) 1216 (med, shoulder) 1201 (str) 1110 (weak).

2.6.3 Synthesis of $\text{Mo}_2(\text{OAc})_4$ (**1**)

A round bottom flask of acetic anhydride in glacial acetic acid (100 mL, 40 % v/v) and 5 mL hexanes was degassed by sparging with Argon for approximately 15 minutes. $\text{Mo}(\text{CO})_6$ (1.563 g, 5.54 mmol) was then added and the reaction brought to reflux for 48 hours. On cooling the micro-crystalline yellow solid (**1**) is isolated (1.623 g, 51 %) by filtration and washed with several portions of hexanes, and ice cold Et_2O .

2.6.4 Synthesis of $\text{Mo}_2(\text{DTolF})_4$ (**2**)

$\text{Mo}(\text{CO})_6$ (1.563 g, 5.54 mmol) and HDAniF (2.4836 g, 11.1 mmol) was added to a Schlenk and suspended in 1,2-dichlorobenzene (25 mL) and THF (4 mL). The reaction was refluxed for 24 hours before being reduced to dryness *in vacuo* and addition of hexane (30 mL). The resultant yellow solid was suspended in hexane (40 mL) and isolated by filtration (2.02 g, 67 %) and washed with EtOH (10 mL) and Et₂O (10 mL). ¹H NMR (400 MHz) CDCl₃: 8.42 (s, 4H, N-CH-N) 6.69 (d, *J* = 8.5 Hz, 4H, *o* Ar-H) 6.09 (d, 4H, *m* Ar-H) 2.18 (s, 6H, Ar-CH₃). IR FTR diamond tip: $\bar{\nu}$ (cm⁻¹) 2008 (med) 1890 (med, shoulder) 1859 (strong, shoulder) 1824 (strong, split) 1638 (med) 1603 (weak, shoulder) 1588 (weak, shoulder) 1519 (weak, shoulder) 1504 (med) 1361 (weak) 1318 (med, broad) 1212, 1201 (weak, split). MALDI-TOF calculated FW 1088.3 g mol⁻¹ found *m/z*: 1085.5. g mol⁻¹.

2.6.5 Synthesis of $\text{Mo}_2(\text{DTolF})_3(\text{OAc})$ (**3**)

A Schlenk flask was charged with with $\text{Mo}_2(\text{OAc})_4$ (1.50 g, 3.51 mmol) and HDAniF (2.36 g, 10.54 mmol) and suspended in DCM (40 mL). Addition of sodium tertbutoxide (1.013 g, 10.60 mmol) resulted immediate colour change to brown. The reaction was fitted with a reflux condenser and refluxed for 12 hours causing the reaction solution to darken significantly giving a very dark yellow solution that was filtered over celite to remove and sodium acetate and excess sodium tertbutoxide. The filtrate solvent was reduced to 10 % volume *in vacuo* and addition of EtOH gave precipitation of a yellow solid (0.708 g, 89 %) that was isolated by filtration and washed with hexane (2 x 10 mL). ¹H NMR (400 MHz) CDCl₃: δ_{H} 8.49 (s, 2H, -NCH-N), 8.39 (s, H, -NCH-N), 6.81 (d, *J* = 8.1 Hz, 8H, Ar-H) 6.60 (d, *J* = 8.4 Hz, 4H, Ar-H), 6.37, (d, *J* = 8.1 Hz, 8H, Ar-H), 6.11 (d, *J* = 8.8 Hz, 4H, Ar-H), 2.51 (s, 3H, O₂CCH₃), 2.16 (s, 12H, Ar-CH₃), 2.09 (s, 6H, Ar-CH₃). FTIR diamond tip: $\bar{\nu}$ (cm⁻¹) 1568 (str) 1538 (strong, shoulder) 1504 (strong) 1427 (strong, broad) 1307 (med) 1218 (weak, split) 1043 (weak, broad split) 923 (weak) 815 (med). calculated FW 924.2 g mol⁻¹ found *m/z*: 921.3 g mol⁻¹.

2.6.6 Synthesis of *trans*- $\text{Mo}_2(\text{DTolF})_2(\text{OAc})_2$ (**4**)

A Schlenk flask was charged with with $\text{Mo}_2(\text{OAc})_4$ (1.027 g, 2.40 mmol) and HDTolF (1.075 g, 4.80 mmol) suspended in DCM (40 mL). Addition of sodium tertbutoxide (0.488 g, 4.80 mL, mmol) the yellow

slurry changed first to red then finally to a dark brown within 10 minutes at which point a colourless precipitate of NaOAc was also observed. The reaction was then refluxed for 12 hours and a yellow precipitate formed which was isolated by filtration (1.78 g, 75 %) and washed with MeOH (2 x 10 mL). ^1H NMR (400 MHz) CDCl_3 : δ_{H} 8.52 (s, 2H, -NCHN-), 6.93 (d, $J = 8.1$ Hz, 8H, Ar-H), 6.57 (d, $J = 8.1$ Hz, 8H, Ar-H), 2.53 (s, 6H, O_2CCH_3), 2.18 (s, 12H, Ar- CH_3). IR FTR diamond tip: $\bar{\nu}$ (cm^{-1}) 1522 (strong, shoulder) 1505 (strong) 1429 (strong) 1302 (strong) 1205 (med, split) 817 (strong). MALDI-TOF calculated FW 760.1 g mol^{-1} found: 761.3 g mol^{-1} .

2.6.7 Synthesis of *cis*- $\text{Mo}_2(\text{ToIF})_2(\text{OAc})_2$ (**5**)

A Schlenk flask was charged with *cis*- $\text{Mo}_2(\text{DAniF})_2(\text{NCMe})_4 \cdot 2\text{BF}_4$ (0.800 g, 0.77 mmol) and NaOAc (0.200 g, 2.4 mmol). On addition of acetonitrile (20 mL) immediate precipitation of a yellow solid is observed. After 2 hours the reaction mixture was filtered and the yellow solid was extracted with DCM (20 mL), reduced to 10 % volume in vacuo and precipitated out with the addition of EtOH (20 mL). The resultant solid was isolated by filtration (0.263 g, 41 %) and washed with hexane (2 x 5 mL). ^1H NMR (400 MHz) CDCl_3 : δ_{H} 8.39 (s, 2H, -NCH-N), 6.54 (d, $J = 8.8$ Hz, 4H, Ar-H), 6.48 (d, $J = 8.8$ Hz, 4H, Ar-H), 3.65 (s, 12H, Ar- OCH_3), 2.58 (s, 6H, O_2CCH_3). IR FTR diamond tip: $\bar{\nu}$ (cm^{-1}) 2365, 2357 (strong, split) 2340 (med, split shoulder) 1575 (weak) 1533 (weak) 1505 (med) 1431 (weak, broad) 1307 (weak, broad) 1066, 1031 (strong, broad split). MALDI-TOF calculated FW 760.1 g mol^{-1} found m/z : 763.8

2.6.8 Synthesis of *cis*-($\text{Mo}_2(\text{DTolF})_2(\text{NCMe})_4 \cdot (\text{BF}_4)_2 \cdot 2\text{NCMe}$) (**6**)

A Schlenk flask was charged with $\text{Mo}_2(\text{DTolF})_4$ (1.409 g, 1.30 mmol) and suspended in acetonitrile (60 mL). Addition of excess triethyloxonium tetrafluoroborate (1.0 M, 7.8 mL, 7.8 mmol) and degassed H_2O (ca. 0.4 mL) over three hours generated a dark purple solution. The solvent was reduced to minimum *in vacuo* and addition of Et_2O caused a purple precipitate to form. The precipitate was washed with stirring by several portions of Et_2O (4 x 10 mL) to remove any unreacted triethyloxonium tetrafluoroborate yielding a burgundy solid in yields > 95 %. Dark red block-like crystals suitable for single crystal x-ray diffraction were obtained by slow diffusion of an acetonitrile solution into Et_2O . ^1H NMR (400 MHz) CDCl_3 : δ_{H} 8.40 (s, 2H, -NCHN-) 6.92 (d, 8H, *o* Ar-H) 6.44 (d, 8H Ar-H) 2.34 (s, 12H, *p* Ar-

CH_3). FTIR diamond tip: $\bar{\nu}$ (cm^{-1}) 1693 (broad) 1525 (med, shoulder) 1344 (med, broad) 1306 (med, broad) 1216 (med) 1056, 1017 (str, broad split) 815 (str).

2.7 References

- (1) Cotton, F. A.; Murillo, C. A.; Yu, R. *Dalton. Trans.* **2006**, 3900.
- (2) Cotton, F. A.; Liu, C. Y.; Murillo, C. A.; Wang, X. *Inorg. Chem.* **2006** .
- (3) Cotton, F. A.; Lin, C.; Murillo, C. A. *Inorg. Chem.* **2001**, *40*, 575
- (4) Chisholm, M. H.; Patmore, N. J.; Reed, C. R.; Singh, N. *Inorg. Chem.* **2010**, *49*, 7116.
- (5) Wang, L.; Gong, Z.-L.; hu-Ying Li, S.; Hong, W.; Wang, D.; Wan, L.-J. *Angew.Chem. Int.Ed.* **2016**, *55*, 12393.
- (6) Xu, B.; Tao, N. J. *Science.* **2003**, *301*, 1221.
- (7) Chisholm, M. H.; Macintosh, A. M. *Chem. Rev.* **2005**, *105*, 2949.
- (8) Miyasaka, H.; Clérac, R.; Campos-Fernández, C. S.; Dunbar, K. R. *J. Chem. Soc. Dalt. Trans.* **2001**, *2*, 858.
- (9) Vela, S.; Bauroth, S.; Atienza, C.; Molina-Ontoria, A.; Guldi, D. M.; Martín, N. *Angew. Chem. Int. Ed.* **2016**, *55*, 15076.
- (10) Cotton, F. A.; Donahue, J. P.; Lin, C.; Murillo, C. A. *Inorg. Chem.* **2001**, *40*, 1234.
- (11) Mohamed, A. A.; Abdou, H. E.; Irwin, M. D.; López-de-luzuriaga, J. M.; Fackler, J. P. *J. Clust. Sci* **2003**, *14*, 253.

Chapter 3. “Dimers of Dimers” Bridged by the 3,6-Dihydroxypyridazine Ion. How do Electronic Changes in the Bridge Affect Stabilization of the Mixed Valence State?

3.1 Abstract

The Patmore group has previously reported the “dimer of dimers” complex $[\text{Mo}_2(\text{TiPB})_3(\text{HDOP})]_2$ [**9**]₂ where dimerization occurs through a self-complimentary hydrogen bond between the pendant lactam functionalities.¹⁻³ The mixed valence state generated upon single electron oxidation is stabilised through the PCMV mechanism where ET is dependent on the proton coordinate. A series of complexes where the HDOP ligand is now substituted with a range of electron withdrawing and electron withdrawing functionalities have been synthesized giving the series; $\text{Mo}_2(\text{TiPB})_3(3\text{-R}',4\text{-R}'\text{'-HDOP})$ where $\text{R}', \text{R}'' = \text{Cl}, \text{H}$ (**7**), Br, H (**8**), H, H (**9**) Me, H (**10**) and Me, Me (**11**) and also the fused ring system $\text{Mo}_2(\text{TiPB})_3(\text{HPhth})$ (**12**), where HPhth = phthalhydrazide. The stability of the MV state generated upon has been probed by cyclic voltammetry where $\Delta E_{1/2}$ values range from 118 mV in [**7**]₂ to 260 mV in [**11**]₂ indicating the substituent effect of the bridging ligand has a significant effect on the thermodynamic stability of the mixed valence state. The use of UV-Vis NIR spectroscopy confirms the PCMV mechanism is in operation in all cases as no electronic coupling exists between the redox centres evident in a lack of an IVCT in the NIR for the MV state.

3.2 Proton Coupled Mixed Valency

There are three mechanisms that can account for stabilisation of the mixed valence state over a hydrogen bond; simple ET⁴⁻⁶ or PT⁷ or a mechanism in which the ET transfer is somehow related to the proton coordinate in the hydrogen bond, this is dubbed proton coupled mixed valency (PCMV).¹⁻

³ These mechanisms can be distinguished by their electrochemical and spectroscopic behaviour. as discussed in greater detail in sections 1.10 and 1.11.

In all cases a stabilisation of the MV state is observed in the CV, typically as two one electron oxidations or reductions where the separation of these redox processes, $\Delta E_{1/2}$ can be used to determine the comproportionation constant, K_c a thermodynamic measurement of the stability of the MV state.⁸

In a mixed valence state stabilised by ET there must be direct orbital overlap between the donor-bridge-acceptor orbitals. An IVCT is observed in the NIR of the MV state and the electronic coupling parameter, H_{ab} can determined by Hush analysis.⁹ Electron self-exchange rates in MV complexes faster than 10^{-10} s can be determined by IR spectral coalescence.¹⁰⁻¹⁴ Proton transfer by contrast is a much slower process that occurs on the NMR timescale (10^{-5} s) so can be monitored by NMR line broadening techniques.^{15,16}

The existing complexes reported by our group that are believed to be stabilised by the PCMV mechanism are the dimers $[\text{Mo}_2(\text{TiPB})_3(\text{HDON})]_2$ and $[\text{Mo}_2(\text{TiPB})_3(\text{HDOP})]_2$ (Figure 3.1).¹⁻³ In the PCMV mechanism there is no electronic communication so no IVCT band is observed in the NIR nor is there is a proton hole to allow PT. The precise ET rates in these systems is currently not know but it is faster than the NMR (10^{-5} s) and slower than the EPR (10^{-9} s) timescale.

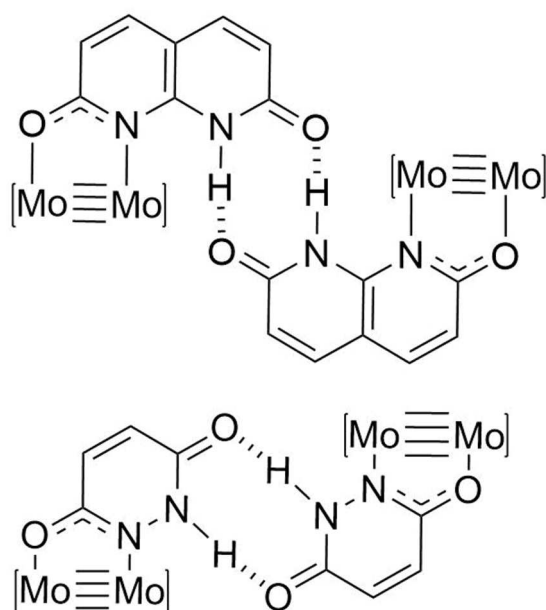


Figure 3.1. Self-complementary hydrogen-bonding motifs in $[\text{Mo}_2(\text{TiPB}_3)(\text{DOP})]_2$ and $[\text{Mo}_2(\text{TiPB}_3)(\text{DOP})]_2$ [9]₂. The TiPB ligands are omitted for clarity.

Based on DFT modelling the current description of PCMV is a “dipole induced electron self-exchange mechanism.” Partial proton transfer from the neutral side of the dimer towards the oxidised half generates a large dipole across the molecule which induces spontaneous ET (Figure 3.2).¹

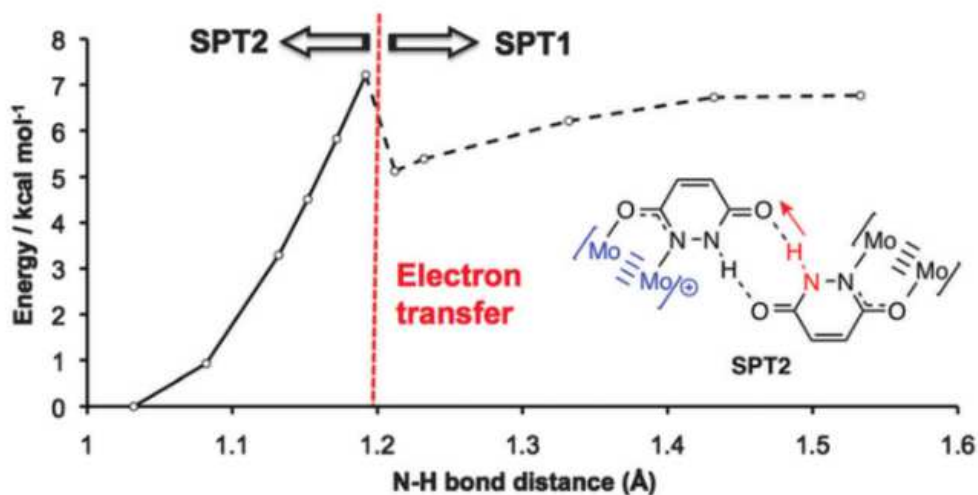


Figure 3.2. DFT model of proton transfer from the unoxidized half of the dimer towards the oxidised side. A large dipole is generated that induces electron transfer.

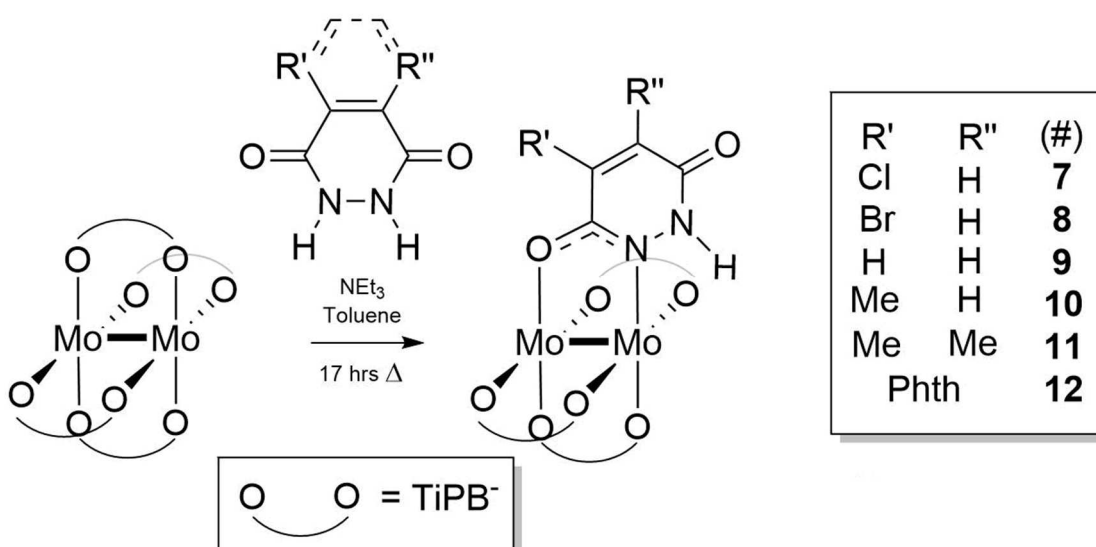
3.3 Aims

It is commonly observed in covalently bridged mixed valence systems that electronic modification of the bridging ligand π -system can have a large impact on the extent of electronic communication between redox centres.^{17,18} Our current mechanistic understanding of PCMV precludes electronic coupling between the donor-bridge-acceptor which is evident from the lack of an IVCT transition in the NIR region upon generation of the MV state. It is not clear how such modifications to the bridge would affect stabilisation of the mixed valence state in hydrogen bonded MV dimers. To this effect a series of complexes based on the previously reported $[\text{Mo}_2(\text{TiPB})_3(\text{HDOP})]_2$ system were targeted where the HDOP ligand is substituted with electron-donating or withdrawing groups.

This is the first systematic study of bridging ligand effects on stabilisation of the MV state in hydrogen bonded dimers. The aim is to determine whether the extent of stabilisation can be tuned by substitution of electron-donating or –withdrawing groups into the bridge as is possible in covalent systems. This will improve the potential for incorporation of such complexes into materials with interesting charge-transfer properties.

3.4 Discussion

3.4.1 Synthesis & Structural Characterisation



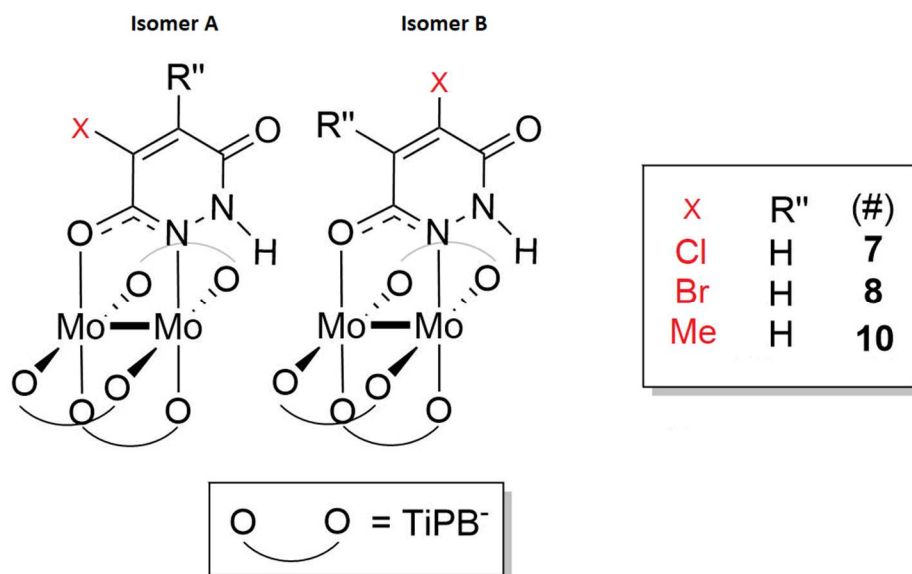
Scheme 3.1. Synthesis of $\text{Mo}_2(\text{TiPB})_3(3\text{-R}',4\text{-R}''\text{-HDOP})$ where $\text{R}', \text{R}'' = \text{Cl}, \text{H}$ (**7**), Br, H (**8**), H, H (**9**), Me, H (**10**) and Me, Me (**11**) and $\text{Mo}_2(\text{TiPB})_3(\text{Phth})$ (**12**).

The synthesis of $\text{Mo}_2(\text{TiPB})_3(\text{HDOP})$ (**9**) has been previously reported by our group, by simple 1:1 reaction of $\text{Mo}_2(\text{TiPB})_4$ and H_2DOP in toluene.² In initial studies, former group member Dr Luke Wilkinson demonstrated that $\text{Mo}_2(\text{TiPB})_4$ could similarly be reacted with commercially available DOP analogues bearing electron withdrawing and donating groups to generate the following series of complexes; $\text{Mo}_2(\text{TiPB})_3(\text{R}',\text{R}''\text{-HDOP})$ where $\text{R}', \text{R}'' = \text{Cl}, \text{H}$ (**7**), Br, H (**8**), Me, H (**10**) and Me, Me (**11**) and the fused ring system $\text{Mo}_2(\text{TiPB})_3(\text{Phth})$ (**12**) where $\text{HPhth} = \text{phthalhydrazide}$.

Unfortunately, these complexes couldn't be isolated cleanly via this method. The typical impurities were *trans*- $\text{Mo}_2(\text{TiPB})_2(\text{R}',\text{R}''\text{DOP})_2$, unreacted $\text{Mo}_2(\text{TiPB})_4$ starting material or coordination isomers when the asymmetric ligands $\text{R}',\text{R}'' = \text{Cl}, \text{H}$ (**7**), Br, H (**8**), Me, H (**10**) are employed. To this effect, postdoctoral research fellow Dr Kevin Vincent proposed the use of column silica chromatography as a means of purification. This allowed the clean isolation of the desired complexes and allowed collection of spectroscopic and electrochemical data on analytically pure compounds. Given the air sensitive nature of the product complexes purification was practically challenging but their stability on silica was quite surprising. Basic alumina by contrast was found to be unsuitable leading to rapid decomposition.

The use of NEt_3 as a base was also found to improve yields (Scheme 3.1) but because the TiPB ligands are labile it was necessary to keep the Mo_2 starting material in a slight excess (5 %) to minimise over-substitution.

In complexes **7** ($\text{R}', \text{R}'' = \text{Cl}, \text{H}$), **8** ($\text{R}', \text{R}'' = \text{Br}, \text{H}$) and **10** ($\text{R}', \text{R}'' = \text{Me}, \text{H}$) the ^1H NMR spectra of the crude reaction mixtures showed two coordination isomers but following column chromatography only one isomer was isolated. This was confirmed as isomer A (Scheme 3.2) by 2D NMR spectroscopy; COSY, DOSY, HSQC and HMBC.



Scheme 3.2. Two coordination isomers possible in the mono-substituted $\text{Mo}_2(\text{R}', \text{R}''\text{DOP})$ complexes **7**, **8** and **10**.

The product bands are eluted using varying ratios of DCM : THF and the resultant complexes of the products ranges from purple in **7** – **9**, red in **10** and **11** to orange in **12**. The complexes are extremely soluble in all common organic solvents such as THF, DCM and hexanes but insoluble in water. Numerous efforts have been made to crystallise the hydrogen bonded dimers but have been unsuccessful due to the high solubilities in solvents that would not disrupt the formation of the hydrogen bond such as hexanes and DCM.

Evidence for the formation of a dimer in the solution state instead comes from DOSY NMR where the calculated hydrodynamic volumes range from 2986 (**12**) \AA^3 to 3574(**7**) \AA^3 but approximately half on addition of DMSO, consistent with a splitting apart of the dimer to form two monomeric units.

3.4.1.1 ^1H NMR Spectroscopy

The ^1H NMR spectra of complexes **7** – **12** in CDCl_3 are shown in Figure 3.3. The previously reported spectra for complex **9** is included for comparison. The chemical shifts of the TiPB proton environments are consistent across the series so will not be discussed in detail. The TiPB Ar-CH(CH)₃ protons are observed as septets with a integration pattern of 4 : 3 : 2 : 1. The TiPB Ar-H signals have an integration

pattern of 4 : 2. For TiPB *i*-Pr signals there is significant overlap of peaks the splitting patterns thus varies from complex to complex.

The DOP proton signals are much more diagnostic. The DOP *NH* proton chemical shifts range from 11.57 ppm in **7** to 12.15 ppm in **12**. The signals are very broad in **11** and **12**. The down-field shift is proportional to increasing electron donating nature of the substituent. This is contradictory if compared to a substituent effect alone but can be rationalised by considering the extent of ligand π -donation to the Mo₂ core. When the substituent(s) on the DOP ligand are electron donating there is increased electron density donated to the Mo₂ core, less localised on the ligand and thus imparting a de-shielding effect. Conversely, when substituent(s) are electron donating there is reduced π -donation to the Mo₂ core, increased electron density located on the DOP ligand and thus a shielding effect. The DOP *NH* environments in complexes **7** – **10** appears as a doublets due to long range coupling to the R'' = H proton environment of the DOP ligand.

The DOP R'' = H proton environments in complexes **7** – **10** themselves range from 6.45 ppm in **10** to 6.92 ppm in **8**. There is no apparent correlation to overall electron donating nature of the ligand likely or the R' substituent. In **7**, **8** and **10** R'' is a substituent to which no coupling is observed so the DOP R'' = H signal appears as doublet in all cases due to coupling to the DOP *NH*. In **9**, both R' and R'' = H so the R'' = H signal is instead a doublet of doublets with J = 3 Hz and J = 10 Hz.

The additional CH₃ environment(s) in complexes **10** and **11** occur as singlets at 2.25 ppm and 2.22 and 2.45 ppm respectively. The four proton environments of the phthalhydrazide aromatic backbone occur as three broad multiplets (integration 2 : 1 : 1) between 7.64 and 8.84 ppm.

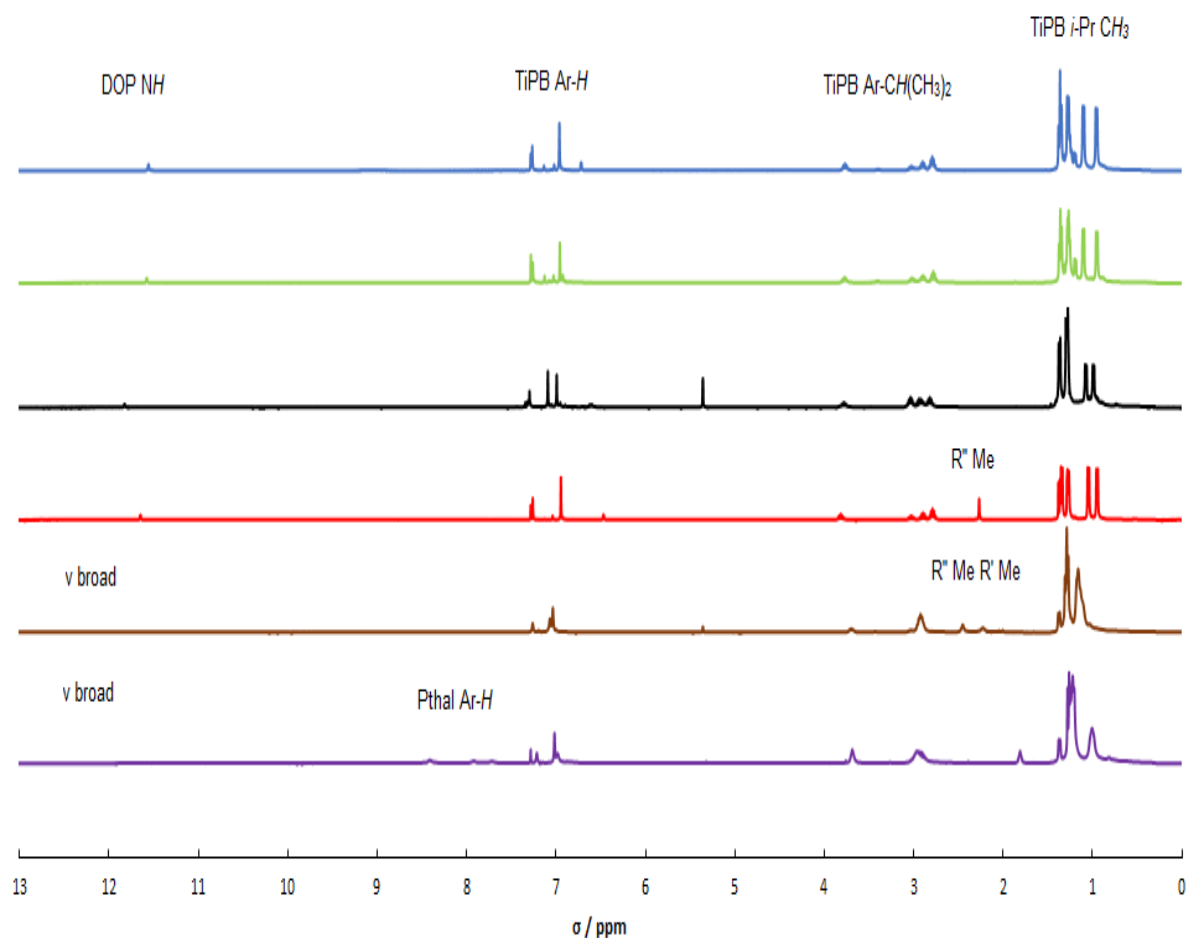


Figure 3.3. ^1H NMR spectra of complexes **7** – **12** (top to bottom) in CDCl_3 .

3.4.1.2 IR Spectroscopy

The IR spectra of complexes **7** – **12** is shown in Figure 3.4. The expected $\text{C}=\text{O}$ lactam stretches are observed in the range of 1635 (**7**) – 1646 (**10**) cm^{-1} with no apparent correlation to the R'' substituent effect. It is also evident in **11** and **12** that lactam : lactim equilibrium lies more in favour of the lactim tautomer evident in the presence of intense NH stretches at $\text{ca.} 1740 \text{ cm}^{-1}$ and a broad OH stretch at $\text{ca.} 3475 \text{ cm}^{-1}$ (not depicted) in each case most intense in **12**. The affect that this could impact upon the observed stabilisation of the MV state is currently being modelled through additional DFT calculations.

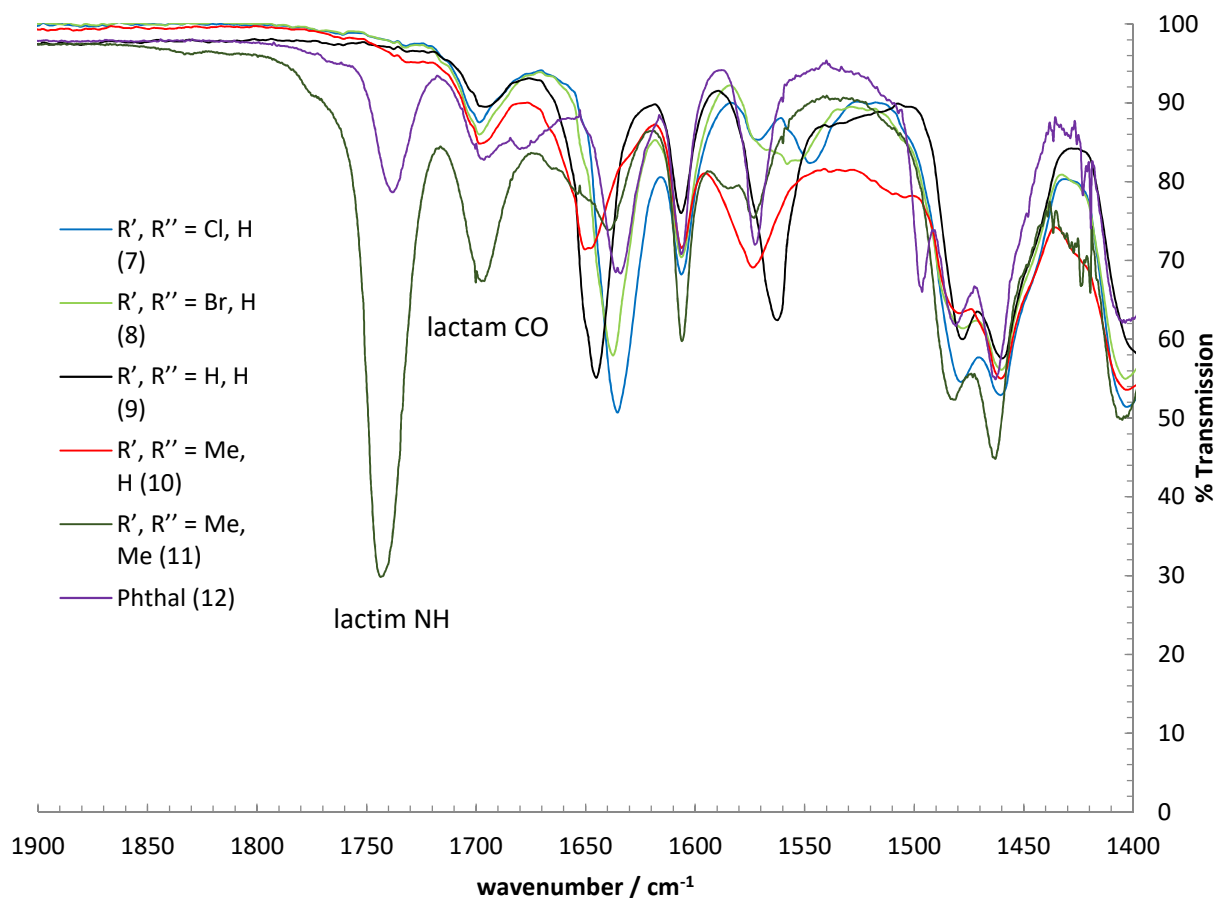


Figure 3.4. A portion of the IR spectra of complexes **7** (blue), **8** (green), **9** (black), **10** (red), **11** (brown) and **12** (purple).

3.4.2 Cyclic Voltammetry

Electrochemical data for complexes **7** – **12** is shown in Figure 3.5. Cyclic voltammograms were obtained in DCM and THF. Differential pulse voltammetry (DPV) was also used to help resolve poorly separated redox processes in DCM. Two reversible oxidations are observed for the unsubstituted complex **9** ($R' = H, R'' = H$), $E_{1/2}(1) = 0.203$ V and $E_{1/2}(2) = 0.362$ V, $\Delta E_{1/2} = 0.159$ V accounting for a K_c of 487 calculated using equation 3.1. The use of this equation is further discussed in section 1.3.5. The initial oxidation in the electron withdrawing substituted complexes **8** ($R' = Cl, R'' = H$) and **9** and ($R' = Br, R'' = H$) are anodically shifted to 0.231 V and 0.329 V respectively, so are more difficult to oxidise. The former does not appear to produce a thermodynamically stable mixed valence state as only a single reversible oxidation is observed. The latter shows two reversible peaks indicating that a MV

state is generated with $\Delta E_{1/2} = 0.118$ V accounting for a K_c of 99. The MV state is therefore less stable than complex **9** with respect to disproportionation.

$$K_c = \exp\left(\frac{\Delta E_{1/2} n_1 n_2 F}{RT}\right) \quad \text{eqn. 3.1}$$

In the electron donating substituted complexes **10** ($R' = \text{Me}$, $R'' = \text{H}$), **11** ($R' = \text{Me}$, $R'' = \text{Me}$) and **12** (Phthal) the initial oxidations are all cathodically shifted from **9** so are more easily oxidised. For complex **10** $E_{1/2}(1) = 0.188$ V but in complexes **11** and **12** the oxidations are irreversible, so the cathodic peak centre is quoted instead, $E_{pc} = 0.147$ V (**11**) and 0.183 V (**12**). In complex **10** $\Delta E_{1/2} = 0.185$ accounting for a K_c of 1341 so is more thermodynamically stable than complex **9**. The second oxidations, $E_{pc}(2)$ in complexes **11** and **12** are also irreversible. The $\Delta E_{1/2}$'s calculated from $E_{pc}(2) - E_{pc}(1)$ are 0.260 V (**11**) and 0.173 V (**12**) respectively, so are larger than that of **9** but because they are irreversible they cannot be used to determine a K_c value. The increase $\Delta E_{1/2}$'s are still indicative of a further increase in thermodynamic stability of the mixed valence state.

$\Delta E_{1/2}$ and K_c are often related to the extent of electronic coupling in covalent mixed valence system. But there are many examples where this thermodynamic property under- or over-estimates the extent of electronic coupling.⁸ This is discussed in more detail in section 1.3.5 but typically, K_c values greater than 10^5 indicate strongly coupled behaviour for mono-metallic systems¹⁹. In covalent dimers of dimolybdenum modest K_c values of just 10^4 are indicative of strong electronic coupling. This is because the charge is more diffuse being delocalised over both Mo atoms in the Mo_2 δ -bond.^{20,21} The K_c value of 1341 for the MV state in $[\mathbf{10}]_2^+$ could thus be indicative of good charge transfer between the Mo_2 units.

The CV measurements in THF all indicate that the hydrogen bonded dimer is disrupted. In complex **7** this observed as a large reduction in the separation between the oxidation and reduction peak centres. What appeared to be a single redox event in DCM could in fact be two very poorly separated processes. In complexes **8** – **12** the effect is more obvious. Only a single oxidation of approximately

twice the current intensity is observed because the MV state cannot be generated. In all cases the potential for the single oxidation to the 1⁺ state is cathodically shifted by approximately 0.150 V. The CV data for all the complexes is collated in Table 3.1.

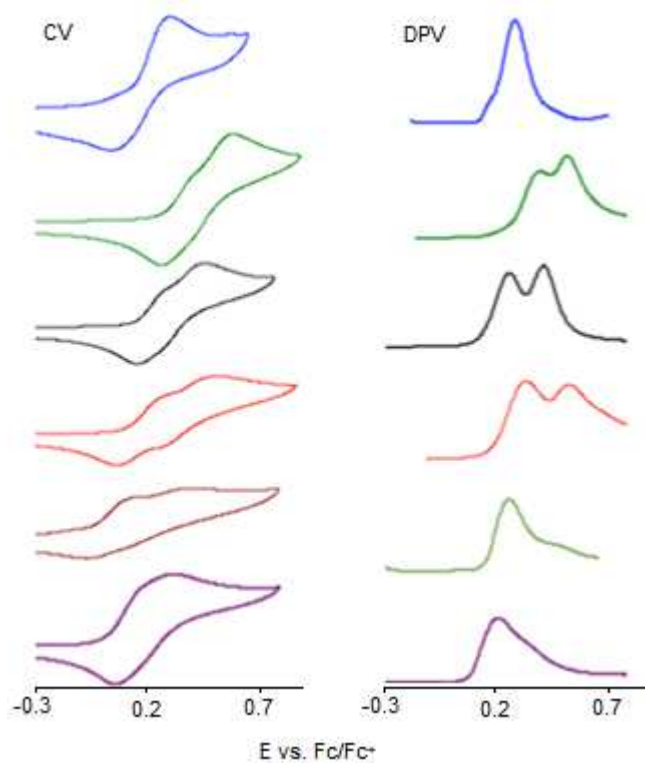


Figure 3.5. CV (left) and DPV (right) for complexes **7** – **12** (top to bottom) collected in 0.1 M TBAPF₆ at 100 mVs⁻¹ scan rate referenced vs Fc/Fc⁺.

Table 3.1. Cyclic voltammetry data for compounds **7** - **12** recorded in 0.1 M TBAPF₆ at 100 mVs⁻¹ scan rate. Analyte concentration of 5 mM in DCM and 2.5 mM in THF. Potentials referenced vs the Fc/Fc⁺ redox couple occurring at 0.00 V.

| Compound | Solvent | $E_{1/2}(1)$ (V) | $E_{1/2}(2)$ (V) | $\Delta E_{1/2}$ (V) | K_c |
|----------------------------|------------------|------------------|--------------------|----------------------|-------|
| [7] ₂ | DCM | 0.231 | - | - | - |
| 7 | THF | 0.068 | - | - | - |
| [8] ₂ | DCM | 0.329 | 0.447 | 0.118 | 99 |
| 8 | THF | 0.247 | - | - | - |
| [9] ₂ | DCM | 0.203 | 0.362 | 0.159 | 487 |
| 9 | THF | 0.085 | - | - | - |
| [10] ₂ | DCM | 0.188 | 0.373 | 0.185 | 1341 |
| 10 | THF | -0.007 | | | |
| [11] ₂ | DCM | 0.147 | 0.459 ^a | 0.260 ^b | - |
| 11 | THF | -0.030 | | | |
| [12] ₂ | DCM ₂ | 0.183 | 0.399 ^b | 0.173 ^b | - |
| 12 | THF | 0.060 | | | |

^a E_{pc} value reported due to irreversibility. ^b calculated from $\Delta E_{pc}(2) - \Delta E_{pc}(1)$.

3.4.3 UV-Vis NIR SEC

Even if ET is very fast it is likely to be slower than the femtosecond timescale for electronic absorption spectroscopy. The UV-Vis NIR SEC for complex **9** is reproduced in Figure 3.6. The absence of an IVCT band in the NIR for the MV state is commensurate with the proposal of the PCMV mechanism. If a standard ET stabilised MV mechanism was in effect the Mo₂ $\delta \rightarrow$ DOP π^* MLCT transitions for the MV state would be expected to be a superposition between that of the neutral and doubly oxidised species and so a single isosbestic point is observed for both the neutral $\rightarrow 1^+$ and $1^+ \rightarrow 2^+$ oxidation. Instead, two separate isosbestic points are observed for the neutral $\rightarrow 1^+$ and $1^+ \rightarrow 2^+$ oxidations. This is because

upon oxidation, the pK_a change on one half of the dimer results in a reduction of $\text{Mo}_2 \delta \rightarrow \text{DOP } \pi^*$ back bonding and thus affects the energy and appearance of the MLCT transition.

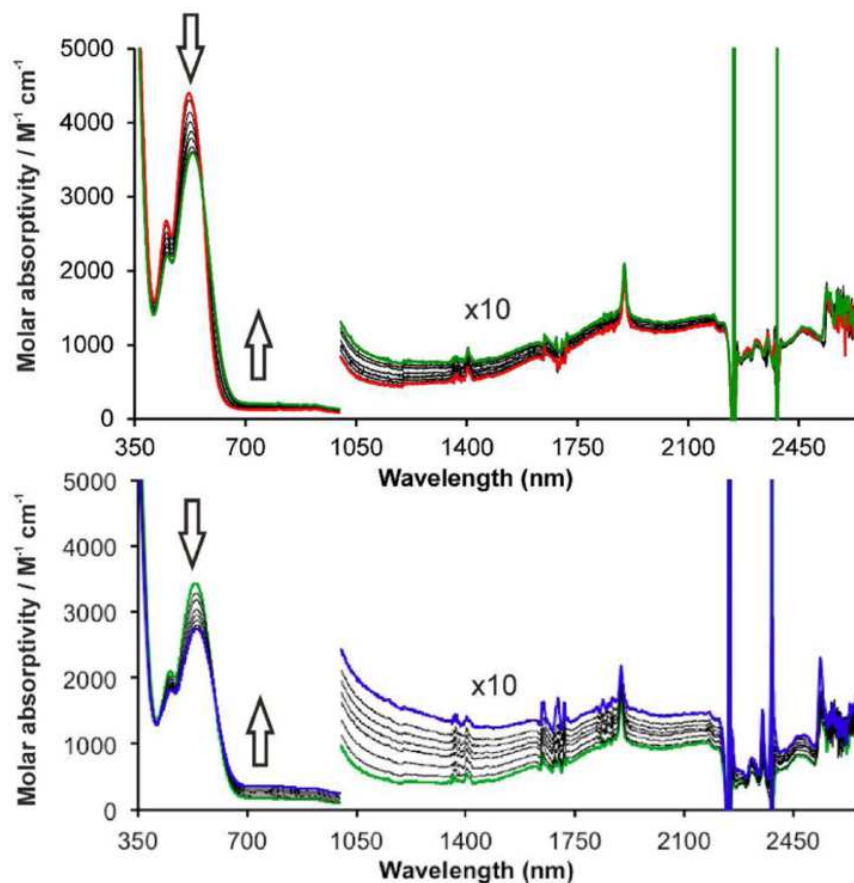


Figure 3.6. UV-Vis NIR SEC of complex **9** 0.1M TBAPF₆ electrolyte in DCM. At -20 °C. Transition from neutral [9]₂ (red) → [9]₂⁺ top and from [9]₂⁺ → [9]₂²⁺ (blue) bottom. Reproduced from reference with permission of the ACS.²

3.4.3.1 UV-Vis NIR SEC of $\text{Mo}_2(\text{TiPB})_3(4\text{-ClHDOP})$ (**7**)

The UV-Vis NIR SEC for complex **7** is shown in Figure 3.7. with the isosbestic points observed in the $\text{Mo}_2 \delta \rightarrow \text{DOP } \pi^*$ MLCT transition expanded in Figure 3.8. No NIR transitions are observed in the NIR spectra. As no stabilisation of the mixed valence state was observed in the CV an ICVT would not be expected regardless of the mechanism of ET.

The DOP MLCT upon oxidation from the neutral (black) to MV state (green), shows a slight decrease in intensity a slight red shifting of the peak maxima from *ca.* 18350 cm^{-1} (545 nm) to 18200 cm^{-1} (549 nm) and the peak is broadened in comparison to the neutral state. In the doubly oxidised state there

is both a more prominent red shift to *ca.* 17400 cm^{-1} (575 nm) and an increase in peak intensity identical with that of the neutral state. Thus, the broadened appearance of the MV state appears to be an approximate superposition of the peak centres of the neutral and doubly oxidised state and this is consistent with the formation of a MV state. Figure 3.8. shows an expansion of the spectra where the two isosbestic points for the neutral $\rightarrow 1^+$ oxidation and $1^+ \rightarrow 2^+$ oxidation occur at *ca.* 17100 cm^{-1} (585 nm) and 17860 cm^{-1} (560 nm). The appearance of two such isosbestic points is consistent with that previously reported for complex **9** and the generation of a MV state stabilised through the PCMV mechanism. This supports the assignment that there are in fact two very poorly separated redox processes in the CV measurement in DCM.

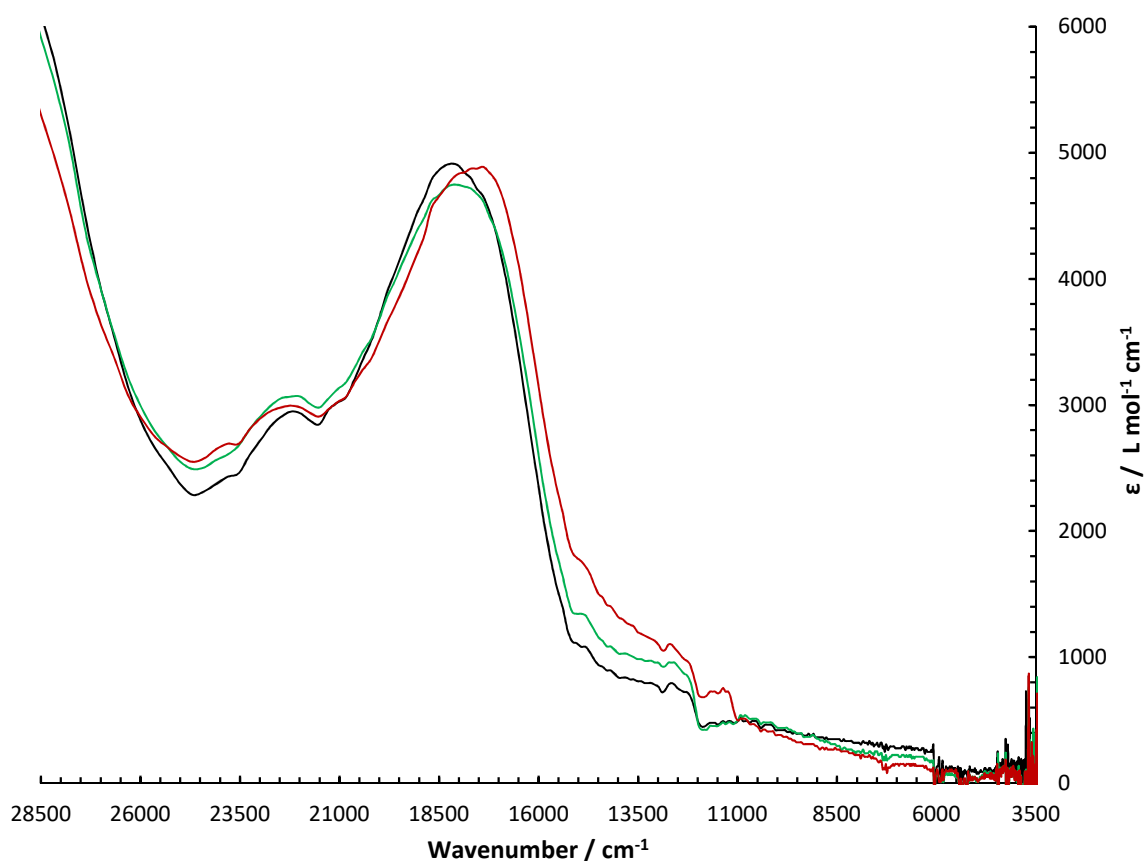


Figure 3.7. The UV-Vis NIR SEC on complex **7** in 0.1M TBAPF₆ electrolyte in DCM. Neutral (black), 1⁺ (green) and 2⁺ (red).

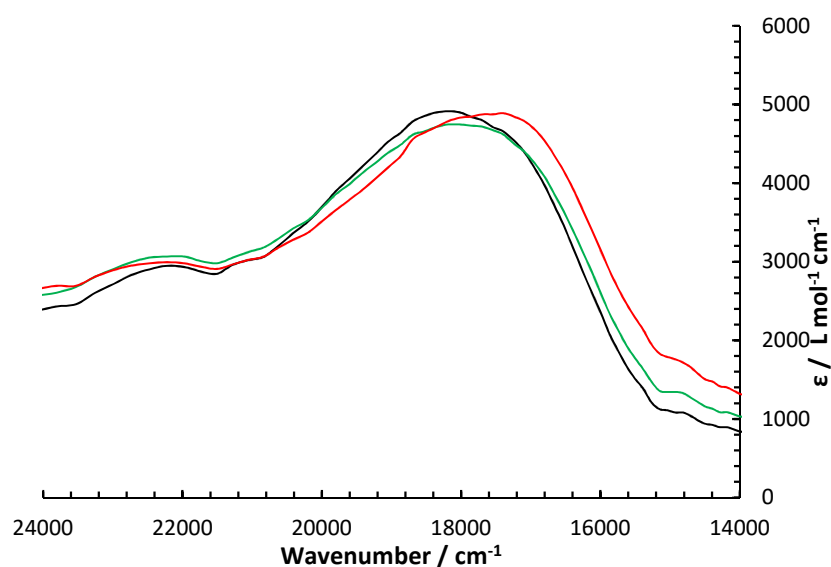


Figure 3.8. An expanded portion of the UV-Vis region highlighting the changes observed in the $\text{Mo}_2 \delta \rightarrow \text{DOP } \pi^*$ MLCT transition in the UV-Vis NIR SEC of complex **7**.

3.4.3.2 UV-Vis NIR SEC of $\text{Mo}_2(\text{TiPB})_3(4\text{-BrHDOP})$ (**8**)

The UV-Vis NIR SEC for complex **8** in DCM is shown in Figure 3.9. No NIR transition is observed in the MV state consistent with that criteria of the PCMV mechanism. Like complex **7**, oxidation from the neutral state (black) to the mixed valence state (green) produces a fall in intensity and a very slight broadening of the DOP MLCT but the peak centre remains fairly consistent. In contrast to complex **7** however, in the doubly oxidised state the MLCT rapidly diminishes in intensity. But a similar prominent red shift is observed from *ca.* 18350 cm^{-1} (545 nm) to 17400 cm^{-1} (575 nm). The two isosbestic points (shown in the expansion in Figure 3.10) occur at 16000 cm^{-1} (625 nm) (neutral $\rightarrow 1^+$) and 16528 cm^{-1} (605 nm) ($1^+ \rightarrow 2^+$) so are less separated than in complex **7** (760 cm^{-1} separation).

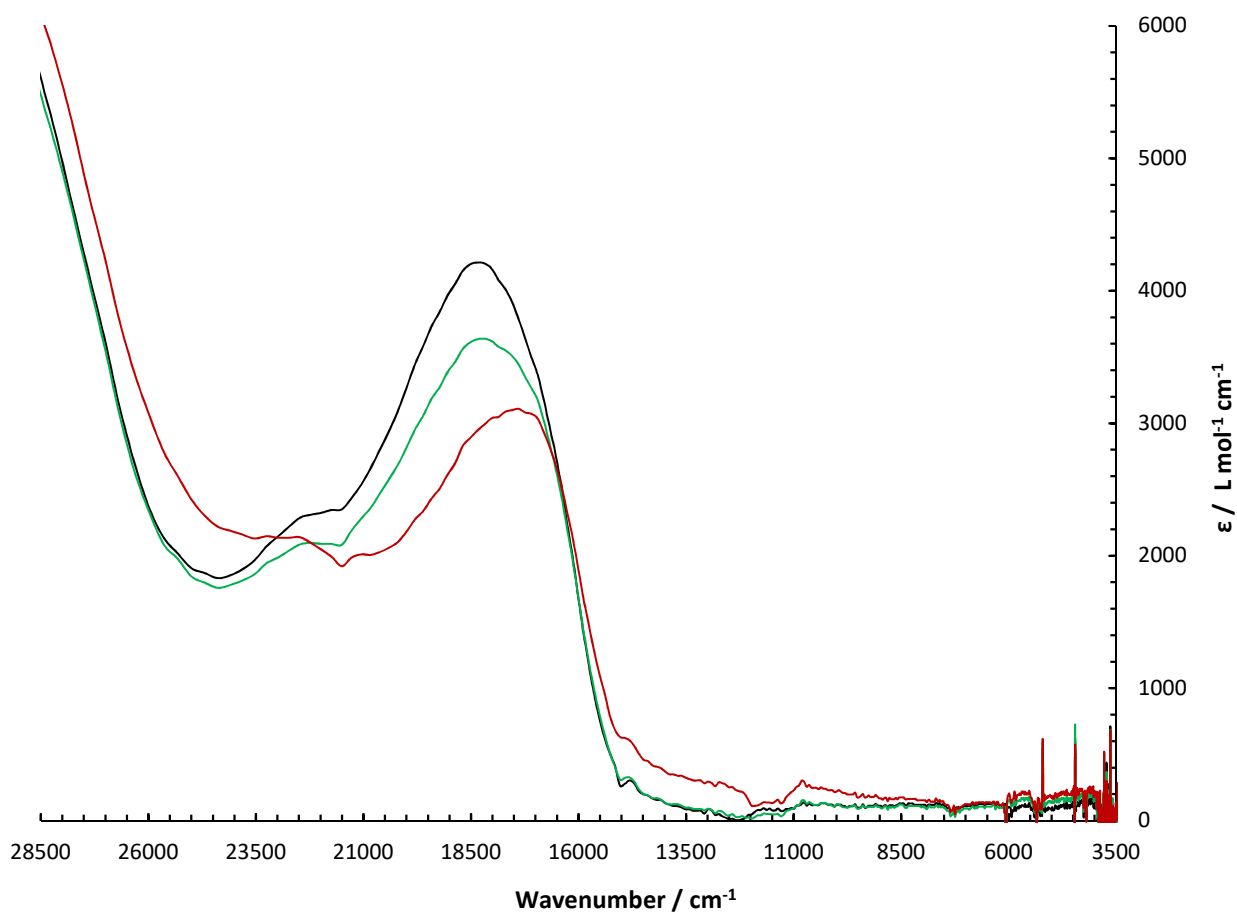


Figure 3.9. UV-Vis NIR SEC of complex **8** in 0.1M TBAPF₆ electrolyte in DCM. Neutral (black), 1⁺ (green) and 2⁺ (red).

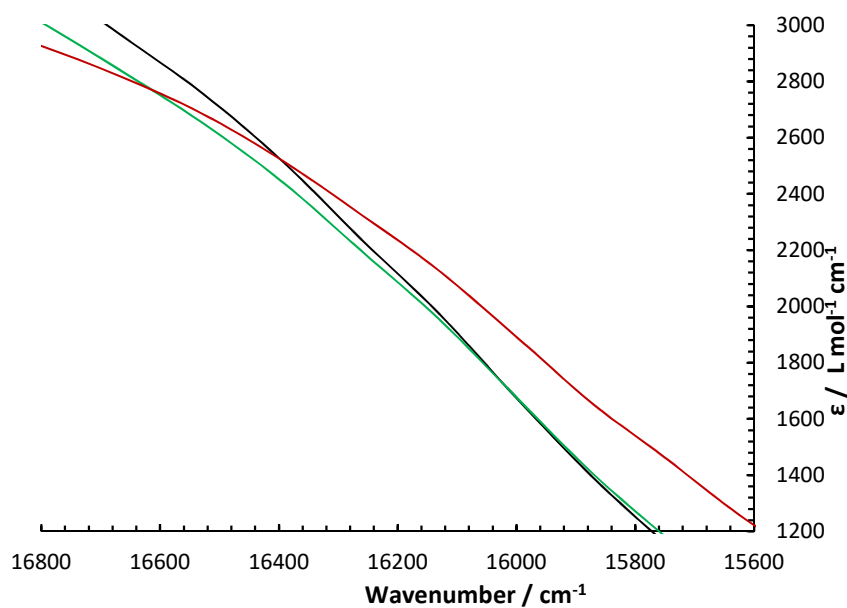


Figure 3.10. An expanded portion of the UV-Vis region highlighting the isosbestic points for the Mo₂ $\delta \rightarrow$ DOP π^* MLCT transitions in the UV-Vis NIR SEC of complex **8**.

3.4.3.3 UV-Vis NIR SEC of $\text{Mo}_2(\text{TiPB})_3(4\text{-MeHDOP})$ (**10**)

The UV-Vis NIR SEC for complex **10** in DCM is shown in Figure 3.11. No IVCT transition is observed in the NIR. Like complex **9** oxidation from the neutral state (black) to the mixed valence (green) state produces a decrease in intensity of the $\text{Mo}_2 \delta \rightarrow \text{DOP } \pi^*$ MLCT but only a marginal red shifting from ca. 19600 cm^{-1} (510 nm) to 19500 cm^{-1} (513 nm) and a broadening of the peak. In the doubly oxidised state (red) a significant fall in intensity and a large red shift to ca. 18600 cm^{-1} (574 nm) is observed. The isosbestic points observed in the MLCT transition upon oxidation are shown in Figure 3.12. occurring at ca. 18025 cm^{-1} (545 nm) (neutral $\rightarrow 1^+$) and 18210 cm^{-1} (549 nm) ($1^+ \rightarrow 2^+$) so are separated by just 185 cm^{-1} .

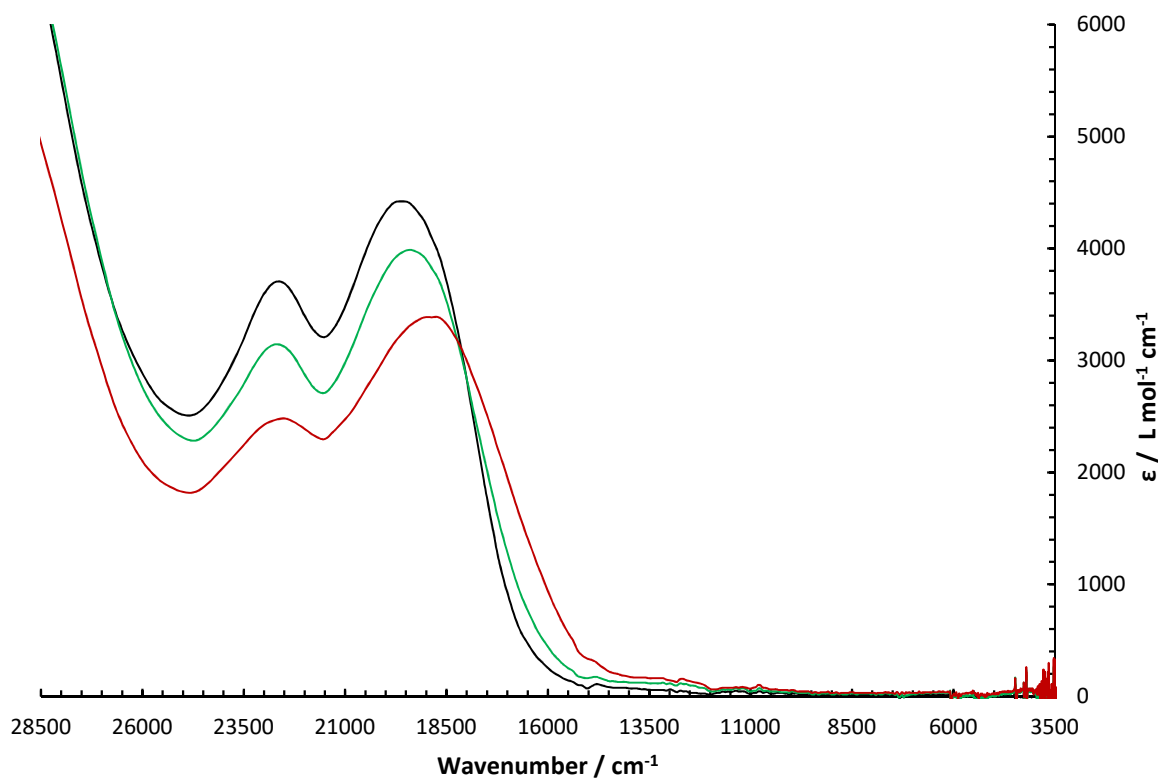


Figure 3.11. UV-Vis NIR SEC of complex **10** in 0.1M TBAPF₆ electrolyte in DCM. Neutral (black), 1^+ (green) and 2^+ (red).

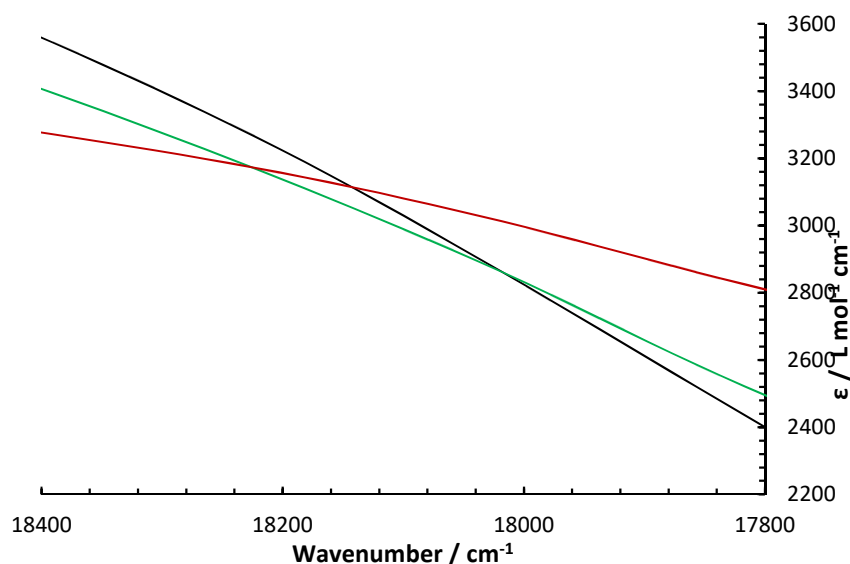


Figure 3.12. An expanded portion of the UV-Vis region highlighting the isosbestic points for the $\text{Mo}_2 \delta \rightarrow \text{DOP } \pi^*$ MLCT transitions in the UV-Vis NIR SEC of complex **10**.

3.4.3.4 UV-Vis NIR SEC of $\text{Mo}_2(\text{TiPB})_3(3\text{-Me},4\text{-MeDOP})$ (**11**)

The UV-Vis NIR SEC for complex **11** in DCM is shown in Figure 3.13. No IVCT transition is observed in the NIR. Initial oxidation to the MV state (black \rightarrow green) produces a fall in intensity in the $\delta \rightarrow \text{DOP } \pi^*$ MLCT (right) but only a minor red shift from *ca.* 20500 cm^{-1} (488 nm) to 20400 cm^{-1} (490 nm). The intensity of the transition increases again in the doubly oxidised state (red) and there is a much more significant red shift to *ca.* 20000 cm^{-1} (500 nm) is observed. The shift in peak centres is consistent across the entire series of complexes but the fall and rise of peak intensity resembles the Cl DOP system, complex **6**. The isosbestic points observed in the transitions are expanded in Figure 3.14. The higher energy (left-hand) MLCT transition displays no isosbestic points for the neutral $\rightarrow 1^+$ (black \rightarrow green) transition so was disregarded. In the right-hand transition the expected two isosbestic points are observed at *ca.* 19600 cm^{-1} (510 nm) (neutral $\rightarrow 1^+$) and 21505 cm^{-1} (465 nm) ($1^+ \rightarrow 2^+$).

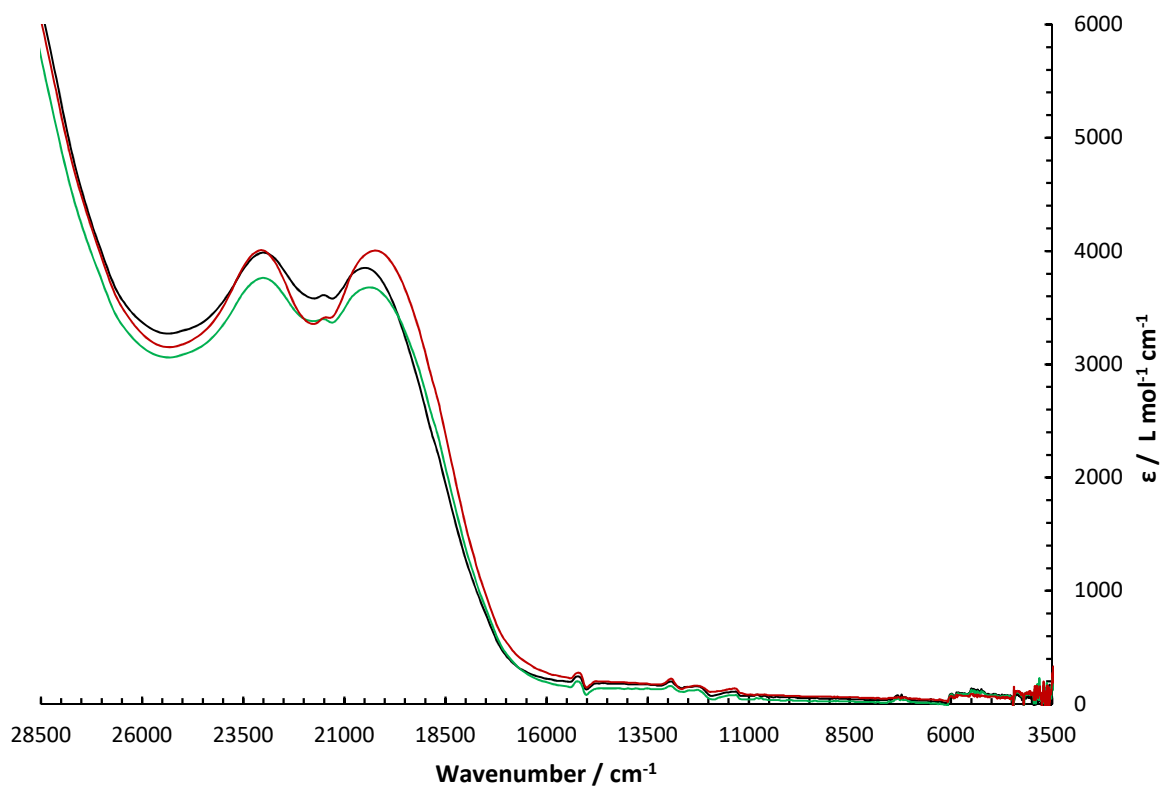


Figure 3.13. UV-Vis NIR SEC of complex **11** in 0.1M TBAPF₆ electrolyte in DCM. Neutral (black), 1⁺ (green) and 2⁺ (red).

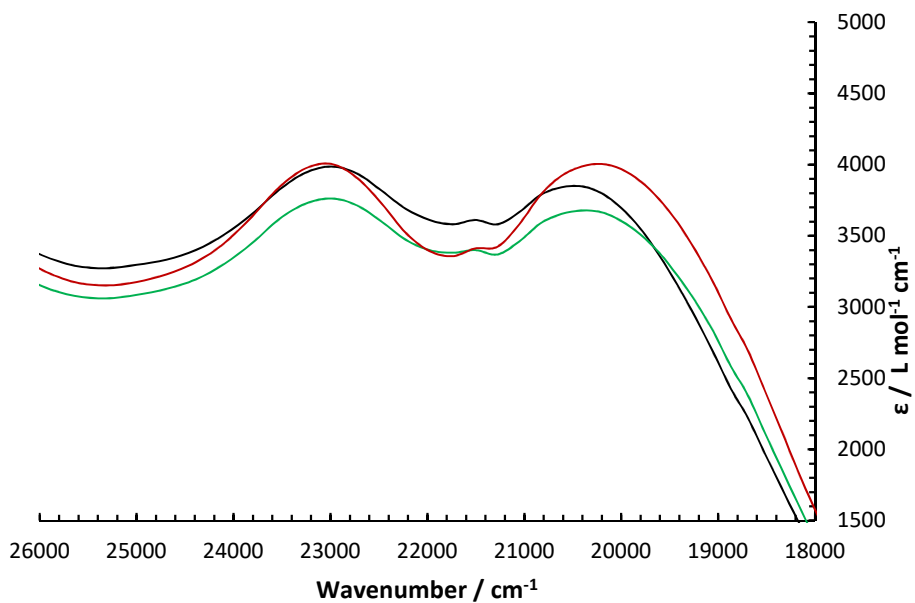


Figure 3.14. An expanded portion of the UV-Vis region highlighting the changes in the Mo₂ δ → DOP π* MLCT transitions in the UV-Vis NIR SEC of complex **11**.

3.4.3.5 UV-Vis NIR SEC of $\text{Mo}_2(\text{TiPB})_3(\text{Phth})$ (**12**)

The UV-Vis NIR SEC for complex **12** is shown in Figure 3.15. No IVCT is observed in the NIR region. The changes observed in the $\text{Mo}_2 \delta \rightarrow \text{DOP} \pi^*$ MLCT transition is unlike that observed in the other complexes of the series. Initial oxidation of the neutral to MV state produces an increase in peak intensity, and significant broadening of the peaks. Oxidation to the doubly oxidised state produces even further broadening but also a very large fall in intensity. Furthermore, there is no isosbestic point observed for the $1^+ \rightarrow 2^+$ oxidation, this might be attributed to the irreversibility of the oxidations in the CV experiment.

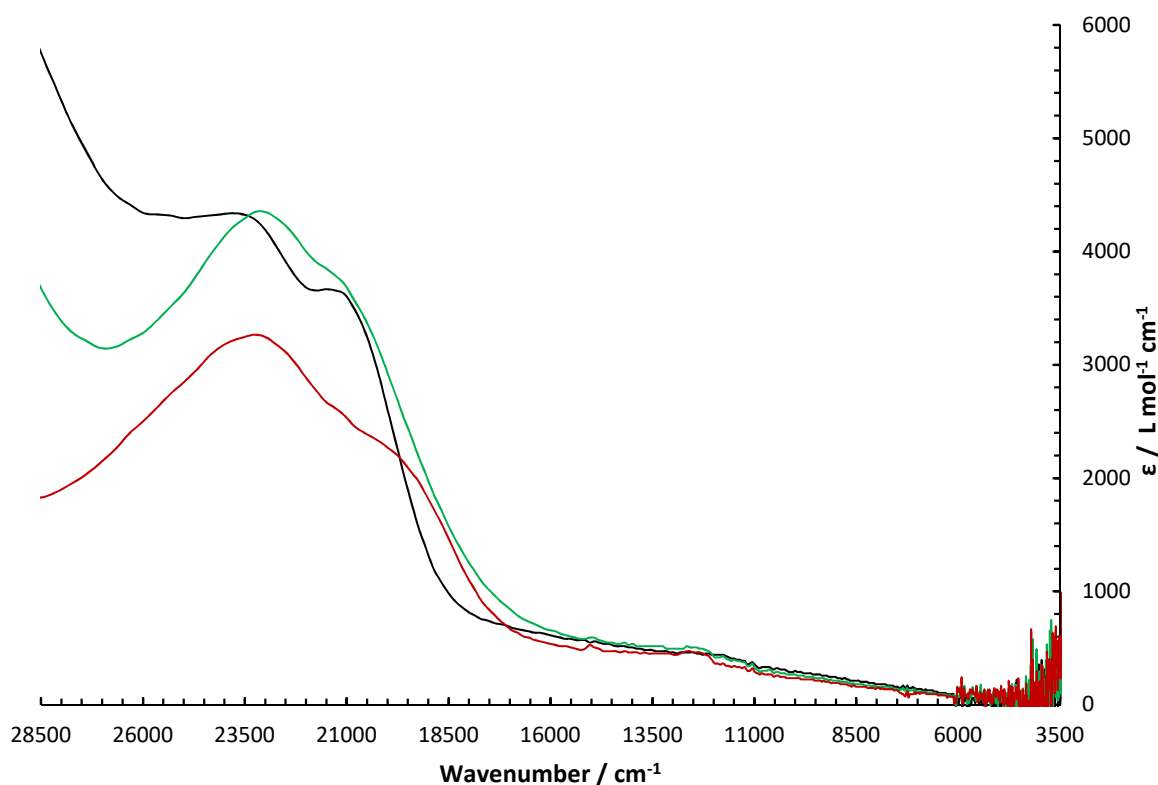


Figure 3.15. UV-Vis NIR SEC of complex **12** in 0.1M TBAPF₆ electrolyte in DCM. Neutral (black), 1⁺ (green) and 2⁺ (red).

3.5 Conclusions

A series of complexes of the form $\text{Mo}_2(\text{TiPB})_3(\text{R}'\text{R}''\text{HDOP})$ where R' , $\text{R}'' = \text{Cl}$, H (**7**), Br, H (**8**), H, H (**9**), Me (**10**) and Me, Me (**11**) and also the fused ring system $\text{Mo}_2(\text{TiPB})_3(\text{HPhth})$ (**12**), where HPhth = phthalhydrazide were synthesized. These complexes form “dimer of dimers” structures of $[\text{Mo}_2(\text{TiPB})_3(\text{R}'\text{R}''\text{HDOP})]_2$ in DCM. One electron oxidations produce a stable MV state in all cases as

observed in the CV measurements taken in DCM. Though it is not obvious in **7** a large decrease in the ΔE_{pc} , the difference between the oxidative and reductive peak centres is observed on switching from DCM to THF indicative of dimer dissociation and CT in a less diffuse system. The $\Delta E_{1/2}$ values in complexes **8** – **12** range from 0.118 to 0.260 V accounting for for K_c 's of 99, 487 and 1431 in **8** - **10**. Due to the irreversibility of the oxidations in complexes **11** and **12**, K_c values could not be determined but an increase in $\Delta E_{1/2}$ was still observed. The MV state thus becomes more thermodynamically stable as the bridging ligand becomes more electron donating.

This increase in thermodynamic stabilisation is rationalised by the ligand π -donor properties. As the DOP ligand becomes more electron rich it donates more readily to the Mo_2 core. Upon oxidation to generate the MV state the oxidised half of the molecule can be viewed as a singly occupied $Mo_2 \delta$ so more readily accepts electron density and is thus more impacted by the electronic change in the ligand. An electron donating substituted results in an increase in π -donation stabilising the generated charge where an electron withdrawing donating decreases π -donation and produces a thermodynamic destabilisation.

In the UV-Vis NIR SEC no IVCT transitions are observed for any of the complexes precluding electronic communication through direct donor-bridge-acceptor orbital overlap, consistent with the PCMV mechanism. Previously reported results for complex **9** showed that two isosbestic points were observed in the $M \delta \rightarrow DOP \pi^*$ MLCT for the neutral $\rightarrow 1^+$ and $1^+ \rightarrow 2^+$ transition because upon oxidation to the MV state the pKa changes on one half of the dimer reduces back bonding and thus affects the MLCT transition. In complexes **7**, **8** and **10** - **12** two isosbestic points are again observed in the $M \delta \rightarrow DOP \pi^*$ MLCT confirming the PCMV mechanism is in operation in all cases.

3.6 Experimental

3.6.1 *Materials and Physical Methods*

Materials and physical methods were as described previously in 2.4.1. Complex **9** was synthesized following the previously reported procedure and required no further purification.²

3.6.2 Synthesis of $\text{Mo}_2(\text{TiPB})_3(4\text{-Cl-HDOP})$ (**7**)

A Schlenk flask was charged with with 4-chloro-3,6-dioxypyridazine (4-Cl-H₂DOP) (0.036 g, 0.249 mmol) and $\text{Mo}_2(\text{TiPB})_4$ (0.300 g, 0.254 mmol). Toluene (10 mL) and NEt_3 (35 μL , 0.249 mmol) were added, and the reaction stirred for 17 hours at room temperature. The solvent was removed *in vacuo*, and the products extracted in to hexane (2 mL) and purified by silica column chromatography (eluent: hexanes \rightarrow hexanes/dichloromethane (70:30 (v/v))) collecting the first purple band to afford **1** as a purple solid. Yield: 0.078 g (29%). ¹H NMR (400 MHz, CDCl_3) δ 11.57 (d, $J = 2.5$ Hz, 1H, DOP NH), 7.25 (s, 2H, *trans*-TiBP *m* Ar-H), 6.94 (s, 4H, *cis*-TiBP *m* Ar-H), 6.70 (d, $J = 2.5$ Hz, 1H, DOP Ar-H), 3.81 – 3.68 (m, 2H, *cis*-TiPB *p*-CH(CH₃)₂), 3.07 – 2.97 (m, 1H, *trans*-TiPB *p*-CH(CH₃)₂), 2.90 – 2.82 (m, 2H, *trans*-TiPB σ -CH(CH₃)₂), 2.82 – 2.69 (m, 4H, *cis*-TiPB σ -CH(CH₃)₂), 1.39 – 1.32 (m, 18H, *i*-Pr), 1.25 (d, $J = 6.8$ Hz, 12H, *i*-Pr), 1.08 (d, $J = 6.8$ Hz, 12H), 0.94 (d, $J = 6.8$ Hz, 12H, *i*-Pr). MALDI-TOF-MS calcd. monoisotopic MW for $\text{Mo}_2\text{C}_{52}\text{H}_{71}\text{O}_8\text{N}_2\text{Cl}$, 1079.41, found m/z 1080.6. $[\text{M}+\text{H}]^+$. Anal. Calcd. for $\text{Mo}_2\text{C}_{52}\text{H}_{71}\text{O}_8\text{N}_2\text{Cl}$, C, 57.86; H, 6.63; N, 2.59; found C, 51.23; H, 6.97; N, 2.26

3.6.3 Synthesis of $\text{Mo}_2(\text{TiPB})_3(4\text{-Br-HDOP})$ (**8**)

A Schlenk flask was charged with with 4-bromo-3,6-dioxypyridazine (4-Br-H₂DOP) (0.048 g, 0.249 mmol) and $\text{Mo}_2(\text{TiPB})_4$ (0.300 g, 0.254 mmol). Toluene (10 mL) and NEt_3 (35 μL , 0.149 mmol) were added to the flask, and the reaction stirred for 17 hours. The solvent was remove *in vacuo*, and the products extracted in to hexane (2 mL) and purified by silica column chromatography (eluent: hexanes \rightarrow hexanes/dichloromethane (70:30 (v/v))) collecting the first purple band to afford **7** as a purple solid. Yield 0.098 g (35%). ¹H NMR (400 MHz, CDCl_3) δ 11.58 (d, $J = 2.3$ Hz, 1H), 7.25 (s, 2H), 6.95 (s, 4H), 6.92 (d, $J = 2.3$ Hz, 1H), 3.82 – 3.70 (m, 2H), 3.07 – 2.97 (m, 1H), 2.97 – 2.83 (m, 2H), 2.83 – 2.70 (m, 4H), 1.39 – 1.31 (m, 18H), 1.26 (d, $J = 6.6$ Hz, 12H), 1.10 (d, $J = 6.6$ Hz, 12H), 0.94 (d, $J = 6.6$ Hz, 12H). MALDI-TOF-MS calcd. monoisotopic MW for $\text{Mo}_2\text{C}_{52}\text{H}_{71}\text{O}_8\text{N}_2\text{Br}$, 1023.9, found m/z 1026.3 (M⁺). Anal. Calcd. for $\text{Mo}_2\text{C}_{52}\text{H}_{71}\text{O}_8\text{N}_2\text{Br}$, C, 55.57; H, 6.36; N, 2.49; found C, 55.42; H, 6.28; N, 2.42.

3.6.4 Synthesis of $\text{Mo}_2(\text{TiPB})_3(4\text{-Me-HDOP})$ (**10**)

A Schlenk flask was charged with with 4-methyl-3,6-dioxypyridazine (4-Me-H₂DOP) (0.031 g, 0.249 mmol) and $\text{Mo}_2(\text{TiPB})_4$ (0.300 g, 0.254 mmol). Toluene (10 mL) and NEt_3 (35 μL , 0.149 mmol) was added, and the reaction stirred for 17 hours. The solvent was removed *in vacuo*, and the products extracted in to hexane (2 mL) and purified by silica column chromatography (eluent: hexanes \rightarrow dichloromethane) collecting the first red band to afford **9** as a red solid. Yield 0.086 g (33%). ¹H NMR (400 MHz, CDCl_3) δ 11.63 (s, 1H), 7.24 (s, 2H), 6.93 (s, 4H), 6.45 (s, 1H), 3.84 – 3.74 (m, 2H), 3.06 – 2.96 (m, 1H), 2.93 – 2.82 (m, 2H), 2.82 – 2.71 (m, 4H), 2.25 (s, 3H), 1.38 – 1.29 (m, 18H), 1.25 (d, $J = 6.1$ Hz, 12H), 1.03 (d, $J = 6.6$ Hz, 12H), 0.93 (d, $J = 6.6$ Hz, 12H). MALDI-TOF-MS calcd. monoisotopic MW for $\text{Mo}_2\text{C}_{53}\text{H}_{74}\text{O}_8\text{N}_2$, 1058.9, found m/z 1058.6. (M+). Anal. Calcd. for $\text{Mo}_2\text{C}_{53}\text{H}_{74}\text{O}_8\text{N}_2$, C, 60.11; H, 7.04; N, 2.64; found C, 59.91; H, 7.18; N, 2.57.

3.6.5 Synthesis of $\text{Mo}_2(\text{TiPB})_3(4,5\text{-Me}_2\text{-HDOP})$ (**11**)

A Schlenk flask was charged with with 4,5-dimethyl-3,6-dioxypyridazine (4,5-Me₂-H₂DOP) (0.035 g, 0.249 mmol) and $\text{Mo}_2(\text{TiPB})_4$ (0.300 g, 0.254 mmol). Toluene (10 mL) and NEt_3 (35 μL , 0.149 mmol) were added, and the reaction stirred for 17 hours. The solvent was remove *in vacuo*, and the products extracted in to hexane (2 mL) and purified by silica column chromatography (eluent: hexanes \rightarrow dichloromethane \rightarrow dichloromethane/MeCN (70:30 (v/v)) collecting the first red band to afford **10** as a red solid. Yield 0.083 g (30%). ¹H NMR (400 MHz, CD_2Cl_2) δ 7.07 (s, 2H), 7.04 (s, 4H), 3.76 – 3.62 (m, 2H), 3.09 – 2.99 (m, 1H), 2.99 – 2.84 (m, 6H), 2.45 (s, 3H), 2.22 (s, 3H), 1.36 – 1.22 (m, 30H), 1.21 – 1.08 (m, 24H). MALDI-TOF-MS calcd. Monoisotopic MW for $\text{Mo}_2\text{C}_{54}\text{H}_{76}\text{O}_8\text{N}_2$, 1073.02, found m/z 1074.04. [M+H]⁺

3.6.6 Synthesis of $\text{Mo}_2(\text{TiPB})_3(\text{Phthal})$ (**12**)

Phthalhydrazide (HPhthal) (0.041 g, 0.249 mmol) and $\text{Mo}_2(\text{TiPB})_4$ (0.300 g, 0.254 mmol) were charged to an oven dried Schlenk flask. Toluene (10 mL) and NEt_3 (35 μL , 0.149 mmol) were added, and the reaction stirred for 17 hours. The solvent was removed *in vacuo*, and the products extracted in to hexane (2 mL) and purified by silica column chromatography (eluent: hexanes \rightarrow dichloromethane \rightarrow

dichloromethane/THF (95:5 (v/v)) carefully collecting the first of two close-running red bands to afford **11** as a red solid. Yield 0.167 g (60 %). ^1H NMR (400 MHz, CDCl_3) δ 8.48 – 8.30 (m, 2H), 7.95 – 7.85 (m, 1H), 7.74 – 7.64 (m, 1H), 7.19 (s, 2H), 7.02 – 6.97 (m, 4H), 3.04 – 2.81 (m, 9H), 1.23 – 1.16 (m, 30H), 0.98 (s, 24H).

3.7 References

- (1) Wilkinson, L. A.; Vincent, K. B.; Meijer, A. J. H. M.; Patmore, N. J. *Chem. Commun.* **2016**, 52, 100.
- (2) Wilkinson, L. A.; McNeill, L.; Meijer, A. J. H. M.; Patmore, N. J. *J. Am. Chem. Soc.* **2013**, 135 (5), 1723.
- (3) Wilkinson, L. A.; McNeill, L.; Scattergood, P. A.; Patmore, N. J. *Inorg. Chem.* **2013**, 52, 9683.
- (4) Sun, H.; Steeb, J.; Kaifer, A. E. *J. Am. Chem. Soc.* **2006**, 128, 2820.
- (5) Goeltz, J. C.; Kubiak, C. P. *J. Am. Chem. Soc.* **2010**, 132, 17390.
- (6) Canzi, G.; Goeltz, J. C.; Henderson, J. S.; Park, R. E.; Maruggi, C.; Kubiak, C. P. *J. Am. Chem. Soc.* **2014**, 136, 1710.
- (7) Tadokoro, M.; Inoue, T.; Tamaki, S.; Fujii, K.; Isogai, K.; Nakazawa, H.; Takeda, S.; Isobe, K.; Koga, N.; Ichimura, A.; Nakasuji, K. *Angew. Chem. Int. Ed.* **2007**, 46, 5938.
- (8) Winter, R. F. *Organometallics* **2014**, 1, 4517.
- (9) Marcus, R. A. *Rev. Mod. Phys.* **1992**, 2, 599.
- (10) Salsman, J. C.; Ronco, S.; Londergan, C. H.; Kubiak, C. P. *Inorg. Chem.* **2006**, 45, 547.
- (11) Demadis, K. D.; Neyhart, G. A.; Kober, E. M.; White, P. S.; Meyer, T. J. *J. Am. Chem. Soc.* **1998**, 120, 7121.
- (12) Ito, T.; Hamaguchi, T.; Nagino, H.; Yamaguchi, T.; Kido, H.; Zavarine, I. S.; Richmond, T.; Washington, J.; Kubiak, C. P. *J. Am. Chem. Soc.* **1999**, 121, 4625

- (13) Ito, T.; Hamaguchi, T.; Nagino, H.; Yamaguchi, T.; Washington, J.; Kubiak, C. P. *Science*. **1997**, 277, 660.
- (14) Londergan, C. H.; Kubiak, C. P. *Chem. Eur. J.* **2003**, 9, 5962.
- (15) Mayer, J. M. *Annu. Rev. Phys. Chem.* **2004**, 55, 363.
- (16) Roth, J. P.; Lovell, S.; Mayer, J. M. *J. Am. Chem. Soc.* **2000**, 122, 5486.
- (17) Lambert, C.; Risko, C.; Coropceanu, V.; Schelter, J.; Amthor, S.; Gruhn, N. E.; Durivage, J. C.; Brédas, J.-L. *J. Am. Chem. Soc.* **2005**, 127, 8508.
- (18) Fox, M. A.; Le Guennic, B.; Roberts, R. L.; Brue, D. A.; Yufit, D. S.; Howard, J. A. K.; Manca, G.; Halet, J. F.; Hartl, F.; Low, P. J. *J. Am. Chem. Soc.* **2011**, 133, 18433.
- (19) Malcolm H, C.; Nathan J, P. *Molecular Metal-Metal Bonds: Compounds, Synthesis, Properties*; Liddle, S. T., Ed.; 2015.
- (20) Cayton, R. H.; Chisholm, M. H.; Huffman, J. C.; Lobkovsky, E. B. *J. Am. Chem. Soc.* **1991**, 113, 8709.
- (21) Chisholm, M. H.; Lear, B. J.; Moscatelli, A.; Peteanu, L. A. *Inorg. Chem.* **2010**, 49, 3706.

Chapter 4. “Dimer of Dimers” Bridged by Thio-Lactams: 1,2-dihydropyridazine-3,6-dithione (HSDOP) and 1,4-dihydropyrazine-2,3-dithione (HDSOP).

4.1 Abstract

Substitution of labile acetate ligands occurs when $\text{Mo}_2(\text{DAniF})_3(\text{OAc})$ is reacted with 1,4-dihydropyrazine-2,3-dithione (H_2DSOP) and 1,2-dihydropyridazine-3,6-dithione (H_2SDOP) producing the complexes $\text{Mo}_2(\text{DAniF})_3(\text{HDSOP})$ (**13**) and $\text{Mo}_2(\text{DAniF})_3(\text{HSDOP})$ (**14**). These complexes form “dimers of dimers” structures; $[\mathbf{13}]_2$ and $[\mathbf{14}]_2$ through self-complimentary hydrogen interactions in DCM. K_c values determined by CV measurements in DCM of 3.69×10^4 and 571 indicate a thermodynamically stable MV state with good charge transfer between the Mo_2 units. The UV-Vis NIR SEC confirms these complexes are rare examples of a MV state stabilised by the PCMV mechanism due to the absence of an IVCT in the NIR region.¹⁻³ The use of IR SEC does however show that in the MV and doubly oxidised state $[\mathbf{13}]_2^+$ and $[\mathbf{13}]_2^{2+}$ displays a unique IR centred transition that extends into the NIR region. The same transition is not observed upon oxidation of complex **14**.

4.2 Effects of Coordinating Atom Alterations on Stabilisation of the Mixed Valence State

In Chapter 3 the influence of electronic changes in the bridge through addition of electron donating or withdrawing groups was discussed. Herein the effect of altering the identity of the coordinating atom whilst the structure of the bridge remains constant is discussed herein.

There are a number of studies in the literature investigating how this alteration affects stabilisation of the mixed valence state in dimers having the $\text{Mo}_2(\text{DAniF})_3$ redox terminus. Two of which are provided by the Liu group. Firstly, where the bridge is a thiene di-carboxylate and its derivatives; OO-thi-OO, NS-thi-NS, OS-thi-OS and SS-thi-SS depicted in Figure 4.1. The IVCT band analysis of these systems was discussed in depth section 1.7 but the key points have been summarised here for convenience. N for O for S substitution lowers the HOMO $\text{Mo}_2\text{-}\delta$ to LUMO π^* energy gap between increasing electronic coupling across the series; OO-thi-OO < NS-thi-NS < OS-thi-OS < SS-thi-SS and produces a systemic transition from Class II-III into the Class III regime.

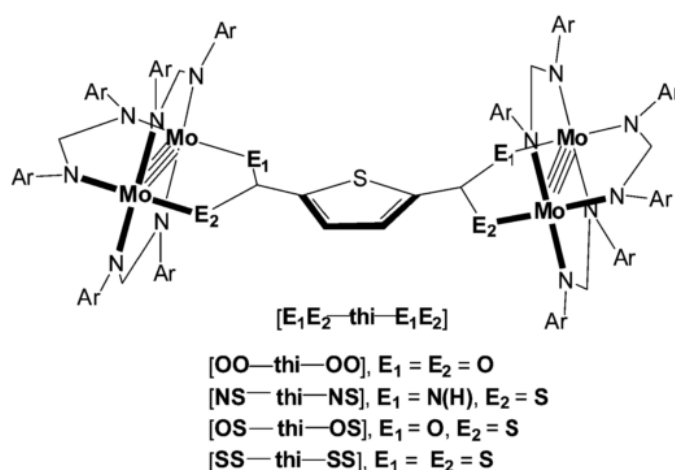
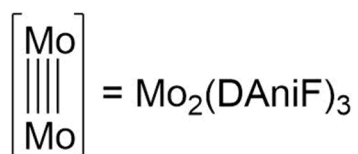


Figure 4.1. E₁E₂-thi-E₁E₂ bridged $[\text{Mo}_2]_2$ complexes reported by Liu et al. Figure reproduced from reference with permission of the RSC.⁴ The ancillary ligands are DAniF where Ar = p-anisyl.

In the second study the bridge is instead terephthalic acid and its N and S containing derivatives (Figure 4.2).⁵⁻⁷ Electronic communication through $d(\delta)\text{-}p(\pi)$ conjugation is related to the hardness of the

coordinating atom. Soft S atoms produce Mo-S bonds of more covalent character increasing conjugation where hard N atoms produce the opposite effect. The increase in electronic coupling is observed directly in the IVCT band analysis as a reduction of the band energy (E_{IVCT}) and narrowing of the band at half-height ($\Delta v_{1/2}$). Stabilisation of the MV state is also observed as increase in K_c determined by cyclic voltammetry.



| K_c | | E_{IVCT} (cm ⁻¹) | $\Delta v_{1/2}$ (cm ⁻¹) |
|-------|--|--------------------------------|--------------------------------------|
| 23 | | 4980 | 8840 |
| 42 | | 4651 | 5242 |
| 49 | | 4240 | 4410 |
| 88 | | 3440 | 3688 |
| 91 | | 3182 | 3290 |
| 2405 | | 2640 | 1770 |

Figure 4.2. Mo₂-bridge-Mo₂ complexes reported by Liu et al. with accompanying electrochemical data (K_c) and IVCT band analysis data, energy (E_{IVCT}) and width at half-height ($\Delta v_{1/2}$).

4.3 Aims

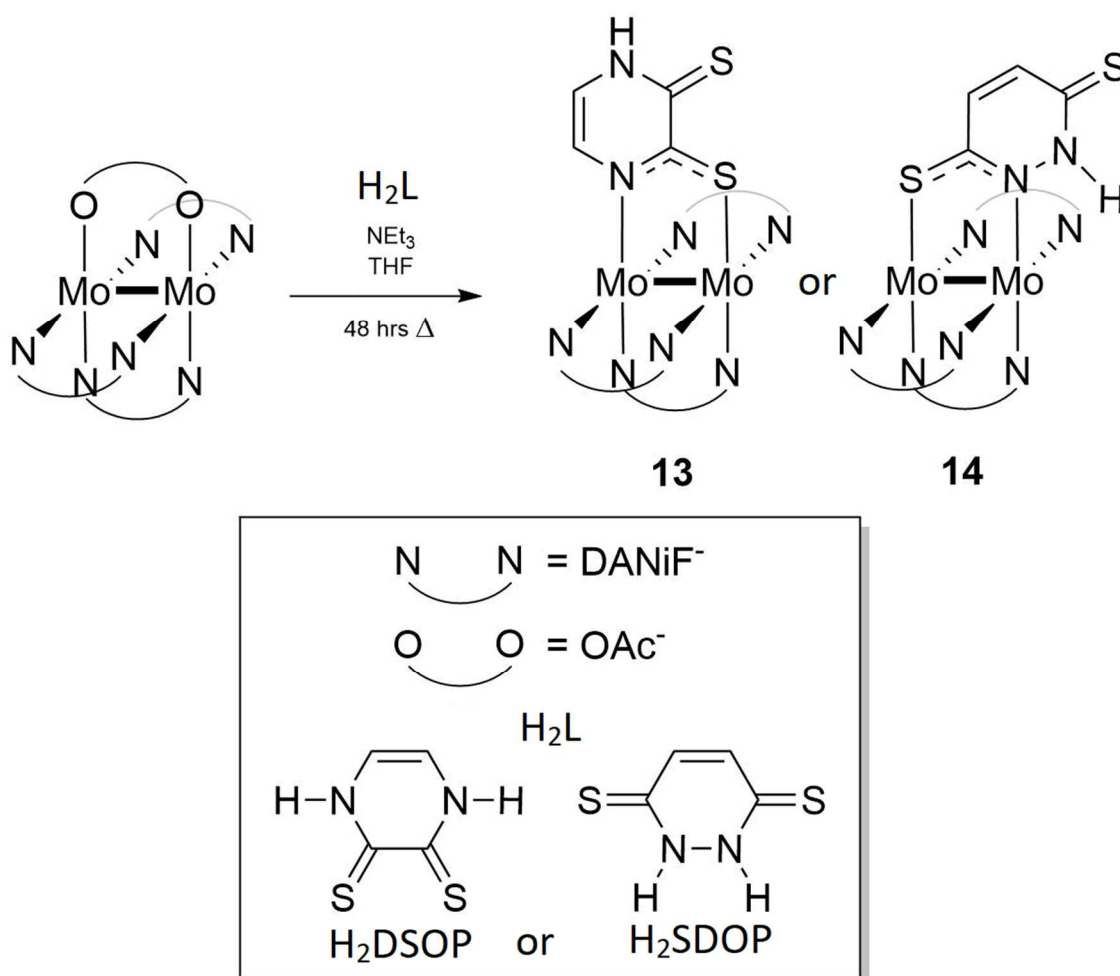
In covalent mixed valence systems substitution of N for O for S coordinating atoms produces an increase in stabilisation of the mixed valence state and can be related to an increase in electronic communication by IVCT band analysis.⁴⁻⁷ The previous examples from our group where stabilisation of the MV state occurs via the PCMV mechanism have employed the HDOP or HDON ligands, where the coordinating atoms are N and O.¹⁻³

The effect of coordinating atom substitution on the PCMV mechanism is not known prompting synthesis of new systems. The H₂SDOP ligands is a direct structural analogue of the H₂DOP ligand where O atoms are substituted for S atoms, and the H₂DSOP ligand is the structural isomer of this compound. New systems are also desirable as it could produce an ET rate that can be observed on the NMR or IR time-scales by spectral coalescence that was not possible in the Mo₂(TiPB)₃(R'R''DOP) series.

4.4 Discussion

4.4.1 Synthesis and Characterisation

The synthetic procedure for complexes $\text{Mo}_2(\text{DANiF})_3(\text{HDSOP})$ (**13**) and $\text{Mo}_2(\text{DANiF})_3(\text{HSDOP})$ (**14**) is presented in Scheme 4.1. The procedure is based largely on a combination of the insights gained from the attempted substitution reactions of the $\text{Mo}_2(\text{DTolF})_{4-n}(\text{OAc})_n$ series (chapter 2.3.4) and synthesis of the $\text{Mo}_2(\text{TIPB})_3(\text{R}'\text{R}''\text{DOP})$ series (chapter 3.3.1).



Scheme 4.1. Synthesis of $\text{Mo}_2(\text{DANiF})_3(\text{DSOP})$ (**13**) and $\text{Mo}_2(\text{DANiF})_3(\text{SDOP})$ (**14**). The aromatic backbone of the HL ligand is numbered by standard conventions.

The H_2SDOP molecule is a direct structural analogue of the H_2DOP where O atoms are substituted for S atoms. The H_2DSOP molecule is a structural isomer of H_2DOP where oxygen atoms are substituted

for sulphur. In the resulting complexes the thio-lactam tautomer is presented in both cases which is favoured in $\text{Mo}_2(\text{TIPB})_3(\text{R}'\text{R}''\text{DOP})$ series. The balance of the tautomer equilibrium is still unclear at this stage from ^1H NMR and IR spectroscopy data discussed later.

$\text{Mo}_2(\text{DAniF})_3(\text{OAc})$ is prepared as described in the literature by reaction of $\text{Mo}_2(\text{OAc})_4$ with three equivalents HDAniF and NaOMe in THF.⁸ Complexes **13** and **14** are prepared by reaction of $\text{Mo}_2(\text{DAniF})_3(\text{OAc})$ with H_2L and NEt_3 . The bridging ligand H_2L and NEt_3 are added in a 5 mol % excess relative to the Mo_2 starting material to promote substitution of the OAc ligand. Over-substitution is not a concern given the reduced lability of the formamidinate ligands relative to TIPB ligands discussed in section 3.4.1. The reaction is performed in THF as any success with substitution in the formamidinate complexes was found in this solvent (section 2.4.4.) $\text{Mo}_2(\text{DAniF})_3(\text{OAc})$ (yellow) is THF soluble but the H_2L compounds are insoluble. The reaction is considered complete when a homogenous blue (**13**) or green (**14**) solution is formed, typically within 48 hours.

Silica column chromatography is used to purify the crude reaction mixtures. This was somewhat complicated by the solvatochromism displayed by the target complexes described later. The impurities in the crude reaction mixture are typically unreacted H_2L which is insoluble, $\text{Mo}_2(\text{DAniF})_3(\text{OAc})$ which is eluted prior to the products in DCM and oxidative decomposition products that only elute when the THF fraction is increased. The product complexes **13** and **14** are eluted by gradually increasing the THF fraction which must be done carefully to ensure good separation from these impurities.

The resultant complexes are turquoise (**13**) and dark blue (**14**) solids that are moderately stable in the solid state with discoloration occurring after *ca.* 10 minutes in air, but significantly more sensitive in solution decomposing entirely within *ca.* 2 minutes. The complexes are soluble in DCM, THF and DMSO but insoluble in non-polar, non-coordinating solvents such as hexanes and are also insoluble in water. Both complexes display solvatochromism when switching from DCM to THF. Complex **13**, is a turquoise solid but turns blue in DCM and blue-green in THF. Complex **14**, is a dark blue solid that is

purple in DCM and appears redder in THF. The changes correlate with a blue shift in DCM due to increased solvent polarity and red shift in THF, a less polar solvent as observed in UV-Vis spectra in section 4.4.3. Extensive attempts have been made to crystallise the complexes both in the monomeric and dimeric form but have been unsuccessful.

Visually the reactions are quite interesting and should prompt further analysis of intermediate species/ competitive products that was not possible at this time. First consider the reaction with the H₂SDOP ligand to yield **13**. The yellow Mo₂ starting material and red/ brown H₂DSOP ligand are charged to a Schlenk flask. Addition of THF generates a yellow solution with a suspension of the red insoluble H₂DSOP ligand. After addition of NEt₃ a green solution is produced within 10 minutes though the majority of the insoluble DSOP ligand remains. A colour change to dark blue is observed after around 30 minutes. In a few cases the green coloration has persisted and a slight warming (*ca.* 40 °C) of the reaction mixture for around 20 minutes is sufficient to produce a colour change to blue. For the H₂DSOP ligand (yellow) similar behaviour is observed; where the intermediate coloration is blue, and the completed reaction mixture **14** is purple. This intermediate coloration could be accounted to either a kinetic product such as a coordination isomer or an intermediate reactive species with **13/ 14** being the ultimate thermodynamic product.

Coloured intermediates are often observed in related chemistry. For instance, in the synthesis of complexes such as Mo₂(DAniF)₃(L) where L = perfluorophenyl or isonicotine.⁹⁻¹¹ The precursor complex in these reaction is also Mo₂(DAniF)₃(OAc) and is presumed to react with NaOMe prior to coordination of new carboxylate ligand generating red intermediate solutions of Mo₂(DAniF)₃(OCH₃)(CH₃OH). This speciation is often short-lived by comparison *ca.* 1 minute. To this author's knowledge there are no reports of characterisation of such a species.

These intermediate coloured species (green and blue); are also sometimes observed during column chromatography. The resultant bands remain stationary on the column in all but the most polar solvent systems such as MeOH in THF 10 : 90 v/v but could never be isolated in any appreciable

quantity for characterisation. The distinct solubility profiles of the intermediate and final products are promising that if the correct conditions to favour the formation of the intermediate were established it could potentially be isolated cleanly from the product complexes described herein.

4.4.1.1 ^1H NMR Spectroscopy.

The ^1H NMR spectra of complexes **13** and **14** in CDCl_3 are presented in Figure 4.3. Upon substitution of the OAc- ligand in the precursor complex $\text{Mo}_2(\text{DAniF})_3(\text{OAc})$ for the HDSOP/ HSDOP ligand there are now two different coordinating atoms in the HDSOP/ HSDOP (N and S) coordinating the Mo_2 centre. This reduces the symmetry across the molecule such that not only are the two *cis*- and one *trans*-DAniF ligands inequivalent, the *p*-anisyl substituents on each side of the DAniF ligands are rendered inequivalent. The expected integration pattern is thus 4 : 4 : 4 : 4 : 2 : 2 : 2 : 2 for the *ortho* and *meta* Ar-H. In **13** this splitting pattern is well observed. There is some overlap of signals in **14** that produces a 6 : 6 : 4 : 4 : 2 : 2 split.

The integration pattern expected for the *p*-OCH₃ is 6 : 6 : 3. In the observed spectra there are again varying degrees of peak overlap with a 12 : 3 : 3 split observed in **13** and 9 : 6 : 3 in **14**. The DAniF formamidinate protons, C-NH-N remain in a 2 : 1 integration pattern.

There are three proton environments in the HDSOP / HSDOP ligand, the NH and the 3 and 4 positions of the aromatic backbone. The aromatic protons in the 3 position should produce a doublet, while the 4 position a double of doublets, if coupling to the NH environment is observed as in complexes **7** – **10** of the $\text{Mo}_2(\text{TiPB})_3(\text{R}'\text{R}''\text{DOP})$ series. Experimentally each is observed as a broad doublet and a multiplet; at 6.19 and 6.12-6.16 ppm in **13** and at 6.10 and 6.06 - 6.09 ppm in **14**.

The NH produces a doublet at 8.40 ppm $J = 2.8$ Hz confirming coupling to the 4 position Ar-H in **13** but in **14** multiple broad resonances are instead observed in this region.

Further purification is desired but the presence of a Mo₂ based impurity at even picomolar level concentrations would produce a response in the CV experiment that is not observed. Dynamic and 2D NMR techniques will be required to make an unequivocal assignment regarding the lactam and lactim tautomerism that was not possible at this time.

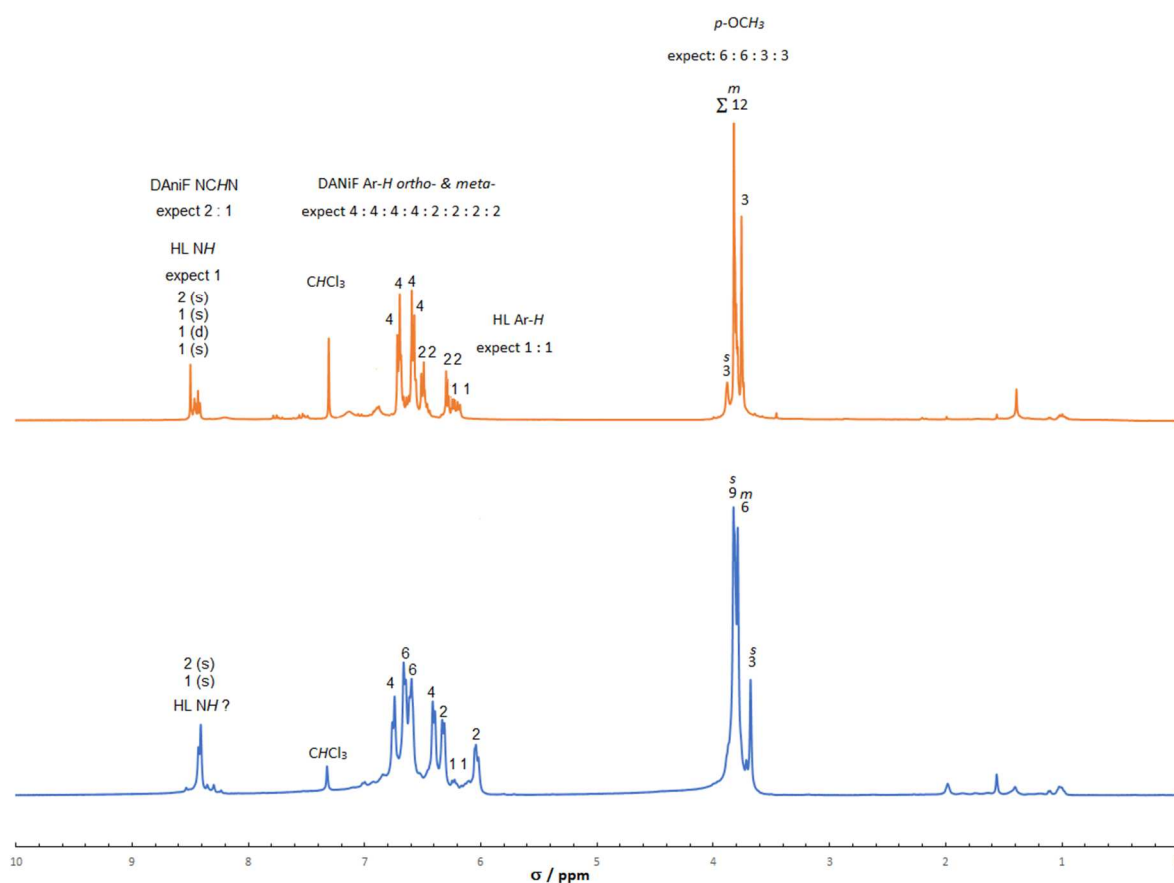


Figure 4.3. ¹H NMR of complexes 13 and 14 in CDCl₃.

4.4.2 Cyclic Voltammetry

The CV of complex [13]₂ (Figure 4.4) displays three reversible redox processes in DCM, $E_{1/2}(1) = -0.270$ V, $E_{1/2}(2) = -0.055$ V and $E_{1/2}(3) = 0.142$ V. The first two redox processes are assigned to both of the Mo₂ cores followed by an oxidation of one of the bridging ligands. A K_c value of 3.69×10^4 was determined from $\Delta E_{1/2} = 0.270$ V between $E_{1/2}(1)$ and $E_{1/2}(2)$. This is significantly larger even than the most thermodynamically stable of the DOP series, complex Mo₂(TiPB)₃(R'-Me, R''-HDOP) (10) and is comparable to values determined for strongly coupled covalently bridged Mo₂ dimers^{12,13} suggesting

very good charge transfer between the Mo₂ centres. The redox events are greatly cathodically shifted in comparison to [10]₂ where all redox events occur at positive potentials.

On addition of 0.1 mL DMSO only two processes are observed. This can be accounted to the breaking apart of the dimer forming the monomeric unit [13] which is oxidised to [13]⁺. The current response does not increase two-fold as would be expected for two equivalences of [13] now being oxidised at equal potential without generation of the MV state. The second oxidation ([13]₂⁺ → [13]₂²⁺) that is present in DCM but disappears on addition of DMSO can be seen more clearly in the DPV results displayed in Figure 4.5. The ligand oxidation thus undergoes a quite significant cathodic shift of 167 mV on addition of DMSO.

The CV of dimer [14]₂ in DCM is presented in Figure 4.6 (blue). Disregarding the internal reference Fe(Cp^{*})₂ / Fe(Cp^{*})₂⁺ redox couple occurring at E_{1/2}(ref) = -0.48 V, three oxidations are observed. The first two corresponding to oxidation to the MV state [14]₂⁺ and doubly oxidised dimer [14]₂²⁺ which occur at E_{1/2}(1) = -0.268 and E_{1/2}(2) = -0.105 V. The initial oxidation thus occurs at an almost identical potential in 13. The ΔE_{1/2} of 0.163 V accounts for a K_c of 571, so is much smaller and thus the mixed valence state is less thermodynamically stable than for [13]₂⁺. The third oxidation at E_{pc}(3) = 0.283 V is a bridging ligand oxidation so is both anodically shifted and irreversible in comparison to that seen in complex 13.

On addition of 0.1 mL DMSO (red) the second reversible redox process disappears commensurate with disruption of the hydrogen bonded dimer. While the E_{1/2}(1) potential remains fairly constant the ligand oxidation E_{pc}(3) is shifted cathodically by 45 mV to 0.238 V.

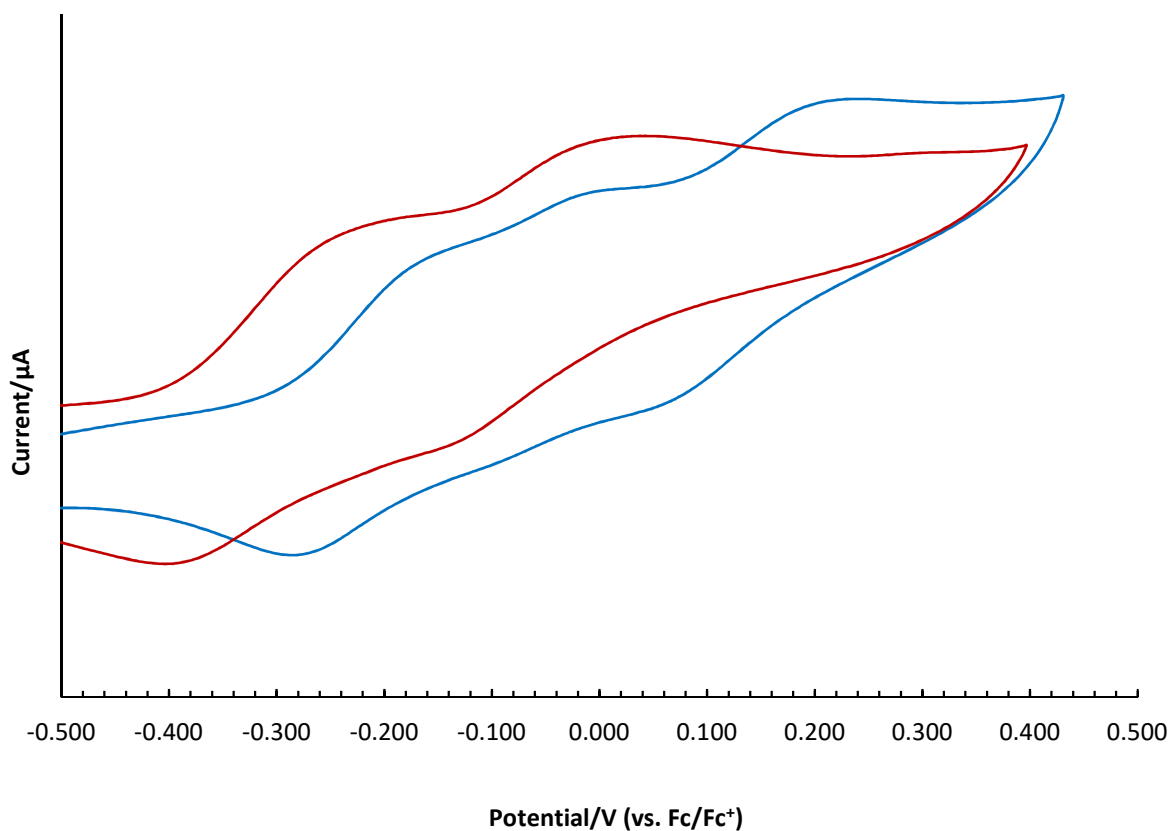


Figure 4.4. CV of $[\text{Mo}_2(\text{DAniF})_3(\text{DSOP})]_2$ dimer **[13]₂** DCM (red) and monomer **[13]** after addition of 0.1 mL DMSO (red). Measurement taken in 0.1M TBAPF₆ electrolyte in 100 mVs⁻¹ scan rate.

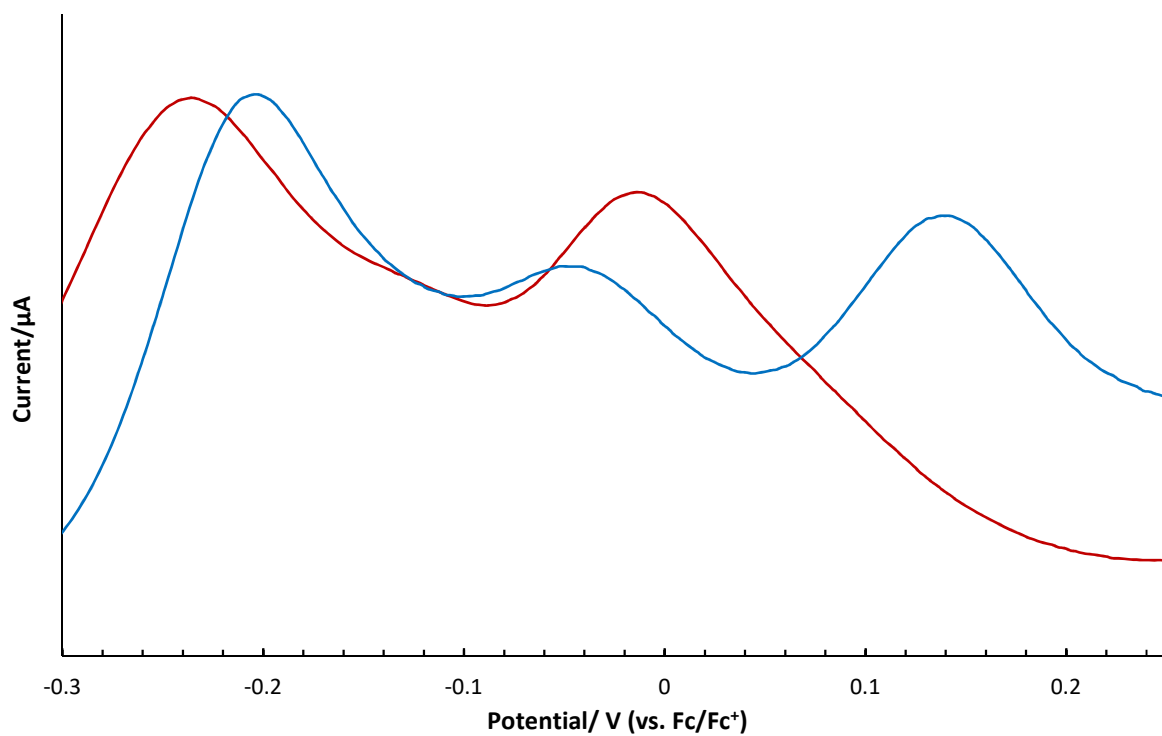


Figure 4.5. DPV of dimer **[13]₂** in DCM (red) and monomer **[13]** after addition of 0.1 mL DMSO. Measurement taken in 0.1M TBAPF₆ electrolyte in 5 mVs⁻¹ scan rate.

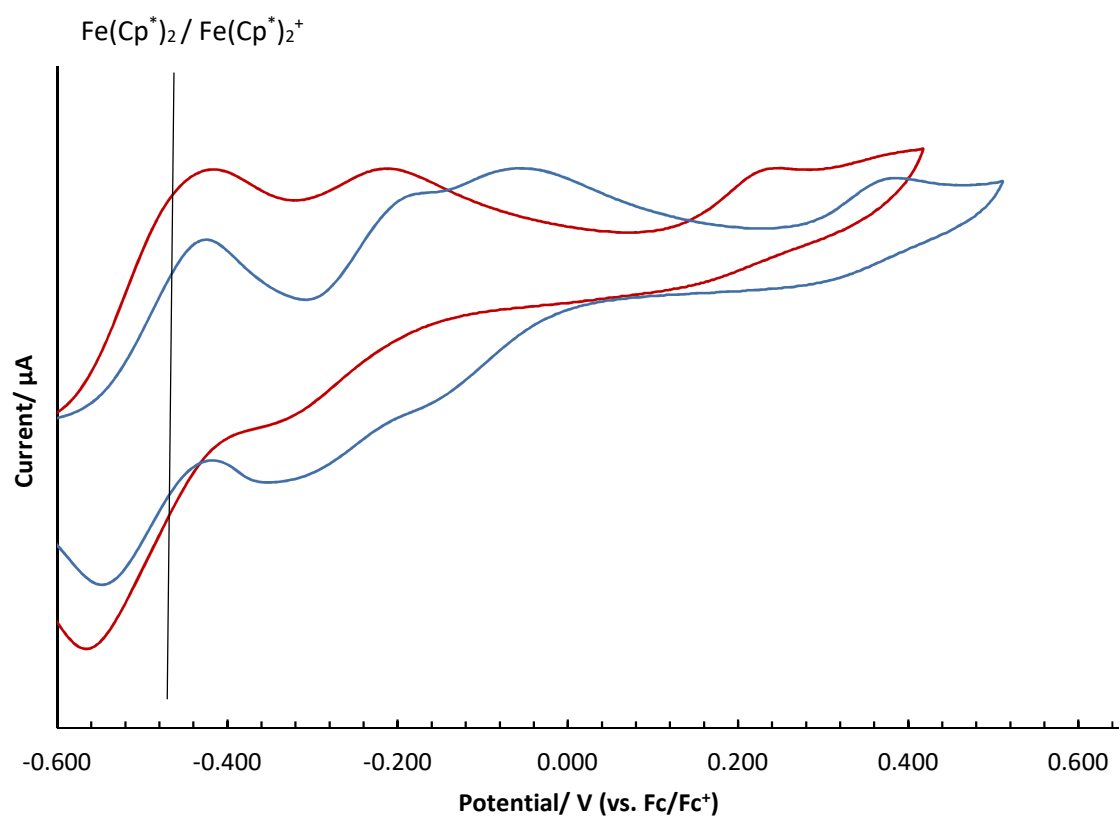


Figure 4.6. CV of $[\text{Mo}_2(\text{DAniF})_3(\text{SDOP})]_2$ dimer **[14]**₂ DCM (red) and monomer **[13]** after addition of 0.1 mL DMSO (red). Measurement taken in 0.1M TBAPF₆ electrolyte in 100 mVs⁻¹ scan rate.

Table 4.1. Cyclic voltammetry data for compounds **13** and **14** recorded in DCM 0.1 M TBAPF₆ at 100 mVs⁻¹ scan rate and with addition of 0.1 mL DMSO. Analyte concentration of 5 mM. Potentials referenced vs the Fc/Fc⁺ redox couple occurring at 0.00 V.

| Complex | $E_{1/2}(1) / \text{V}$ | $E_{1/2}(2) / \text{V}$ | $E_{1/2}(3) / \text{V}$ | $\Delta E_{1/2}(2)-(1) / \text{V}$ | K_c |
|---|-------------------------|-------------------------|-------------------------|------------------------------------|--------------------|
| $[\text{Mo}_2(\text{DAniF})_3(\text{DSOP})]_2$ [13] ₂ DCM | -0.270 | -0.055 | 0.142 | 270 | 3.69×10^4 |
| $[\text{Mo}_2(\text{DAniF})_3(\text{DSOP})]_2$ 13 DMSO | -0.277 | - | -0.025 | - | - |
| $[\text{Mo}_2(\text{DAniF})_3(\text{SDOP})]_2$ [14] ₂ DCM | -0.268 | -0.105 | ^a 0.283 | 163 | 571 |
| $[\text{Mo}_2(\text{DAniF})_3(\text{SDOP})]_2$ 14 DMSO | -0.265 | - | ^a 0.238 | - | - |

^a E_{pc} quoted due to irreversibility.

4.4.3 UV-Vis NIR SEC

4.4.3.1 UV-VIS NIR SEC of $\text{Mo}_2(\text{DAniF})_3(\text{HDSOP})$ (**13**) in DCM

The UV-Vis NIR SEC for complex **13** is shown in Figure 4.7. By contrast to the MLCT's observed for the $\text{Mo}_2(\text{TiPB})_3(\text{R}',\text{R}''\text{DOP})$ series the MLCT transition for the DSOP ligand is much lower in energy occurring at 16393 cm^{-1} (610 nm) in the neutral species (black) compared even to the most electron withdrawing analogue $\text{R}' = \text{Cl}$ $\text{R}'' = \text{H}$ occurring at 18083 cm^{-1} (553 nm). The HSDOP π^* LUMO therefore must be extremely low lying in energy. The weaker transition at 21978 cm^{-1} (455 nm) is likely an MLCT transition to the DAniF ligand trans to the HSDOP ligand.

Upon oxidation to the MV state (green) the HSDOP MLCT decreases rather significantly in intensity but retains some of the shouldered appearance of the neutral complex. In the doubly oxidised state it becomes a single peak, but contrary to the $\text{Mo}_2(\text{TiPB})_3(\text{R}',\text{R}''\text{DOP})$ series where all MLCT's became red shifted, it becomes slightly blue shifted appearing at 16528 cm^{-1} (605 nm).

A new transition appears in the 1^+ and 2^+ state at *ca.* 13500 cm^{-1} (740 nm) appearing as a shoulder to the HSDOP MLCT that was absent in the neutral state. This is assigned as a DSOP $\pi \rightarrow \text{Mo}_2 \delta^*$ LMCT as in the neutral state the $\text{Mo}_2 \delta$ is fully occupied so the transition is not possible, following each single electron oxidation an electron is removed from this orbital and the peak intensity increases.

Two isosbestic points are observed for both the HSDOP MLCT and LMCT transitions shown in Figures 4.8 and 4.9 respectively. The neutral $\rightarrow 1^+$ (black \rightarrow green) and $1^+ \rightarrow 2^+$ (green \rightarrow red) isosbestic points being separated by just 100 cm^{-1} in each case.

The $\text{Mo}_2 \delta \rightarrow \text{DAniF} \pi^*$ MLCT also undergoes changes upon oxidation. Upon oxidation to the MV state it increases in intensity but becomes slightly broader and is also slightly blue shifted. Upon oxidation to the doubly oxidised state, it becomes very broad as to appear effectively as a shoulder to the intense $\pi \rightarrow \pi^*$ transitions occurring below 28500 cm^{-1} (350 nm) and has no distinct peak maxima. Another set of very closely separated isosbestic points are observed for this transition as shown in Figure 4.10 being separated by *ca.* 180 cm^{-1} .

The most interesting transition however is observed in the very far NIR. We can see a very broad and very intense transition grows in as the complex is oxidised to both the MV state and then doubly oxidised state. We can confirm this is not an IVCT as it is present (and most intense) in the doubly oxidised state. Furthermore, from the peak shape it is evident that the peak centre will be observed in the IR region. This was confirmed this by performing the IR SEC which is discussed in section 4.2.4.

Upon reduction back to the neutral state (black dashed, Figure 4.7) the peak disappears. The MLCT features are similarly restored, the stability of the MV and doubly oxidised states and the reversibility of the processes at room temperature in the experimental set up is quite remarkable as Mo_2^{5+} normally decompose slowly at room temperature.

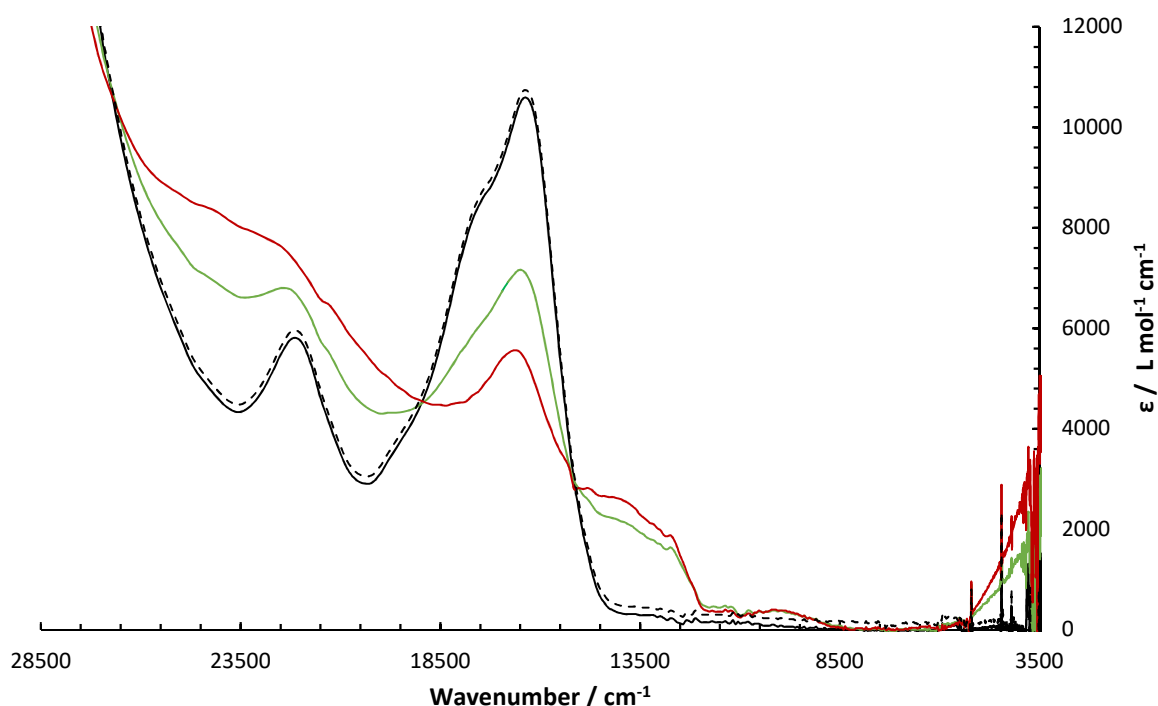


Figure 4.7. The UV-Vis NIR SEC of complex **13** in 0.1M TBAPF_6 electrolyte in DCM. Neutral $[\mathbf{13}]_2$ (black), $1^+ [\mathbf{13}]_2^+$ (green), $2^+ [\mathbf{13}]_2^{2+}$ (red) and neutral $[\mathbf{13}]_2$ reversed (black, dashed).

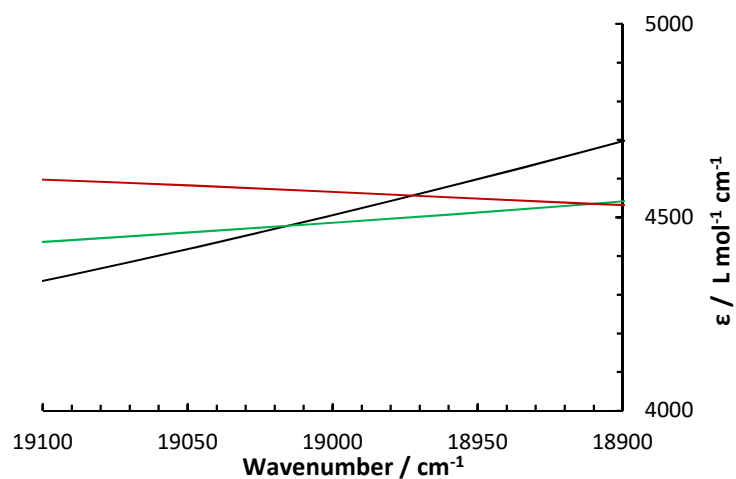


Figure 4.8. An expanded portion of the UV-Vis region highlighting the isosbestic points observed in the $\text{Mo}_2 \delta \rightarrow \text{DSOP } \pi^*$ MLCT transition (high energy end) in the UV-Vis NIR SEC of complex **13**.

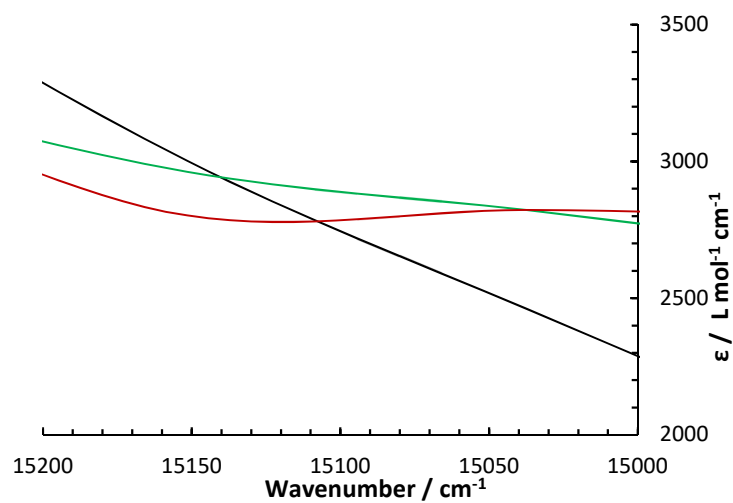


Figure 4.9. An expanded portion of the UV-Vis region highlighting the isosbestic points observed in the $\text{DSOP } \pi \rightarrow \text{Mo}_2 \delta$ LNCT transition (low energy end) in the UV-Vis NIR SEC of complex **13**.

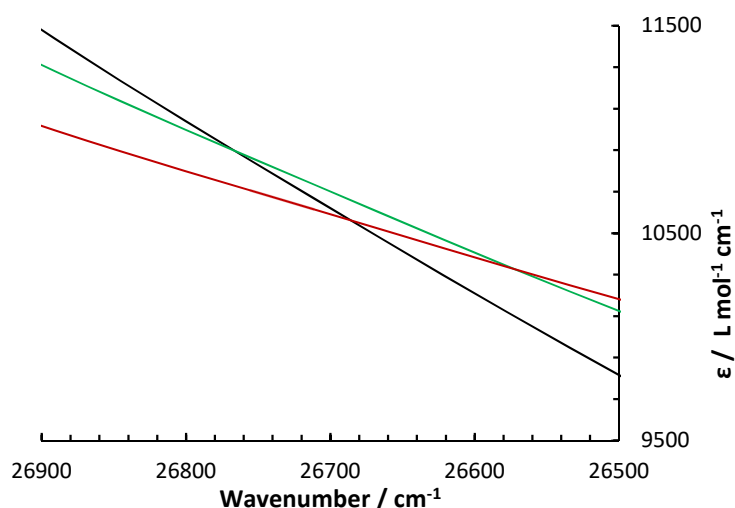


Figure 4.10. An expanded portion of the UV-Vis region highlighting the isosbestic points for the $\text{Mo}_2 \delta \rightarrow \text{DAniF } \pi^*$ MLCT transition in the UV-Vis NIR SEC of complex **13**.

Though the transition is not an IVCT, it could be for instance a DSOP ligand-based transition it still may be related to the generation of the MV state and thus be dependent on the formation of the hydrogen-bonded dimer. To explore this possibility the UV-Vis NIR SEC was performed in THF solvent to break apart the hydrogen bonded dimer.

4.4.3.2 UV-VIS NIR SEC of $\text{Mo}_2(\text{DAniF})_3(\text{HDSOP})$ (**13**) in THF

The UV-Vis NIR SEC for complex **13** in THF is shown in Figure 4.11. showing the oxidation of the neutral monomeric Mo_2^{4+} complex (black) to the mono-oxidised Mo_2^{5+} (green). Switching from DCM to THF the spectra of the neutral complex remains fairly consistent. The $\text{Mo}_2 \delta \rightarrow \text{DAniF } \pi^*$ MLCT is largely unchanged occurring at *ca.* 22220 cm^{-1} (450 nm) in both solvents. The $\text{Mo}_2 \delta \rightarrow \text{HDSOP } \pi^*$ MLCT that appears more as a single shouldered feature in DCM is now distinctly two peaks and is of equal intensity to the $\text{Mo}_2 \delta \rightarrow \text{DAniF } \pi^*$ MLCT where in DCM it was much more intense. Upon oxidation all of these transitions increase in intensity and there is a slight red shift in all cases of around 140 cm^{-1} . By contrast in DCM a fall intensity and blue shift of the $\text{Mo}_2 \delta \rightarrow \text{HDSOP } \pi^*$ MLCT was observed.

Upon oxidation to the 1⁺ state (green) a single isosbestic point is observed at *ca.* 15880 cm⁻¹ (630 nm). Below this energy where an LMCT transition was observed in the 1⁺ oxidation state in DCM, no such transition is observed in THF.

The stability/ reversibility of the oxidised complex in THF was very poor so is not shown. Oxidative decomposition leading to spectral bleaching was observed on prolonged measurements and the spectral response for the neutral complex was never restored when holding the cell at cathodic potentials. This is likely due to the coordinating nature of THF causes it to react with the Mo₂⁺ core resulting in decomposition. The instability of Mo₂⁵⁺ cations is well known, with only a few examples ever isolated.¹⁴

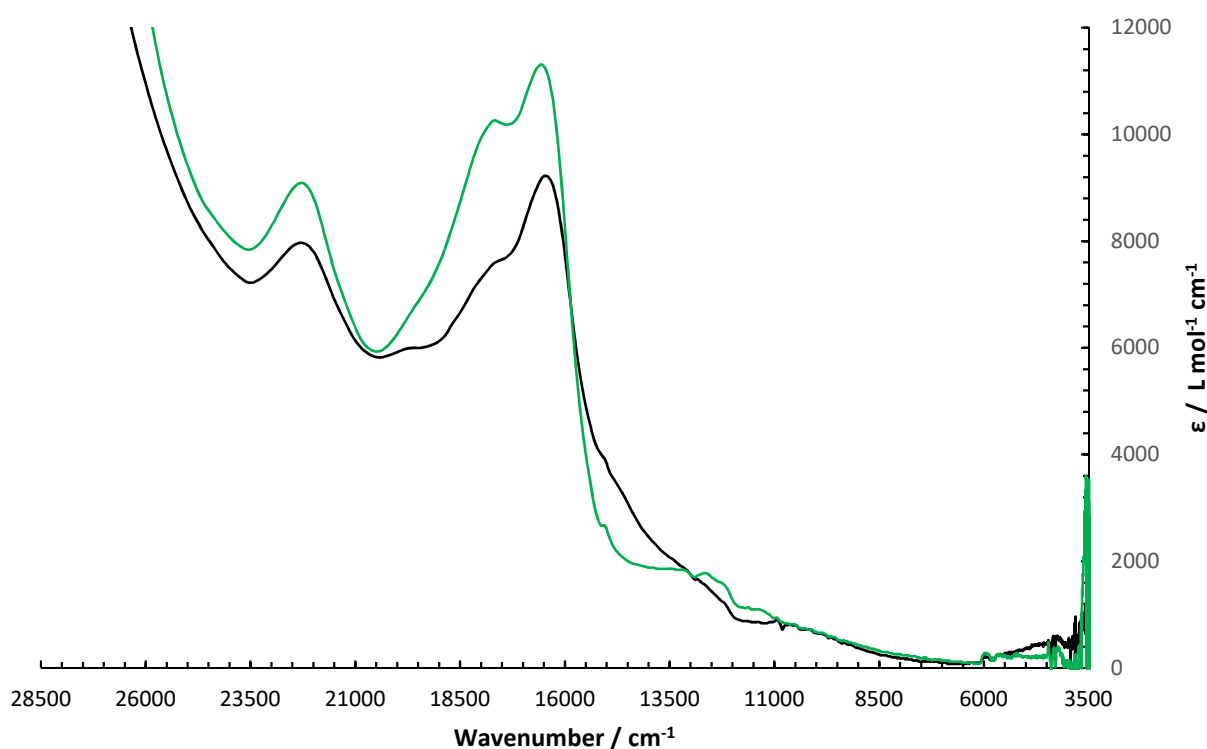


Figure 4.11. The UV-Vis NIR SEC of complex **13** in 0.1M TBAPF₆ electrolyte in THF. Neutral [**13**] (black) and 1⁺ [**13**]⁺ (green).

While the results in the different solvent are clearly distinct in this portion of the spectra the key difference lies in the NIR. The broad intense transition observed both in the MV and doubly oxidised state in DCM is absent here. What may appear as a peak is seen on the very borderline of the IR but

is certainly an artefact of the spectrometer. The appearance is completely different to that seen in DCM and is generally too sharp to be an electronic transition and spectral responses are typically noisy in this region.

4.4.3.3 UV-VIS NIR SEC of $\text{Mo}_2(\text{DAniF})_3(\text{HSDOP})$ (**14**) in DCM

The UV-Vis NIR SEC for complex **14** in DCM is shown in Figure 4.12. The appearance of the neutral complex is quite like that of **13** though the trans $\text{Mo}_2 \delta \rightarrow \text{DAniF}$ and $\text{HSDOP} \pi^*$ MLCT's are quite similar in intensity and less separated in energy by comparison appearing at 23530 cm^{-1} (425 nm) and 18018 cm^{-1} (555 nm) respectively.

In the MV (green) and doubly oxidised state (red) the SDOP MLCT falls in intensity and loses its distinct peak shape and appears more as a shoulder to the $\text{Mo}_2 \delta \rightarrow \text{DAniF} \pi^*$ MLCT. The DAniF MLCT by contrast becomes much more intense and is red shifted.

An $\text{HSDOP} \pi \rightarrow \text{Mo}_2 \delta^*$ LMCT is again observed in the 1^+ and 2^+ state. It is less pronounced than the analogous transition in complex **13** having a much more shouldered appearance but appears in a similar region *ca.* 14000 cm^{-1} (714 nm).

Two sets of isosbestic points are observed for the $\text{Mo}_2 \delta \rightarrow \text{SDOP} \pi^*$ MLCT and the $\text{HSDOP} \pi \rightarrow \text{Mo}_2 \delta^*$ LMCT as shown in Figures 4.13 and 4.14 respectively. The isosbestic points for the neutral $\rightarrow 1^+$ transition (black \rightarrow green) and in the $1^+ \rightarrow 2^+$ (green \rightarrow red) are separated by 340 cm^{-1} .

The reversibility of the oxidations in the SEC experiment is very good again, the structure and peak intensity of the MLCT transitions is almost entirely restored. Some of the LMCT character appears to be retained but as there is a net intensity absorbance across all the transitions it is likely more due to oxidative decomposition causing bleaching of the entire spectral response.

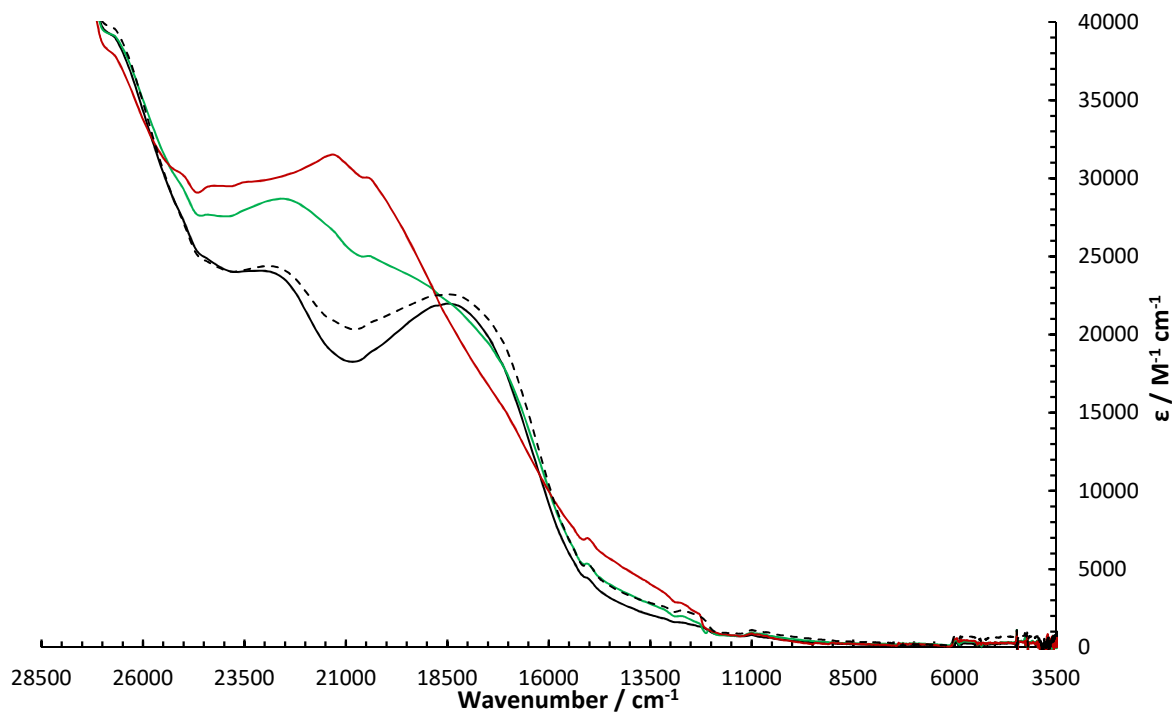


Figure 4.12. The UV-Vis NIR SEC of complex **14** in 0.1M TBAPF₆ electrolyte in DCM. Neutral [14]₂ (black), 1⁺ [14]₂⁺ (green), 2⁺ [14]₂²⁺ (red) and neutral [14]₂ reversed (black, dashed).

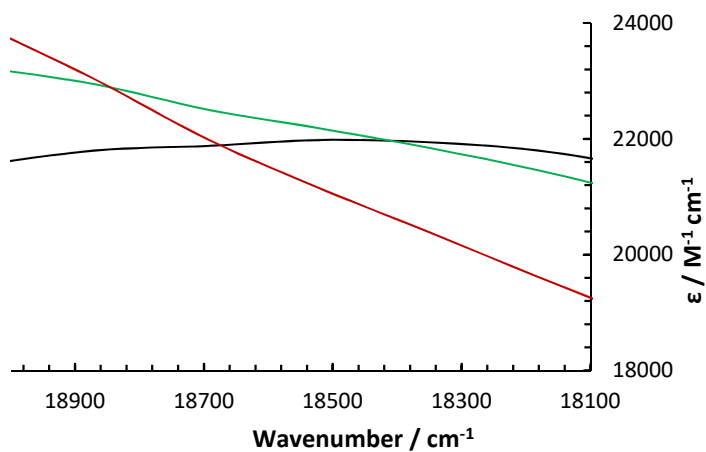


Figure 4.13. An expanded portion of the UV-Vis region highlighting the isosbestic points for the Mo2 $\delta \rightarrow$ SDOP π^* MLCT transition (high energy end) in the UV-Vis NIR SEC of complex **14**.

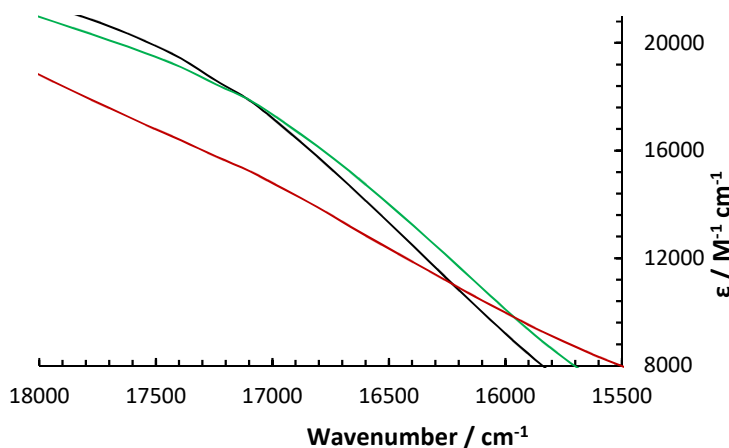


Figure 4.14. An expanded portion of the UV-Vis region highlighting the isosbestic points for the $\text{Mo}_2 \delta \rightarrow \text{SDOP } \pi^*$ MLCT transition (low energy end) in the UV-Vis NIR SEC of complex **14**.

4.4.3.4 UV-VIS NIR SEC of $\text{Mo}_2(\text{DAniF})_3(\text{HSDOP})$ (**14**) in THF

The UV-Vis NIR of complex **14** in THF is shown in Figure 4.15. The neutral spectrum (black) is largely unchanged. Both the $\text{Mo}_2 \delta \rightarrow \text{DAniF } \pi^*$ MLCT and $\text{Mo}_2 \delta \rightarrow \text{HSDOP } \pi^*$ MLCT are slightly blue shifted but the ratio of their intensities is unchanged where in **13** the latter became less intense when switching from DCM to THF. Upon oxidation (green) a single isosbestic point at the low energy end of the $\text{DSOP } \pi^*$ MLCT is observed at *ca.* 15050 cm^{-1} (664 nm) but there is no LMCT transition observed as in DCM.

Both the $\text{Mo}_2 \delta \rightarrow \text{DAniF } \pi^*$ and MLCT and $\text{Mo}_2 \delta \rightarrow \text{HSDOP } \pi^*$ MLCT increase in intensity and are further blue shifted upon oxidation to the 1^+ state. In the case of the $\text{Mo}_2 \delta \rightarrow \text{DAniF } \pi^*$ MLCT this is consistent with the transition from the neutral $\rightarrow 1^+$ spectral response in DCM but the $\text{Mo}_2 \delta \rightarrow \text{DAniF } \pi^*$ MLCT became so broad as to be effectively a shoulder to the higher energy transition.

The key feature is that the NIR transition present in **13** in DCM but absent in **14** in DCM is not observed for either complex in THF. This gives weight to the argument this transition is in some way dependent upon the formation of the dimer and while observed upon the formation of the MV state is not an IVCT because it persists and is most intense into the doubly oxidised state in **13**. The exact difference between the two complexes and the origin of transition is still unclear but could be related to the large

increase in K_c observed in **13**, 3.69×10^4 vs. 571 in **14**. DFT calculations are currently being performed in an attempt to explain the origin of this transition.

The stability/ reversibility of the oxidised state and reversibility in THF was again very poor in contrast to the behaviour in DCM (Figure 4.12) so is not shown.

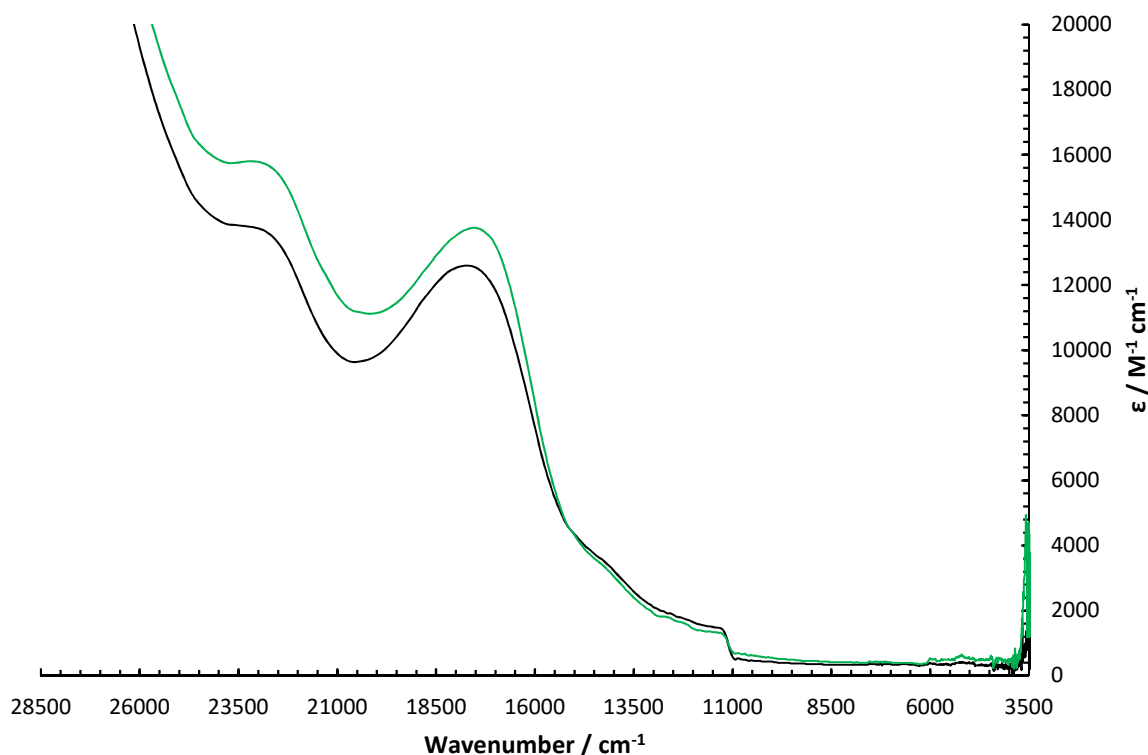


Figure 4.15. The UV-Vis NIR SEC of complex **13** in 0.1M TBAPF₆ electrolyte in THF. Neutral [**13**] (black) and 1+ [**13**]⁺ (green).

4.4.4 IR SEC

The IR SEC of complex **9**, Mo₂(TiPB)₃(H,H'DOP) has been previously reported by our group and is reproduced here in Figure 4.16 for ease of comparison. A single peak is observed for the lactam C=O stretch in both the neutral state at 1647 cm⁻¹ and doubly oxidised state at 1659 cm⁻¹. The shift to a higher wavenumber is due to reduced Mo₂ δ → DOP π* MLCT back bonding upon oxidation. The MV state is composite of both individual peaks occurring at 1646 and 1654 cm⁻¹. Because spectral coalescence is not observed the electron transfer rare is slower than the IR timescale (< 10⁻¹⁰ s) in this complex.¹⁵⁻¹⁷ A second HDOP resonance at approximately 1575 cm⁻¹ displays identical behaviour. The

peak at approximately 1600 cm^{-1} is attributed to a ring breathing resonance consistent with that observed in the oxidation of the $\text{Mo}_2(\text{TiPB})_4$ precursor.

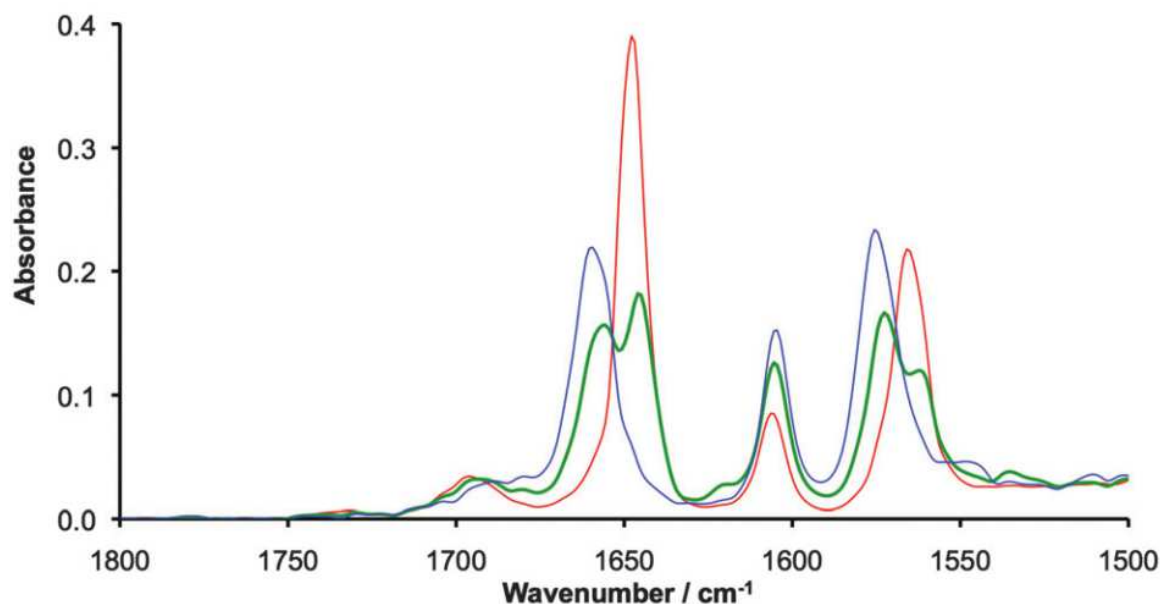


Figure 4.16. A portion of the IR SEC of complex $[\mathbf{8}]_2$ red, $[\mathbf{8}]_2^+$ green and $[\mathbf{8}]_2^{2+}$ blue showing the lactam C=O stretches of the DOP ligand and ring expansion resonances of the TiPB ligands. Reproduced from reference with permission of the RSC.¹

4.4.4.1 IR SEC of $\text{Mo}_2(\text{DAniF})_3(\text{DSOP})$ (**13**) in DCM

The IR SEC of complex $[\mathbf{13}]_2$ in DCM is shown in Figure 4.17. The intense IR transition of which tails into the NIR as seen in the UV-VIS NIR SEC (Figure 4.7) has a peak maximum at 3300 cm^{-1} and grows in intensity as it is oxidised through the MV and into the doubly oxidised state. This confirms that it is not an IVCT transition as this transition would only be observed in the mixed valence state. The peaks between 2800 and 2900 cm^{-1} remain largely unchanged, as they are due to the DAniF OMe and NH stretches. A portion of the spectra ($1200 - 1280\text{ cm}^{-1}$) has been omitted as it contained a THF solvent absorbance.

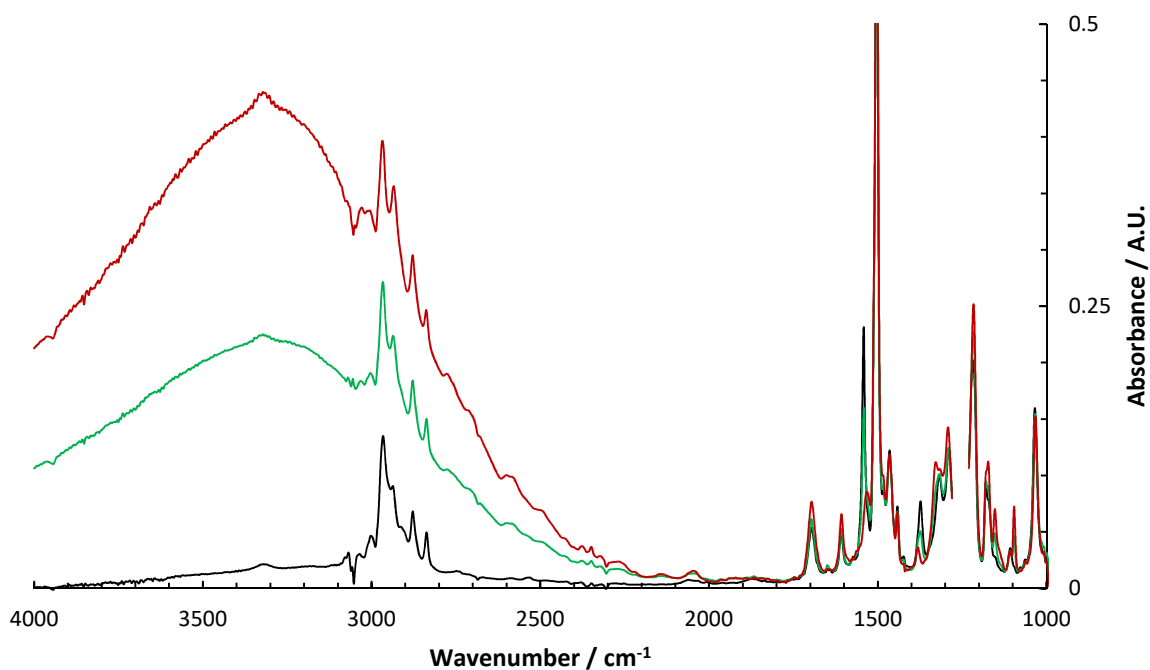


Figure 4.17. IR SEC of complex **13** in 0.1M TBAPF₆ electrolyte in DCM. Neutral (black), 1⁺ (green) and 2⁺ (red).

An expansion of the spectra highlighting the C=S stretches equivalent to those seen in complex **9** (Figure 4.16) is shown in Figure 4.18. Two sets of related resonances are observed at *ca.* 1540 cm⁻¹ and 1380 cm⁻¹. In both cases the peaks shift several wavenumbers from the neutral complex to the doubly oxidised state but while the former shifts to a lower wavenumber the latter shifts to a higher. As a result, it is impossible to relate this to the extent of metal to ligand back bonding as in complex **9**. In both cases the neutral complex displays a sharp peak while the doubly oxidised complex has a broader, less intense peak. Because of the very different peaks shapes determining whether coalescence occurs in the MV state is less clear-cut than in complex **8**. The peak at 1380 cm⁻¹ seems most indicative to this effect and appears to be two poorly resolved peaks not coalesced. The spectral response at 1100cm⁻¹ further supports this.

Two ring breathing resonances growing in from the neutral to doubly oxidised state are observed for the DAniF phenyl rings owing to the two ligands environments occurring at around 1700 (cis) and 1605 cm⁻¹ (trans).

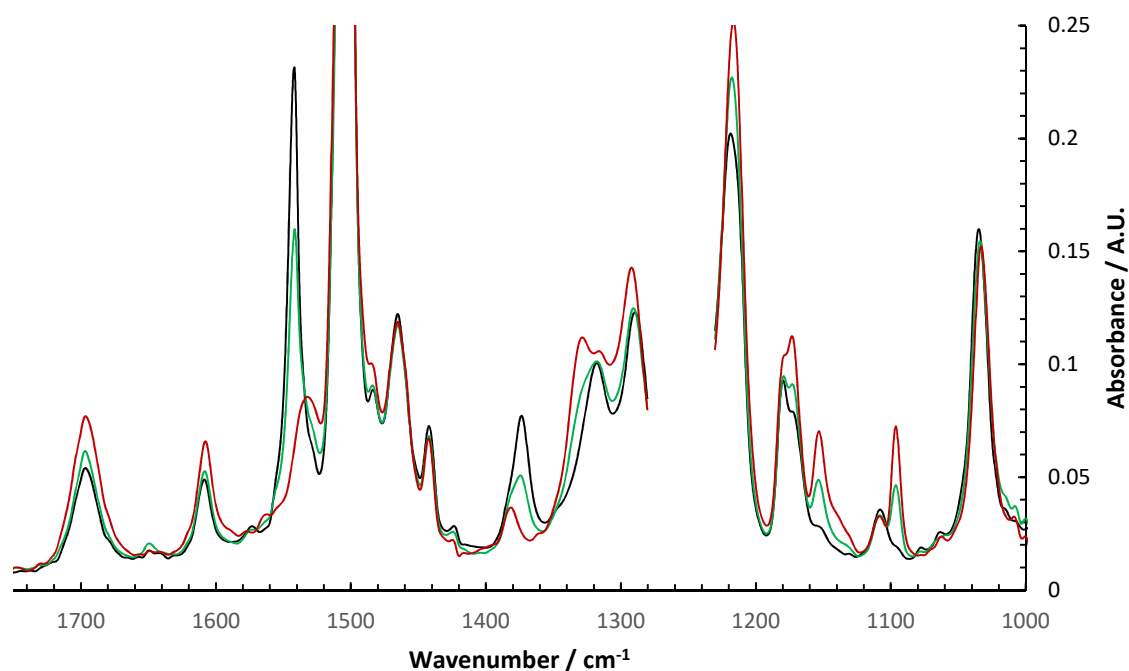


Figure 4.18. An expansion of the IR SEC showing the C=S stretches of the DSOP ligand and ring expansion resonances of the DAniF ligands.

4.4.4.2 IR SEC of $\text{Mo}_2(\text{DAniF})_3(\text{SDOP})$ (**14**) in DCM

The IR SEC of complex [**14**]₂ in DCM is shown in Figure 4.19. The intense IR transition in complex **13** that extended into the NIR that was absent in NIR of complex **13** is indeed absent in the IR. An additional portion of the spectra (2750 – 3300 cm⁻¹) has been omitted due to a physical fault with the apparatus causing the THF solvent to strongly absorb here. Based on the DFT calculations no transitions are anticipated in this region for complex **14** and based on the spectral response of **13** any peaks that would be present would likely be unaltered upon oxidation.

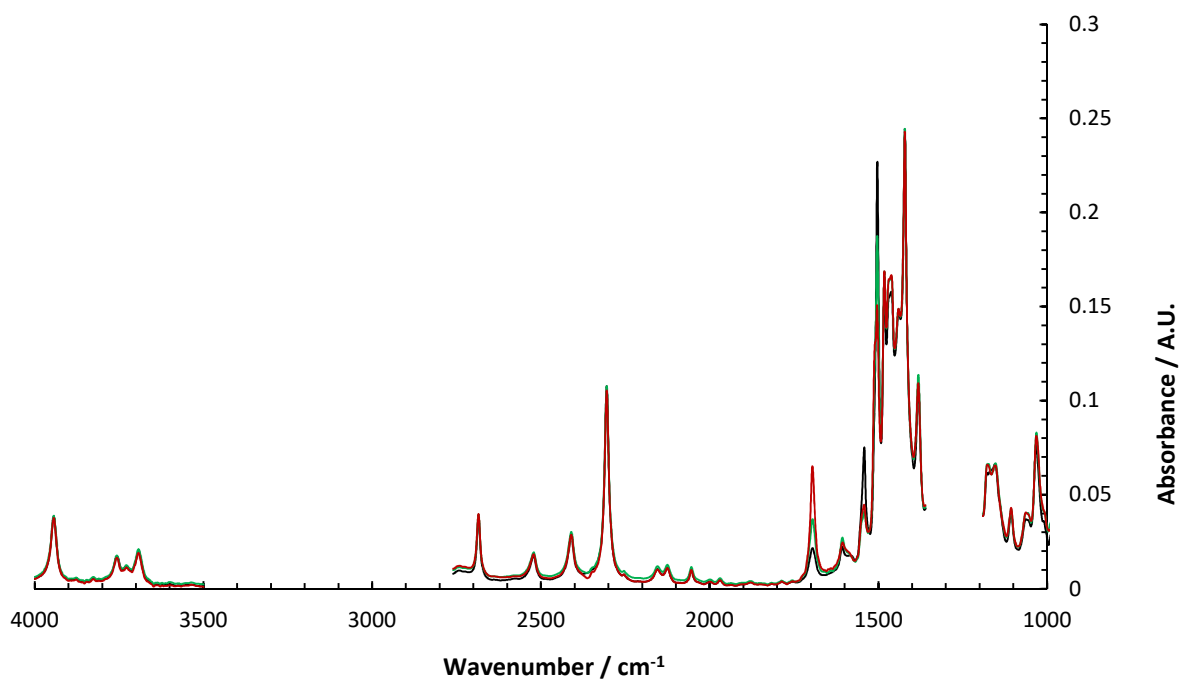


Figure 4.19. IR SEC of complex **14** in 0.1M TBAPF₆ electrolyte in DCM. Neutral (black), 1⁺ (green) and 2⁺ (red).

The C=S stretches of the SDOP ligand are highlighted in an expansion of the spectra shown in Figure 4.20. The two resonances of interest occur around 1510 and 1545 cm⁻¹. In both cases oxidation from the neutral to doubly oxidised state produces a shift to a higher wavenumber indicative of reduced metal to ligand back bonding. In the doubly oxidised state both resonances are observed as a shouldered double peak. In the MV state the resonance at 1510 cm⁻¹ is a single peak but with an obvious shoulder feature at 1545 cm⁻¹ is very similar in appearance to the doubly reduced state but broader. No coalescence is observed so in both complexes hence ET is slower than the IR timescale.

Two sets of ring breathing are again observed occurring at identical positions to complex **13**, 1700 (cis) and 1605 cm⁻¹ (trans). Though a slight discrepancy in the latter is that a fall in intensity is observed on oxidation from the neutral to doubly oxidised state where in **9** and **13** a stepwise increase was observed in the sequential oxidations.

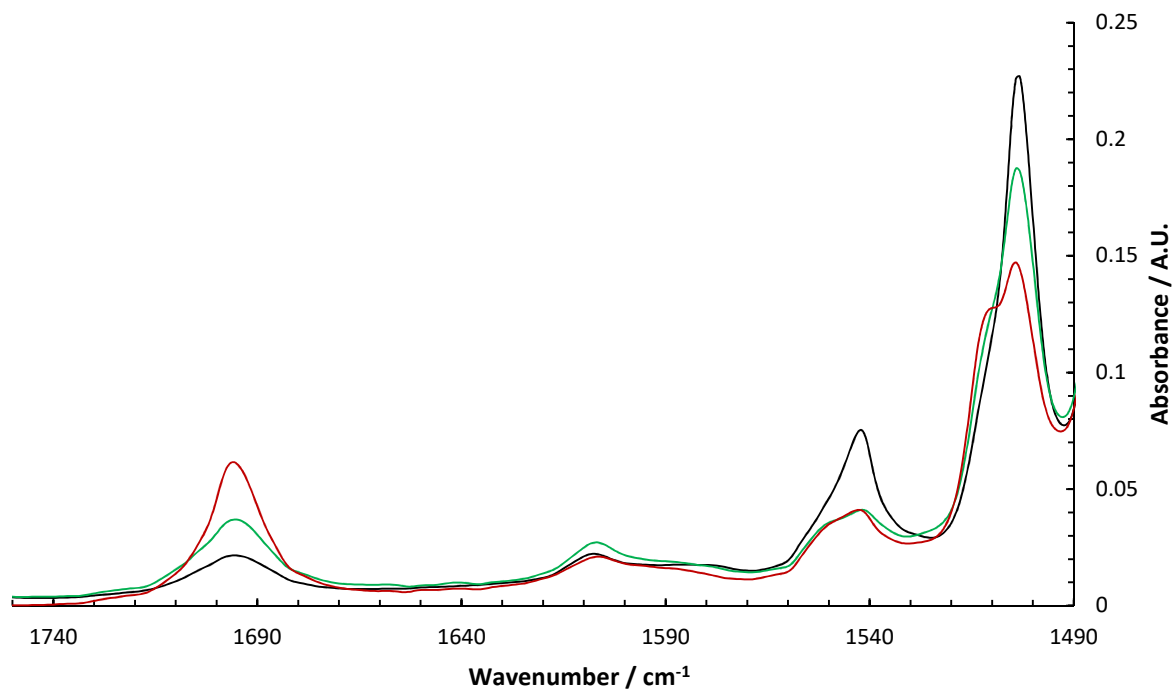


Figure 4.20. An expansion of the IR SEC showing the C=S stretches of the SDOP ligand and ring expansion resonances of the DAniF ligands.

4.5 Conclusions

By substitution of the labile acetate ligand in $\text{Mo}_2(\text{DAniF})_3(\text{OAc})$ two new complexes $\text{Mo}_2(\text{DAniF})_3(\text{DSOP})$ (**13**) and $\text{Mo}_2(\text{DAniF})_3(\text{SDOP})$ (**14**) have been generated. The CV data in DCM suggests that the dimer structures $[\mathbf{13}]_2$ and $[\mathbf{14}]_2$ are formed through self-complementary hydrogen bonds and a stable MV state can be generated upon oxidation. On addition of DMSO the hydrogen-bond is disrupted and no MV state is generated.

K_c values of 3.69×10^4 and 571 were determined for $[\mathbf{13}]_2^+$ and $[\mathbf{14}]_2^+$ respectively meaning the MV state in both these complexes is therefore more thermodynamically stable than that of the unsubstituted DOP complex $[\text{Mo}_2(\text{TiPB})_3(\text{R}'\text{-H}, \text{R}''\text{-HDOP})]_2^+$ [**9**] $_2^+$. In the case of **13** K_c is actually comparable to strongly coupled covalent Mo_2 dimers in the literature^{18,19} and is indicative of very good charge transfer between the two Mo_2 cores.

In both complexes **13** and **14** the $\text{Mo}_2 \delta \rightarrow \text{HL} \pi^*$ MLCT's show two isosbestic points for the neutral $\rightarrow 1^+$ and $1^+ \rightarrow 2^+$ transition consistent with the PCMV mechanism. In complex **13** a unique IR centred

transition that extends in to the NIR is observed in DCM. Because it is present and most intense in the 2⁺ oxidation state it is not an IVCT.

When the SEC experiment is repeated in THF this transition is also not observed meaning it is in some way related to formation of the hydrogen bonded dimer and the MV state. Complex **14** does not display such a transition.

The exact origin of the transition is not understood. Preliminary DFT studies are underway in attempt explain the nature of this transition and the differences between the two complexes. While the current model generally shows good agreement with the ground state UV-Vis NIR and IR spectra it does not account for the unique IR centred transition in complex **13** upon oxidation. The substituent of the formamidinate ligands appears to have a large impact on the energy of electronic transitions observed in the UV-Vis NIR region, particularly the low energy LMCT transition. As such full modelling of the *p*-OMe groups is required, these calculations are computationally demanding and still underway.

4.6 Experimental

4.6.1 Materials and Physical Methods

Materials and physical methods were as described previously in 2.4.1. Mo₂(DAniF)₃(OAc) is synthesised as reported in the literature without modification.⁸

4.6.2 *Synthesis of N,N'*-bis(4-methoxyphenyl)formimidamide

Modified from existing literature precedent.²⁰ *p*-anisidine (9.50 g, 77 mmol) and triethyl orthoformate (7.68 mL, 77 mmol) were added to a round bottom flask and refluxed for 2 hours. The ethanol formed was then removed by distillation. A brown solid was obtained on cooling and recrystallized from toluene : ethyl acetate (90:10 v/v) to obtain grey-blue crystals (6.98 g, 70 %). ¹H NMR (400 MHz) CDCl₃: δ_H 8.04 (s, 1H, N=CH-N) 6.97 (d, 4H, J_H = 8.5Hz, *o* Ar-H) 6.86 (d, 4H, J_H = 8.5Hz, *m* Ar-H) 3.8 (s, 6H, *p*-OCH₃). FTIR diamond tip: $\bar{\nu}$ (cm⁻¹) 3364 (med, broad) 2723 (med, broad) 1626 (med) 1501 (str)

1452 (med, shoulder) 1435 (med, shoulder) 1397 (weak, shoulder) 1320, 1308 (str, split) 1284 (med, shoulder) 1104 (med) 1010 (str).

4.6.3 Synthesis of $\text{Mo}_2(\text{DAniF})_3(\text{HDSOP})$ (**13**)

A Schlenk flask was charged with $\text{Mo}_2(\text{DAniF})_3(\text{OAc})$ (254 mg, 0.25 mmol) and 1,4-dihydropyrazine-2,3-dithione (H_2DSOP) (36 mg, 0.25 mmol) and THF (12 mL) added. Addition of NEt_3 (34.8 μL , 0.25 mmol) caused a slight colour change of the solution to green but a red precipitate persists. The reaction was then allowed to continue stirring for 48 hours. The resulting dark blue solution was reduced to dryness *in vacuo* and the products extracted in to 50:50 DCM/ hexanes (v/v) (2 mL) and purified by silica column chromatography (eluent: hexanes \rightarrow dichloromethane \rightarrow dichloromethane/THF (90:10 (v/v)) collecting the first of two close-running blue bands to afford **13** (113 mg, 42%) as a turquoise solid. ^1H NMR (400 MHz, CD_2Cl_2) δ 8.48 (s, 2H), 8.45 (s, 1H), 8.41 (s, 1H), 6.68 (s, 4H, $J = 8.26$ Hz), 6.61 (d, 6H, $J = 7.61$ Hz), 6.56 (d, 6H, $J = 7.61$ Hz), 6.35 (d, 4H, $J = 7.61$ Hz), 6.27 (m, 2H, $J = 7.61$ Hz), 6.43–6.45 (m, 2H), 6.24 (d, 4H, $J = 8.8$ Hz), 6.08 - 6.12 (m, 1H), 6.06 - 6.09 (m, 1H), 3.80 (s, 3H), 3.70 - 3.74 (m, 12 H), 3.68 (s, 3H). IR DCM: $\bar{\nu}$ (cm^{-1}) 2969 (med), 2938 (weak, shoulder), 2880 (weak), 2837 (weak), 1698 (med), 1607 (med), 1541 (strong), 1504 (v. strong), 1466 (med), 1444 (med), 1374 (med) 1320 (med), 1296 (med), 1249 (strong), 1221 (strong), 1181 (med), 1868 (med, shoulder), 1109 (weak), 1034 (med).

4.6.4 Synthesis of $\text{Mo}_2(\text{DAniF})_3(\text{HSDOP})$ (**14**)

A Schlenk flask was charged with with $\text{Mo}_2(\text{DAniF})_3(\text{OAc})$ (254 mg, 0.25 mmol) and 1,2-dihydropyridazine-3,6-dithione (H_2SDOP) (36 mg, 0.25 mmol) and THF (12 mL) added. Addition of NEt_3 (34.8 μL , 0.25 mmol) caused a rapid colour change to blue. The reaction was then allowed to continue stirring for 48 hours. The resulting purple solution was reduced to dryness *in vacuo* and the products extracted in to 50:50 DCM/ hexanes (v/v) (2 mL) and purified by silica column chromatography (eluent: hexanes \rightarrow dichloromethane \rightarrow dichloromethane/THF (90:10 (v/v)) collecting the purple band to afford **14** (154 mg, 56 %) as a dark purple solid. ^1H NMR (400 MHz, CD_2Cl_2) δ 8.41 (s, 1H), 8.39 (s, 2H), 8.41 (s, 1H), 6.71 (s, 4H), 6.65 (d, 6H, $J = 7.5$ Hz), 6.55 (d, 6H, $J = 7.5$ Hz), 6.36 (d, 4H, $J = 8.0$ Hz), 6.28

(d, 2H, $J = 8.0$), 6.43–6.45 (m, 2H), 6.24 (d, 4H, $J = 8.0$ Hz), 6.08 - 6.12 (m, 1H), 6.06 - 6.09 (m, 1H), 5.98 (d, 2H, $J = 8.6$ Hz), 3.75 (s, 9H), 3.70 (s, 6H), 3.60 (s, 3H). IR DCM: $\bar{\nu}$ (cm^{-1}) 3943 (med), 3755 (weak), 3587 (weak), 2684 (weak), 2520 (weak), 2409 (weak), 2305 (strong), 2154 (weak), 2125 (weak), 1683 (weak), 1542 (med) 1504 (strong), 1482 (strong), 1249 (strong), 1457 (strong, shoulder), 1422 (strong), 1380 (med), 1176 (med, shoulder), 1154 (med), 1106 (weak), 1033 (med).

4.7 References

- (1) Wilkinson, L. A.; Vincent, K. B.; Meijer, A. J. H. M.; Patmore, N. J. *Chem. Commun.* **2016**, 52, 100.
- (2) Wilkinson, L. A.; McNeill, L.; Scattergood, P. A.; Patmore, N. J. *Inorg. Chem.* **2013**, 52, 9683.
- (3) Wilkinson, L. A.; McNeill, L.; Meijer, A. J. H. M.; Patmore, N. J. *J. Am. Chem. Soc.* **2013**, 135, 1723
- (4) Yang Wu, Y.; Meng, M.; Yi Wang, G.; Feng, P.; Liu, C. Y. *Chem. Commun* **2017**, 3030 .
- (5) Shu, Y.; Lei, H.; Tan, Y. N.; Meng, M.; Zhang, X. C.; Liu, C. Y. *Dalton. Trans.* **2014**, 43 (39), 14756.
- (6) Han, M. J.; Llu, C. Y.; Tian, P. F. *Inorg. Chem.* **2009**, 48, 6347–6349.
- (7) Xiao, X.; Liu, C. Y.; He, Q.; Han, M. J.; Meng, M.; Lei, H.; Lu, X. *Inorg. Chem.* **2013**, 52, 12624.
- (8) Cotton, F. A.; Liu, C. Y.; Murillo, C. a; Villagrán, D.; Wang, X. *J. Am. Chem. Soc.* **2003**, 125 , 13564.
- (9) Cotton, F. A.; Jin, J.-Y.; Li, Z.; Liu, C. Y.; Murillo, C. A. *Dalton Trans.* **2007**, 22, 2328.
- (10) Han, L. J.; Fan, L. Y.; Meng, M.; Wang, X.; Liu, C. Y. *Dalt. Trans.* **2011**, 40, 12832.
- (11) Cotton, F. A.; Li, Z.; Liu, C. Y.; Murillo, C. a.; Villagrán, D. *Inorg. Chem.* **2006**, 45, 767.
- (12) Cayton, R. H.; Chisholm, M. H.; Huffman, J. C.; Lobkovsky, E. B. *J. Am. Chem. Soc.* **1991**, 113, 8709.
- (13) Chisholm, M. H.; Lear, B. J.; Moscatelli, A.; Peteanu, L. A. *Inorg. Chem.* **2010**, 49, 3706.
- (14) Cotton, F. A.; Daniels, L. M.; Hillard, E. A.; Murillo, C. A. *Inorg. Chem.* **2002**, 41, 1639.
- (15) Londergan, C. H.; Kubiak, C. P. *Chem. Eur. J.* **2003**, 9, 5962.

- (16) Kubiak, C.P.; Porter, T. M.; Heim, G. P. *Chem. Sci.* 2017, **8**, 7324
- (17) Ito, T.; Hamaguchi, T.; Nagino, H.; Yamaguchi, T.; Kido, H.; Zavarine, I. S.; Richmond, T.; Washington, J.; Kubiak, C. P. *J. Am. Chem. Soc.* **1999**, *121*, 4625
- (18) Cayton, R. H.; Chisholm, M. H.; Huffman, J. C.; Lobkovsky, E. B. *J. Am. Chem. Soc.* **1991**, *113*, 8709.
- (19) Chisholm, M. H.; Patmore, N. J.; Reed, C. R.; Singh, N. *Inorg. Chem.* **2010**, *49*, 7116.
- (20) Mohamed, A. A.; Abdou, H. E.; Irwin, M. D.; López-de-luzuriaga, J. M.; Fackler, J. P. *J. Clust. Sci* **2003**, *14*, 253.

Chapter 5. Part 1 Conclusion

5.1 Summary

Electron transfer is ubiquitous in the chemical sciences and biology. The process is not only fundamental to life in processes such as photosynthesis¹ but its study is essential to the development of future energy technologies one of the most important challenges facing modern society.² Mixed valence compounds are valuable models that can allow many fundamental properties of ET to be measured and give insight into these much more complex systems.

We have previously reported “dimer of dimers” complexes $[\text{Mo}_2(\text{TiPB})_3(\text{HDOP})]_2$ and $[\text{Mo}_2(\text{TiPB})_3(\text{HDON})]_2$ that are formed through self-complimentary hydrogen bonds in the pendant lactam functionalities in DCM.³⁻⁵ Stabilisation of the mixed valence state is observed in CV. The absence of an IVCT in the UV-Vis NIR necessitates a mechanism of stabilisation distinct from those previously reported in the literature that are simply due to proton or electron transfer. Stabilisation in these systems is dependent on the proton coordinate in the hydrogen bond but total PT does not occur. This mechanism is dubbed Proton Couple Mixed Valency and is described as a “dipole induced ET self-exchange reaction.”³

Many fundamental questions still remain surrounding the PCMV mechanism such as ET transfer rates and in an effort to further the understanding of this mechanism, new model complexes were sought.

In Chapter 2 a series of new precursor complexes of the form $\text{Mo}_2(\text{DTolF})_{4-n}(\text{OAc})_n$ ($n = 1, 2$ *cis*- and *trans*-3), where DTolF = N,N'-di-p-tolylformamidinate (complexes **3** – **6**) were synthesised. These complexes were characterisation through X-ray crystallography, cyclic voltammetry and ¹H NMR and UV-Vis spectroscopy.

The DTolF ligand is a rigid non-labile spectator ligand that makes these complexes attractive building blocks in forming higher assemblies. Through substitution of the labile acetate ligand for ligands capable of self-complimentary hydrogen bonding, synthesis of new “dimer of dimers”, oligomeric molecular shapes and molecular wires were targeted. While unsuccessful a host of bridging ligands

and reaction conditions were screened, and the synthetic insights gained were used to inform later work.

In Chapter 3 electron-donating and electron-withdrawing groups were introduced into the bridging ligand of the $[\text{Mo}_2(\text{TiPB})_3(\text{HDOP})]_2$ (**9**)₂ complex to probe the affect this would impact on stabilisation of the mixed valence state. The series of complexes $\text{Mo}_2(\text{TiPB})_3(3\text{-R}',4\text{-R}''\text{-HDOP})$ where $\text{R}', \text{R}'' = \text{H, Cl}$ (**7**), H, Br (**8**), H, Me (**10**) and Me, Me (**11**) and also the fused ring system $\text{Mo}_2(\text{TiPB})_3(\text{HPhth})$ (**12**), where HPhth = phthalhydrazide were synthesised. The stability of the mixed valence state was probed using cyclic voltammetry. K_c values could be determined for complexes **8 – 10** and were seen to increase across the series from 99 to 1341 as the DOP ligand was substituted with a more electron-donating substituent. Complex **7** did not appear to produce a thermodynamically stable MV state. The redox processes in **11** and **12** were irreversible so K_c could not be determined but increasing $\Delta E_{1/2}$ values was still suggestive of increasing stability with increasing electron donating substituents.

The increase in thermodynamic stability is rationalised by the ligand π -donor properties. As the DOP ligand becomes more electron rich it donates more readily to the Mo_2 core. Upon oxidation to generate the MV state the oxidised half of the molecule can be viewed as a singly occupied $\text{Mo}_2 \delta$ so more readily accepts electron density and is thus more impacted by the electronic change in the ligand. This observation could be vital to the implementation of these systems into materials with tuneable charge transfer properties.

The UV-NIR SEC of complexes **8 – 11** all showed two isosbestic points for the $\text{Mo}_2 \delta \rightarrow \text{DOP } \pi^*$ MLCT, one each for the neutral $\rightarrow 1^+$ and $1^+ \rightarrow 2^+$ oxidations. This is consistent with the PCMV mechanism as upon oxidation of one half of the dimer to generate the MV state, the pK_a change reduces $\text{Mo}_2 \delta \rightarrow \text{DOP } \pi^*$ back bonding.³ In complex **12** an isosbestic point was not observed for the $1^+ \rightarrow 2^+$ oxidation and can only be reasoned to be due to the irreversibility of the oxidations and decomposition.

In Chapter 4 two further analogous “dimer of dimers” complexes were synthesized. The novel complexes $\text{Mo}_2(\text{DAniF})_3(\text{HDSOP})$ (**13**) ($\text{H}_2\text{DSOP} = 1,2\text{-dihydropyridazine-3,6-dithione}$) and

Mo₂(DAniF)₃(HSDOP) (**14**) (H₂SDOP = 1,4-dihydropyrazine-2,3-dithione). K_c values of 6.9×10^4 and 571 were determined from the CV. K_c Both are indicative of a thermodynamically stable MV state with good charge transfer properties and in complex **13** is comparable with strongly electronically coupled covalent dimers of Mo₂.

The UV-Vis NIR of these complexes was consistent with criteria of the PCMV mechanism but in complex **13** a unique IR centred transition that extended into the NIR region was observed for the MV and doubly oxidised states; [**13**]₂⁺ and [**13**]₂²⁺. Because it is present and most intense in the doubly oxidised state it is not an IVCT transition. The same transition was not observed for [**14**]₂⁺ or [**14**]₂²⁺. DFT was employed in an attempt to explain the exact nature of this transition and the specific differences between the two complexes but preliminary results are inconclusive. The DFT calculations otherwise well supported the ground state UV-Vis and IR spectra.

The complexes described in Chapter 3 and 4 are valuable, rare models for investigating the PCMV mechanism. The synthetic insights gained throughout will be vital in producing further complexes that will allow the remaining questions surrounding the mechanism to be answered. For instance, short bridge “dimer of dimers” based on the oxalate or oxamic acid moieties could produce an ET rate occurring on the IR timescale where dynamic IR spectral coalescence can be used to determine an ET rate.⁶⁻⁸ Furthermore, a growing understanding of the unique spectroscopic behaviour displayed by these complexes is helping to reveal the underlying electronic structures that govern these properties.

5.2 References

- (1) Launay, J. P. In *Delhaes P., Drillon M. Organic and Inorganic Low-Dimensional Crystalline Materials. NATO ASI Series (Series B: Physics)*; Springer, New York, NY, 1987.
- (2) Huynh, M. H. V.; Meyer, T. J. *Chem. Rev.* **2007**, 107, 5004.
- (3) Wilkinson, L. A.; Vincent, K. B.; Meijer, A. J. H. M.; Patmore, N. J. *Chem. Commun.* **2016**, 52, 100–103.

- (4) Wilkinson, L. A.; McNeill, L.; Scattergood, P. A.; Patmore, N. J. *Inorg. Chem.* **2013**, *52*, 968.
- (5) Wilkinson, L. A.; McNeill, L.; Meijer, A. J. H. M.; Patmore, N. J. *J. Am. Chem. Soc.* **2013**, *135*, 1723.
- (6) Londergan, C. H.; Kubiak, C. P. *Chem. Eur. J.* **2003**, *9*, 5962.
- (7) Ito, T.; Hamaguchi, T.; Nagino, H.; Yamaguchi, T.; Kido, H.; Zavarine, I. S.; Richmond, T.; Washington, J.; Kubiak, C. P. *J. Am. Chem. Soc.* **1999**, *121*, 4625
- (8) Ito, T.; Hamaguchi, T.; Nagino, H.; Yamaguchi, T.; Washington, J.; Kubiak, C. P. *Science*. **1997**, *277*, 660.

Part 2. New Reactive Intermediates in
Tris(acetylacetonato)iron Catalysed Kumada
Cross-Coupling Reactions.

Chapter 6. Iron Catalysed Kumada Cross-Coupling Reactions.

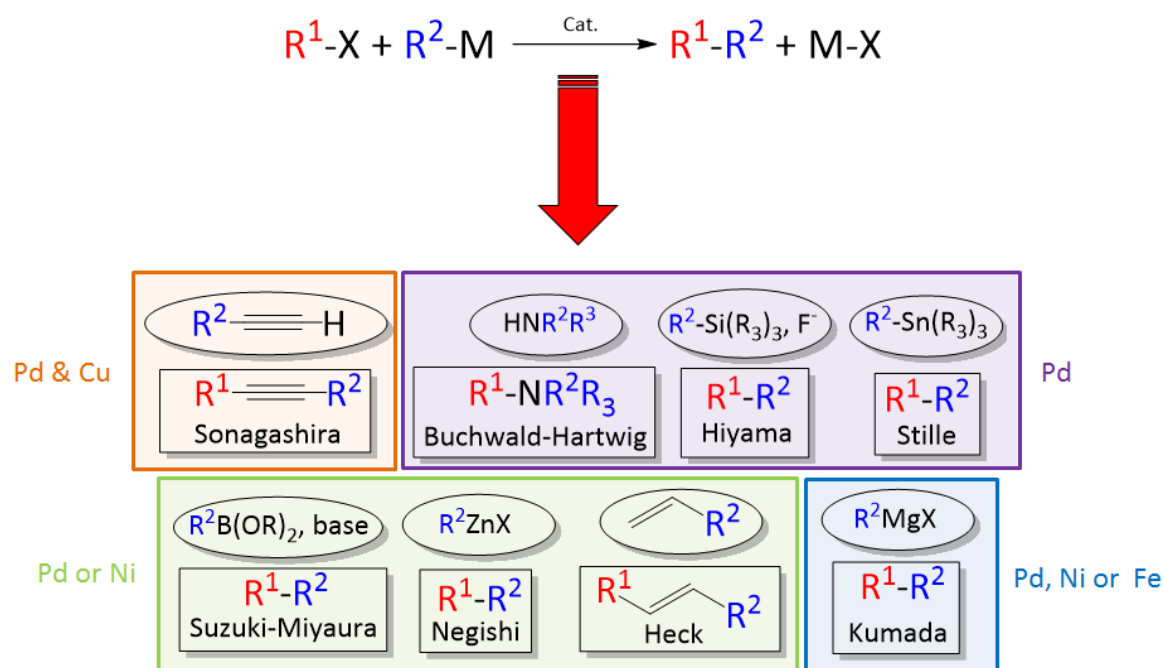
6.1 General Introduction; Kumada Couplings and the Appeal of Iron.

A 'coupling reaction' is a general term given to the connection of two hydrocarbon moieties typically catalysed by a transition metal. Coupling of identical moieties or coupling of a reagent to itself is referred to as homo-coupling while a cross-coupling reaction couples two different hydrocarbon moieties or identical moieties originating from different reagents.^{1,2}

The substrate to be coupled must contain a suitably active bond. Most commonly this will be a carbon-halide bond or a carbon-pseudo halide bond such a triflate (^-OTf) or tosylate (^-OTs). Less commonly a carbon-hydrogen bond is activated. This reactivity is typically more challenging because of the strength of the C-H bond given the similar electronegativity of the two elements. Significant interest in this field has developed in last decade and iron catalysis in particular has shown great promise.³

Because cross-coupling reactions generate new C-C bonds they allow the transformation of low value commodity hydrocarbon fragments into higher value architectures for use in the pharmaceutical, agrochemical and the fine chemical industry.⁴ They are amongst the most indispensable class of reactions to modern society and are fundamental to research in the chemical sciences.

A selection of the more common cross-coupling reactions are summarised in Scheme 6.1.



Scheme 6.1. Summary of common name cross-coupling reactions. Where in $M-R^2$ is an organometallic species and couples with an organic molecule having a suitably activated $R-X$ bond.

The modern field of cross-coupling could be said to be born in 1971 when Tamura and Kochi reported the cross-coupling of Grignard reagents with vinyl halides, using Fe, Cu or Ag catalyst.⁵⁻⁷ The groups of Robert Corriu and Makoto Kumada extended this work, independently reported the coupling of a greater range of sp^2 and sp^3 hybridised Grignard reagents with aryl halides using Fe and Ni catalysts in 1972.⁸ Murahashi group published the first example of Pd catalysed couplings with Grignard reagents in 1975.⁹

The use of Fe remained largely unexplored thereafter not gaining significant interest again until the turn of the millennium. There appears to be two major reasons for this. Firstly, the fact that the Pd catalysed reactions (Heck, Negishi and Suzuki) demonstrated such broad versatility and high efficiency there was little drive to research alternatives.¹⁰ Secondly, a simple Pd(0)/(II) redox couple can be applied to these reactions. This simpler, more intuitive mechanism allows for rational ligand and reagent design to direct reactivity. By contrast, Fe can display a much greater range of oxidation states:

from -4 to +6, but commonly -2 to +3 in the context of cross-coupling. As such the range of mechanisms in effect could be much more varied and so no robust general mechanistic cycle exists for Fe.

Other problems include the comparatively narrow reagent scope relative to Pd systems, in part due to the limited number of ligands found to promote these transformations. Desirable sp^3 - sp^3 cross-coupled products are far less efficient with iron catalysts and examples of Heck-type and enantioselective transformations are quite rare. But with the resurgence in the field novel and dramatic advances are being reported periodically in these areas.¹¹

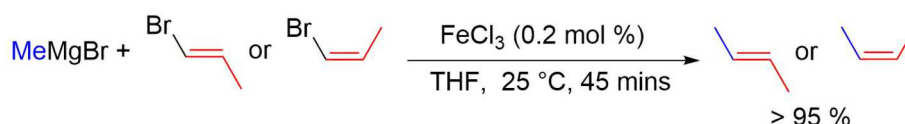
This recent resurgence in the field can largely be attributed to the drive towards greener chemistry and the low cost of iron catalysts. The abundance of Fe in the earth's crust is many orders of magnitude in excess of Pd or Ni, the next most common element used in catalysis.¹¹ The price of Pd is generally on the increase due to dwindling supplies. The imbalanced global distribution and the ever changing political climate renders the market volatile and uncertain for the future. Chemical (metal) scarcity is a very real and challenging issue facing not only the chemical industry but society as whole.¹² It is intrinsically linked with the well know issue of depleting fossil fuel reserves and so the importance of research into employing alternative earth abundant metals cannot be understated.

The dependence of the pharmaceutical industry on cross-coupling reactions means that the risk of potential metal contamination in products is monitored very closely. Iron, being prominent in biological systems, is often considered as being biologically benign. In reality, Fe toxicity is not well understood, research in this area is similarly undergoing a surge of interest. So while Fe toxicity is often understated, relative to Ni and Pd the risks are still significantly reduced, particularly in the context of in pharmaceutical contamination.¹² In 2008 the European Medicines Agency set a contamination limit of 1300 ppm for Fe compared to 10 ppm for Ni and Pd.

Finally, there are potential synthetic advantages to the use of Fe, which has been shown in some cases to improve efficiency and exhibit greater functional-group tolerance. The broad range of accessible oxidation states could also in theory facilitate a diverse range of reactivity.¹¹

6.1.1 Early Work.

In 1971 Tamura and Kochi reported the coupling of vinyl bromides with alkyl Grignard reagents catalysed by FeCl_3 .⁵ MeMgBr was converted (> 95 %) by reaction with excess 1-propenyl bromide at 25 °C. The reaction proceeds with stereo retention; *cis*- and *trans*-propenyl bromide generating *cis*- and *trans*-but-2-ene respectively (Scheme 6.2).



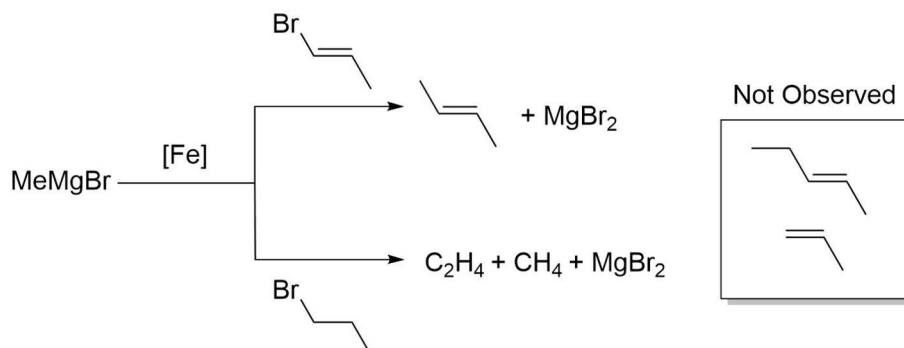
Scheme 6.2. Vinylation of alkyl Grignard's catalysed by FeCl_3 . Tamura and Kochi 1971.⁵

The authors observed that the *trans*-isomer reacted fifteen times faster than the *cis*-analogue in THF and four times faster in Et_2O . Neither reaction was affected by the addition of styrene, a radical trapping substrate. Kinetic studies showed that the formation of but-2-ene was first order in propenyl bromide but inversely proportional to MeMgBr thus necessitating an excess of the alkyl halide. Contrarily in latter publications we can see that an excess of the Grignard reagent is used. The inhibition of catalytic turn over, based on addition of MeMgBr and PPh_3 suggests competitive coordination with the vinyl halide.

The contrasting behaviour of alkyl halide substrates was also briefly discussed. Where excellent conversion is observed for 1-propenyl bromide with MeMgBr , no cross-coupling product is observed for ethyl bromide. Instead an equimolar amount of ethylene and ethane is produced.

The competitive reaction of MeMgBr in the presence of both ethyl and ethenyl bromide is presented Scheme 6.3. The exact reaction conditions were not made clear. Neither the cross-over product pent-2-ene or propylene is observed. The authors state the absence of the latter excludes mechanisms involving a propenyl iron species or the reaction of an ethyl iron species with the Grignard reagent. It is thus concluded that the alkenylation process must occur via an "Fe-assisted displacement of the

alkenyl halide by the Grignard reagent [with]... an intramolecular delivery of the Grignard reagent, a process which may be made possible by a ternary complex.”



Scheme 6.3. Reaction of MeMgBr with a mixture of 1-propenyl bromide and ethyl bromide catalysed by FeCl₃.

Later Kochi reported that improvements in yield and catalysts stability were obtained by moving from FeCl₃ to Fe(dbm)₃ (dbm = dibenzoylmethino).¹³ Ultimately, the requirement to use an excess of the vinyl halide limited the appeal of the reaction.

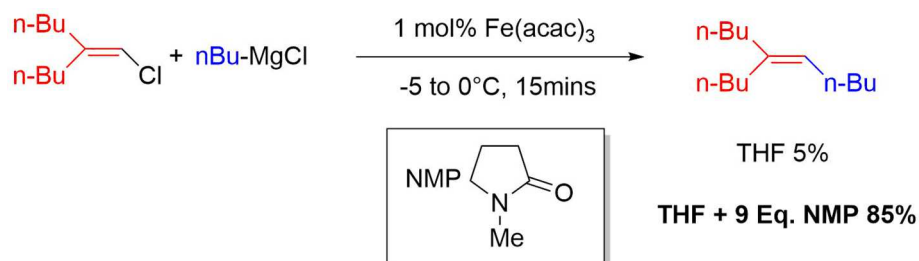
6.1.2 Resurgence and the Modern Field.

The next thirty years were relatively quiet for publications in the field. It was not until the late 90's and early 2000's that interest in the field began to rekindle. A number of seminal papers were published demonstrating the largely untapped potential of iron catalysed Kumada cross-coupling reactions.

The work of Cahiez *et al.* presented a major breakthrough in vinyl halide cross-couplings, demonstrating that Fe(acac)₃ (acac = acetylacetonato) could catalyse a large range of complexly functionalised substrates when reacted with a variety of traditional and non-traditional Grignard reagents.¹⁴⁻¹⁶ The electrophile was also expanded to include the use of tosylates and triflates having comparable reactivity in most cases but incompatible with vinyl Grignards.

Most importantly though, they demonstrated that the use of the solvent additive NMP (N-methyl pyrrolidone) negated the need to use and maintain an excess of the vinyl halide thus massively

improving the economic and practical desirability of the reaction.¹⁴ Furthermore, in some cases the addition of NMP was also found to produce remarkable improvements in conversion, see for instance Scheme 6.4.



Scheme 6.4. A remarkable yield improvement observed in the coupling of a vinyl chloride and an alkyl Grignard with addition of NMP. NMP equivalences relative to vinyl halide.¹⁴

In 2002 Fürstner *et al.* published the largest scope expanding study thus far.^{17,18} The simple iron salts Fe(acac)_n and FeCl_n ($n = 2$ or 3) were seen to effectively catalyse the reactions of electron-deficient aryl chlorides and tosylates, N and S heterocycles and electron-rich aryl triflates with aryl Grignard reagents. The mechanistic contributions of this work also popularised the commonly referenced catalytic cycle, that involving an “Inorganic Grignard Reagents” having formal composition Fe(MgX)_2 . The proposition of such a highly reduced active species highlighted a key advantage of the Fe system over Pd where the reducing ability of Grignard reagents would cause precipitation of Pd black that typically arrest catalysis.

Fürstner also correctly predicted that functionalized Grignard reagents would become prominent in the literature and bring further utility to Fe catalysis.^{19–21}

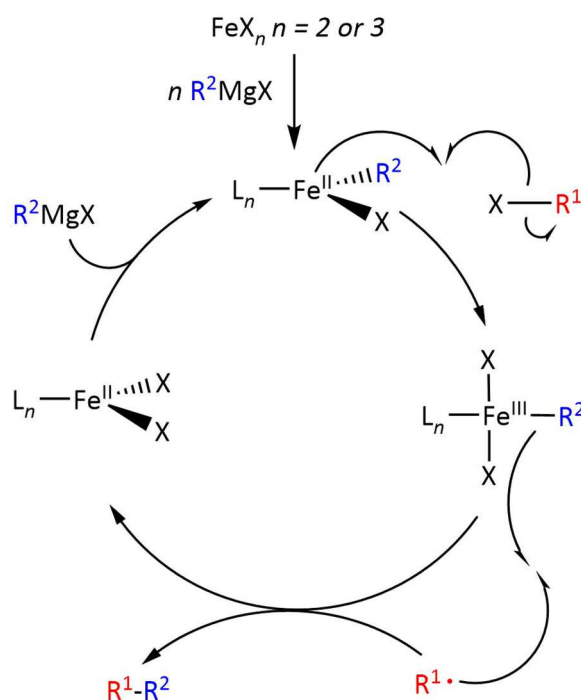
6.1.3 Substrate Scope.

Iron catalysts have been shown to successfully facilitate the cross-coupling of aryl, vinyl and alkynyl halides with aryl, alkyl and alkynyl Grignard reagents summarised in Scheme 6.5. Further discussion in this topic is beyond the scope of this work but a number of recent reviews that clearly illustrate the broad scope of Fe catalysed cross-coupling reactions are presented.^{11,22,23}

elimination. Furthermore, similar observations were made for a Pd system which are known to proceed via two-electron processes exclusively.^{25,26}

Numerous such studies have been conducted and alone the results of these experiments are insufficient to confirm a radical component, but a number of complimentary studies exist in the literature. The Norrby group found that linear free energy relationships also correlated well with a radical mechanism.²⁷⁻²⁹ Fürstner,³⁰ Nakamura³¹ and Hoffmann³² independently report that enantiomerically enriched or diastereomerically pure Grignard reagents undergo racemization as a result of C-X bond homolyses. Finally, the Tonzetich group have demonstrated that the use of radical scavengers can inhibit cross coupling.³³ The combined evidence of these studies gives a somewhat stronger argument for a radical mechanism.

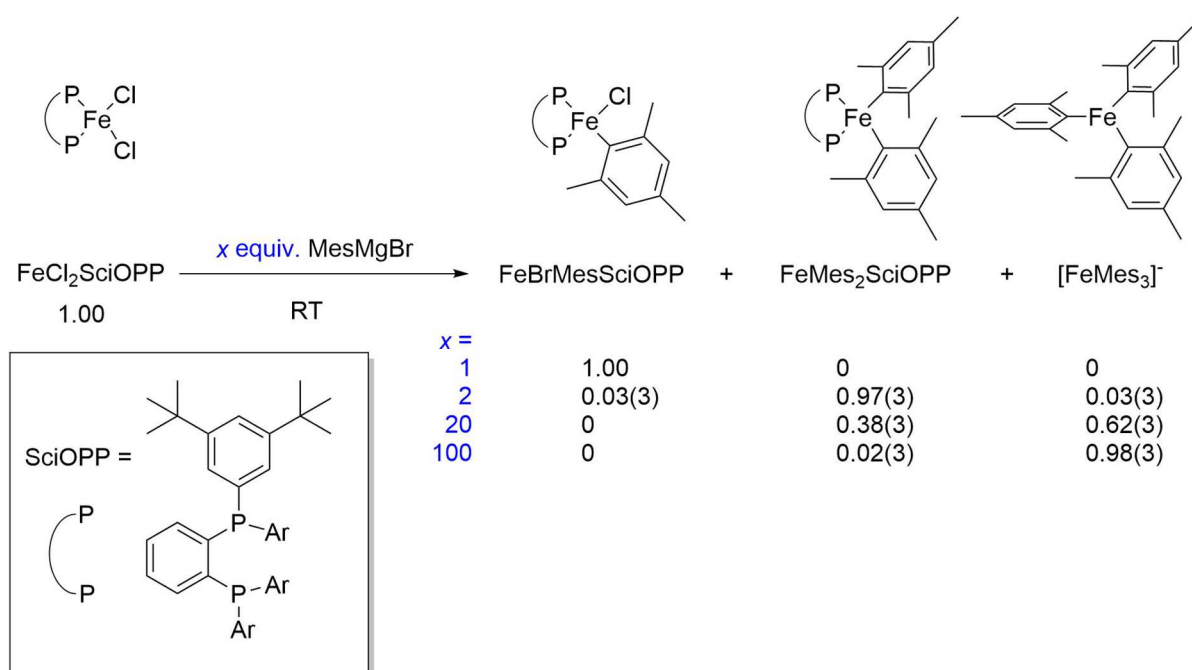
Scheme 6.6. shows a generic Fe(II)/(III) SET catalytic cycle. The Ferrous iron salts undergo ligand exchange with the Grignard reagent. Bond homolysis of the organohalide substrate produces an organic radical and an Fe(III) complex. Reductive elimination produces the cross-coupled product regenerating the ferrous salt.



Scheme 6.6. A proposed Fe(II)/(III) SET catalytic cycle employing an Fe(II) pre-catalyst.

6.2.1.1 SET: Fe(II)/(III) catalytic cycles.

The Fe(II) bisphosphine complex $\text{FeCl}_2(\text{SciOPP})$ (Scheme 6.7) is an effective catalyst in many Kumada couplings first reported by Nakamura *et al.*^{24,34} The Neidig group has performed a number of rigorous mechanistic studies using this complex. These include *in situ* Mössbauer and MCD spectroscopies utilizing isotopically pure samples of $^{57}\text{FeCl}_2(\text{SciOPP})$.³⁵ Reaction of $^{57}\text{FeCl}_2(\text{SciOPP})$ with one equivalent MesMgBr (Mes = 2,4,6-trimethylbenzene) produces $\text{FeBrMes}(\text{SciOPP})$ while two equivalents produces the bis-mesylated complex $\text{FeMes}_2(\text{SciOPP})$, which can be compared to genuine isolable sample characterized by x-ray crystallography.



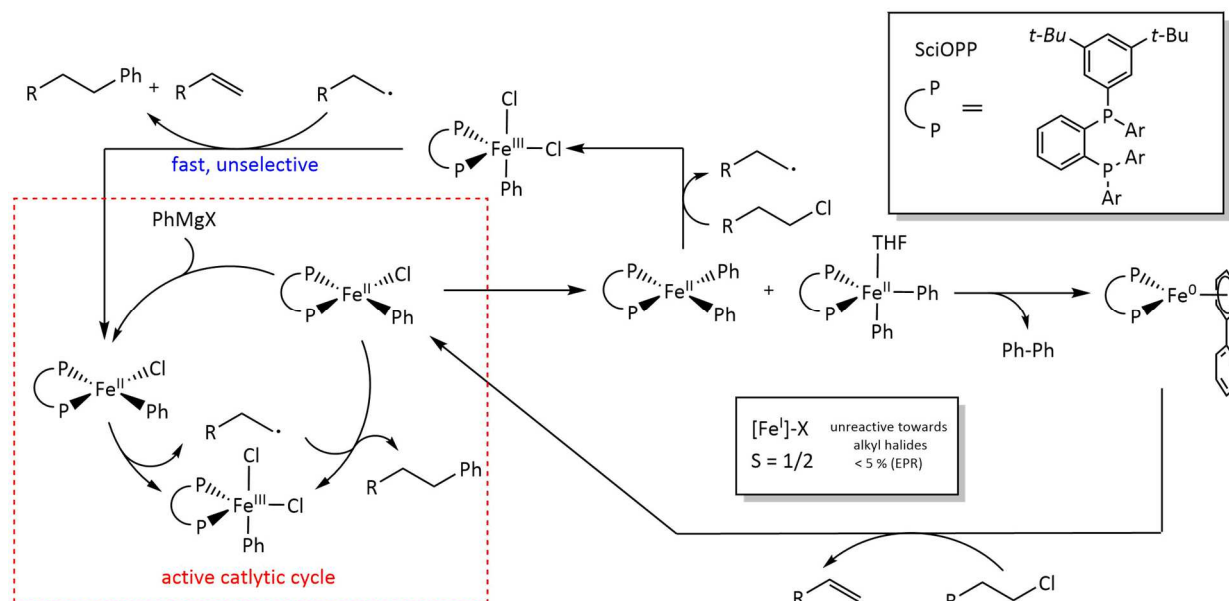
Scheme 6.7. Stoichiometric reactions of $\text{FeCl}_2(\text{SciOPP})$ with x equivalents of MesMgBr, molar ratios of products.

Large excesses of MesMgBr (20 and 100 equivalents) instead favour the production of $[\text{Mg}_2\text{X}_3(\text{THF})_6][\text{FeMes}_3]$ (Scheme 6.7). $\text{FeMes}_2(\text{SciOPP})$ while diminished, is present in both cases suggesting that in the presence of SciOPP the two species would be interchangeable. Indeed, the equimolar reaction of a solution of $[\text{Mg}_2\text{X}_3(\text{THF})_6][\text{FeMes}_3]$ with the free SciOPP ligand produces an 80 % to 20 % mix of $\text{FeMes}_2(\text{SciOPP})$ and $[\text{Mg}_2\text{X}_3(\text{THF})_6][\text{FeMes}_3]$ respectively.

To draw more catalytically relevant conclusions, the *in-situ* analyses with integrated EPR were performed as a function of time in the presence of 20 equivalents of 1-iododecane. Two equivalents of MesMgBr produces $\text{FeMes}_2(\text{SciOPP})$ and accounts for 90 % of the total iron content at $t = 0$. After 20 minutes, it is almost entirely depleted with near total conversion to $\text{FeBrMes}(\text{SciOPP})$. After 2 hours a 97 % yield of mesityldecane is produced with no production of decane or decene. Upon addition of further equivalents of Grignard reagent or electrophile to the resultant mixture, $\text{FeBrMes}(\text{SciOPP})$ is not further consumed, thus contrasting its reactivity to the bis-mesyated species. The FeMes_3^- species is shown to be reactive towards the electrophile but demonstrates poor selectivity as near equimolar amounts of mesityldecane and decene are produced.

The proposed catalytic cycle is a standard Fe(II)/(III) redox couple as per Scheme 6.6 provided that a slow addition of the Grignard reagent is maintained to sequester production of the non-selective side product $\text{Mg}_2\text{X}_3(\text{THF})_6[\text{FeMes}_3]$. In the original works of Nakamura *et al.*, nucleophiles such as alkynyl and phenyl Grignard reagents were predicted to have analogous mechanisms with the SciOPP pre-catalyst. However, the reaction rates and yields vary greatly, so following the work of Neidig the Bedford group suspected that this could be indicative of different mechanisms.^{34,36} Phenyl Grignard reagents were for instance, suspected to facilitate the generation of low valent iron active species.³⁷

The Neidig group demonstrated that the reaction of $\text{FeCl}_2(\text{SciOPP})$ with one and two equivalents of PhMgBr produces analogous mono- and bis-phenylated complexes, $\text{FeXPh}(\text{SciOPP})$ ($X = \text{Br}$ or Cl) and $\text{FePh}_2(\text{SciOPP})$.³⁷ But the reactivity differs. Firstly, reductive elimination of the bis-phenylated species can now produce an Fe(0) complex, $\text{Fe}(\text{SciOPP})(\eta^6\text{-biphenyl})$, but reacts far too slowly with the electrophiles explored to be catalytically relevant. Secondly, in contrast to the mesityl analogues both the mono- and bis-phenylated complexes are suitably reactive with electrophiles to be considered active species, but the former is more selective in production of the cross-coupled product. A yet unidentified minor $S = \frac{1}{2}$ complex *ca.* 5 % total Fe content by EPR is also produced but is similarly too kinetically inert to be the active species. The entire picture is illustrated in Scheme 6.8.

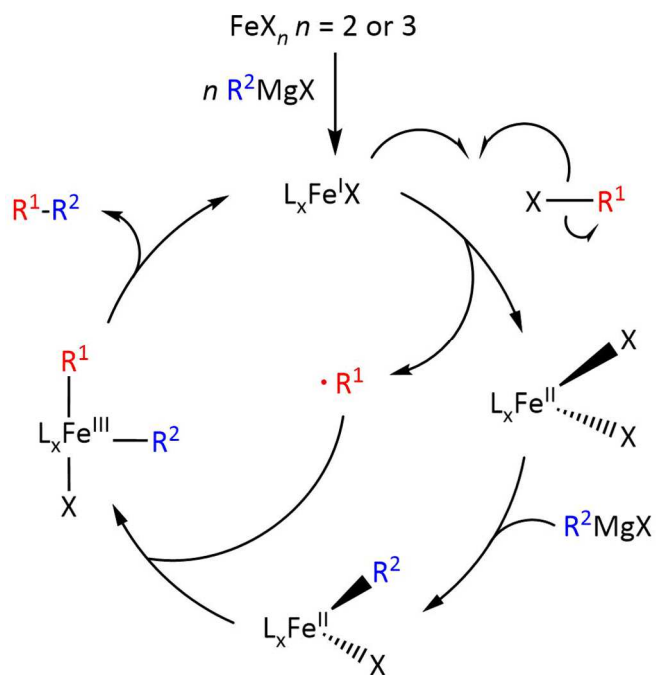


Scheme 6.8. An Fe(II)/III catalytic cycle with a second divergent unselective Fe(II) and minor unreactive Fe(I) and Fe(0) side products presented by Neidig. Figure reproduced from reference with permission of the RSC.³⁸

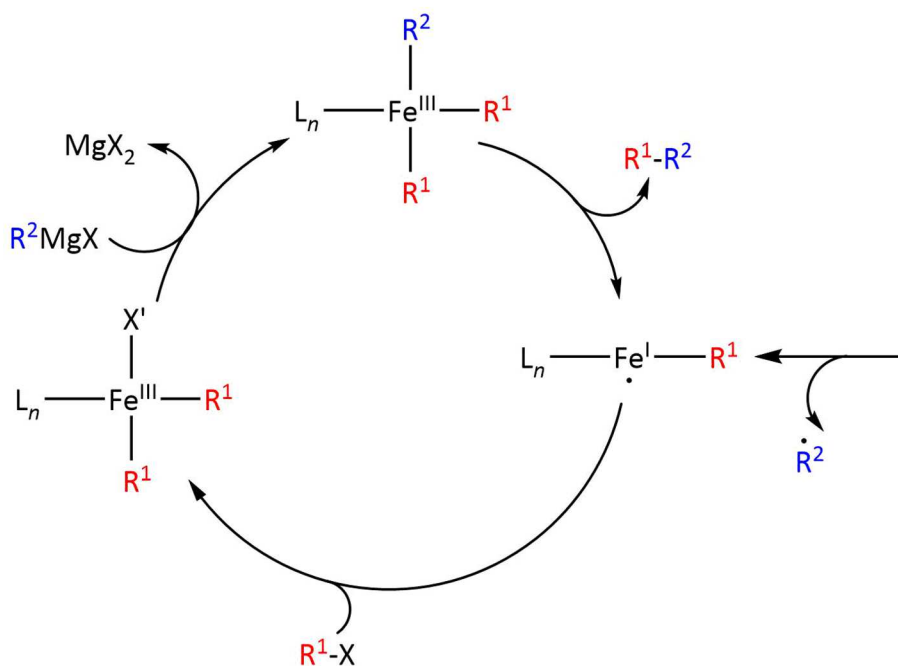
6.2.1.2 SET: Fe(I)/III catalytic cycles.

The groups of Norrby and Bedford have both proposed an Fe(I)/III as per scheme 6.9. The existence of an Fe(I) intermediate was originally proposed based on the observation that in the initial stages of cross-coupling, half an equivalent of biphenyl being produced per equivalent of Fe(II) precursor, the Fe(II) having undergone a single electron reduction.^{39,40} Bond homolysis of the alkyl halide substrate produces an Fe(II) species and an organic radical. Exchange with the Grignard reagent produces an Fe(II) species now coordinated with the organic component of the Grignard reagent that on addition of the substrate alkyl radical produces an Fe(III). This Fe(III) species now bearing both organic components of the product which is produced by reductive elimination thus regenerating the Fe(I) complex.

Fürstner proposed that an alkylated Fe(I) redox species could be instead formed by homolysis of the Fe-R bond in an Fe(II) complex (scheme 6.10). Such an interconnected catalytic cycle is presented and discussed later in section 6.2.6.



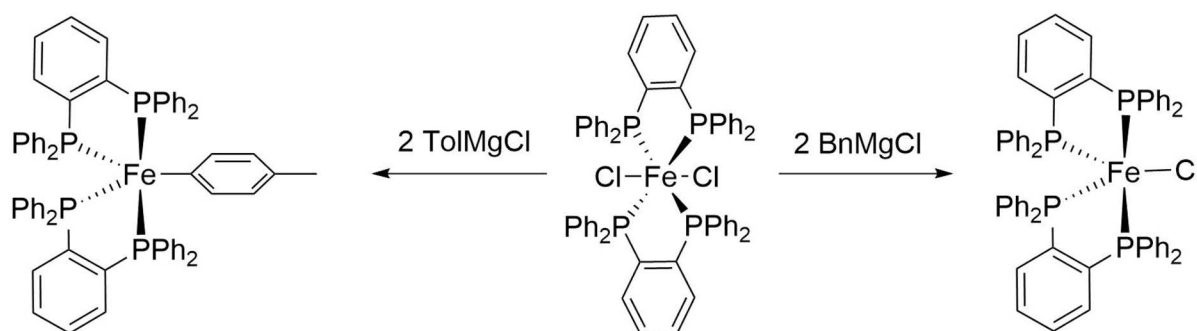
Scheme 6.9. An Fe(I)/(III) catalytic cycle initiating from reduction of and Fe(II) species by Grignard reagents.



Scheme 6.10. An Fe(I)/(III) catalytic cycle initiated from bond homolysis in a Fe(II) species.

Bedford *et al.* have successfully isolated Fe(I) complexes by reaction of $\text{Fe}(\text{dppbz})_2\text{Br}_2$ with Grignard reagents (Scheme 6.11).³⁹ $\text{Fe}(\text{dppbz})_2\text{Br}$ is produced upon reaction with two equivalents of BnMgBr at

room temperature (Bn = benzyl). $\text{Fe}(\text{dppbz})_2(\text{tol})$ is produced upon reaction with two equivalents of 4-tolMgBr at -40°C . Both complexes were found to be catalytically competent in Negishi reactions using $\text{Zn}(\text{Tol})_2$ but the latter was not deemed kinetically labile enough to be the active species based on observed reaction rates. The catalytic complexes are to this author's knowledge, unexplored in Kumada conditions, but are relevant given the conditions of their formation.

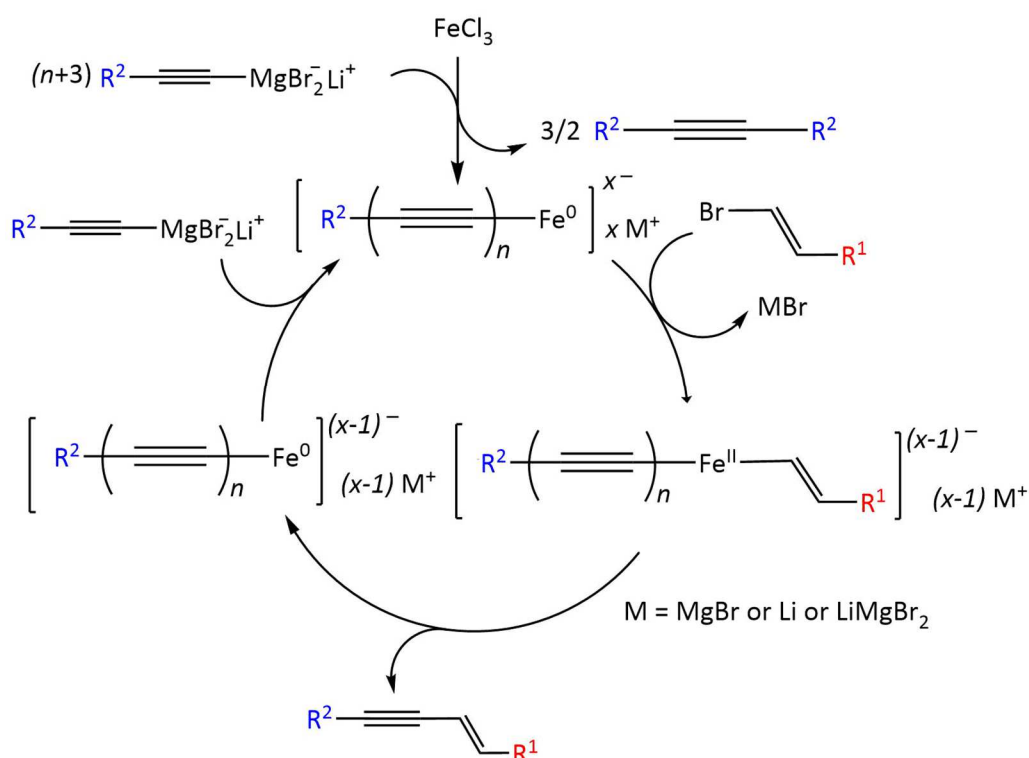


Scheme 6.11. The reactions of $\text{Fe}(\text{dppbz})\text{Cl}_2$ with two equivalents of tolylMgBr and BnMgCl produces the penta-coordinate Fe(I) complexes $\text{Fe}(\text{dppbz})_2\text{tol}$ and $\text{Fe}(\text{dppbz})_2\text{Cl}$ respectively.³⁹

6.2.2 Low Valent Active Species

6.2.2.1 Fe(0)/(II) Cycle.

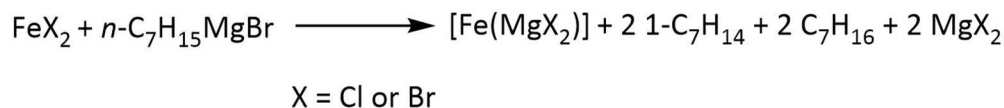
Nakamura *et al.* have proposed an Fe(0)/(II) redox couple based on rate profiles and side-product analysis for the reaction of alkynyl Grignard reagents with vinyl bromides in the presence of LiBr.⁴¹ The proposed cycle is presented in Scheme 6.12. Three equivalents of RMgX reduce the Fe(III) pre-catalyst directly to an Fe(0) alkynyl complex. In the absence of lithium salts, this reduction is proposed to occur very slowly due to the high stability of the intermediate Fe(II)alkynyl complexes.⁴² Oxidative addition of the alkenyl halide produces an Fe(II) with both the alkyl and alkenyl component of the product which is produced upon reductive elimination and regenerates an alkynyl Fe(0) species. This species then adds one more alkynyl ligand via transmetalation from the lithiated alkynyl Grignard moiety and regenerates the active Fe(0) alkynyl species.



Scheme 6.12. An Fe(0)/(II) active catalyst cycle proposed by Nakamura et al.⁴¹

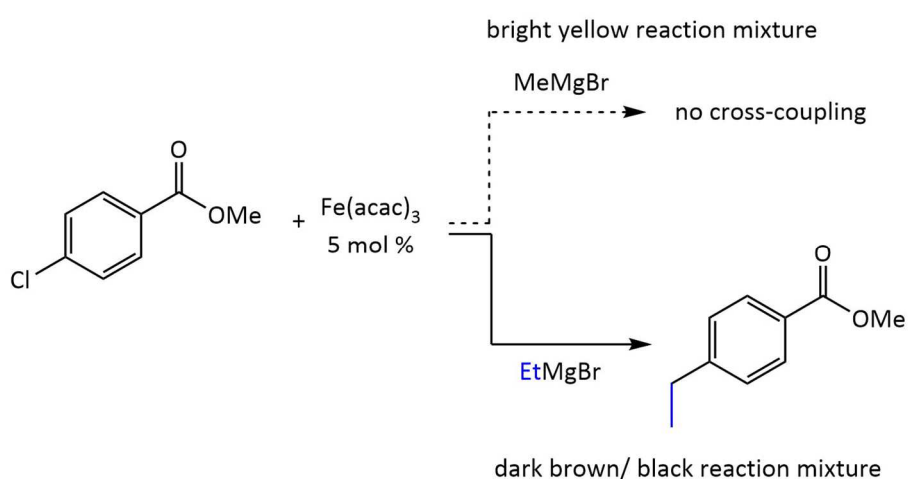
6.2.2.2 Fe(0)/(-II) "Inorganic Grignard" Cycle

Fürstner popularized the low valent "Inorganic Grignard" mechanism based on the original observations of Bagdonovic *et al.* which suggests that FeCl₂ will react with 4 equivalents of alkyl Grignard to generate stoichiometrically a species of formal composition [Fe(MgX)₂].⁴³ The total reaction equation with observed side products is presented in Scheme 6.13. The formal Fe(-2) species was expected to be highly nucleophilic as to oxidatively add aryl halides thus generating an Fe(0) complex. This Fe(0) species in turn will reductively eliminate the cross-coupled product regenerating the "inorganic Grignard reagent."

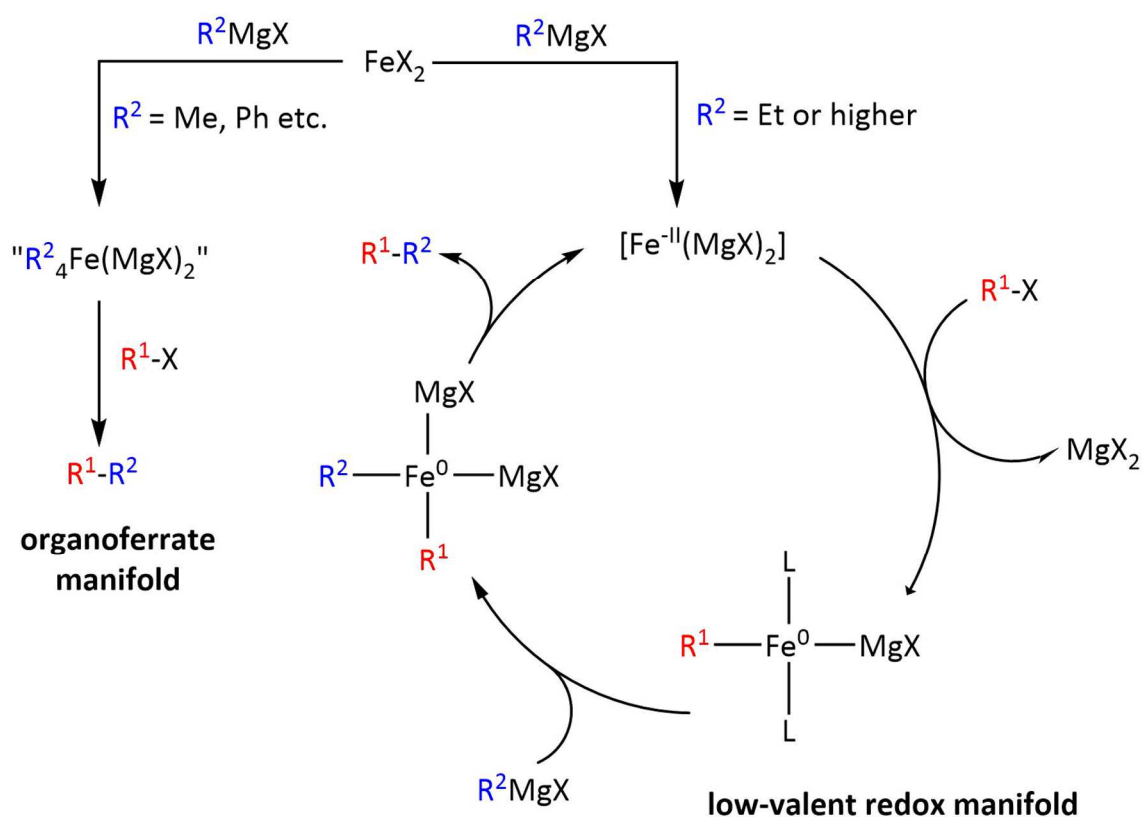


Scheme 6.13. Generation of the "Inorganic Grignard reagent" and observed hydrocarbon products from the reaction of FeX₂ X = Br or Cl with 4 equivalents of n-heptane.⁴³

Fürstner also demonstrated the now classic example of the remarkably different reactivity observed for Me and EtMgBr with 4-chloromethylbenzoate, see Scheme 6.14.^{17,18,44} This was accounted to the lack of a β -hydrogen, preventing access to the low valent cycle for MeMgBr. Instead it follows that catalysis must proceed with the Me Grignard simply alkylating the iron center to generate a “super-ate” complex (Scheme 6.15).



Scheme 6.14. Contrasting reactivity of Me and EtMgBr with 4-chloromethylbenzoate.

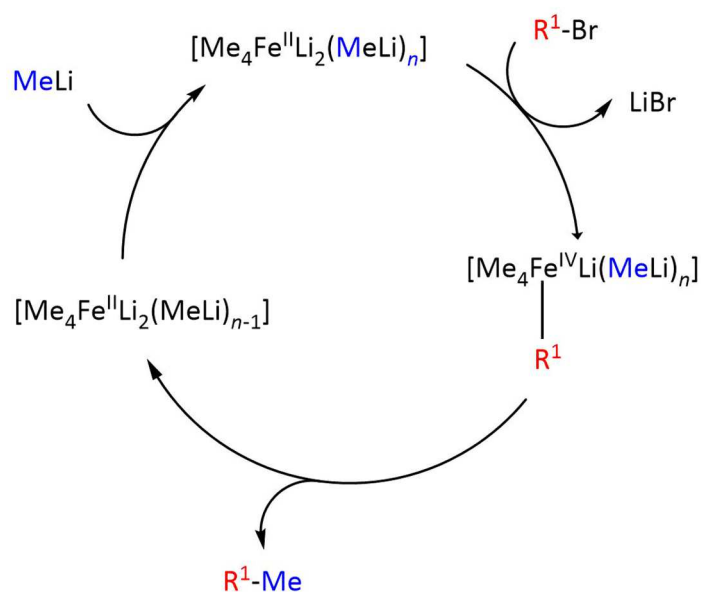


Scheme 6.15. Proposed mechanistic differences between Grignard reagents without a β -hydride (left) and alkyl Grignard reagents with a β -hydride (right).

6.2.3 "Super-ate" Complexes.

Kaufmann reports a catalytic cycle involving the Fe(II)/ Fe(IV) redox couple and the "highly selective super-ate complex as a catalyst".⁴⁵ In this study complexes of the form Me_nFeCl_{n-2} are prepared by the reaction of FeCl₂ with *n* equivalents of MeLi. These complexes are considered analogous to the ferric salts used in standard Fe catalysis on the basis that Me₄FeLi₂ is converted to Me₃FeLi upon reaction with 1-alkenyl bromides and can be regenerated by addition of further MeLi. These species were tested for their catalytic competence in the cross coupling of 1-alkenyl bromides with acyl chlorides (MeLi + 5 mol% FeCl₃) The results suggested the existence of the "super-ate" complexes [Me₄FeLi₂ · (MeLi)_n] or [Me₄Fe(MgBr)₂ · (MeMgBr)_n].

The overall catalytic cycle is presented in Scheme 6.16. The ferrous salt analogue $[\text{Me}_4\text{Fe}^{\text{II}}\text{Li}_2(\text{MeLi})_n]$ undergoes addition of the organohalide forming an Fe(IV) complex. This Fe(IV) complex then reductively eliminates the cross-coupled product and produces an Fe(II) complex that is re-solvated with MeLi.



Scheme 6.16. Proposed catalytic cycle for cross coupling of 1-alkenyl bromides via $[\text{MeLi} + 5 \text{ mol } \% \text{FeCl}_3]$ as reported by Kauffmann.⁴⁵

Ten years later Fürstner *et al.* confirmed the structure of the “super-ate” complexes having the full spectrum of formal oxidation states proposed in catalysis, -2, through to +4.^{46,47} Notably the complexes $[(\text{Me}_4\text{Fe})(\text{MeLi})][\text{Li}(\text{OEt}_2)_2]$ (Figure 6.1) and $[\text{Ph}_4\text{Fe}][\text{Li}(\text{Et}_2\text{O})_2][\text{Li}(1,4\text{-dioxane})]$ isolated from the reaction of FeCl_3 with MeLi and PhLi / PhMgBr respectively. But these complexes were in fact much less nucleophilic than anticipated and only capable of alkylating highly reactive electrophiles such as acyl chlorides or alkenyl triflates and were largely unreactive to aryl chlorides. The high chemoselectivity of these species was accounted to their crowded outer-sphere consisting of MeLi or MeMgBr and solvent molecules thus prohibiting the reactivity of larger organohalides.

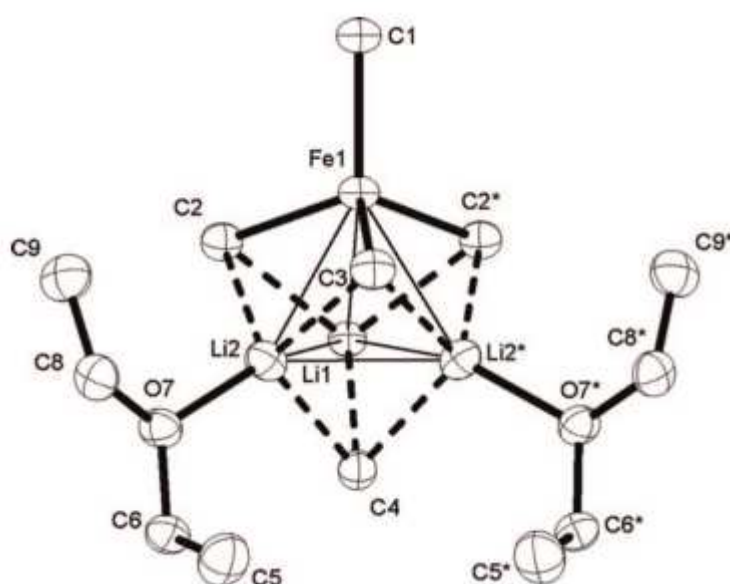
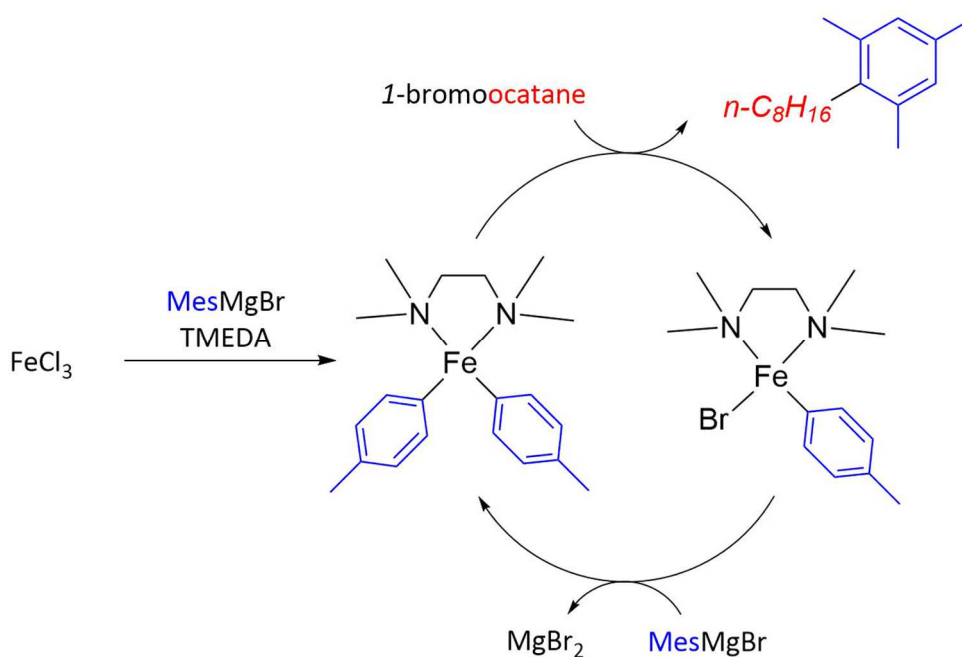


Figure 6.1. Crystal structure of the “super-ate” complex $[(\text{Me}_4\text{Fe})(\text{MeLi})][\text{Li}(\text{OEt}_2)_2]$ reported by Füstner *et al.* Reproduced from reference with permission of Wiley and sons.⁴⁷

Bedford does report an active super-ate complex in the coupling of MesMgBr with bromo-octane catalysed by FeCl_3 in THF with addition of TMEDA.⁴⁸ Nagashima *et al.* first reported that the reaction of FeCl_3 with three equivalents MesMgBr in the presence of eight equivalents TMEDA produced the complex $(\text{TMEDA})\text{FeMes}_2$.⁴⁹ Naghashima *et al.* proposed the catalytic cycle presented in Scheme 6.17 based on the fact that this isolable complex would react with bromo-octane to produce cross-coupled product.



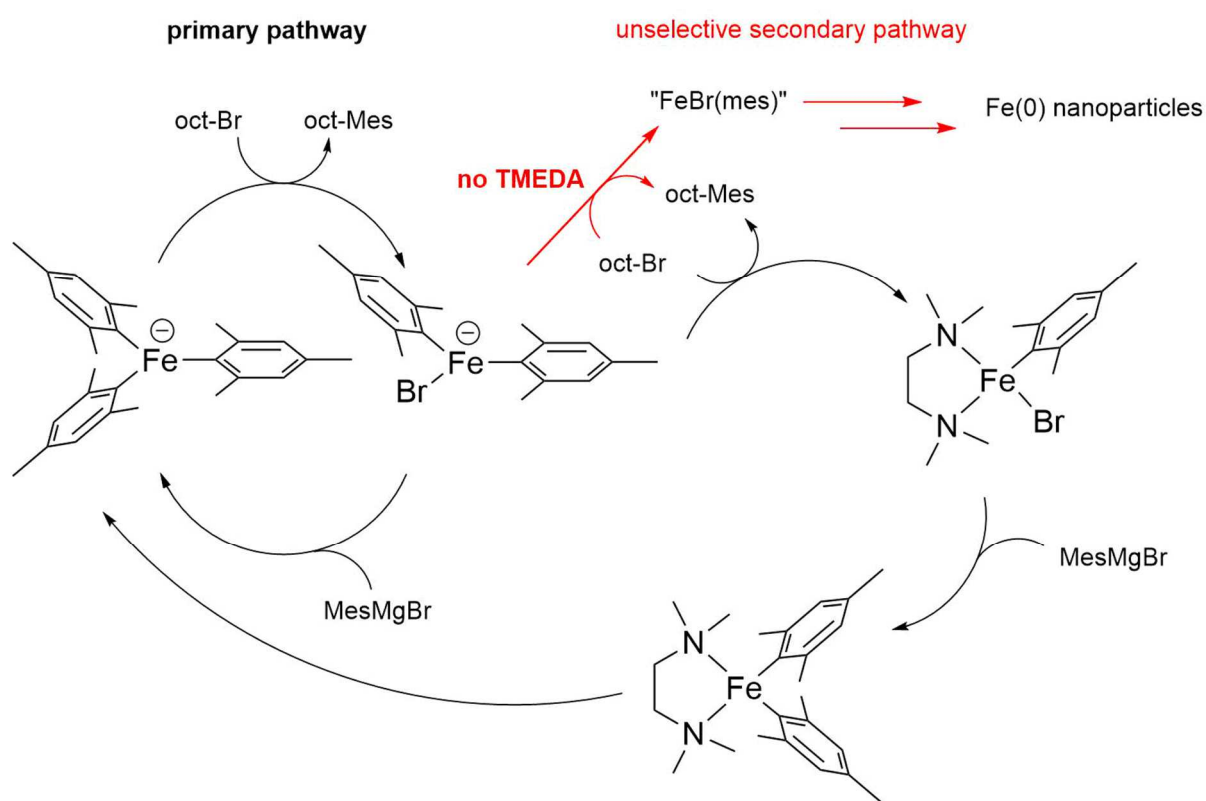
Scheme 6.17. Catalytic cycle proposed by Nagashima *et al.* for the coupling of 1-bromoocatane with MesMgBr by FeCl_3 in the presence of TMEDA .⁴⁹

The active species proposed by Nagashima is akin to those reported by Neidig *et al.* when employing the bis-phosphine SciOPP ligand (see 6.2.2). But in Neidig's example the super-ate complex generated upon treatment with excess MesMgBr was largely unreactive towards the electrophile and unselective towards the cross-coupled product.

Following Nagashima's work two pertinent questions remained. Firstly, the effect a large excess of Grignard (as in catalytic conditions) and secondly, the role of TMEDA . Thus, prompting the subsequent study by Bedford *et al.*⁴⁸

While the bis-mesityl species is the dominant species with three equivalences of MesMgBr upon addition of five equivalences the major product becomes instead the super-ate complex $[\text{FeMes}_3]^-$ which at eight equivalents becomes the sole product as observed by ^1H NMR spectroscopy. $[\text{FeMes}_3]^-$ also proved to be the more reactive species towards the electrophile and thus more likely the active species under catalytic conditions. Upon reaction with the electrophile, a complex is observed that was tentatively assigned as $[\text{FeBr}(\text{Mes})_2]^-$.

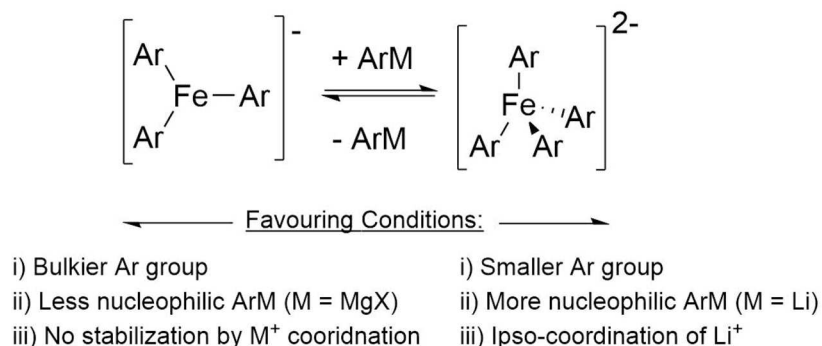
The reaction conditions as described by Nagashima but with the removal of TMEDA were actually shown to produce a slight increase in the yield of the cross-coupled product (32 \rightarrow 36 %). However, less of the unreacted bromo-octane was recovered with an increase in octane and octene side products. The conclusion was that while not essential to catalysis, the TMEDA must play a role in sequestering the unspecific side reactions. As such, Bedford proposed the revised catalytic cycle presented in Scheme 6.18.



Scheme 6.18. Catalytic cycle for the coupling bromo octane with MesMgBr. A secondary, unselective pathway exists in the absence of TMEDA. Figure reproduced from reference with permission of John Wiley & Sons.⁵⁰

Bedford described the influence that chelating ligands impart on the equilibrium of the typically bis-mesylated chelate complexes and the super-ate complex,⁵⁰ and that an equilibrium may exist between three- and four-coordinate super-ate complexes. The conditions favouring the generation of each form are summarised in Scheme 6.19. The fact that many stable, isolable three-coordinate complexes have been reported, while four-coordinate complexes have only been observed transiently

shows that the latter are prone to facile reductive elimination. Bedford has proposed that this is the pathway through which Fe nanoparticles, themselves active pre-catalysts can be produced.⁵¹ The importance of iron nanoparticles in catalysis is a largely unexplored but still an issue of much



contention.

Scheme 6.19. Conditions affecting the equilibria between three- and four-coordinate "ate" complexes. Adapted from reference.

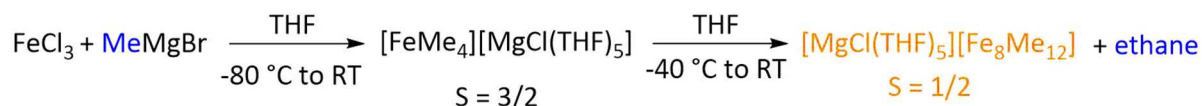
In 2016 Neidig *et al.* somewhat complicated the picture further. Demonstrating that while largely unreactive towards electrophiles itself, a four-coordinate super-ate complex formed upon reaction of FeCl₃ with MeMgBr was an intermediate in the reductive pathway to an active complex.⁵² In turn they also solved a long-standing mystery, the identity of the S = ½ species observed in the very early mechanistic studies of Kochi.¹³

When FeCl₃ is reacted with four equivalents of MeMgBr at – 80 °C in THF, the S = 3/2 complex [Fe(Me)₄][MgCl(THF)₅] is produced (Scheme 6.20) this being the first report of a methylated Fe(III) homoleptic "ate complex". Warming the reaction mixture to – 40 °C a mixture of this S = 3/2 species and an S = ½ species is observed by EPR. Upon warming the reaction mixture again to room temperature only the S = ½ species is observed with concomitant evolution of ethane gas confirmed by GC/MS suggesting a reductive elimination pathway.

Kochi *Et al.*



Neidig *Et al.*



Scheme 6.20. Observations of the reactivity of FeCl₃ with MeMgBr by Neidig and Kochi et al. Spin of the detected Fe species is reported as detected by EPR spectroscopy.^{13,53}

Consistent with the observations of Kochi, this $S = 1/2$ species is thermally unstable decaying within 15 minutes. To promote the formation and subsequent stabilisation of the $S = 1/2$ species the reaction mixture was warmed to 0 °C for 5 minutes before cooling again to -80 °C. The complex was successfully crystallised and revealed to be the mixed valence cluster $[\text{MgCl}(\text{THF})_5][\text{Fe}_8\text{Me}_{12}]$ (Figure 6.2).

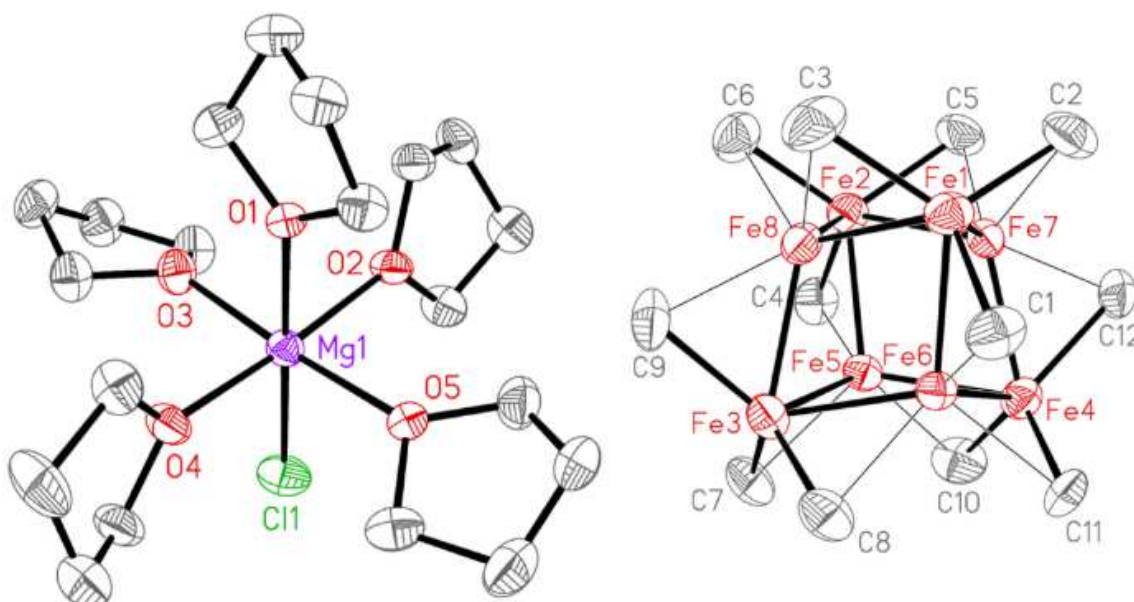
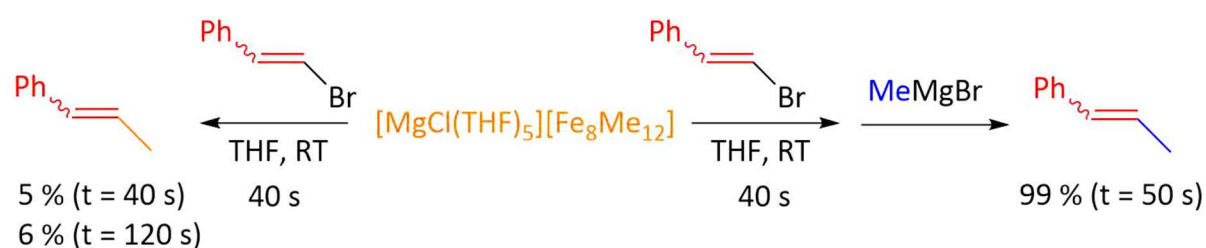


Figure 6.2. Crystal structure of the mixed valence cluster $[\text{MgCl}(\text{THF})_5][\text{Fe}_8\text{Me}_{12}]$ as reported by Neidig et al. Hydrogen atoms are not shown for clarity.⁵²

Reaction of $\text{MgCl}(\text{THF})_5[\text{Fe}_8\text{Me}_{12}]$ with β -bromostyrene only produced 5 % of the cross-coupled product β -methylstyrene after 40 seconds with little increase at extended reaction times, just 6 %



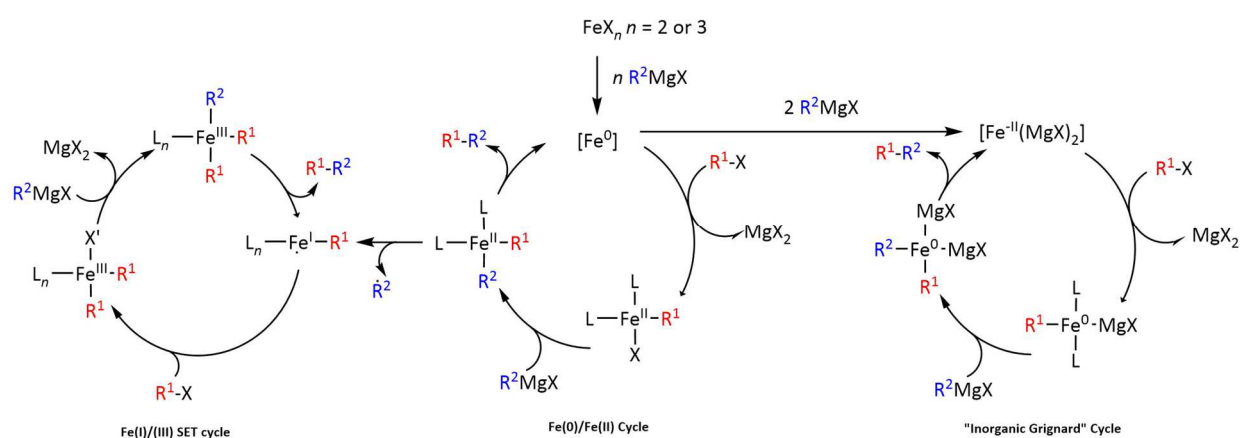
total after 120 seconds. No new EPR active species were observed. Kochi's original studies also suggested that reaction of the iron active species with electrophile would first require the generation of an intermediate species upon reaction with additional MeMgBr . This hypothesis proves to be highly likely. Upon reaction of $\text{MgCl}(\text{THF})_5[\text{Fe}_8\text{Me}_{12}]$ with 1.25 additional equivalents of MeMgBr (relative to β -bromostyrene) 99 % conversion to β -methylstyrene was observed after just 40 s and with near quantitative regeneration of $\text{MgCl}(\text{THF})_5[\text{Fe}_8\text{Me}_{12}]$ by EPR (Scheme 6.21)

Scheme 6.21. Contrasting reactivity of $\text{MgCl}(\text{THF})_5[\text{Fe}_8\text{Me}_{12}]$ with β -bromostyrene in the absence and presence of additional MeMgBr .⁵²

6.2.4 Conclusions

Despite the large number of mechanistic studies that have appeared in the last 10 years there is still a lot of division amongst the scientific community towards the commonly referenced catalytic cycles discussed above. The earliest mechanistic assignments in synthetic reports of the 1970's were based on qualitative synthetic observations. With the resurgence of the field in the 1990's came a number of studies employing more rigorous spectroscopic analysis, but often these results were correlated to poorly defined species from the predating literature and were often just one of many iron species present. The fact that assignments had been so complex led Fürstner to propose that in some cases

multiple catalytically active oxidation states are accessible for a single Grignard reagent where any electron rich low valent Fe species is produced (Scheme 6.22).⁴⁷



Scheme 6.22. Three interconnected catalytic cycles as suggested by Fürstner et al. Figure adapted from reference.⁴⁷

In the last ten years there have been numerous reports of isolable catalytically relevant species, which are beginning to replace the tentative assignments such as the proposed "Inorganic Grignard" reagent, $[\text{Fe}(\text{MgX})_2]$. These studies have revealed that rather subtle structural and electronic differences can impact significant differences in the reactivity of complexes of identical oxidation state. For instance in the works of Niedig *et al.* $\text{FeMesBr}(\text{SciOPP})$ is kinetically inert whereas in the analogous Ph complexes, both $\text{FePh}_2(\text{SciOPP})$ and $\text{FePhBr}(\text{SciOPP})$ are catalytically active, but have different selectivity towards the cross-coupled product.^{35,54}

The choice of ligand, solvent, temperature and even rates of addition of the Grignard reagent can all have a remarkable influence on speciation. This especially apparent in the formation of super-ate complexes, which are in some cases in equilibria with the aforementioned chelated species^{19,46,48,51} and the recently reported mixed valence cluster reported by Neidig *et al.*^{52,53}

The choice of Fe precalayst is of course also expected to play a large influence on the speciation of the active species. Early mechanistic studies in the field usually employed the simple iron haide salts where latter studies spearheaded by authors such as Neidig have turned to iron salts bearing more complex bi-phosphine ligands. There is therefore a noteworthy gap in the literature of applying the

more modern “physical-inorganic” approach to other iron salts such as $\text{Fe}(\text{acac})_3$. $\text{Fe}(\text{acac})_3$ is the next most commonly employed Fe precatalysts following FeCl_3 , it is desirable for its improved handling with regards to moisture and potential improvements of efficiency.^{44,55} The ongoing efforts of the Patmore group in this are discussed in the following chapters.

In chapter 7 the equimolar reaction of $\text{Fe}(\text{acac})_3$ with Grignard reagents (RMgX) is shown to produce half an equivalent each of two Fe(II) species, $\text{Fe}(\text{acac})_2$ and the novel $\text{Fe}^{\text{III}}\text{Mg}$ intermetallic, $\text{FeX}_2(\mu\text{-acac})_2\text{Mg}(\text{THF})_2$ X = Br, Cl or I. Two potentially competing catalytic species are thus produced in the first step of initiating the catalytic reaction.

These Fe(II) species are also substituted in place of $\text{Fe}(\text{acac})_3$ in a series of literature cross-coupling reactions. The catalytic activity of these species is contrasted based on isolated yields of the cross-coupled product.

In chapter 8 the reactions of $\text{Fe}(\text{acac})_3$, $\text{Fe}(\text{acac})_2$ and $\text{FeBr}_2(\mu\text{-acac})_2\text{Mg}(\text{THF})_2$ with further equivalence (> 1 equivalent) of Grignard reagents is investigated with aims to identify if a common catalytically active species exists. The reactivity of these species in the presence of an electrophilic substrate is also explored.

6.3 References

- (1) *Organic Synthesis Using Transition Metals, 2nd Edition*; Bates, R., Ed.; Wiley & Sons, 2012.
- (2) *MetalCatalyzed Cross-Coupling Reactions 2nd Edition*; A. de Meijere, F. D., Ed.; Wiley & Sons, 2004.
- (3) Shang, R.; Ilies, L.; Nakamura, E. *Chem. Rev.* **2017**, *117*, 9086.
- (4) Torborg, C.; Beller, M. *Adv. Synth. Catal.* **2009**, *351*, 3027.
- (5) Tamura, M.; Kochi, J. *J. Am. Chem. Soc.* **1971**, *93*, 1487.
- (6) Tamura, M.; Kochi, J. *J. Am. Chem. Soc.* **1971**, *63*, 1483.

- (7) Tamura, M.; Kochi, J. *J. Am. Chem. Soc.* **1971**, *93*, 1485.
- (8) Corriu, J.P. & Masse, J. P. *J.C.S. Chem. Comm.* **1972**, 144.
- (9) Yamamura, M.; Moritani, I.; Murahashi, S. I. *J. Organomet. Chem.* **1975**, *91*, 39.
- (10) Johansson Seechurn, C. C. C.; Kitching, M. O.; Colacot, T. J.; Snieckus, V. *Angew. Chem. Int. Ed.* **2012**, *51*, 5062.
- (11) Fürstner, A. *ACS Cent. Sci.* **2016**, *2*, 778.
- (12) Nakamura, E.; Sato, K. *Nat. Mater.* **2011**, *10*, 158–161.
- (13) Smith, R. S.; Kochi, J. *J. Org. Chem.* **1976**, *41*, 502.
- (14) Cahiez, G.; Avedissian, H. *Synthesis (Stuttg.)* **1998**, 1199.
- (15) Cahiez, G.; Marquais, S. *Pure Appl. Chem.* **1996**, *68*, 53.
- (16) Dohle, W.; Kopp, F.; Cahiez, G.; Knochel, P. *Synlett* **2001**, 1901.
- (17) Fürstner, A.; Leitner, A.; Krause, H. *J. Am. Chem. Soc.* **2002**, *124*, 13856.
- (18) Fürstner, A.; Leitner, A. *Angew. Chem. Int. ed.* **2002**, *41*, 609.
- (19) Sherry, B. D.; Fürstner, A. *Acc. Chem. Res.* **2008**, *41*, 1500.
- (20) Nakamura, M.; Matsuo, K.; Ito, S.; Nakamura, E. *J. Am. Chem. Soc.* **2004**, *126*, 3686.
- (21) Manolikakes, G.; Knochel, P. *Angew. Chem. Int. Ed.* **2009**, *48*, 205.
- (22) Jana, R.; Pathak, T. P.; Sigman, M. S. *Chem. Rev.* **2011**, *111*, 1417.
- (23) Bolm, C.; Legros, J.; Paih, J. Le; Zani, L. *Chem. Rev.* **2004**, *104*, 6217.
- (24) Hatakeyama, T.; Fujiwara, Y.; Okada, Y.; Itoh, T.; Hashimoto, T.; Kawamura, S.; Ogata, K.; Takaya, H.; Nakamura, M. *Chem. Lett.* **2011**, *40*, 1030.
- (25) Yang, Y.; Huang, X. *Synlett* **2008**, *9*, 1366.

- (26) Kambe, N.; Iwasaki, T.; Terao, J. *Chem. Soc. Rev.* **2011**, *40*, 4937.
- (27) Kleimark, J.; Hedström, A.; Larsson, P. F.; Johansson, C.; Norrby, P. O. *Chem. Cat. Chem* **2009**, *1*, 152.
- (28) Hedström, A.; Izakian, Z.; Vreto, I.; Wallentin, C. J.; Norrby, P. O. *Chem. Eur. J.* **2015**, *21*, 5946.
- (29) Hedström, A.; Bollmann, U.; Bravidor, J.; Norrby, P. O. *Chem. Eur. J.* **2011**, *17*, 11991.
- (30) Bauer, I.; Kn, H.; Bond, C. Å. H.; Cross, F. *Chem. Rev.*, **2015**, *115*, 3170–3387
- (31) Ghorai, S. K.; Jin, M.; Hatakeyama, T.; Nakamura, M. *Org. Lett.* **2012**, *14*, 1066.
- (32) Hölzer, B.; Hoffmann, R. W. *Chem. Commun.* **2003**, *3*, 732.
- (33) Przyojski, J. A.; Veggeberg, K. P.; Arman, H. D.; Tonzetich, Z. J. *ACS Catal.* **2015**, *5*, 5938.
- (34) Hatakeyama, T.; Okada, Y.; Yoshimoto, Y.; Nakamura, M. *Angew. Chem. Int. Ed.* **2011**, *50*, 10973.
- (35) Daifuku, S. L.; Al-afyouni, M. H.; Snyder, B. E. R.; Kneebone, J. L.; Neidig, M. L. *J. Am. Chem. Soc.* **2014**, *136*, 9132.
- (36) Hatakeyama, T.; Hashimoto, T.; Kondo, Y.; Fujiwara, Y.; Seike, H.; Takaya, H.; Tamada, Y.; Ono, T.; Nakamura, M. *J. Am. Chem. Soc.* **2010**, *132*, 10674.
- (37) Daifuku, S. L.; Kneebone, J. L.; Snyder, B. E. R.; Neidig, M. L. *J. Am. Chem. Soc.* **2015**, *137*, 11432.
- (38) Mako, T. L.; Byers, J. a. *Inorg. Chem. Front.* **2016**, *3*, 766.
- (39) Adams, C.; Bedford, R. *J. Am. Chem. Soc.* **2012**, *134*, 10333.
- (40) Hedström, A.; Izakian, Z.; Vreto, I.; Wallentin, C. J.; Norrby, P. O. *Chem. Eur. J.* **2015**, *21*, 5946.
- (41) Hatakeyama, T.; Yoshimoto, Y.; Gabriel, T.; Nakamura, M. *Org. Lett.* **2008**, *10*, 5431.
- (42) Wang, X.; Zhang, J.; Wang, L.; Deng, L. *Organometallics* **2015**, *34*, 2775.
- (43) Bogdanovi, B.; Schwickardi, M. *Angew. Chem. Int. Ed.* **2000**, *39*, 4610.

- (44) Scheiper, B.; Bonnekessel, M.; Krause, H.; Fürstner, A. *J. Org. Chem.* **2004**, *69*, 3943.
- (45) Kauffmann, T. *Angew. Chem. Int. Ed.* **1996**, *35*, 386.
- (46) Fürstner, A.; Krause, H.; Lehmann, C. W. *Angew. Chemie - Int. Ed.* **2006**, *45*, 440.
- (47) Fürstner, A.; Martin, R.; Krause, H.; Seidel, G.; Goddard, R.; Lehmann, C. W. *J. Am. Chem. Soc.* **2008**, *130*, 8773.
- (48) Bedford, R. B.; Brenner, P. B.; Carter, E.; Cogswell, P. M.; Haddow, M. F.; Harvey, J. N.; Murphy, D. M.; Nunn, J.; Woodall, C. H. *Angew. Chem. Int. Ed.* **2014**, *53*, 1804.
- (49) Noda, D.; Sunada, Y.; Hatakeyama, T.; Nakamura, M.; Nagashima, H. *J. Am. Chem. Soc.* **2009**, *131*, 6078.
- (50) Bedford, R. B. *Acc. Chem. Res.* **2015**, *48*, 1485.
- (51) Bedford, R. B.; Betham, M.; Bruce, D. W.; Davis, S. A.; Frost, R. M.; Hird, M. *Chem. Commun.* **2006**, *13*, 1398.
- (52) Muñoz, S. B.; Daifuku, S. L.; Brennessel, W. W.; Neidig, M. L. *J. Am. Chem. Soc.* **2016**, *138*, 7492.
- (53) Al-afyouni, M. H.; Fillman, K. L.; Brennessel, W. W.; Neidig, M. L. *J. Am. Chem. Soc.* **2014**, *136*, 15457.
- (54) Carpenter, S. H.; Neidig, M. L. *Isr. J. Chem.* **2017**, *57*, 1106.
- (55) Hedström, A.; Lindstedt, E.; Norrby, P. O. *J. Organomet. Chem.* **2013**, *748*, 51.

Chapter 7. The Reaction Products of Fe(acac)₃ with One Equivalent of Grignard Reagents.

7.1 Abstract

The reaction products of Fe(acac)₃ with one equivalent of Grignard reagent are assigned unequivocally for the first time. Two Fe(II) complexes are produced, an Fe--Mg intermetallic complex X₂Fe(μ-acac)₂Mg(THF)₂ where X = Br (**15**), Cl (**16**) or I (**17**) and Fe(acac)₂. These complexes are characterised using ¹H NMR and IR spectroscopy, magnetic susceptibility measurements, cyclic voltammetry and single crystal X-ray crystallography.

The same reaction mixture is shown to be generated using a range of alkyl, allyl, alkynyl and aryl Grignards indicating the initial reduction of the Fe(III) salt prior to catalysis is identical in all cases.

Complexes **15** – **17** could also be prepared in high yields (> 95 %) by reaction of ferrous salts, FeX₂ X = Cl, Br or I with Mg(acac)₂.

7.2 Reduced Products of Fe(acac)₃

It is evident from the literature there is no consensus on the oxidation state of the catalytically active species operating in iron-catalysed Kumada couplings.¹ Multiple catalytic mechanisms may be valid, but the plausibility of highly reduced species is a topic of much contention.² Though the initial reduction of the pre-catalyst by the Grignard is well regarded canonically, there is in fact no consensus on the ultimate reductive capability of the Grignard reagents.

The earliest mechanistic studies in the field focused around the use of iron halide salts¹ and the recent contributions have been made by the groups of Bedford^{3,4} and Neidig⁵⁻¹¹ on bis-phosphine coordinated complexes. To the author's knowledge there are just two reports in the literature to elucidate the reaction products of Fe(acac)₃ when stoichiometrically reacted with Grignard reagents.

The first study by Bauer *et al.* employs a combination of EXAFS (Extended X-ray Absorption Fine Structure) and XANES (X-ray Absorption Near Edge Structure) to attempt to determine the catalytically active species in situ.¹² The combined techniques allow for structural assignments based on element specific responses as well as identification of local structure and oxidation state to determine ligand coordination numbers and their proximity to the metal centre. From the literature five possible, structurally distinct iron active species are proposed along with their predicted spectroscopic response;

- 1) Kochi's soluble aggregates of unspecified oxidation state (described in section 6.1.1) would give Fe-Fe pairs characteristic of iron clusters.¹³
- 2) Bogdonavic / Furstner's inorganic Grignard complex formatively assigned as [Fe(MgX)₂]_n (described in section 6.2.2) would show Fe-Mg pairing.¹⁴⁻¹⁷
- 3) Furstner's organo-ferrate complexes (section 6.2.3) would instead show Fe-C bonding.²

4) A bi-aryl Fe(II) complex such as the (TEMDA)FeMes₂ complexes reported by Nakamura *et al.* (described in section 6.2.1) would appear similar to organo-ferrates (3).¹⁸

5) Norby *et al.* have proposed an Fe(I) active species (described in section 6.2.1) which will be identifiable by oxidation state.¹⁹

Based on the work of Bagdanovic *et al.*^{14,15} four equivalents of Grignard reagent are required to generate an active iron species of formal composition [Fe(MgX)₂]_n so the authors treated Fe(acac)₃ with one to four equivalents of PhMgBr in THF / NMP. Based on the EXAFS response the first equivalent reduces the Fe(III) to Fe(II) and then by the third equivalent it is reduced to Fe(I) with no further change upon addition of the fourth equivalent. The potential for the generation of Fe(0) nanoparticles was proposed but ultimately ruled out.

Bauer *et al.* also demonstrated that quantification of biphenyl by GC also parallels the result of the reduction proposed by the X-ray studies. The first equivalent of Grignard reagent producing stoichiometrically half-equivalent of biphenyl while two equivalents produced only 65 % of the expected biphenyl and accounts for a formal oxidation of +1.7. As only 1.3 equivalences of the Grignard reagent are consumed 0.7 equivalences are still available to coordinate to the iron. The combined results of these experiments are summarised in Table 7.1.

Table 7.1. Reaction of one equivalent Fe(acac)₃ with n equivalents PhMgCl. Transferred electrons based on biphenyl quantification by GC MS and Fe speciation by EXAFS/ XANES. Data collected from reference.¹²

| <i>n</i> equiv. PhMgCl | Transferred electrons* | Fe oxidation state | Fe-Fe coordination number | Fe-Fe bond distance (Å) |
|------------------------|------------------------|--------------------|---------------------------|-------------------------|
| 1 | 1 equiv. | + 2.0 | 0.7 ± 0.3 | 2.55 |
| 2 | 1.3 equiv. | + 1.7 | 5.1 ± 0.5 | 2.42 |
| 3 | 2 equiv. | + 1.0 | 2.0 ± 0.4 | 2.53 |
| 4 | 2.3 equiv. | + 0.7 | 2.6 ± 0.4 | 2.53 |

The formation of a non-integer oxidation state necessitates the generation of some form of iron cluster. The iron-iron distance is calculated to be 2.42 Å which is on the lower side of those reported for multinuclear Fe(II) complexes and comparable with a structure such as Fe₂Mes₄ where the Fe-Fe bond distance is 2.371(4) Å.²⁰ Most importantly though is that the addition of three and four equivalences of PhMgBr is shown to produce a decrease in aggregation from Fe₁₃ to Fe₃₋₄. In the proposed Fe₃ and Fe₄ clusters there is also evidence for strong covalent interactions between magnesium and the Fe cores.

In the second study by Lefèvre *et al.* reduction of Fe(acac)₃ by PhMgBr in THF is monitored and characterised by ¹H NMR spectroscopy and CV.²¹ The Fe(acac)₃ is shown by CV to display one reversible reduction attributed to the formation of the anionic complex [Fe^{II}(acac)₃]⁻. In the presence of one equivalent of PhMgBr a new irreversible reduction is observed indicating that the Fe^{II}(acac)₃ has now reacted with the PhMgBr to generate a new species. The species is assigned as [PhFe^{II}(acac)(THF)_n] and can also be generated by reduction of a commercial sample of Fe(acac)₂ with PhMgBr. In the CV experiment seven equivalents of PhMgBr were required to reduce 80 % of the Fe(acac)₃ to [PhFe^{II}(acac)(THF)_n].

Analysis by ¹H NMR spectroscopy required the use of 3.8 equivalents of PhMgBr to see total consumption of Fe(acac)₃. The paramagnetic species generated is assigned again as [PhFe^{II}(acac)(THF)_n] and displays three resonances at 29.7, 15.2 and -82.4 ppm though no integrations are provided. The other major product is Fe(acac)₂. After 8.7 equivalences of PhMgBr a 3:1 mixture of [PhFe^{II}(acac)(THF)_n] and a new paramagnetic Fe^I species was generated proposed to be [PhFe^I(acac)(THF)_n].

7.3 Aims

There are a significant number of literature studies that have focused on mechanistic studies of Kumada cross-coupling employing iron halide salts¹ or iron bisphosphine³⁻¹¹ pre-catalysts. The mechanistic studies approached through a combination of isolation of reactive species, reaction kinetics and *in-situ* spectroscopy.

The use of the $\text{Fe}(\text{acac})_3$ salt is prominent in the literature. Displaying improved handling with regards to moisture²² and potential improvements of efficiency²³ to halide salts and is far more commonly employed than bis-phosphine ligated complexes. The stoichiometric reaction of the iron pre-catalysts with Grignard reagents is an effective approach to develop an initial understanding of the reaction chemistry. The reactive species generated are typically identified by a technique such as ^1H NMR or EPR spectroscopy, but in many cases these spectroscopic responses are not matched unerringly with that of genuine isolable materials.

To the authors knowledge there are only two studies in the literature that have performed such studies with $\text{Fe}(\text{acac})_3$. These studies did not provide a conclusive structural determination of the products, and disagree with respect to how many equivalents of the Grignard would ultimately be required for total consumption of the Fe(III) pre-catalyst.

To this effect we commenced a study into the reaction of $\text{Fe}(\text{acac})_3$ with Grignard reagents beginning with the equimolar reaction aiming to provide an unequivocal structural assignment supported by spectroscopic characterisation.

7.4 Discussion

7.4.1 *The Reaction Products of $\text{Fe}(\text{acac})_3$ and One Equivalent 4-biphenyl-MgBr.*



Scheme 7.1. The reaction products for the equimolar reaction of $\text{Fe}(\text{acac})_3$ and 4-biPhMgBr are not defined in the literature.

Both the works of Bauer and Lefèvre *et al.* agree that a single equivalent of Grignard reagent will reduce $\text{Fe}(\text{acac})_3$ to an Fe(II) species in part. The identity of this Fe(II) species is unestablished in the former study and assigned as $[\text{PhFe}^{\text{II}}(\text{acac})(\text{THF})]$ in the latter. Furthermore, the total number of equivalents require for total consumption of the Fe(III) differs in each case.

In an effort to understand this reaction more thoroughly solutions of $\text{Fe}(\text{acac})_3$ in THF were treated with one equivalent of 4-biphenylMgBr. The choice of the single solvent system and Grignard reagent were to simplify the reaction as the homo-coupled by-product (4-quaterphenyl) can easily be removed from the reaction media by filtration as it is insoluble in THF.

7.4.2 *Experimental Observations: Isolation of the $\text{FeBr}_2(\mu\text{-acac})_2\text{Mg}(\text{THF})_2$ intermetallic (**15**).*

$\text{Fe}(\text{acac})_3$ is readily soluble in THF producing red solutions. Dropwise addition of 4-biphenylMgBr creates a dark brown/ black solution upon contact with $\text{Fe}(\text{acac})_3$ solution that quickly dissipates. After a large portion of the Grignard is added, in excess of around 0.75 equivalents the reaction mixture often looks slightly paler but is largely unchanged. Though some precipitation of 4-quaterphenyl is observed. It is not until the full equivalent is added that a remarkably fast colour change is observed, going from red to yellow and often concentrated enough as to appear dark brown. This reaction mixture is then filtered to remove 4-quaterphenyl. Mass recordings of the 4-quaterphenyl were consistent with total conversion of the Fe(III) to Fe(II) by a 1 : 1 reaction with 4-biphenyl-MgBr producing half an equivalent of 4-quaterphenyl.

Slow diffusion of the reaction mixture into hexanes at $-25\text{ }^\circ\text{C}$ yielded a crop of large yellow/ brown blocks of $\text{FeBr}_2(\mu\text{-acac})_2\text{Mg}(\text{THF})_2$ (**15**) (see section 7.3.1.2) in a *ca.* 40 % yield.

The crystal structure of **15** obtained by single-crystal XRD is shown in Figure 7.1 The Fe centre is tetrahedral coordinated by two Br atoms and two O atoms from the acac^- ligand that bridges both the Fe and Mg centres. The Mg is octahedral coordinated by two acac^- ligands in the typical chelating fashion and two THF solvent molecules. There is no $\text{Fe}\cdots\text{Mg}$ bonding character because the internuclear separation, $3.1631(12)\text{ \AA}$ is greater than covalent radii of the two metals. The bond lengths and angles of complex **15** are discussed in more detail in section 7.4.6.3.

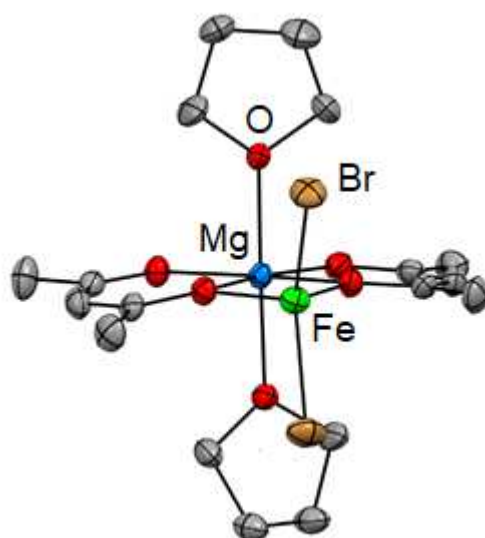


Figure 7.1. Solid-state structure of $\text{FeBr}_2(\mu\text{-acac})_2\text{Mg}(\text{THF})_2$ (**15**) as determined by single-crystal XRD. Thermal ellipsoids shown at 50 % probability level. Hydrogen atoms omitted for clarity.

The reaction stoichiometry and yield in which **15** was obtained indicated that a second iron species must be produced. To confirm this analysis of the reaction filtrate by ^1H NMR spectroscopy and infrared spectroscopy was required.

7.4.3 Analysis of Reaction Filtrate

7.4.3.1 ^1H NMR Spectroscopy

To identify the other species present in the reaction mixture a ^1H NMR spectrum of the reaction filtrate was obtained by removing the reaction solvent *in vacuo* and re-dissolving in d_8 -THF. The resulting spectrum is shown in Figure 7.2. The peaks belonging to small amounts of the intermetallic **15** that did not recrystallize from the reaction mixture can be identified by comparison to the spectra of a genuine crystalline sample.

There are four other peaks belonging to paramagnetic species. Two belong to the other resulting Fe(II) species, $\text{Fe}(\text{acac})_2$ with corresponding peaks appearing at 27.3 and -31.2 ppm being consistent with the literature or comparison to a genuine sample.

The minor peaks at 20.7 and -45.2 ppm belong to $\text{Fe}(\text{acac})_3$, a result of inadvertent exposure trace amounts of oxygen. The diamagnetic species $\text{Mg}(\text{acac})_2$ having signals at 5.02 and 1.79 ppm, the latter obscured by THF completes the reaction stoichiometry as shown in Scheme 7.1.

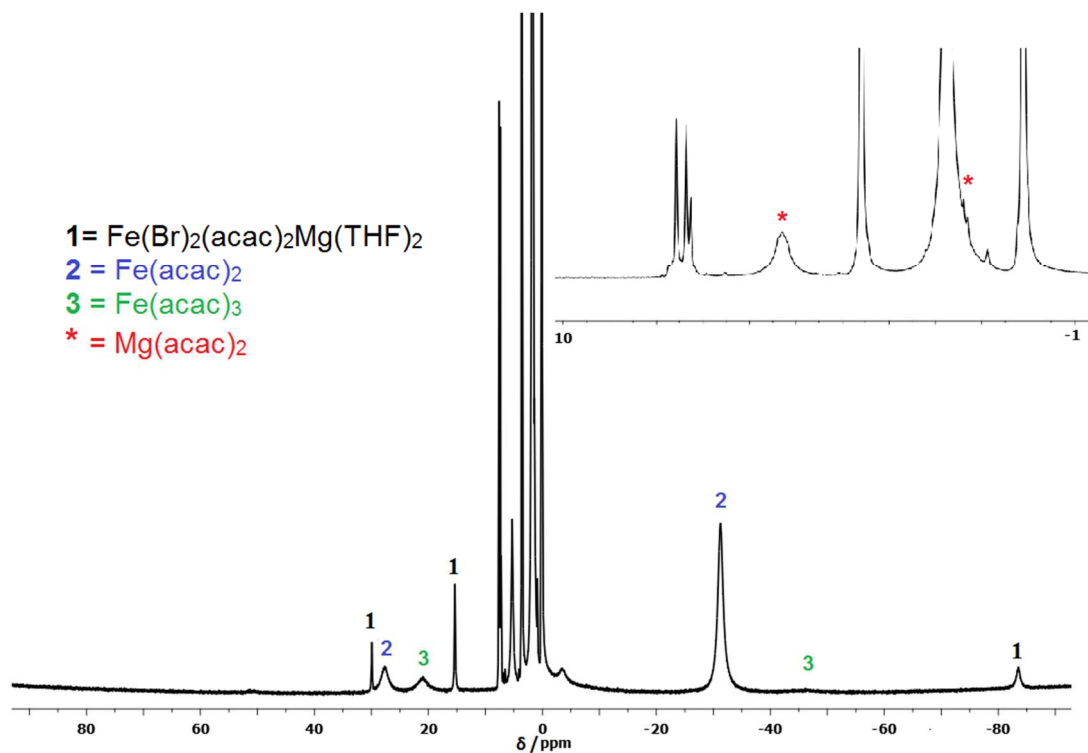
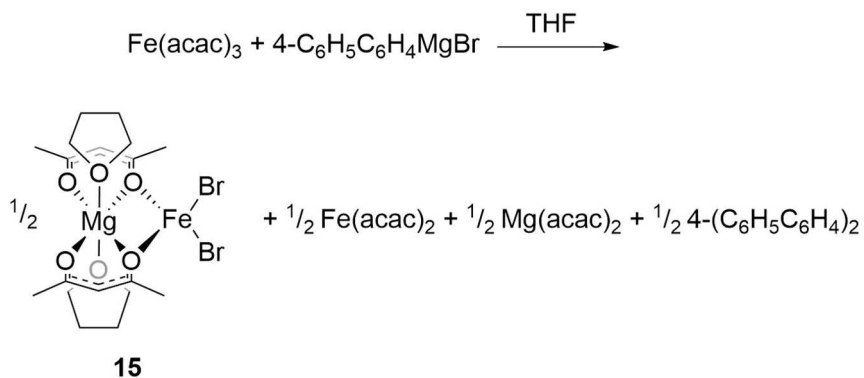


Figure 7.2. Annotated ^1H NMR spectra of the reaction filtrate following removal of 4-quaterphenyl in the reaction of $\text{Fe}(\text{acac})_3$ with one equivalent of 4-biPhMgBr. A portion of the diamagnetic region has been enlarged to show the peaks belonging to $\text{Mg}(\text{acac})_2$.

The overall reaction stoichiometry can now be defined as presented in Scheme 7.1. An equimolar reaction between $\text{Fe}(\text{acac})_3$ and 4-biphenylMgBr produces half an equivalent each of $\text{FeBr}_2(\mu\text{-acac})_2\text{Mg}(\text{THF})_2$ (**15**), $\text{Fe}(\text{acac})_2$, $\text{Mg}(\text{acac})_2$ and 4-quaterphenyl.



Scheme 7.2. The equimolar reaction of $\text{Fe}(\text{acac})_3$ and 4-biPhMgBr.

The reaction mixture produced is highly air sensitive, when exposed to air the dark yellow/ brown solution near immediately turns red. ^1H NMR spectroscopy confirms this is consummate with the reformation of $\text{Fe}(\text{acac})_3$. $\text{Fe}(\text{acac})_2$ appears to be slightly more air sensitive than **15** as when the sample is deliberately exposed to air and a ^1H NMR spectrum taken periodically the $\text{Fe}(\text{acac})_2$ peak becomes depleted first while $\text{Fe}(\text{acac})_3$ grows in.

7.4.3.2 *Infra-Red Spectroscopy.*

An IR spectrum of the reaction filtrate was also collected. The Fe species can be identified by the acac^- C-O, C-C and C-H stretches as presented in Figure 7.3. An aliquot of the reaction filtrate produces the spectral response represented by the black solid line. The two Fe(II) species can be confirmed by comparison to the spectra obtained for genuine samples (dashed lines) of **15** (orange) and $\text{Fe}(\text{acac})_2$ (blue). Similar to the ^1H NMR spectrum the IR spectrum is contaminated with small amounts of $\text{Fe}(\text{acac})_3$ (red) owing to the high air sensitivity.

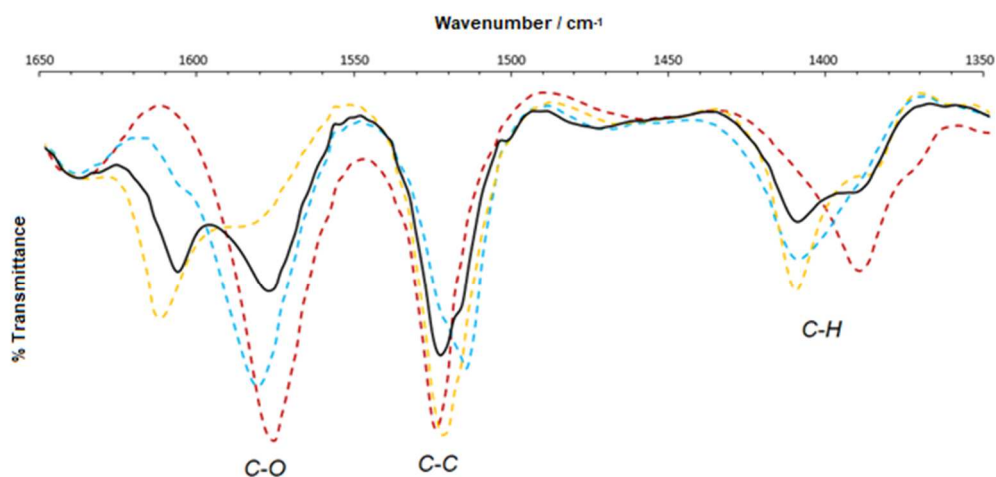
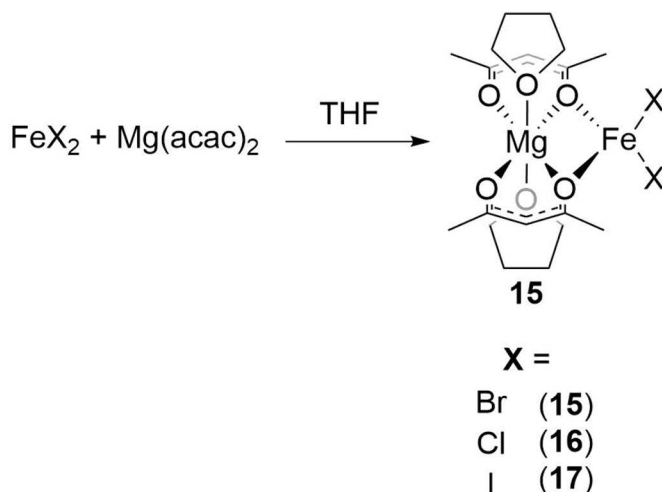


Figure 7.3. Comparison of the IR spectra of the crude reaction mixture resulting from the equimolar reaction of $\text{Fe}(\text{acac})_3$ with 4-biPhMgBr (black, solid line), to genuine samples of **15** (orange, dashed line), $\text{Fe}(\text{acac})_2$ (blue, dashed line) and $\text{Fe}(\text{acac})_3$ (red, dashed line).

7.4.4 An Alternate Grignard Free Route to Fe-Mg Intermetallic Pre-Catalysts.

In interest of producing the intermetallic complex in greater yields FeBr_2 was found to react with $\text{Mg}(\text{acac})_2$ in THF on slight warming (*ca.* 40 °C) producing bright yellow solutions of **15** (Scheme 7.2). The reaction proceeds stoichiometrically with yields in excess of 90 % following crystallisation by slow diffusion of hexanes into the reaction mixture. By contrast MgBr_2 was found to be unreactive with $\text{Fe}(\text{acac})_2$ even at reflux in THF. The energy requirements for total ligand exchange are therefore much less favourable, perhaps due to the high lattice enthalpy of MgBr_2 .



Scheme 7.3. The synthesis of $\text{X}_2\text{Fe}(\mu\text{-acac})_2\text{Mg}(\text{THF})_2\text{X}$ (X = Br, Cl or I (**15** – **17**)) by reaction of ferrous halide salts FeX_2 , X = Br, Cl or I with $\text{Mg}(\text{acac})_2$.

The reactions of FeCl_2 and FeI_2 with $\text{Mg}(\text{acac})_2$ similarly proceed to produce $\text{X}_2\text{Fe}(\mu\text{-acac})_2\text{Mg}(\text{THF})_2\text{X}$ = Cl (**16**) and I (**17**) respectively (Scheme 7.2). Because the ferrous salts are poorly soluble in THF they were typically ground into a fine precipitate in a pestle and mortar to aid dissolution. In the process it was discovered that FeI_2 would in fact react with $\text{Mg}(\text{acac})_2$ in the solid state to produce yellow precipitates of **17**.

Because $\text{Mg}(\text{diketone})_2$ derivatives can be synthesised very easily, this route could potentially allow the generation of a diverse range of pre-catalyst complexes, a more convenient route than preparation via the related Fe(III) complex and Grignard reagents.

7.4.5 Grignard Screening.

The initial choice of Grignard reagent, 4-biPhMgBr was made for convenience of isolation and spectroscopic assignment. But because different Grignard reagents clearly display very different reactivity in catalysis. It is therefore important to determine if the generation of the two Fe(II) species will be the same regardless of the choice of Grignard reagent. The difference in reactivity is usually attributed to the presence or absence of a β -hydride or less often, to the reductive capacity of the Grignard. To this effect Figure 7.4. shows the ^1H NMR spectra of the crude reaction mixture when

$\text{Fe}(\text{acac})_3$ is reacted with one equivalent of RMgBr where $\text{R} = \text{Ph, Tol, Mes, Me, allyl}$ and 1-propynyl . In all cases this initial reduction indeed produces both $\text{Fe}(\text{acac})_2$ and **15** in all cases.

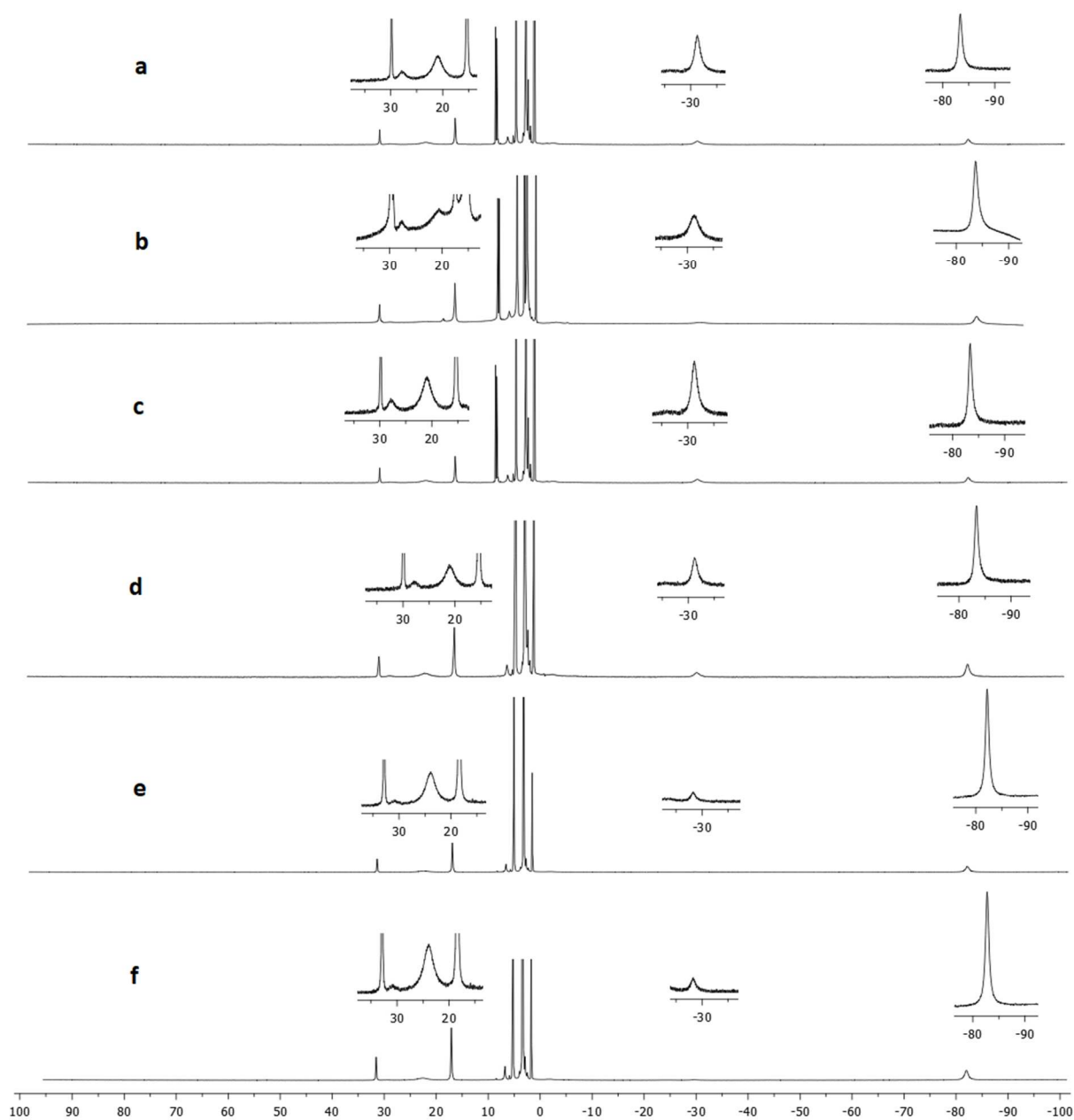
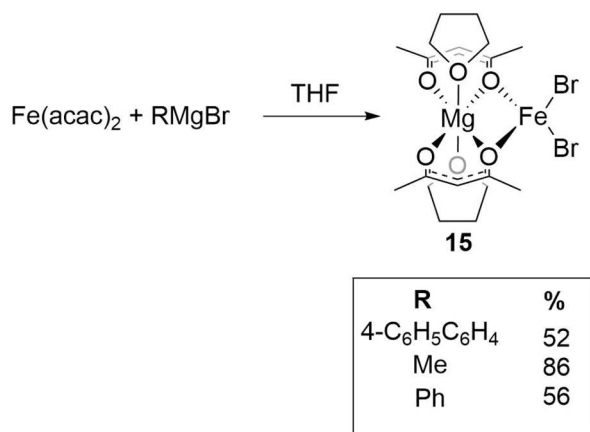


Figure 7.4. ^1H NMR spectra of the crude reaction mixtures for the reaction of $\text{Fe}(\text{acac})_3$ with one equivalent of a) PhMgBr b) TolMgBr c) MesMgBr d) MeMgBr , e) allylMgBr and f) 1-propynylMgBr .

The choice of Grignard generally has a small impact upon the isolated yields of **15**, several Grignard reagents are contrasted in Scheme 7.4 but the use of MeMgBr gives a significant improvement. This can potentially be attributed to an increased entropic driving force because the homo-coupled by-product, ethane is a gas but the removal for the requirement of filtration also reduces transfer loss and inadvertent exposure to air.



Scheme 7.4. Isolated yields of **15** based on choice of Grignard reagent.

The identity of the halide in the Grignard reagent also dictates the identity of the halide in the intermetallic complex. Complexes **16** (X = Cl) and **17** (X = I) can similarly be produced alongside Fe(acac)₂ when Fe(acac)₃ is reduced with a chloro or iodo Grignard respectively. Figure 7.5 shows the crude reaction mixtures generated when Fe(acac)₃ is treated with one equivalent of PhMgX where X = Br, Cl or I.

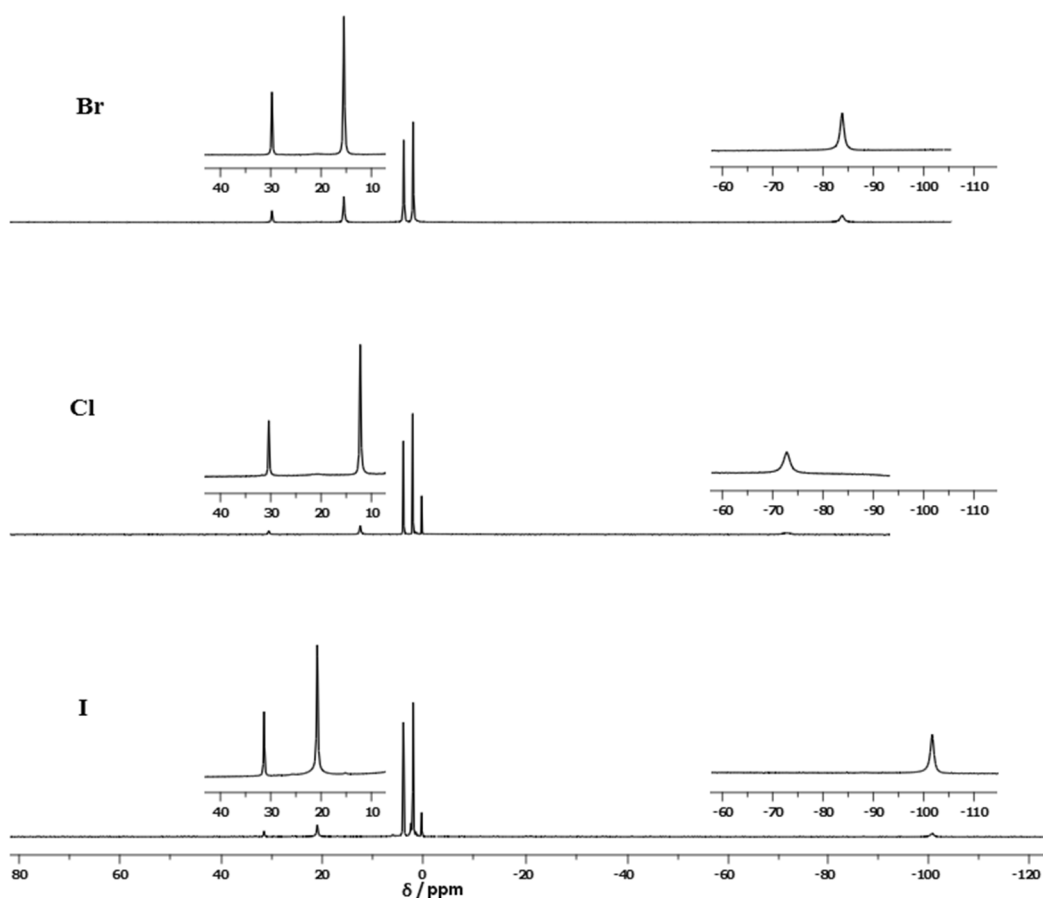


Figure 7.5. ^1H NMR spectra of the crude reaction mixtures resulting from treatment of $\text{Fe}(\text{acac})_3$ in THF treated with one equivalent PhMgBr (top), PhMgCl (middle) and PhMgI (bottom).

7.4.6 Characterisation.

7.4.6.1 ^1H NMR Spectroscopy

The ^1H NMR spectra of crystalline samples of **15** - **17** in d_8 -THF is presented in Figure 7.6. The complexes have three unique proton environments, two of which fall in the downfield region and one in the upfield region.

The peaks integrate to 3 : 1 : 3 and correlate to acac^- methyl, methine and methyl protons respectively. The complexes are paramagnetic and the methyl group that lies over the Fe is significantly shielded by the metal d-electrons hence the large shift upfield.

The identity of the halide produces a very minimal shift in the CH_3 group distant from the metal centre and a moderate shift in the acac^- methine such that it becomes less separated from the upfield CH_3

environment. The CH₃ environment which is shielded by the Fe centre sees a very large chemical shift and the extent of the shift up-field can be directly related to the π-donor capacity of the halide (I > Br > Cl) -101.8, -83.49 and -73.22 ppm respectively. The chemical shifts for all three proton environments are summarised in Table 7.2.

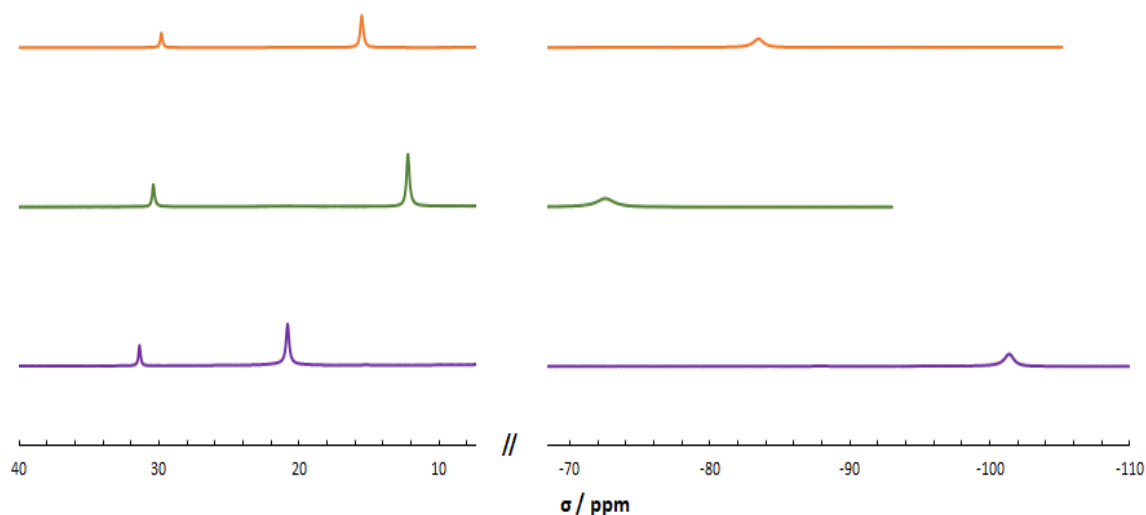


Figure 7.6. ¹H NMR spectra of complexes **15** (orange), **16** (green) and **17** (purple). The diamagnetic region of the spectra containing only residual solvent peaks has been omitted.

Table 7.2. ¹H NMR spectroscopy chemical shifts of FeX₂(μ-acac)₂Mg(THF)₂ X = Br, Cl or I (**15** – **17**).

| chemical shift δ / ppm | | | |
|------------------------|-----------------|-------|-----------------|
| Complex | CH ₃ | CH | CH ₃ |
| X = Br (15) | 29.90 | 15.40 | -83.49 |
| X = Cl (16) | 30.02 | 12.35 | -73.22 |
| X = I (17) | 31.36 | 20.88 | -101.8 |

7.4.6.2 Magnetic Susceptibility

Fe(acac)₂ and complex **15** are both paramagnetic. The magnetic susceptibility, χ (units of Bohr magnetons) for each complex was determined by the Evans method. In brief this method compares the chemical shift of the NMR solvent (*d*₈-THF in this case) in the absence and presence of the paramagnetic species.^{24,25} The spin-only contribution can be calculated using equation 7.1 where *n* is

the number of unpaired electrons. The calculated values described herein account for diamagnetic ligand contributions.

$$\mu_{so} = \sqrt{n(n + 2)} \quad \text{eqn. 7.1}$$

The magnetic moment for $\text{Fe}(\text{acac})_3$ was determined to be $\mu_{\text{eff}} = 5.86$ B.M. This is consistent with an octahedral d^5 HS complex, $\mu_{so} = 5.92$ B.M. after ligand corrections and as reported in the literature.²⁶

Complexes **15** has an electron configuration $[\text{Ar}] 3d^6$ but is pseudo tetrahedral. Tetrahedral complexes are almost exclusively HS so 4 unpaired electrons are expected. The calculated magnetic moments, $\chi = 6.02$ B.M. is higher than typical for a HS Fe(II) complex. Complexes **16** and **17** were consistent within experimental error. The observed magnetic moment for a related complex, $\text{Fe}(\text{Br})_2(\mu\text{-Br})_2\text{Mg}(\text{THF})_4$ has been previously reported by Kobayashi *et al.*²⁷ was similar at $\chi = 6.14$ B.M. and attributed to ferromagnetic coupling between aggregated species.

$\text{Fe}(\text{acac})_2$ has an electron configuration $[\text{Ar}] 3d^6$ and forms the octahedral complex $\text{trans-Fe}(\text{acac})_2(\text{THF})_2$ on coordination of THF solvent molecules. A HS complex with 4 unpaired electrons is expected as acac^- ligands are relatively poor π -acceptors so are weak-field ligands and likely to produce a small crystal field splitting (Δ). The calculated magnetic moment, $\chi = 4.06$ B.M. is much less than the spin only contribution $\mu_{so} = 4.9$ or expected values for an octahedral HS Fe(II) complexes.

7.4.6.3 X-Ray Crystallography

The solid-state structures of **15** - **17** as determined by single crystal x-ray diffraction are presented in Figures 7.7, 7.8 and 7.9 respectively along with selected bond lengths and angles. A number of key bond lengths and angles for all three complexes are collected for ease of comparison in Tables 7.3 and 4.

Table 7.3. Selected bond lengths for the series $\text{FeX}_2(\mu\text{-acac})_2\text{Mg}(\text{THF})_2$ X = Br (**15**), Cl (**16**) and I (**17**).

| Complex | Average Values (Å) | | | | | |
|----------------------|--------------------|------------|----------|----------------------|---------------------|---------------------|
| | Fe – Mg (Å) | Fe-X | Fe-O | Mg-O _{acac} | Mg-O _{THF} | C-O _{acac} |
| X = Br (15) | 3.1631(12) | 2.4168(7) | 2.052(3) | 2.030(2) | 2.119(3) | 1.280(4) |
| X = Cl (16) | 3.1900(12) | 2.2391(11) | 2.070(3) | 2.027(2) | 2.109(3) | 1.280(4) |
| X = I (17) | 3.1607(9) | 2.5920(4) | 2.048(3) | 2.033(19) | 2.107(7) | 1.282(3) |

Table 7.4. Selected bond angles (°) for the series $\text{FeX}_2(\mu\text{-acac})_2\text{Mg}(\text{THF})_2$ X = Br (**15**), Cl (**16**) and I (**17**).

| Complex | X1-Fe-X2 | O1-Fe-O2 | O1-Fe-X1 | O1-Mg-O2 | O5-Mg-O6 |
|----------------------|-------------|----------|-----------|-----------|------------|
| X = Br (15) | 126.47(3) | 79.34(9) | 114.27(7) | 79.18(10) | 177.68(12) |
| X = Cl (16) | 125.52(5) | 77.72(9) | 110.91(8) | 78.80(10) | 177.15(12) |
| X = I (17) | 125.390(16) | 79.79(7) | 112.76(5) | 79.14(7) | 178.37(8) |

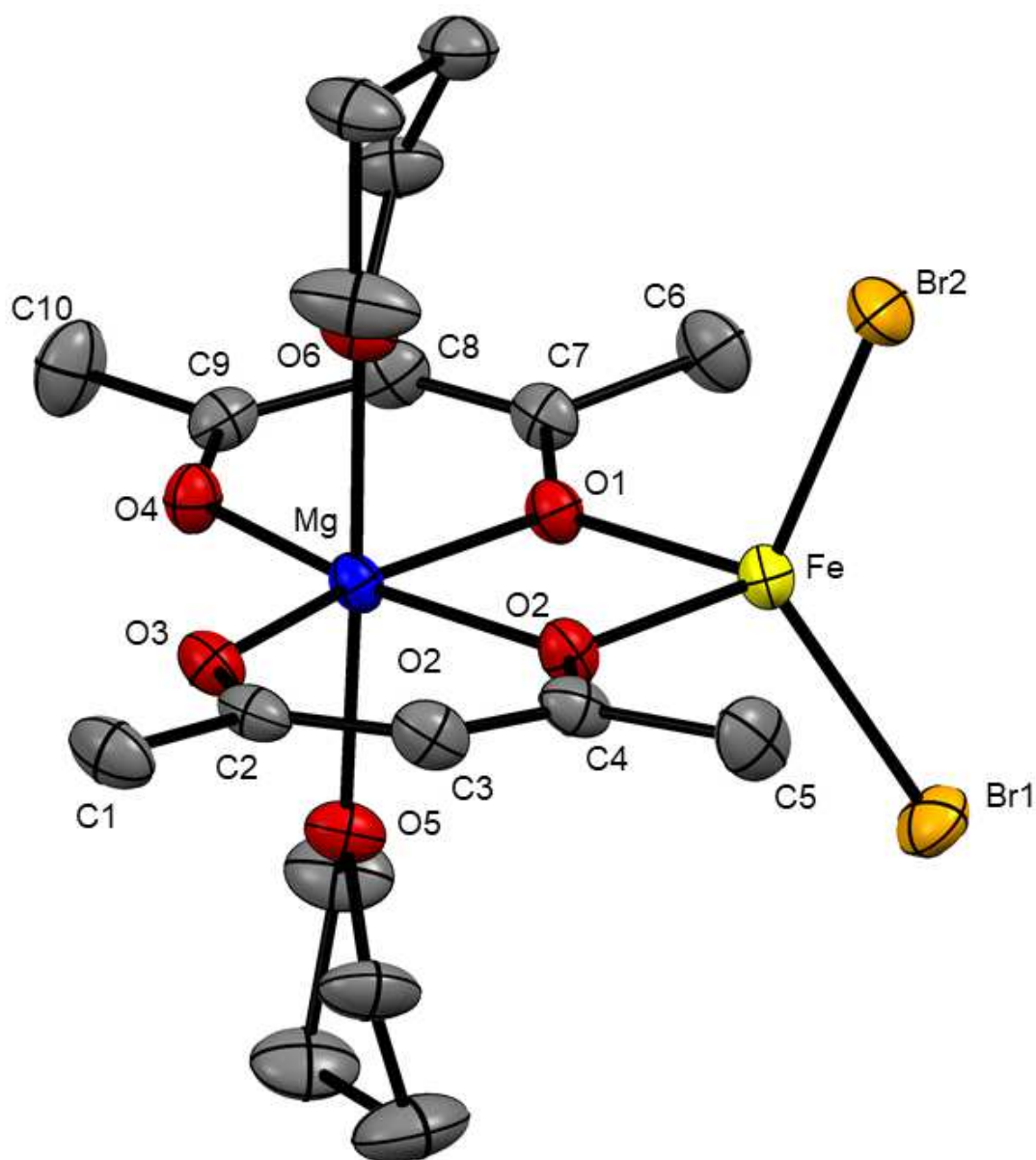


Figure 7.7. Crystal structure of $\text{FeBr}_2(\mu\text{-acac})_2\text{Mg}(\text{THF})_2$ (**15**) determined by single crystal XRD. Thermal ellipsoids shown at 50 % probability. Hydrogen atoms removed for clarity. Selected bond lengths (\AA): Fe...Mg = 3.1631(12), Fe-Br1 = 2.4411(7), Fe-Br2 = 2.3925(6), Fe-O1 = 2.058(2), Fe-O2 = 2.046(2), Mg-O1 = 2.056(3), Mg-O2 = 2.054(3), Mg-O3 = 2.002(3), Mg-O4 = 2.007(3), Mg-O5 = 2.098(3), O1-C7 = 1.302(4), O2-C4 = 1.307(4), O3-C2 = 1.256(4), O4-C9 = 1.255(4). Selected bond angles ($^\circ$): Br1-Fe-Br2 = 126.47(3), O1-Fe-O2 = 79.34(9), O1-Mg-O2 = 79.18(10), O3-Mg-O4 = 107.18(11), O5-Mg-O6 = 177.68(12).

The Fe...Mg distance in **15** is 3.1631(12) Å, beyond the covalent radii of the two metals (1.41 Å Mg and 1.52 Å Fe)²⁸ indicating there is no bonding character between the metals. The separation is shorter than that found in FeBr₂(μ-Br)₂Mg(THF)₄ at 3.656 Å (X = Br) reported by Kobayashi *et. al.*²⁷ The Fe-Br bond lengths are 2.4411(7) and 2.3925(6) Å. The Fe centre can be considered pseudo-tetrahedral; the Br-Fe-Br bond angle is 126.47(3) °, the average O-Fe-Br bond angle is 113.49(7) ° but the O1-Fe-O2 bond angle is just 79.34(9) °. The O atoms are effectively pushed together due to their requirement to bridge both metal centres while the halogen can spread out in a relatively uncrowded position in the coordination environment. The bond lengths between the bridging O atom to each of the metals is however identical within statistical error. The Fe-O1 and Fe-O2 bond lengths are 2.056(2) and 2.058(2) Å where the analogous Mg-O bond lengths are 2.056(3) and 2.054(3) Å. The magnesium centre is octahedral. The bond angles across the chelating bonds in each acac⁻ ligand are slightly reduced from 90 ° at 86.90(10) ° in O1-Mg-O4 and 86.75(11) in O2-Mg-O3 and the bond angle between the THF molecules, O5-Mg-O6 being close to 180 ° at 177.68(12). The Mg-O bond lengths between the μ-O atoms (O1 and O2) Fe are shorter than those on the other half of the molecule (O1 and O3) the averages being 2.055(3) and 2.005(3) Å respectively. The opposite trend is observed in the O-C bond lengths, with those closer to Fe centre (O1-C7 and O2-C4) being longer at 1.302(4) and 1.307(4) Å and those distant from the Fe centre (O3-C2 and O4-C9) being shorter at 1.256(4) and 1.255(4) Å).

The average Mg-O bond length in the acac⁻ ligands is 2.030(3) Å, much shorter than the Mg-O bond length to the THF solvent molecules where the average bond length is 2.119(3) Å. The chelating binding mode in acac⁻ ligand is expected to produce a stronger bond compared to that between the coordination of a soft ligand to a hard metal such as the Mg²⁺ cation.

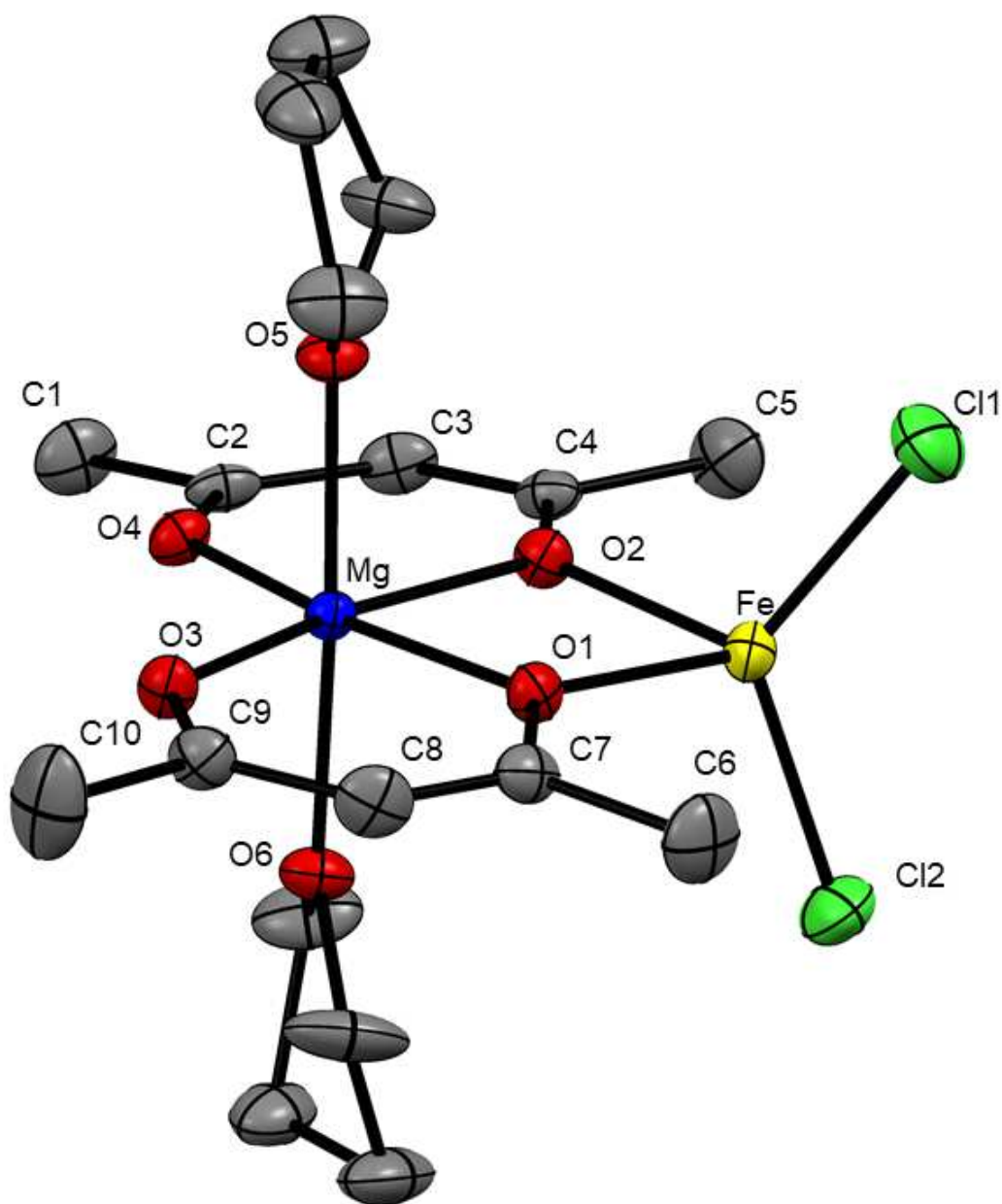


Figure 7.8. Crystal structure of $\text{FeCl}_2(\mu\text{-acac})_2\text{Mg}(\text{THF})_2$ (**16**) determined by single crystal XRD. Thermal ellipsoids shown at 50 % probability. Hydrogen atoms removed for clarity. Selected bond lengths (\AA): Fe–Mg = 3.1900(12), Fe–Cl1 = 2.2368(11), Fe–Cl2 = 2.2413(11), Fe–O1 = 2.076(2), Fe–O2 = 2.064(2) \AA , Mg–O1 = 2.051(3), Mg–O2 = 2.042(3), Mg–O3 = 2.004(2), Mg–O4 = 2.010(3), Mg–O5 = 2.104(3), Mg–O6 = 2.114(3), O1–C7 = 1.302(4), O2–C4 = 1.306(4), O3–C2 = 1.256(4), O4–C9 = 1.256(4). Selected bond angles ($^\circ$): Cl1–Fe–Cl2 = 125.52(5), O1–Fe1–O2 = 77.72(9), O1–Mg–O2 = 78.80(10), O3–Mg–O4 = 107.28(11), O5–Mg–O6 = 177.15(12).

The Fe...Mg distance is longest in **16** at 3.1900(12) Å but is again shorter than found in the analogous $\text{FeCl}_2(\mu\text{-Cl})_2 \text{Mg}(\text{THF})_4$ at 3.455(3) Å, reported by Sorota *et. al.*²⁹ By contrast the Fe-X bond lengths Fe-Cl1 and FeCl2 are the shortest of the series at 2.2368(11) Å and 2.2413(11) Å, respectively. The Cl-Fe-Cl bond angle is reduced from **15** at 125.52(5) ° and similarly, the average O-Fe-Cl and the O1-Fe-O2 bond angles are also reduced at 108.90(8) ° and 77.72(9) respectively. Separation from the Mg centre thus produces a tightening of the bond angles in the coordination environment around the Fe centre.

The decrease in the Fe-Cl bond length is compensated by an increase in the average Fe-O bond length to 2.070(2) Å from 2.058(2) Å. This bond lengthening produces the increase in the Fe...Mg separation as the Mg-O1 and Mg-O2 bond lengths remain fairly constant, the average being just slightly short than in **15** at 2.050(3) vs being 2.055(3) Å. The average Mg-O3 and Mg-O4 bond lengths and O1-Mg-O2 bond angle are also within error, consistent with **15**.

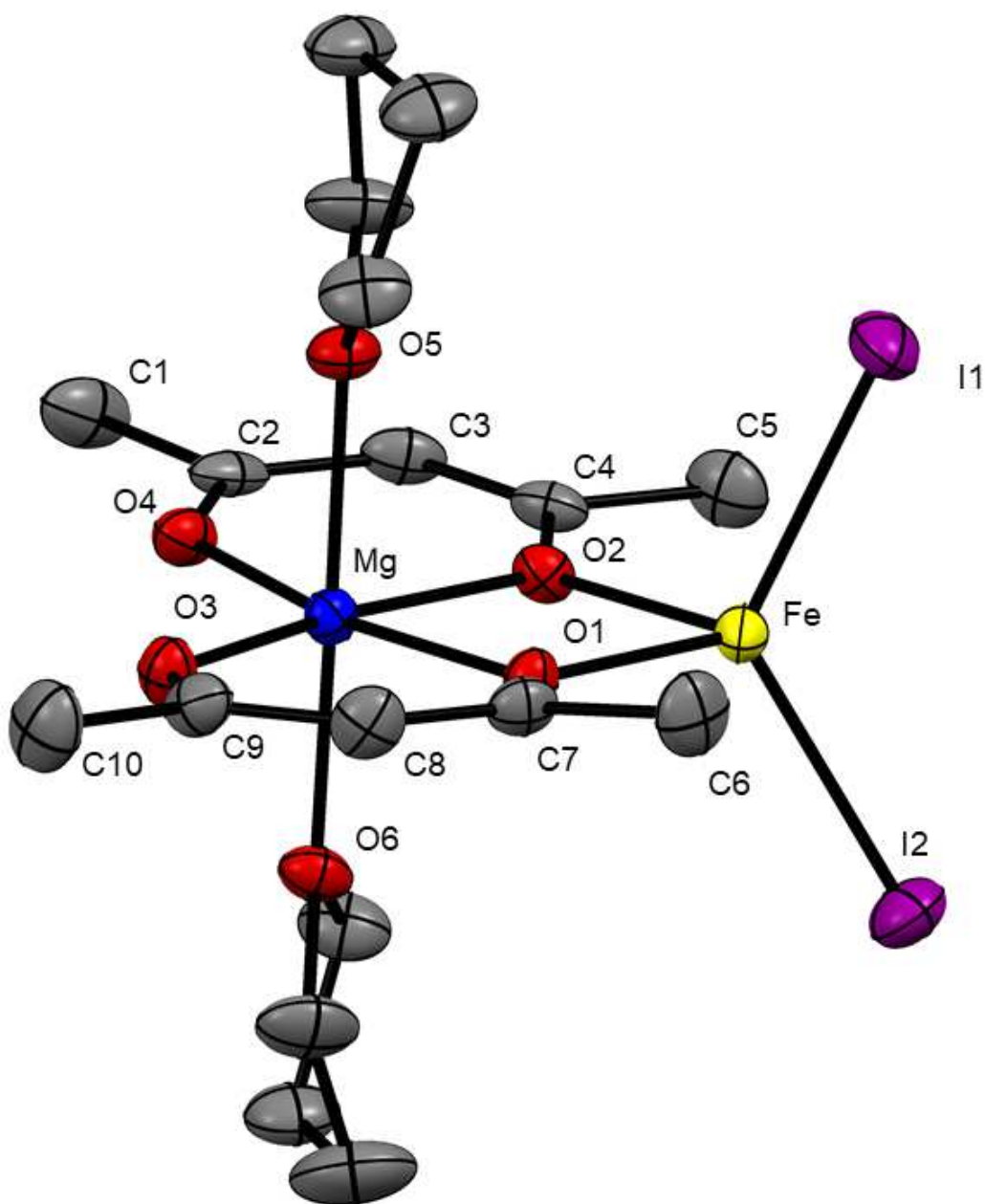


Figure 7.9. Crystal structure of $\text{Fe}_2(\mu\text{-acac})_2\text{Mg}(\text{THF})_2$ (**17**) determined by single crystal XRD. Thermal ellipsoids shown at 50 % probability. Hydrogen atoms removed for clarity. Selected bond lengths (Å): Fe–Mg = 3.1607(9), Fe–I1 = 2.5943(4), Fe–I2 = 2.5905(4), Fe–O1 = 2.0429(17), Fe–O2 = 2.0530(18), Mg–O1 = 2.0594(19), Mg–O2 = 2.0646(18), Mg–O3 = 2.0068(19), Mg–O4 = 2.0016(19), Mg–O5 = 2.101(2), Mg–O6 = 2.1334(19), O1–C7 = 1.310(3), O2–C4 = 1.305(3), O3–C2 = 1.257(3), O4–C9 = 1.257(3). Selected bond angles (°): I1–Fe–I2 = 125.390(16), O1–Fe–O2 = 79.79(7), O1–Mg–O2 = 79.14(7), O3–Mg–O4 = 106.81(8), O5–Mg–O6 = 178.37(8).

The Fe^{III}Mg distance is shortest in **17** at 3.1607(9) Å. No analogous FeCl₂(μ-Cl)₂Mg(THF)₄ complex is available in the literature. The Fe-X bond lengths Fe-I1 at 2.5905(4) Å and Fe-I2 at 2.5943(4) Å are the largest of the series, and the X1-Fe-X2 bond angle of 125.390(16) ° the smallest.

The reduced Fe^{III}Mg distance is reflected in the shortest Fe-O1 and Fe-O2 bond lengths of 2.0429(17) and 2.0530(18) and a slightly widened O1-Fe-O2 bond angle of 79.97 °. The Mg-O1 and Mg-O2 bond lengths and O1-Mg-O2 bond angles are closely matched throughout the series.

The identity of the halogen atoms has little impact upon the coordination environment of the Mg atom, even the Mg-O1 and Mg-O2 bond lengths and O1-Mg-O2 bond angle remain fairly consistent across the series. Unsurprisingly, it is the Fe coordination environment that is affected most significantly. If related to the strength of the ligand π-donation, increasing in the series Cl < Br < I the following trends are observed;

- The Fe-X bond length increases.
- The Fe-O bond length decreases.
- The O-Fe-O bond angle increases.
- The Fe^{III}Mg separation decreases.

7.4.6.4 *Infra-Red Spectroscopy.*

The IR spectra of complexes **15** – **17** are presented in Figure 7.10. Only minimal shifts of 1 – 3 cm⁻¹ are observed for the acac⁻ C-O, C-C and C-H stretches. This is consistent with the x-ray crystal structures where the identity of halogen atom only has a minimal impact upon the acac⁻ coordination environment in terms of bond lengths and angles.

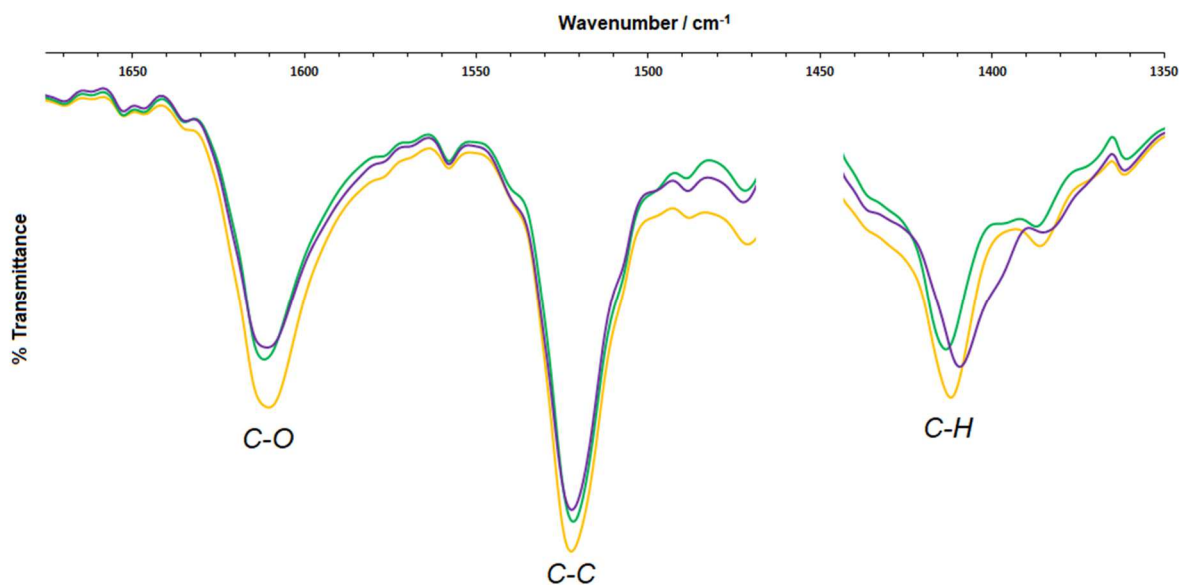


Figure 7.10. The IR spectra for complexes **15** (yellow), **16** (green) and **17** (purple) containing acac- C-O, C-C and C-H stretches. A portion of the spectra has been omitted as it contained a strong THF absorbance.

7.4.6.5 Cyclic Voltammetry

In ^1H NMR spectra containing equimolar amounts of **15** and $\text{Fe}(\text{acac})_2$, the latter is the more easily oxidised of the two Fe(II) complexes. Upon exposure to air the peaks corresponding to $\text{Fe}(\text{acac})_2$ are first depleted as $\text{Fe}(\text{acac})_3$ peaks grow. Oxidation of **15** also regenerates $\text{Fe}(\text{acac})_3$ based on ^1H NMR and infra-red spectroscopy.

The reduction potentials of the two species are of more interest in the context of catalysis. To quantify this cyclic voltammetry was performed. Figure 7.11 shows the CV's of complexes **15** – **17** and $\text{Fe}(\text{acac})_2$ performed in THF using 0.1 M TBAPF₆ electrolyte at 100 mVs⁻¹ scan rate. Information taken from the CV experiment is collated in Table 7.5. All potentials are referenced vs. the Fc/Fc^+ redox couple occurring at 0.0 V.

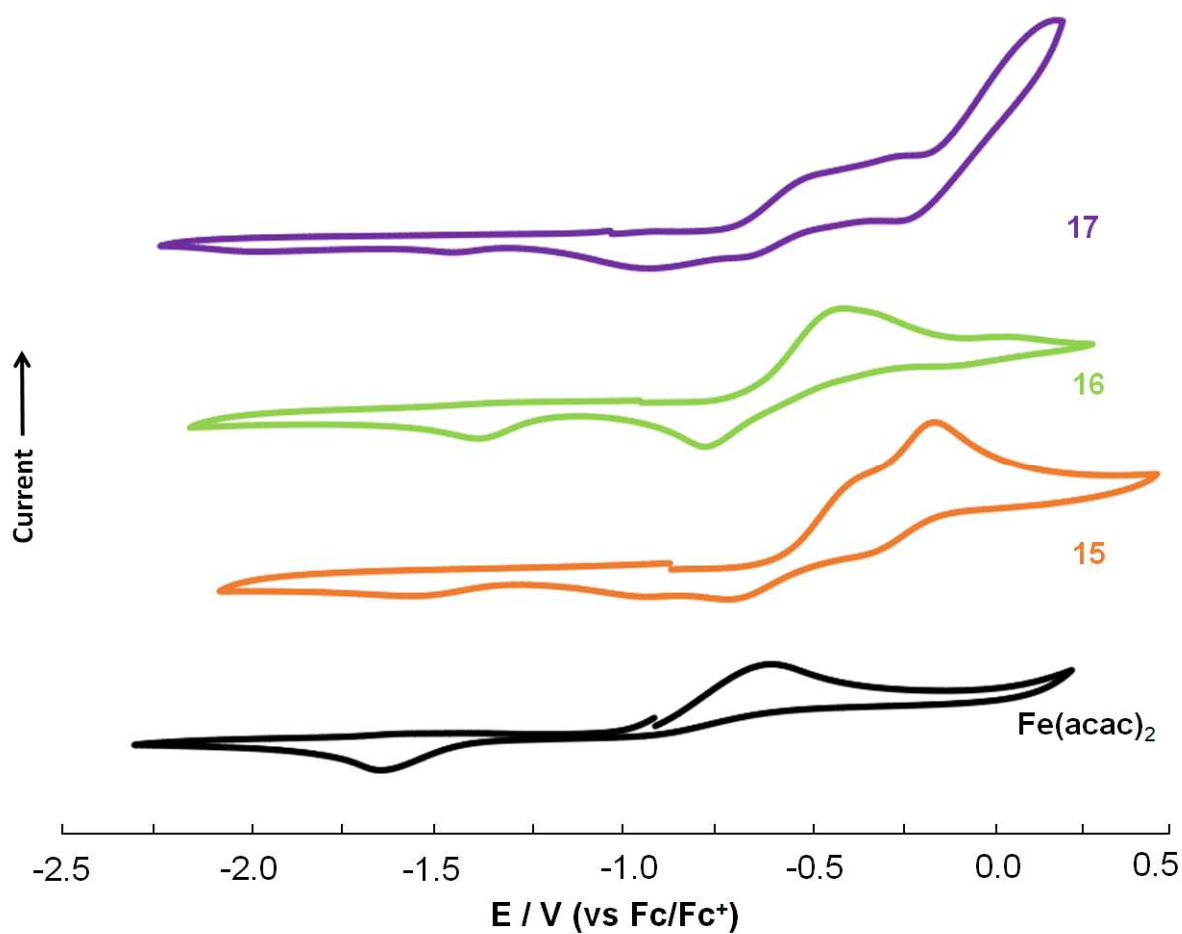


Figure 7.11. Cyclic Voltammograms of $\text{Fe}(\text{acac})_2$ (black) and $\text{FeX}_2(\mu\text{-acac})_2\text{Mg}(\text{THF})_2$ X = Br (**15**, orange), X = Cl (**16**, green) and X = I (**17**, purple). Measurements taken in THF 0.1 M TBAPF electrolyte at 100mVs^{-1} scan rate. Referenced vs Fc/Fc^+ redox couple.

Table 7.5. Electrochemical data for Fe(acac)₂ and FeX₂(μ-acac)₂Mg(THF)₂ X = Br, Cl and I (**15** – **17**).

| Complex | E _{pc} (1) ^{red} / V | E _{1/2} (2) ^{ox} / V | E(3) / V |
|-----------------------|--|--|----------|
| X = I (17) | -1.39 | several overlapping processes | |
| X = Cl (16) | -1.33 | -0.51 | --- |
| X = Br (15) | -1.51 | -0.49 | -0.23 |
| Fe(acac) ₂ | -1.61 | -0.63 | --- |

In complexes **15** - **17** multiple oxidations are observed. There are two well resolved pseudo-reversible processes observed for **15** occurring at E_{1/2}(1)^{ox} = -0.49 and E_{1/2}(2)^{ox} = - 0.23 V. In **16** what appears as a single pseudo-reversible at E_{1/2}(1)^{ox} = -0.51 V but given the broad appearance, it may be two poorly resolved processes. Use of DPV was ineffective in clarifying this issue. In **17** it is more complex, but this complex did appear the most prone to decomposition in the experimental setup so may be attributed to oxidative decomposition. In Fe(acac)₂ a single irreversible oxidation is observed at E_{pc}(1) = -0.15 V, assigned as the Fe(acac)₂ / Fe(acac)₂⁺ couple. This couple is cathodically shifted, and thus easier to oxidise by comparison to complexes **15** – **17**. This is consistent with the previously discussed observation in the ¹H NMR spectroscopy experiments that Fe(acac)₂ decomposes to Fe(acac)₃ preferentially upon oxidation.

The reductions are of more interest as they could be informative of the complexes capacity to be further reduced by Grignard reagents as in catalytic conditions. There is one irreversible reduction common to each complex occurring at E_{pc}(1)^{red} = -1.51, -1.33 and -1.39 V in complexes **15** – **17** and -1.61 V in Fe(acac)₂. Fe(acac)₂ is thus the most difficult to reduce of the four complexes, anodically shifted by 0.10 V from **15**. By contrast a separation of 0.20 V exists between the most easily reduced complex (**16**) and difficult to reduce (**15**) complex of that series. The differences in reduction potentials are quite subtle and unlikely to produce significant differences in reactivity. The identical catalytic

activity discussed in chapter 8 and results of the stoichiometric reactions of complexes **15** and $\text{Fe}(\text{acac})_2$ with Grignard reagents discussed in chapter 9 all give credence to a shared catalytic species.

7.5 Competing Pre-Catalysts?

7.5.1 Comparison of Pre-Catalyst Activity in Literature Reactions.

The fact that two Fe(II) species are produced upon addition of only one equivalent of Grignard means there is potential for divergent catalytic processes from the onset. To test this hypothesis the pre-catalysts were first employed in place of $\text{Fe}(\text{acac})_3$ in the spirocyclisation of 2-[(2-iodophenoxy)methyl]furan (entry 1, Table 7.6) originally reported by our collaborators, Sweeney *et al.*³⁰ Following this, the Fe(II) species were used in place of $\text{Fe}(\text{acac})_3$ in a series of more traditional literature cross-coupling reactions. The catalytic activity of the pre-catalysts was compared based on isolated product yields. Table 8.6 presents the results of these experiments. The isolated yields for the literature $\text{Fe}(\text{acac})_3$ catalysed reaction is also noted in brackets for comparison. The activity of the $\text{FeX}_2(\mu\text{-acac})_2\text{Mg}(\text{THF})_2$ X = Cl and X = I complexes, **16** and **17** respectively were also explored, but as identical behaviour was expected and in the interests of time they were only employed in entry 2.

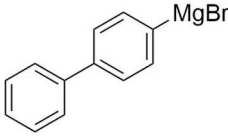
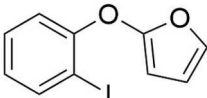
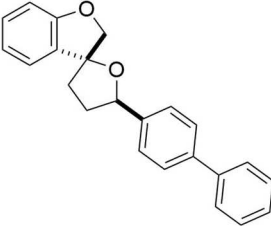
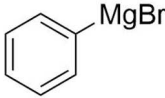
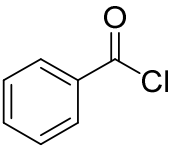
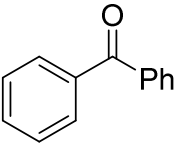
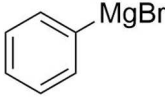
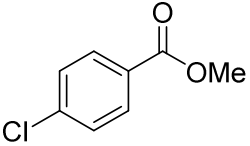
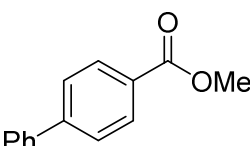
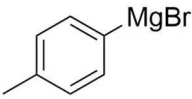
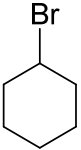
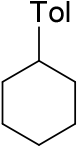
Initially the selected reactions were limited to the use of aryl Grignard reagents as at this stage the use of other Grignard reagents as discussed in section 8.3.2 was not confirmed. The air-sensitive reaction procedure in entries 1 – 9 were performed by myself with subsequent isolation and purification by Dr Birkett. In all cases the isolated yields are comparable between $\text{Fe}(\text{acac})_3$ and the two Fe(II) complexes. The isolated yields for $\text{Fe}(\text{acac})_3$ were in most cases comparable to that quoted in the literature but in a few cases the yields were reduced, but always consistent with the results of the two Fe(II) complexes.

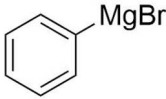
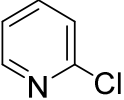
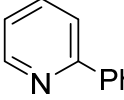
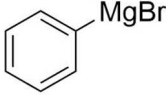
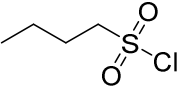
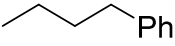
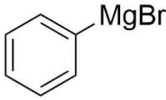
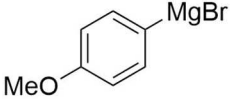
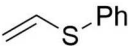
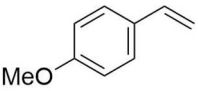
This information serves to confirm the two Fe(II) species are both pre-catalysts, it suggests that each may ultimately be converted to an identical catalytic species. It is not however sufficient evidence alone to confirm this nor rule out the possibility of one dominant species with any number of minor

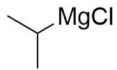
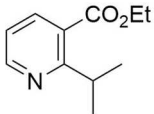
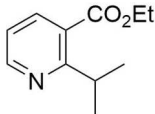
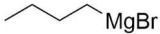
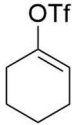
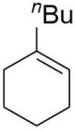
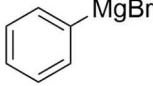
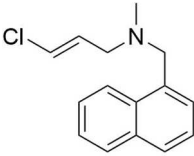
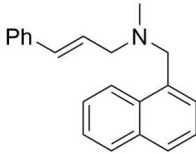
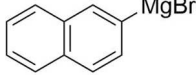
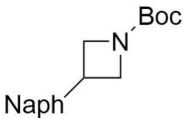
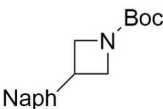
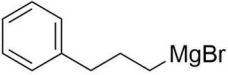
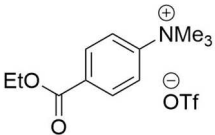
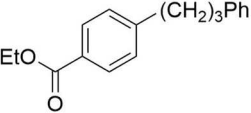
less kinetically labile competing species. In future work we aim to perform the kinetic studies that will be necessary to determine this.

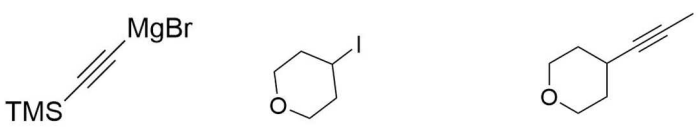
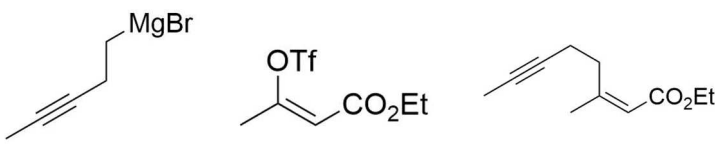
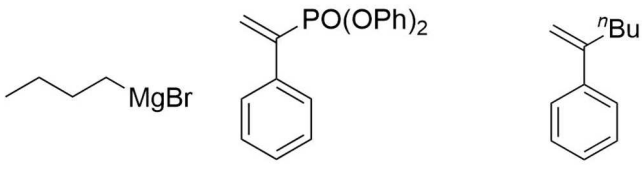
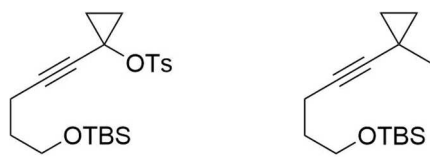
As it became clear the two Fe(II) species have identical behaviour, the scope of this work was expanded for publication to show this would apply for a more diverse substrate and Grignard scope. Post-doctoral researcher Dr Anthony Ball was responsible for the selection of these reactions and the experimental work therein. This work is included for comparison. The table was now extended to 17 entries. The performance of Fe(acac)₃, **15** and Fe(acac)₂ is identical again in all cases so is further evidence that the initial reduction to produce the two Fe(II) is the first step irrespective of reaction conditions.

Table 7.6. Selected literature $\text{Fe}(\text{acac})_3$ catalyzed cross-coupling reactions where the catalyst is substituted for $\text{FeX}_2(\mu\text{-acac})_2\text{Mg}(\text{THF})_2$ $\text{X} = \text{Cl}, \text{Br}$ or I (**15** – **17**), $\text{Fe}(\text{acac})_2$. The isolated yield reported for $\text{Fe}(\text{acac})_3$ in the original publication is noted in brackets. Entries 1- 9 by Lee Brown & James Birkett. Entries 10 – 17 by Dr Anthony Ball.

| Entry | Grignard | Substrate | Product | Catalyst | Isolated Yield (%) |
|----------------------------|---|---|--|----------------------------|--------------------|
| 1 ³⁰ |  |  |  | $\text{Fe}(\text{acac})_3$ | 98 (98) |
| | | | | 15 | 97 |
| | | | | $\text{Fe}(\text{acac})_2$ | 97 |
| 2 ³¹ |  |  |  | $\text{Fe}(\text{acac})_3$ | 62(75) |
| | | | | 15 | 61 |
| | | | | 16 | 61 |
| | | | | 17 | 60 |
| $\text{Fe}(\text{acac})_2$ | 58 | | | | |
| 3 ³² |  |  |  | $\text{Fe}(\text{acac})_3$ | 24 |
| | | | | 15 | 24 |
| | | | | $\text{Fe}(\text{acac})_2$ | 22 |
| 4 ³³ |  |  |  | $\text{Fe}(\text{acac})_3$ | 54 |
| | | | | 15 | 53 |
| | | | | $\text{Fe}(\text{acac})_2$ | 51 |

| | | | | | |
|-----------------|---|---|--|-----------------------|--------|
| 5 ³⁴ |  |  |  | Fe(acac) ₃ | 61(61) |
| | | | | 15 | 61 |
| | | | | Fe(acac) ₂ | 58 |
| | | | | | 59 |
| 6 ³² |  |  |  | Fe(acac) ₃ | 71(73) |
| | | | | 15 | 71 |
| | | | | Fe(acac) ₂ | 70 |
| | | | | | |
| 7 ³⁵ |  |  |  | Fe(acac) ₃ | 70(74) |
| | | | | 15 | 68 |
| | | | | Fe(acac) ₂ | 68 |
| | | | | | |
| 8 ³⁶ |  |  |  | Fe(acac) ₃ | 72(66) |
| | | | | 15 | 75 |
| | | | | Fe(acac) ₂ | 63 |
| | | | | | |

| | | | | | |
|------------------|---|---|--|-----------------------|---------|
| 9 ³⁷ |  |  |  | Fe(acac) ₃ | 51(57) |
| | | | | 15 | 49 |
| | | | | Fe(acac) ₂ | 49 |
| 10 ³⁸ |  |  |  | 15 | 66 |
| | | | | Fe(acac) ₂ | 66 |
| | | | | | |
| 11 ³⁹ |  |  |  | Fe(acac) ₃ | 76(80) |
| | | | | 15 | 76 |
| | | | | Fe(acac) ₂ | 74 |
| 12 ⁴⁰ |  |  |  | Fe(acac) ₃ | 80(89) |
| | | | | 15 | 82 |
| | | | | Fe(acac) ₂ | 80 |
| 13 ³⁹ |  |  |  | Fe(acac) ₃ | 64 (64) |
| | | | | 15 | 68 |
| | | | | Fe(acac) ₂ | 63 |

| | | | |
|------------------|---|-----------------------|---------|
| 14 ⁴¹ |  | Fe(acac) ₃ | 72 |
| | | 15 | 73 |
| | | Fe(acac) ₂ | 72 (77) |
| <hr/> | | | |
| 15 ⁴² |  | Fe(acac) ₃ | 80(90) |
| | | 15 | 80 |
| | | Fe(acac) ₂ | 81 |
| <hr/> | | | |
| 16 ⁴³ |  | Fe(acac) ₃ | 80(90) |
| | | 15 | 78 |
| | | Fe(acac) ₂ | 85 |
| <hr/> | | | |
| 17 ⁴² |  | Fe(acac) ₃ | 81(83) |
| | | 15 | 91 |
| | | Fe(acac) ₂ | 81 |

Reactions conditions: Grignard, substrate, [Fe], solvent, temperature, time. 1) 2.4 mmol, 1.0 mmol, 0.05 mmol, Et₂O, NMP, 25 °C, 6 h. 2) 5.00 mmol, 5.00 mmol, 0.15 mmol, THF, rt, 40 min. 3) 7.00 mmol, 5.86 mmol, 0.29 mmol, THF, NMP, rt, 20 min. 4) 5.20 mmol, 2.60 mmol, 0.13 mmol, THF, rt - reflux, 1 h. 5) 4.20 mmol, 1.82 mmol, 0.09 mmol, THF, -30 °C, 20 min. 6) 9.00 mmol, 3.65 mmol, 0.18 mmol, THF, NMP, 80 °C, 3.5 h. 7) 13 mmol, 10 mmol, 0.50 mmol, TMEDA 1.0 mmol, HMTA 0.50 mmol, THF, 0 °C, 1.5 h. 8) 3.0 mmol, 1.0 mmol, 0.05 mmol, THF, -78 °C - rt, 21 h. 9) 1.87 mmol, 1.1 mmol, 0.08 mmol, THF, NMP, -20 °C, 30 min. 10) 0.6 mmol, 0.5 mmol, 0.025 mmol, THF, NMP, -30 °C, 15 min. 11) 2.1 mmol, 1.3 mmol, 0.013 mmol, THF, NMP, 0 °C - rt, 1.5 h. 12) 1.06 mmol, 0.353 mmol, 0.035 mmol TMEDA 1.06 mmol, THF, -20 °C - rt, 2 h. 13) 1.0 mmol, 0.5 mmol, 0.05 mmol, THF, NMP, 25 °C, 1 h. 14) 0.75 mmol, 0.5 mmol, 0.05 mmol, THF, NMP, 25 °C, 16 h. 15) 0.73 mmol, 0.61 mmol, 0.06 mmol, THF, -30 °C, 25 min. 16) 1.36 mmol, 1.13 mmol, 0.03 mmol, THF, NMP, -20 °C - rt, 2 h. 17) 0.242 mmol, 0.186 mmol, 0.009 mmol, THF, -20 °C, 10 min.

7.6 Conclusions

The reaction products of $\text{Fe}(\text{acac})_3$ with one equivalent of Grignard reagents have been assigned unequivocally for the first time. Two Fe(II) species are produced $\text{Fe}(\text{acac})_2$ and $\text{FeX}_2(\mu\text{-acac})\text{Mg}(\text{THF})_2$ ($\text{X} = \text{Br}$ (**15**) Cl (**16**) or I (**17**)). The identity of X is based on the halogen of the Grignard reagent RMgX ($\text{X} = \text{Br}$, Cl or I) but the same reaction mixture is generated regardless of the identity of R which can be alkyl, aryl, allyl or alkynyl. The novel complexes **15** – **17** are fully characterised by ^1H NMR and infra-red spectroscopy, single-crystal XRD and cyclic voltammetry.

It is unusual that two iron species with the same oxidation state are produced upon just one equivalent of Grignard reagents. As a result, two competing catalytic cycles may be generated from the onset. As a preliminary investigation to this effect, the two Fe(II) species in place of $\text{Fe}(\text{acac})_3$ in a series of literature cross-coupling reactions. Identical yields were isolated in all cases suggesting a common active species. The necessary kinetics studies to further confirm this are to be performed in future work.

An alternate route to the production of these pre-catalytic complexes was also discovered by the reaction of the relevant ferric halide FeX_2 ($\text{X} = \text{Br}$, Cl or I) with $\text{Mg}(\text{acac})_2$. Through this synthetic route there is potential to produce a diverse range of pre-catalysts by altering the halogen atoms, chelating ligands and solvent ligands.

It would be of particular interest in future to examine the role that NMP plays in the reaction, and determine whether similar pre-catalysts are formed. This could provide valuable information towards explaining the role that NMP play in enhancing the catalytic performance of the iron catalysts. The Neidig group have recently presented results in this area for FeCl_3 pre-catalysed reactions.^{44,45} The reaction of FeCl_3 with 20 equivalents MeMgBr and 9 equivalents NMP (relative to Grignard reagents) produces the catalytically active species, $[\text{Mg}(\text{NMP})_6][\text{FeMe}_3]_2$. Identical conditions with removal of NMP favours the formation of the previously reported $[\text{Mg}(\text{THF})_6][\text{Fe}_8\text{Me}_{12}]$ cluster demonstrating the ligation to the Mg cation still has a drastic influence on the iron speciation.

7.7 Experimental

7.7.1 *Materials and Methods*

All manipulations of air sensitive materials were carried out under inert conditions using standard Schlenk-line and glovebox techniques using argon gas. Chemicals were used as supplied unless specified. All solvents which were dried over a suitable drying agent, typically CaH₂ and distilled under an inert atmosphere. Grignard reagents were degassed by sparging with argon gas and titrated prior to use using phenylhydrazone as an indicator.

Single crystal X-ray diffraction data was collected at 150(2) K on a Bruker Apex Duo diffractometer using a graphite mono-chromated Mo (K_α) radiation source and cold stream of N₂ gas. Crystals were mounted onto a X μm MiTeGen nylon loop using degassed Fomblin Y oil dried over Na metal. IR spectra were obtained on a JASCO 4100 FT-IR using a solution state cell 0.5 mm path length using sample concentrations of 20 mM at room temperature. ¹H NMR spectra were obtained on a Brücker Avance 400 MHz or 500 MHz at room temperature. The Evans method for determination of magnetic susceptibility was obtained on the 500 MHz instrument using concentrations of 12.0 mM **15** and 13.6 mM Fe(acac)₂.

7.7.2 *Sample Synthesis of FeBr₂(μ-acac)₂Mg(THF)₂ (**15**)*

An oven dried Schlenk flask was charged with Fe(acac)₃ (500 mg, 1.42 mmol) and THF (12 mL) added to produce a red solution. Drop wise addition of 4-C₆H₅C₆H₄MgBr (2.84 mL, 0.5 M, 1.42 mmol) produces a gradual precipitation of colourless 4-(C₆H₅C₆H₄)₂ an immediate colour change to yellow / brown was observed upon total addition. The colourless precipitate of 4-(C₆H₅C₆H₄)₂ was isolated by cannula filtration. Slow diffusion of the yellow filtrate into hexanes at -25 °C yielded yellow / brown crystals of **15** (284 mg, 68 %) suitable for single crystal X-ray diffraction. ¹H NMR (500 MHz) *d*₈-THF δ; 29.9 (s, 3H, H₃C-C(O)), 15.4 (s, 1H (O)C-CH-C(O)), -83.9 (s, 3H, C(μ-O)CH₃). IR DCM: $\bar{\nu}$ (cm⁻¹) 1613 (strong), 1523 (v. strong), 1410 (strong), 1264 (med, shoulder) 1257 (med). Anal. Calcd. for FeMgC₁₈H₃₀Br₂O₆, C, 37.12; H, 5.19, found C, 36.97; H, 5.27.

7.7.3 Synthesis of $\text{FeX}_2(\mu\text{-acac})_2\text{Mg}(\text{THF})_2$ ($X = \text{Cl}$ (**16**) or I (**17**)) via FeX_2 .

An oven dried Schlenk flask was charged with FeX_2 ($X = \text{Cl}$ or I) (1.00 mmol) and $\text{Mg}(\text{acac})_2$ (222 mg, 1.00 mmol). Addition of THF produced a yellow-orange (**16**) or orange-brown (**17**) solution. Slow diffusion of this solution into hexanes at $-25\text{ }^\circ\text{C}$ yielded yellow-orange crystals of **16** (354 mg, 72 %) or yellow* **17** (454 mg, 67 %) suitable for single crystal X-ray diffraction. ^1H NMR (500 MHz) d_8 -THF (**16**) δ : 30.2 (s, 3H, $\text{H}_3\text{C-C(O)}$), 12.35 (s, 1H (O)C-CH-C(O $^-$)), -73.22 (s, 3H, C(μ -O $^-$) CH_3). ^1H NMR (500 MHz) d_8 -THF (**17**) δ : 31.36 (s, 3H, $\text{H}_3\text{C-C(O)}$), 20.88 (s, 1H (O)C-CH-C(O $^-$)), -101.8 (s, 3H, C(μ -O $^-$) CH_3). IR DCM (**16**): $\bar{\nu}$ (cm^{-1}) 1612 (strong), 1522 (v. strong), 1413 (strong), 1264 (med, shoulder) 1259 (med). IR DCM (**17**): $\bar{\nu}$ (cm^{-1}) 1612 (strong), 1523 (v. strong), 1409 (strong), 1261 (med, shoulder) 1259 (med). Anal. Calcd. for $\text{FeMgC}_{18}\text{H}_{30}\text{Cl}_2\text{O}_6$ (**16**), C, 43.81; H, 6.13, found C, 43.68; H, 6.23. Anal. Calcd. for $\text{FeMgC}_{18}\text{H}_{30}\text{I}_2\text{O}_6$ (**17**), C, 31.96; H, 4.47, found C, 31.84; H, 4.74.

* yellow crystals of **17** are often covered in a purple/ black precipitate of an unknown composition. This contaminant was physically removed by scraping with a needle prior to mounting for single-crystal XRD. Resolubilising the contaminated solid produced yellow solutions and could be further purified by repeated recrystallisation by slow diffusion into hexanes. This was not found to be necessary as neither the catalytic activity, elemental analysis nor the spectroscopic response in any method utilised was affected.

7.7.4 Synthesis of $\text{Fe}(\text{acac})_2$.

An oven dried Schlenk was charged with with anhydrous FeCl_2 [6.00 g, 47 mmol] and dissolved in Et_2O (200 mL) and THF (10 mL). Acetyl acetone (9.64 mL, 94 mmol) was then added via syringe followed by dropwise addition of piperidine (9.29 mL, 94 mmol) to prevent an excessively exothermic reaction. The mixture is stirred for 2 hours at room temperature then filtered to remove piperidine hydrochloride and washed with Et_2O (2 x 15 mL). The filtrate was reduced to dryness *in vacuo* to yield a dark orange/ red solid that was further purified by vacuum sublimation at $110\text{ }^\circ\text{C}$ to yield an orange solid (5.5 g, 46 %). IR DCM: $\bar{\nu}$ (cm^{-1}) 1581 (strong), 1514 (strong), 1414 (med) 1259 (weak).

7.8 References

- (1) Bedford, R. B. *Acc. Chem. Res.* **2015**, *48*, 1485.
- (2) Fürstner, A.; Krause, H.; Lehmann, C. W. *Angew. Chem. Int. Ed.* **2006**, *45*, 440.
- (3) Bedford, R. B.; Brenner, P. B.; Elorriaga, D.; Harvey, J. N.; Nunn, J. *Dalton. Trans.* **2016**, *45*, 15811.
- (4) Bedford, R. B.; Brenner, P. B.; Carter, E.; Cogswell, P. M.; Haddow, M. F.; Harvey, J. N.; Murphy, D. M.; Nunn, J.; Woodall, C. H. *Angew. Chem. Int. Ed.* **2014**, *53*, 1804.
- (5) Carpenter, S. H.; Neidig, M. L. *Isr. J. Chem.* **2017**, *57*, 1106.
- (6) Bedford, R. B.; Brenner, P. B.; Carter, E.; Clifton, J.; Cogswell, P. M.; Gower, N. J.; Haddow, M. F.; Harvey, J. N.; Kehl, J. a.; Murphy, D. M.; Neeve, E. C.; Neidig, M. L.; Nunn, J.; Snyder, B. E. R.; Taylor, J. *Organometallics* **2014**, *33*, 5767.
- (7) Kneebone, J. L.; Fleischauer, V. E.; Daifuku, S. L.; Shaps, A. A.; Bailey, J. M.; Iannuzzi, T. E.; Neidig, M. L. *Inorg. Chem.* **2016**, *55*, 272.
- (8) Baker, T. M.; Mako, T. L.; Vasilopoulos, A.; Li, B.; Byers, J. A.; Neidig, M. L. *Organometallics* **2016**, *35*, 3692.
- (9) Daifuku, S. L.; Kneebone, J. L.; Snyder, B. E. R.; Neidig, M. L. *J. Am. Chem. Soc.* **2015**, *137*, 11432.
- (10) Daifuku, S. L.; Al-afyouni, M. H.; Snyder, B. E. R.; Kneebone, J. L.; Neidig, M. L. *J. Am. Chem. Soc.* **2014**, *136*, 9132.
- (11) Kneebone, J. L.; Brennessel, W. W.; Neidig, M. L. *J. Am. Chem. Soc.* **2017**, *139*, 6988.
- (12) Schoch, R.; Desens, W.; Werner, T.; Bauer, M. *Chem. Eur. J.* **2013**, *19*, 15816.
- (13) Tamura, M.; Kochi, J. *J. Am. Chem. Soc.* **1971**, *93*, 1487.
- (14) Bogdanovi, B.; Schwickardi, M. *Angew. Chem. Int. Ed.* **2000**, *39*, 4610.
- (15) Aleandri, L. E.; Bogdanović, B.; Bons, P.; Durr, C.; Gaidies, A.; Hartwig, T.; Hockett, S. C.;

- Lagarden, M.; Wilczok, U.; Brand, R. A. *Chem. Mater.* **1995**, *7*, 1153.
- (16) Sherry, B. D.; Fürstner, A. *Acc. Chem. Res.* **2008**, *41*, 1500.
- (17) Fürstner, A.; Martin, R.; Krause, H.; Seidel, G.; Goddard, R.; Lehmann, C. W. *J. Am. Chem. Soc.* **2008**, *130*, 8773.
- (18) Noda, D.; Sunada, Y.; Hatakeyama, T.; Nakamura, M.; Nagashima, H. *J. Am. Chem. Soc.* **2009**, *131*, 6078.
- (19) Kleimark, J.; Hedstrom, A.; Larsson, P. F.; Johansson, C.; Norrby, P. O. *Chem. Cat. Chem* **2009**, *1*, 152.
- (20) Klose, A.; Solari, E.; Floriani, C.; Chiesi-Villa, A.; Rizzoli, C.; Re, N. *J. Am. Chem. Soc.* **1994**, *116*, 9123.
- (21) Lefèvre, G.; Jutand, A. *Chem. Eur. J.* **2014**, *20*, 4796.
- (22) Kauffmann, T. *Angew. Chem. Int. ed.* **1996**, *35*, 386.
- (23) Hedström, A.; Lindstedt, E.; Norrby, P. O. *J. Organomet. Chem.* **2013**, *748*, 51.
- (24) Evans, D. F. *J. Chem. Soc.* **1959**, 2003.
- (25) Grant, D. H. *J. Chem. Educ.* **1995**, *72*, 39.
- (26) Natoli, S. N.; McMillin, D. R. *J. Chem. Educ.* **2018**, *95*, 30.
- (27) Kobayashi, M.; Takashima, A.; Ishii, T.; Naka, H.; Uchiyama, M. *Inorg. Chem.* **2007**, *46*, 1039.
- (28) Cordero, B.; Gómez, V.; Platero-Prats, A. E.; Revés, M.; Echeverría, J.; Cremades, E.; Barragán, F.; Alvarez, S. *J. Chem. Soc. Dalton. Trans.* **2008**, *21*, 2832.
- (29) Sorota, P.; Pluzip, T.; Lis, T. *Polyhedron*, **1984**, *3*, 4.
- (30) Adams, K.; Ball, A. K.; Birkett, J.; Brown, L.; Chappell, B.; Gill, D. M.; Lo, P. K. T.; Patmore, N. J.; Rice, C. R.; Ryan, J.; Raubo, P.; Sweeney, J. B. *Nat. Chem.* **2017**, *9*, 396.

- (31) Fiandanese, V.; Marchese, G.; Martina, V.; Ronzini, L. *Tetrahedron Lett.* **1984**, *25*, 4805.
- (32) Fürstner, A.; Leitner, A. *Angew. Chem. Int. Ed.* **2002**, *41*, 609.
- (33) Nagano, T.; Hayashi, T. *Org. Lett.* **2004**, *6*, 1297.
- (34) Itami, K.; Higashi, S.; Mineno, M.; Yoshida, J. I. *Org. Lett.* **2005**, *7*, 1219.
- (35) Cahiez, G.; Habiak, V.; Duplais, C.; Moyeux, A. *Angew. Chemie - Int. Ed.* **2007**, *46*, 4364.
- (36) Rao Volla, C. M.; Vogel, P. *Angew. Chem. Int. Ed.* **2008**, *47*, 1305.
- (37) Cahiez, G.; Avedissian, H. *Synthesis.* **1998**, 1199.
- (38) Scheiper, B.; Bonnekessel, M.; Krause, H.; Fürstner, A. *J. Org. Chem.* **2004**, *69*, 3943.
- (39) Shakhmaev, R. N.; Sunagatullina, A. S.; Zorin, V. V. *Russ. J. Org. Chem.* **2014**, *50*, 322.
- (40) Parmar, D.; Henkel, L.; Dib, J.; Rueping, M. *Chem. Commun.* **2015**, *51*, 2111.
- (41) Cheung, C. W.; Ren, P.; Hu, X. *Org. Lett.* **2014**, *16*, 2566.
- (42) Fürstner, A.; De Souza, D.; Turet, L.; Fenster, M. D. B.; Parra-Rapado, L.; Wirtz, C.; Mynott, R.; Lehmann, C. W. *Chem. Eur. J.* **2007**, *13*, 115.
- (43) Cahiez, G.; Gager, O.; Habiak, V. *Synthesis.* **2008**, *16*, 2636.
- (44) Sears, J. D.; Neate, P. G. N.; Neidig, M. L. *J. Am. Chem. Soc.* **2018**, *140*, 11872.
- (45) Muñoz, S. B.; Daifuku, S. L.; Sears, J. D.; Baker, T. M.; Carpenter, S. H.; Brennessel, W. W.; Neidig, M. L. *Angew. Chem. Int. Ed.* **2018**, *57*, 6496.

Chapter 8. Reaction of Iron Pre-catalysts With More Than One Equivalent of Grignard Reagent.

8.1 Abstract

The speciation of iron complexes produced in an $\text{Fe}(\text{acac})_3$ -catalysed reaction was investigated by stoichiometric reactions of $\text{Fe}(\text{acac})_3$, $\text{Fe}(\text{acac})_2$ and **15** with Grignard reagents.

The reaction of $\text{Fe}(\text{acac})_3$ with 4-biPhMgBr in the presence of an electrophilic substrate revealed that three equivalents of the Grignard reagent were required to produce turnover of the cross-coupled product. This reaction also produced two isolable, novel Fe species; $\text{FeBr}(\text{I})(\mu\text{-Br})(\mu\text{-acac})\text{Mg}(\text{THF})_3$ (**18**) and $[\text{FeBr}_4.\text{Mg}(\text{THF})_6]$ (**19**).

The reactions of **15** and $\text{Fe}(\text{acac})_2$ with one or two equivalents PhMgBr both produced another novel intermetallic species, $\text{FeBr}_2(\mu\text{-Br})(\mu\text{-acac})\text{Mg}(\text{THF})_3$ (**20**) giving further credence to both Fe(II) species being converted to an identical catalytic species in catalytic conditions.

8.2 Aims

The equimolar reaction of one equivalent of $\text{Fe}(\text{acac})_3$ with Grignard reagents produces half an equivalent each of two Fe(II) species; $\text{FeX}_2(\mu\text{-acac})_2\text{Mg}(\text{THF})_2$ and $\text{Fe}(\text{acac})_2$ X = Br, Cl or I (**15 – 17**) and $\text{Fe}(\text{acac})_2$. Cyclic voltammetry shows that the two Fe(II) species have similar reduction potentials suggesting that a further reduced catalytically active species could be accessible in each cases upon reaction with further equivalences of Grignard reagents.

Each Fe(II) species was seen to have identical activity based on isolated yields of cross-coupled product when substituted for $\text{Fe}(\text{acac})_3$ in a series of literature reactions suggesting a common catalytically active species.

Through the further stoichiometric reactions of $\text{Fe}(\text{acac})_3$, **15** and $\text{Fe}(\text{acac})_2$ with further equivalences of Grignard and in the presence of a suitable a suitable electrophilic substrate we aim accomplish the following;

- 1) Isolation of further reduced species of catalytic relevance that have been proposed in the literature.
- 2) Determine if Fe(acac)₂ and **15** have divergent reactivity or are likely to produce a common catalytically active species as suggested by the results of chapter 8.
- 3) Identify any other species that could be produced during catalysis such as those belonging to a secondary cycle or a kinetically inert species as described in the works of Neidig and Bedford *et al.*

8.3 Further Stoichiometric Reactions with Grignard Reagents.

The crude reaction mixtures of both **15** and Fe(acac)₂ with one equivalent of Grignard reagent or greater is seen to produce paramagnetic species that made peak detection difficult to distinguish from the background signal noise by ¹H NMR spectroscopy. This paramagnetic species does not appear to be the sole stoichiometric product but renders this means of characterisation useless without isolation of this species.

The C-O and C-C stretches of the acac ligands provide handles for infra-red spectroscopy that are suitably diagnostic to distinguishing the intermetallic species from Fe(acac)₂. It is however quite difficult to distinguish complexes **15** – **17** (see section 7.4.6.4) from other another and this technique proven an effective alternative to ¹H NMR spectroscopy in the study of these as of yet undefined paramagnetic species.

As a result, studies are currently limited to structural characterisation through single-crystal XRD on isolable species with future aims to turn to EPR or MCD. Though the isolated species described herein are likely off cycle, they could still be related to and thus informative of those involved with catalysis.

The successful isolation of complexes of interest and experimental observations that may have consequence for catalysis are discussed hereafter. The largest issue encountered was the generation of sticky black oils or precipitates, presumably the species that generate the strongly paramagnetic species in the ¹H NMR spectra. This product often coated the crystals of interest and being totally insoluble in most solvents would physically trap them. The choice of Grignard and electrophilic reagent in these reactions may appear rather arbitrary but were purely selected as on repetition seemed to

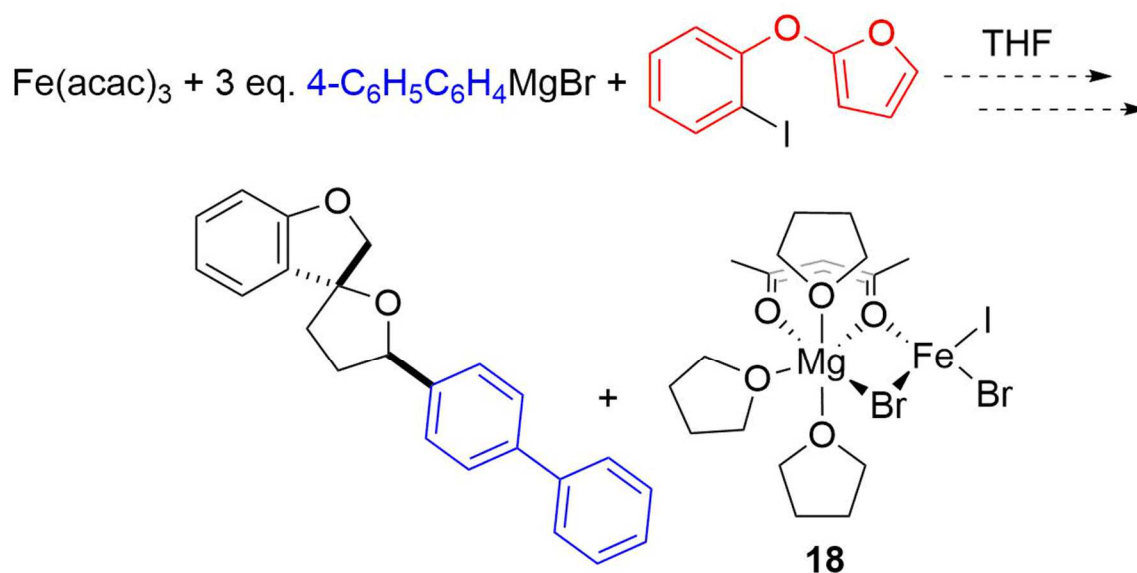
promote the formation of crystalline material and discourage the formation of the black amorphous material. At this stage there is no rationalisation for why certain Grignards or electrophiles would favour production of this contaminant species.

Bedford *et. al* have attributed this black colouration to iron nanoparticles.^{1,2} Several nanoparticulate materials stabilised by imine ligands have been characterised by energy-dispersive x-ray diffraction (EDX) spectroscopy and transmission electron microscopy (TEM).³ These species are shown to be active catalysts in the coupling of alkyl halides with aryl and alkenyl Grignard reagents. The observation of ring closed products from alkenyl Grignards is supportive of a radical mechanism.

Finally, through this work the potential for divergent catalytic cycles between the intermetallic complexes and Fe(acac)₃ can also be further investigated.

8.4 Reaction Product(s) of **15** with RMgBr.

8.4.1 Reaction Product(s) of Fe(acac)₃ with three Equivalents 4-biPhMgBr and one equivalent electrophile.



Reaction color change: Red \longrightarrow Black

Scheme 8.1. Isolable products of the reaction of Fe(acac)₃ with three equivalents of 4-biPhMgBr and one equivalent electrophile, 2-[(2-iodophenoxy)methyl]furan. Dashed double arrows indicate a reaction of unknown stoichiometry. The colour change from the starting reaction mixture to the final addition of Grignard is noted.

Red solutions of $\text{Fe}(\text{acac})_3$ in THF turn yellow upon addition of one equivalent of Grignard reagent indicating the generation of the two $\text{Fe}(\text{II})$ pre-catalyst, **15** and $\text{Fe}(\text{acac})_2$. The same is observed in the presence of the electrophile, 2-[(2-iodophenoxy)methyl]furan previously discussed in Chapter 7. By addition of the third equivalence of Grignard a dark brown-black solution is produced (Scheme 8.1). This coloration is accounted typically in the literature to reduced iron species and as being indicative of an active catalytic species.³⁻⁵ After removal of quarterphenyl the reaction mixture was layered with hexanes at $-25\text{ }^\circ\text{C}$. Two crystalline materials were obtained. Firstly, colourless needles of the cross-coupled spirocycle product, 2-(4'-Biphenyl)-8,9-benzo-1,7-dioxaspiro[4.4]nonane were isolated, confirming that the black solution was indeed an active catalytic reaction. A minimum of three equivalents of Grignard relative to the Fe pre-catalyst are thus required to initiate catalysis. Secondly, small pale-yellow blocks revealed to be $\text{Fe}(\text{Br})(\text{I})(\mu\text{-acac})_2\text{Mg}(\text{THF})_2$ (**18**) were isolated. The solid-state structure of **18** as determined by single-crystal XRD is shown in Figure 8.2. Selected bond lengths and angles are collected in Table 8.1 along with those for complex **15** for contrast.

The $\text{Fe}\cdots\text{Mg}$ separation is $3.241(9)\text{ \AA}$, significantly longer than found in the series **15** – **17** as the bridging bonds $\text{Fe}/\text{Mg}\text{-O1}$ and $\text{Fe}/\text{Mg}\text{-Br1}$ bond lengths are longer in all cases than the equivalent $\text{Fe}/\text{Mg}\text{-O1}$ and $\text{Fe}/\text{Mg}\text{O2}$ bond lengths in that series. The $\text{Fe}\text{-I1}$ bond length at $2.534(11)\text{ \AA}$ is longer than the $\text{Fe}\text{-Br1}$ bond length of $2.392(10)\text{ \AA}$ but the $\text{Fe}\text{-I}$ bond length is longer than the average found in **17** while $\text{Fe}\text{-Br}$ bond is shorter than the average found in **15**.

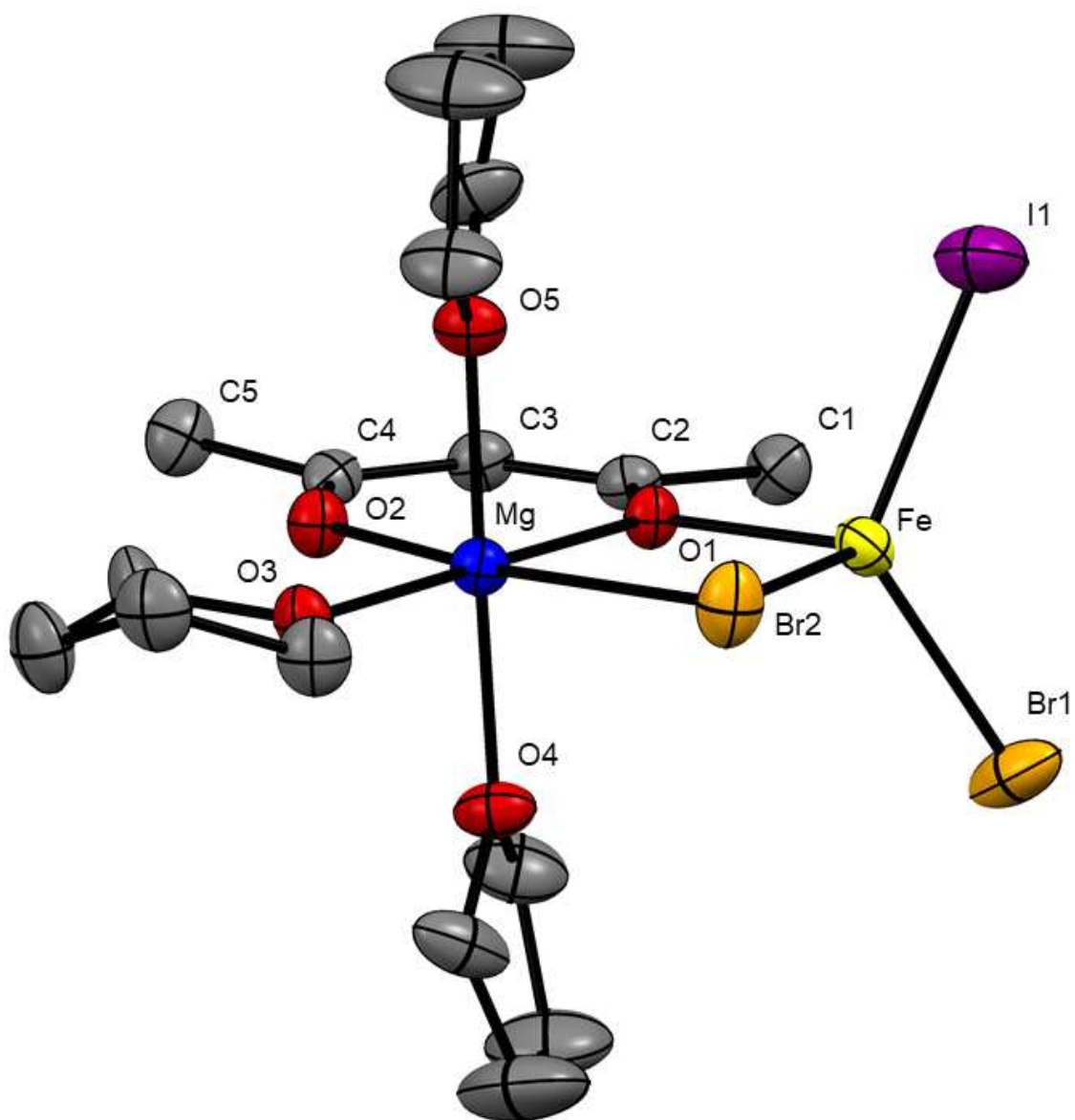


Figure 8.1. Solid-state structure of $\text{Fe}(\text{Br})\text{I}(\mu\text{-Br})\text{Mg}(\text{acac})(\text{THF})_3$ (**18**) as determined by single-crystal XRD. Thermal ellipsoids shown at 50 % probability. Hydrogen atoms omitted for clarity. Selected bond lengths (\AA): $\text{Fe}\cdots\text{Mg} = 3.1631(12)$, $\text{Fe}-\text{Br}1 = 2.429(11)$, $\text{Fe}-\text{I}1 = 2.578(8)$, $\text{Fe}-\text{Br}2 = 2.467(9)$, $\text{Fe}-\text{O}1 = 2.041(10)$, $\text{Mg}-\text{O}1 = 2.076(4)$, $\text{Mg}-\text{O}2 = 1.994(4)$, $\text{Mg}-\text{O}3 = 2.069(4)$, $\text{Mg}-\text{O}4 = 2.098(4)$, $\text{Mg}-\text{O}5 = 2.087(4)$, $\text{O}1-\text{C}2 = 1.303(6)$, $\text{O}2-\text{C}4 = 1.255(6)$. Selected bond angles ($^\circ$): $\text{Br}1-\text{Fe}-\text{Br}2 = 113.4(3)$, $\text{I}1-\text{Fe}1-\text{Br}1 = 122.1(4)$, $\text{I}1-\text{Fe}1-\text{Br}2 = 109.4(3)$, $\text{O}1-\text{Fe}-\text{Br}2 = 92.6(3)$, $\text{O}1-\text{Mg}-\text{Br}2 = 85.70(11)$, $\text{O}3-\text{Mg}-\text{Br}1 = 95.90(12)$, $\text{O}4-\text{Mg}-\text{O}5 = 178.14(18)$.

Table 8.1. Selected bond lengths (Å) of **15** and **18**.

| Complex | Fe-Mg | Fe-Br1 ^a | Fe-Br2 | Fe-I1 | Fe-O1 |
|--|------------|---------------------|-----------|----------|-----------|
| FeBr ₂ (μ-acac) ₂ Mg(THF) ₂ (15) | 3.1631(12) | 2.4411(7) | 2.3925(6) | --- | 2.058(2) |
| Fe(Br)(I)(μ-Br)Mg(acac)(THF) ₃ (18) | 3.241(9) | 2.429(11) | 2.467(9) | 2.578(8) | 2.041(10) |

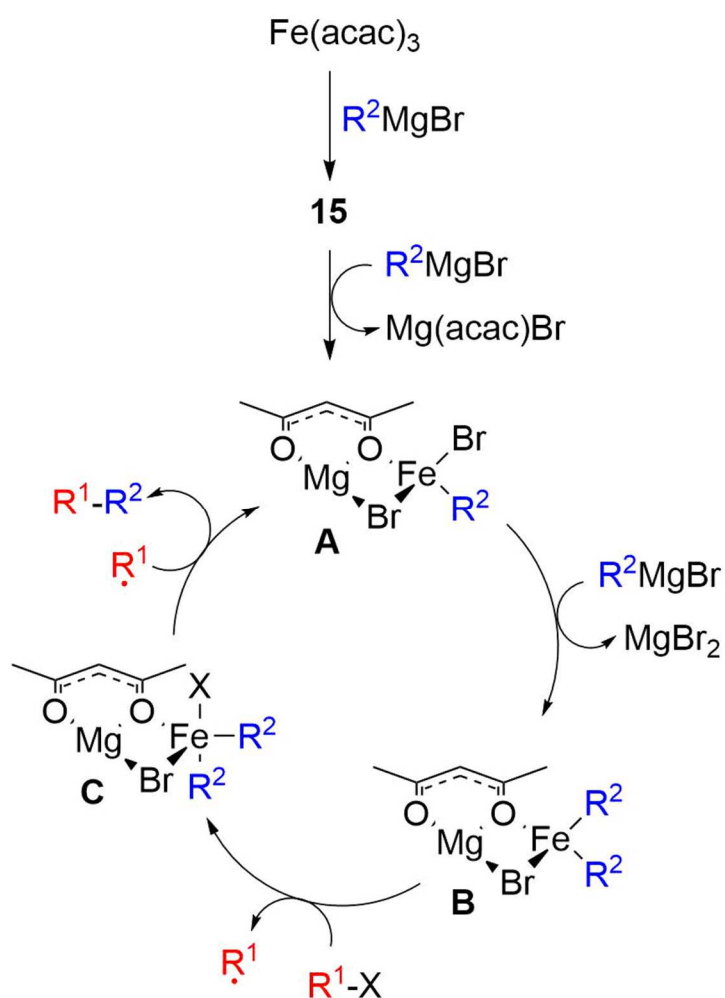
^a Note: identical atoms labels given to atoms in different binding modes, see relevant crystal structures.

The exact speciation of this complex and its role in catalysis are inconclusive, a number of routes could be envisaged to generate this complex but the fact that **18** is structurally akin to the pre-catalytic complex **15** could be indicative that the active species will also be of similar composition. The incorporation of iodine suggests either oxidative addition of the electrophile or homolytic bond fission to produce an aryl radical and coordination of the iodine. The latter mechanism would be consistent with much of the work of Neidig and Bedford in the reactivity of FeCl₂(SciOPP) with PhMgBr and MesMgBr.⁶⁻⁸ Reported therein, the Fe(II) complex Fe^{II}ClPh(SciOPP) species reacts with the alkyl chloride substrate to produce a species of the form, Fe^{III}X₂R(SciOPP). This Fe(III) complex undergoes a single electron reduction producing the cross-coupled product (Scheme 6.8). The authors found that FeCl₂(SciOPP) would react with two equivalents of PhMgBr to produce Fe^{II}Ph₂(SciOPP). Though less selective to the intended product this species was similarly reactive with the electrophile. Such speciation would account for the requirement for three equivalents of Grignard required for turnover in our own observations.

A proposed catalytic cycle is presented in Scheme 8.2. One equivalent of Grignard is required to reduce the Fe(acac)₃ to Fe(II) producing complex **15** when the Grignard halogen is Br (assumed throughout the cycle). Reaction with a second equivalent produces complex A, Fe^{II}BrR(μ-acac)(μ-Br)Mg(THF)₃. The loss of an acac⁻ ligand is based on subsequent observations described in 9.2.3. The third equivalent of Grignard produces the equivalent bis-arylated species complex B, Fe^{II}R₂(μ-acac)(μ-Br)Mg(THF)₃. Homolytic bond fission of the electrophile produces complex C, Fe^{III}R₂Br(μ-acac)(μ-

Br)Mg(THF)₃ that produces the cross-coupled product through reductive elimination regenerating complex A.

Though previous work of the Sweeney group had deemed a radical mechanism unlikely with this specific electrophilic substrate based on radical trapping experiments it could not be ruled out entirely, nor are these conditions completely representative of those in catalysis where a large excess of Grignard would be present.

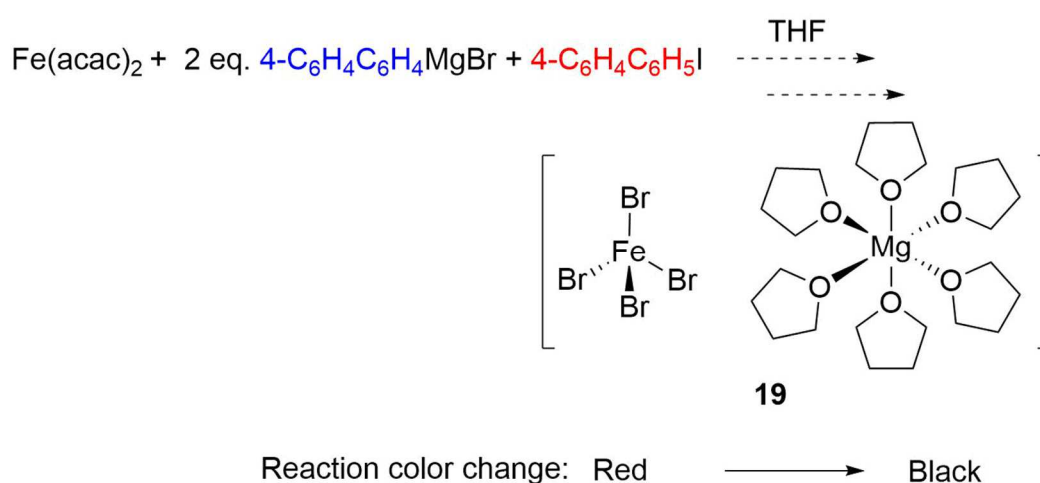


Scheme 8.2. A proposed catalytic cycle for the cross-coupling of R^1-X R^2MgBr by $Fe(acac)_3$. Mg centres are octahedral, coordinately saturated by THF solvent molecules that are omitted for clarity.

Unfortunately, complex **18** was yielded in trace amounts and has been difficult to isolate reproducibly in this manner. It would be desirable to explore the reactivity of this species, so some effort has been made to find alternate reaction conditions. No success has yet been found yet trying to isolate this

complex again from $\text{Fe}(\text{acac})_3$, nor instead from an $\text{Fe}(\text{II})$ species with two equivalents of Grignard in the presence of an electrophile.

The reaction of $\text{Fe}(\text{acac})_3$ with three equivalents of 4-biPhMgBr in the presence of 4-iodo-4-biphenyl instead produced the ionic complex $[\text{FeBr}_4 \cdot \text{Mg}(\text{THF})_6]$ (**19**) (Scheme 8.3). As the quarterphenyl produced by homo- and cross-coupling will be indistinguishable it is omitted from the reaction scheme but was selected for ease of isolation. **19** is likely produced as a result of comproportionation as the conditions that yielded **18** and those described hereafter have all been shown to produce intermetallic



species.

Scheme 8.3. Isolable products of the reaction of $\text{Fe}(\text{acac})_3$ with three equivalents of 4-biPhMgBr and one equivalent electrophile, 4-iodo-4-biphenyl. Dashed double arrows indicate a reaction of unknown stoichiometry. The colour change from the starting reaction mixture to the final addition of Grignard is noted.

Pale yellow crystals of **19** were obtained by slow diffusion of hexanes into the THF reaction mixture at $-25\text{ }^\circ\text{C}$. The solid-state structure obtained by single-crystal XRD is presented in Figure 9.3 with bond lengths and averages collected in Table 9.2. for comparison to complexes **15** and **18**.

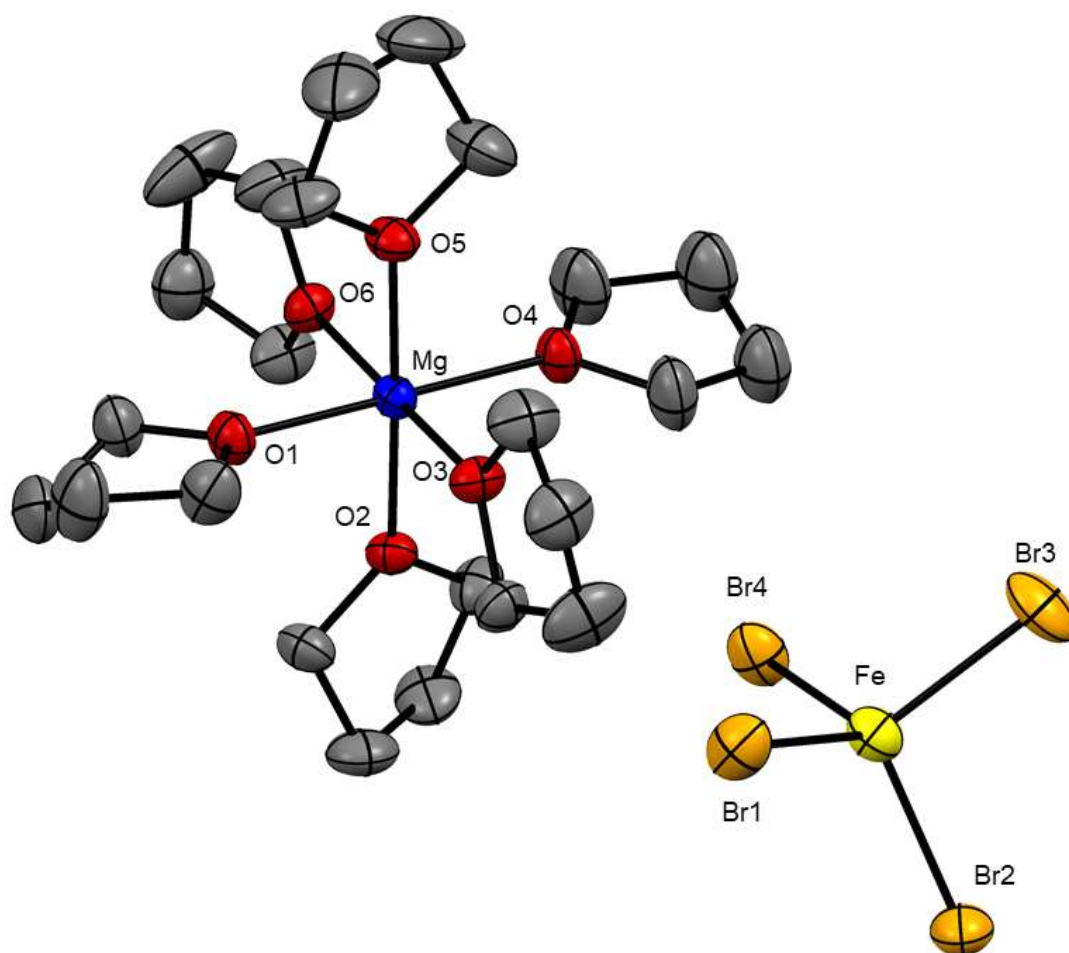


Figure 8.2. Solid-state structure of $[\text{FeBr}_4.\text{Mg}(\text{THF})_6]$ (**19**) as determined by single-crystal XRD. Thermal ellipsoids shown at 50 % probability. Hydrogen atoms omitted for clarity. Selected bond lengths (\AA): Fe-Br1 = 2.440(1), Fe-Br2 = 2.524(1), Fe-Br3 = 2.479(2), Fe-Br4 = 2.498(1), Mg-O1 = 2.087(6), Mg-O2 = 2.082(5), Mg-O3 = 2.107(5), Mg-O4 = 2.096(5), Mg-O5 = 2.091(5), Mg-O6 = 2.125(5). Selected bond angles ($^\circ$): Br1-Fe-Br2 = 113.37(5), Br1-Fe-Br3 = 107.34(5), Br1-Fe-Br4 = 106.17(5), Br2-Fe-Br3 = 106.74(5), O1-Mg-O2 = 90.2(2), O1-Mg-O4 = 179.7(2), O2-Mg-O5 = 178.2(2).

Table 9.2. Average bond lengths found in complexes **15**, **18** and **19**.

| Complex | Average bond length (Å) | | | Bond angles (°) | |
|---|-------------------------|-----------|---------------------|----------------------|----------------------|
| | Fe – Mg | Fe-Br | Mg-O _{THF} | A-Fe-A' ^a | B-Fe-B' ^b |
| FeBr ₂ (μ-acac) ₂ Mg(THF) ₂ (15) | 3.1631(12) | 2.4168(7) | 2.119(3) | 79.34(9) | 126.47(3) |
| Fe(Br)(I)(μ-Br)Mg(acac)(THF) ₃ (18) | 3.1900(12) | 2.448(10) | 2.085(4) | 92.60(3) | 122.1(4) |
| [FeBr ₄ .Mg(THF) ₆] (19) | --- | 2.485(1) | 2.098(5) | 106.17(5) | 106.74(5) |

^a A and A' are the μ-bridging atoms in **15** and **18**. Br1 and Br4 in **19**.

^b B and B' are the terminal halogen atoms in **15** and **18**. Br2 and Br3 in **19**.

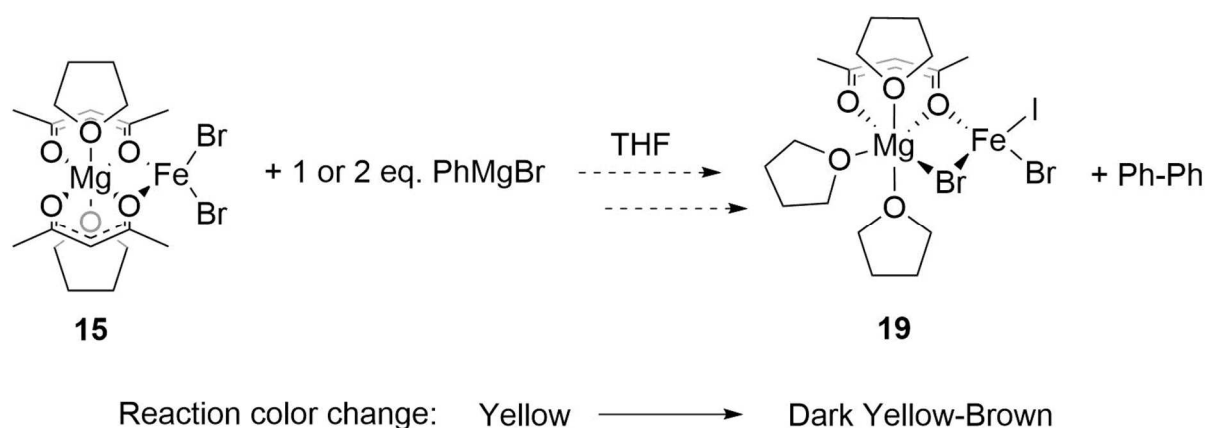
The Fe centre adopts a more tetrahedral conformation as it is no longer chelated to the Mg centre, each Br-Fe-Br bond being close to 109.5°. If we consider the Br1-Fe-Br4 bond angle in **19** to be analogous to the O1-Fe-O2 bond angle in **15** (A-Fe-A') it widens from 79.34(9) to 106.17(5). If we consider the Br2-Fe-Br-3 bond angle analogous to the Br1-Fe-Br2 bond angle in **15**, (B-Fe-B') that bond angle narrows from 126.47(3) to 106.74°. The average Fe-Br bond length is 2.485(1) Å which is also significantly longer than the Fe-Br bonds found in **15** (2.4168(7) Å).

The coordination environment of the Mg centre has been shown to be largely independent of the identity of the halogen atoms in the intermetallic complexes and do not differ significantly from those found in **19** either.

In future work the treatment of the intermetallic complexes FeX₂(μ-acac)₂Mg(THF)₂ X = Br, Cl or I (**15** – **17**) with a Grignard containing a different halogen atom could also provide a direct route to synthesis of **18** and related complexes. Furthermore, it would be interesting to observe how the halide ligands exchange under such conditions. For instance consider again the work of Neidig *et al.* where FeCl₂(SciOPP) is shown to react with one equivalent of MesMgBr to produce FeBrMes(SciOPP).^{9,10}

8.4.2 Reaction Product(s) of **15** with one or two equivalents of PhMgBr.

Yellow solutions of **15** rapidly become very pale in colour when half an equivalence of PhMgBr is added. Further addition of one to two equivalents of PhMgBr results in darkening of the reaction to a brown/ yellow colour. The ^1H NMR spectra of the resulting solutions from 0.5 to 1 equivalent both appear indistinguishable from **15**. At two equivalents **15** is still present in the ^1H NMR spectra though depleted and is observed alongside an unidentified paramagnetic species.



Scheme 8.4. Isolable products of the reaction of **15** with one or two equivalents of PhMgBr. Dashed double arrows indicate a reaction of unknown stoichiometry. The colour change from the starting reaction mixture to the final addition of Grignard is noted.

Slow diffusion of the reaction mixtures produced upon addition of 0.5 and one equivalent PhMgBr into hexanes at $-25\text{ }^\circ\text{C}$ both yielded crops of very pale yellow crystals revealed to be $\text{Fe}(\text{Br})_2(\mu\text{-Br})\text{Mg}(\text{acac})(\text{THF})_2$ (**20**) (Scheme 8.4). The structure obtained from single-crystal XRD is shown in Figure 9.3. Selected bond lengths and angles of complexes $\text{FeBr}_2(\mu\text{-acac})_2\text{Mg}(\text{THF})_2$ (**15**) $\text{Fe}(\text{Br})(\text{I})(\mu\text{-Br})\text{Mg}(\text{acac})(\text{THF})_3$ (**18**) and $\text{Fe}(\text{Br})_2(\mu\text{-Br})(\mu\text{-acac})(\text{THF})_3$ (**19**) are shown Table 9.3.

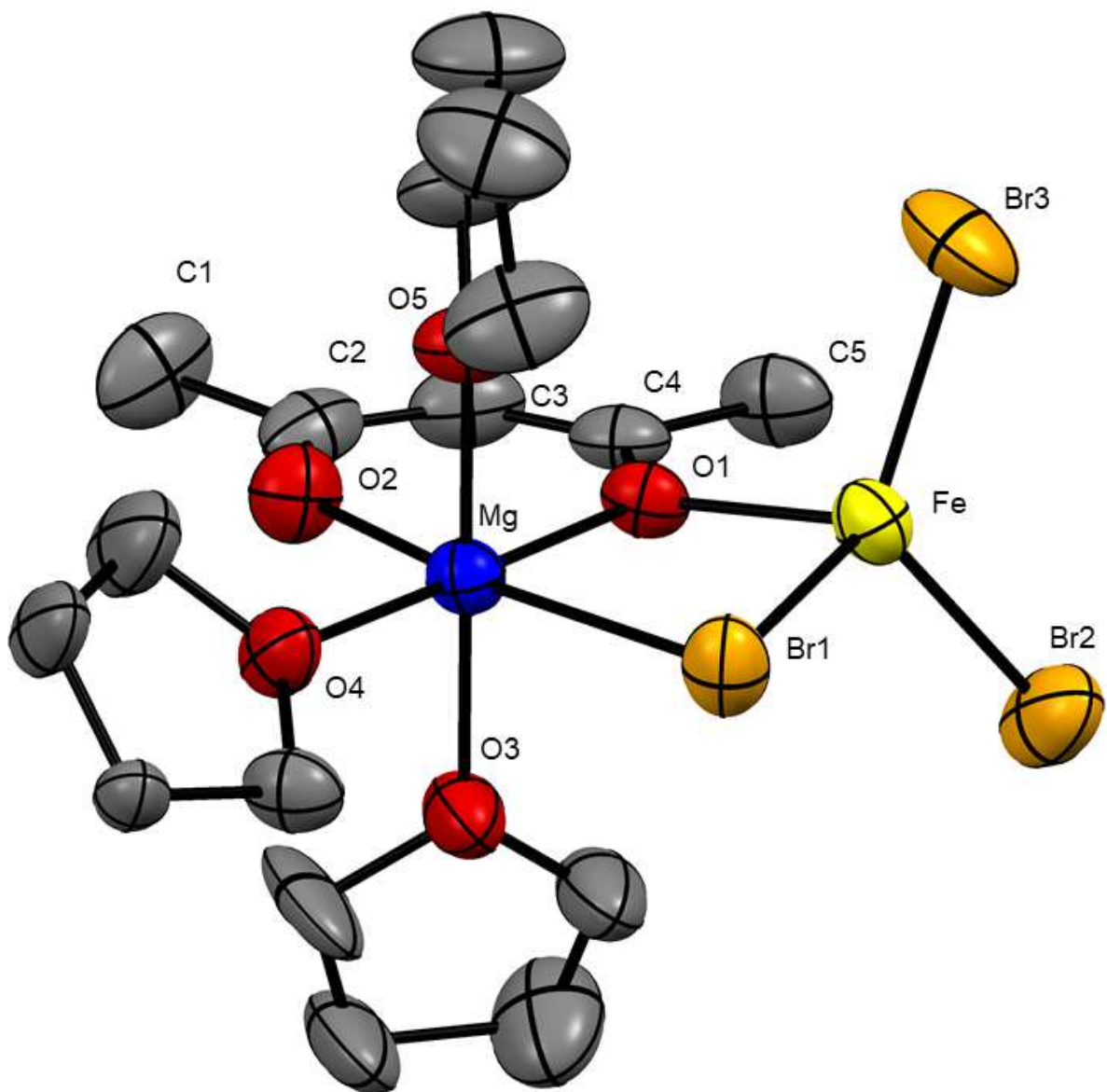


Figure 8.3. Solid-state structure of $\text{FeBr}_2(\mu\text{-Br})(\mu\text{-acac})\text{Mg}(\text{acac})(\text{THF})_3$ (**20**) as determined by single-crystal XRD. Thermal ellipsoids shown at 50 % probability. Hydrogen atoms omitted for clarity. Selected bond lengths (Å): $\text{Fe}\cdots\text{Mg} = 3.001(18)$, $\text{Fe}-\text{Br}1 = 2.5022(9)$, $\text{Fe}-\text{Br}2 = 2.3783(10)$, $\text{Fe}-\text{Br}3 = 2.3844(9)$, $\text{Fe}-\text{O}1 = 2.067(3)$, $\text{Mg}-\text{O}1 = 2.062(3)$, $\text{Mg}-\text{O}2 = 1.990(4)$, $\text{Mg}-\text{O}3 = 2.062(4)$, $\text{Mg}-\text{O}4 = 2.106(4)$, $\text{Mg}-\text{O}5 = 2.090(4)$, $\text{O}1-\text{C}2 = 1.308(6)$, $\text{O}2-\text{C}4 = 1.251(7)$. Selected bond angles ($^\circ$): $\text{Br}1-\text{Fe}-\text{Br}2 = 113.4(3)$, $\text{Br}2-\text{Fe}-\text{Br}3 = 121.64(4)$, $\text{O}1-\text{Fe}-\text{Br}2 = 111.60(9)$, $\text{O}1-\text{Fe}-\text{Br}1 = 89.07(9)$, $\text{O}1-\text{Mg}-\text{O}2 = 87.25(16)$, $\text{O}3-\text{Mg}-\text{Br}1 = 90.34(12)$, $\text{O}3-\text{Mg}-\text{O}5 = 177.90(17)$.

Table 8.2. Collected bond lengths (Å) for intermetallic complexes **15**, **18** and **20**.

| Complex | Fe–Mg | Fe–Br1 | Fe–Br2 | Fe–Br3 | Fe–I1 | Fe–O1 |
|---|------------|------------------------|-----------------------|-----------|----------|-----------|
| FeBr ₂ (μ-acac) ₂ Mg(THF) ₂ (15) | 3.1631(12) | 2.4411(7) | 2.3925(6) | --- | --- | 2.058(2) |
| Fe(Br)(I)(μ-Br)Mg(acac)(THF) ₃ (18) | 3.241(9) | 2.429(11) | 2.467(9) ^a | --- | 2.578(8) | 2.041(10) |
| Fe(Br) ₂ (μ-Br)Mg(acac)(THF) ₂ (20) | 3.3001(18) | 2.5022(9) ^a | 2.3783(10) | 2.3844(9) | --- | 2.067(3) |

^a Note: μ-bridging

The Fe – Mg separation is 3.3001(18) Å the longest of any of the complexes reported by a significant margin. This is consistent with a further increase in the bridging atom bond lengths. For instance, the Fe–Br2 is 2.5022(9) Å is significantly longer than the equivalent bond in **18** (Fe–Br2) which in turn was already longer than the Fe–O bonds found in complex **15** - **17**. The Fe–Br1 and Fe–Br2 bond lengths at 2.3783(10) and 2.3844(9) Å are shorter than the equivalent bonds in **15**.

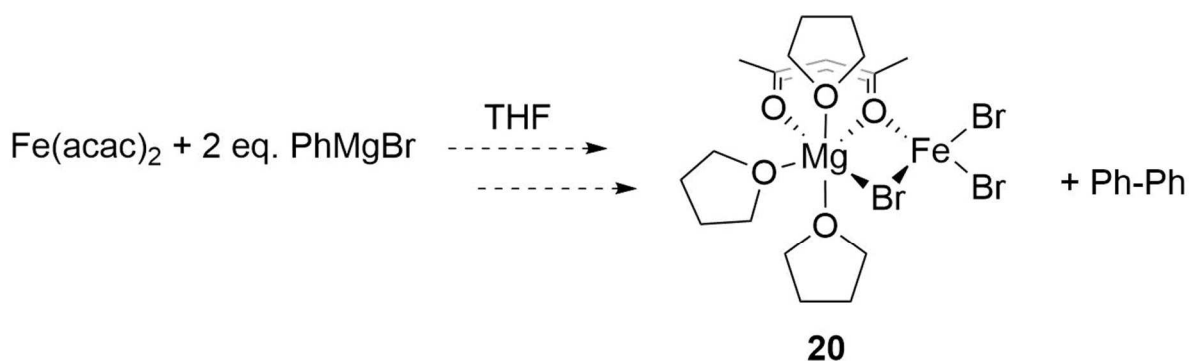
The ¹H NMR spectrum of a crystalline sample of **20** was found to be largely indistinguishable from that of **15** as only extremely small shifts were observed and difficult to quantify as the *d*₈-THF residual solvent peaks are often broadened due to the paramagnetic Fe species.

Crystals of **20** were also isolated alongside a precipitate of the homo-coupled product biphenyl that was not observed in the early stages of the reaction. A species such as Fe^{III}R₂Br(μ-Br)(μ-acac)Mg(THF)₃ could account for this observation where **20** is produced upon reductive elimination in the absence of an electrophilic substrate.

Both complexes **18** and **19** have a μ-Br ligand in place of an acac⁻ ligand. The loss of the acac⁻ ligand could be critical to catalysis in relieving the crowded coordination environment around the Fe centre in a species such as Fe^{III}R₂Br(μ-Br)(μ-acac)Mg(THF)₃ as depicted in Scheme 8.1.

8.5 Reaction Products of Fe(acac)₂ with RMgBr.

8.5.1 Reaction Product(s) of Fe(acac)₂ with two equivalents PhMgBr.



Reaction color change: Orange \longrightarrow Dark Yellow-Brown

Scheme 8.5. Isolable products of the reaction of Fe(acac)₂ with two equivalents of PhMgBr. Dashed double arrows indicate a reaction of unknown stoichiometry. The colour change from the starting reaction mixture to the final addition of Grignard is noted.

Complex **15** is more readily reduced than Fe(acac)₂ based on the CV experiments performed in section 7.4.6.5. Assuming subsequent reduction by the Grignard is required to generate an active catalyst species it would likely be first be produced from complex **15** but does not preclude Fe(acac)₂ having similar reactivity. When orange THF solutions of Fe(acac)₂ were treated with one equivalent of PhMgBr a colour change to yellow was observed (Scheme 8.5). ¹H NMR spectroscopy confirmed that conversion to an intermetallic complex (**15** or **20**, the spectra being near identical) had occurred but does not account for the total reaction stoichiometry.

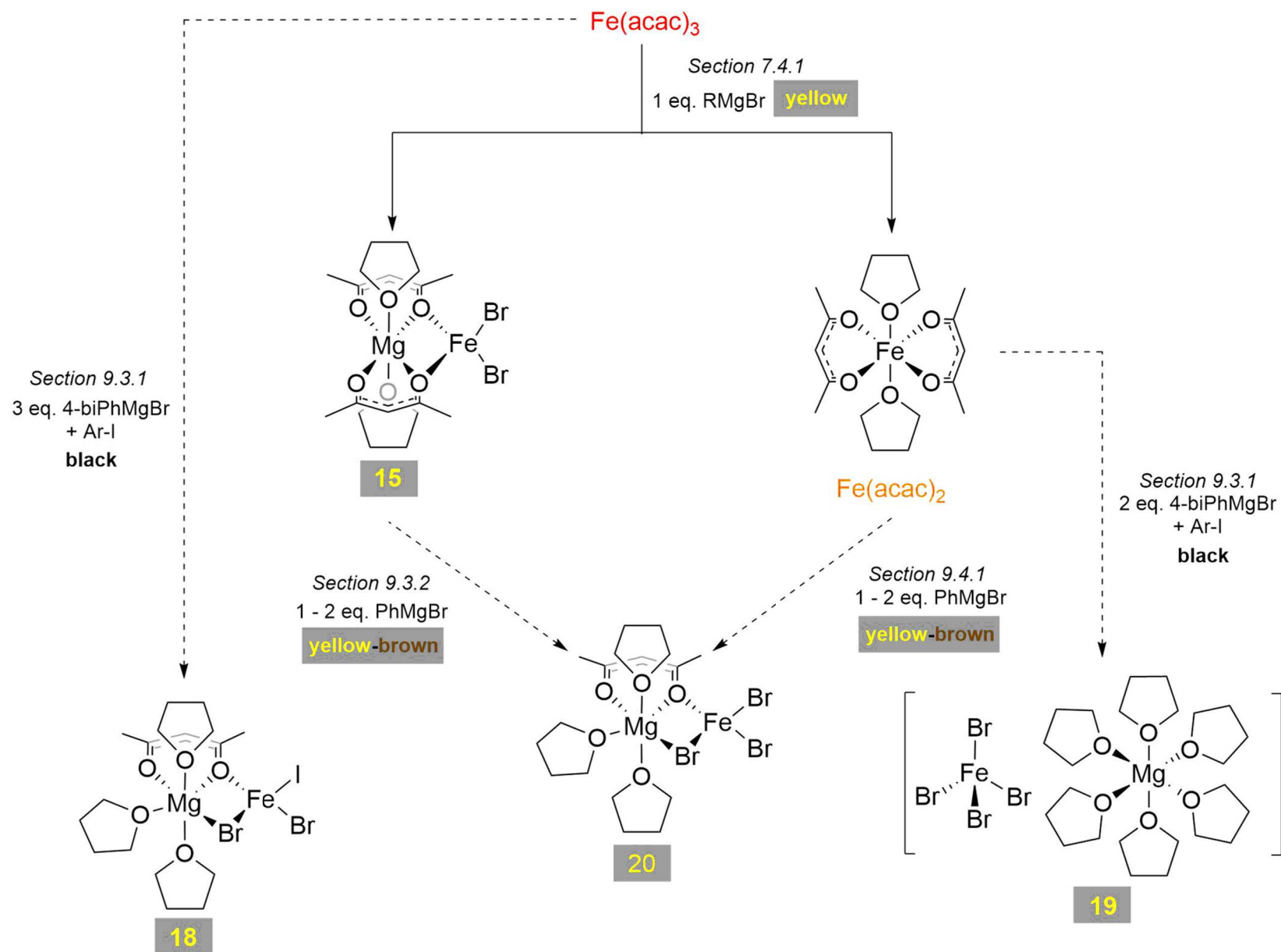
Crystals of **20** were obtained from the reaction of Fe(acac)₂ with two equivalents PhMgBr upon slow diffusion of hexanes into the THF reaction mixture. Fe(acac)₂ and **15** are thus likely converted to an identical catalytic species based on these observations and the results of the competitive reaction yields (Chapter 8.1), complex **20** being produced as an off-cycle resting state.

8.6 Conclusions

Reaction of Fe(acac)₃ with one equivalent of Grignard produces two Fe(II) precatalytic species; FeBr₂(μ-acac)₂Mg(THF)₂ (**15**) and Fe(acac)₂ potentially generating divergent catalytic cycles from the onset.

To identify the catalytically active species in $\text{Fe}(\text{acac})_3$ catalysed Kumada cross-coupling reactions the reactivity of $\text{Fe}(\text{acac})_3$ with Grignards beyond one equivalent was investigated. Furthermore, the reactions of **15** and $\text{Fe}(\text{acac})_2$ with further equivalences of Grignard was performed to establish if each will be converted to a common active species.

The reactions mixtures generated contain one or more unidentified paramagnetic species with severe peak broadening that prevent *in situ* analysis by ^1H NMR spectroscopy. This has been attributed to a black reaction product produced that is often observed following crystallisation as a black amorphous solid. Several crystalline species of interest were isolable and characterised by single-crystal XRD and are summarised together in Scheme 8.6. These species are off-cycle but do provide some interesting potential insights into the catalytic process.



Scheme 8.6. Summary of isolable Fe species arranged by equivalents of Grignard reagent. Dashed arrows indicate a reaction of incomplete stoichiometry. Reaction colours are depicted next to the reaction arrow. The complex name or number is colour coded with the solid state appearance. Reactions are described in more detail in the relevant sections.

The reaction of $\text{Fe}(\text{acac})_3$ with three equivalents 4-biPhMgBr in the presence of the electrophilic substrate Ar-I produced a black reaction mixture from which crystals of the cross-coupled product Ar-Ar and $\text{Fe}(\text{Br})(\text{I})(\mu\text{-Br})\text{Mg}(\text{acac})(\text{THF})_3$ (**18**) were isolated following crystallisation by slow diffusion. An active species that produces turn over of the electrophile is thus expected to be generated on addition of three equivalents of Grignard. The fact that **18** is structurally akin to **15** but turn-over is observed suggests the active species may also be of similar composition. The incorporation of iodine could be indicative of oxidative addition or bond homolyses of the electrophile as per the studies of Neidig *et al.* The loss of the acac^- ligand replaced by a $\mu\text{-Br}$ ligand may be necessary to catalysis in alleviating a crowded coordination environment in an iron species coordinated with the aryl substituent of the Grignard of electrophile in a species such as $\text{Fe}^{\text{III}}\text{R}_2\text{Br}(\mu\text{-Br})(\mu\text{-acac})\text{Mg}(\text{THF})_3$.

The reactions of **15** with one or two equivalents of PhMgBr or $\text{Fe}(\text{acac})_2$ with one equivalents PhMgBr produce yellow to brown solutions. Following crystallisation by slow diffusion $\text{Fe}(\text{Br})_2(\mu\text{-Br})\text{Mg}(\text{acac})(\text{THF})_2$ (**20**) can be isolated alongside a precipitate of homo-couple Grignard. The fact that $\text{Fe}(\text{acac})_2$ produces an intermetallic species upon reaction with further equivalents of Grignard reagent, even if it is not the sole stoichiometric product, is further supportive of a shared active species. As above no further reduction of the metal is observed under these conditions. The unidentified amorphous material is potentially a further reduced species with **19** and the homo-coupled Grignard produced by comproportionation or instead by slow reductive elimination from an arylated Fe species.

Through this study, we aimed to achieve three things;

- 1) Isolation of further reduced species of catalytic relevance that have been proposed in the literature.
- 2) Determine if $\text{Fe}(\text{acac})_2$ and **15** have divergent reactivity or are likely to produce a common catalytically active species.
- 3) Identify any other species that could be produced during catalysis such as those belonging to a secondary cycle or a kinetically inert species.

It is still hypothesised that the black paramagnetic material that accumulates as the stoichiometry of Grignard reagents is increased could belong to a further reduced species. This species seemingly produces the broad paramagnetic response in ^1H NMR spectra and is amorphous so couldn't be characterised at this time. In the future we will turn to alternate spectroscopies such as EPR to determine if we can quantify this species as a function of Grignard concentration.

In combination with the results described in chapter 8 the isolation of an identical species (**20**) when $\text{Fe}(\text{acac})_2$ or **15** is reacted with one to equivalents of Grignard reagent points towards a shared catalytic active species.

A number of other isolable complexes have been identified but their speciation and role in catalysis is still unclear. At this stage they simply serve to highlight the complexity of the chemistry in action.

Due to the labile nature of Fe, neutral mononuclear and intermetallic complexes, -ate complexes,¹¹⁻¹⁴ mixed valence clusters¹⁵ and nanoparticles¹¹ are all potentially active species based on the literature. In our hands Fe(II) intermetallic species are recurring with the low Grignard equivalences explored.

In the future work we aim to perform reactions with greater excesses of Grignard reagents and employ the use of alternate spectroscopies such as EPR and MCD that appear necessary to characterise these reaction products. We also aim to perform kinetic measurements via *in situ* IR spectroscopy to monitor product formation that will allow us to confirm if the catalytic cycles of the Fe(II) species are indeed identical.

8.7 Experimental

8.7.1 *Materials and Physical Methods*

Materials and physical methods were as described previously in 7.6.1. Limited yields of complexes **18** – **20** prevented further characterisation at this stage.

8.7.2 *Isolation of $\text{Fe}(\text{Br})(\text{I})(\mu\text{-acac})_2\text{Mg}(\text{THF})_2$ (**18**)*

An oven dried Schlenk was charged with $\text{Fe}(\text{acac})_3$ (253 mg, 0.67 mmol) to this a solution of 2-[(2-iodophenoxy)methyl]furan (200 mg, 0.67 mmol) in 12 mL THF was added to produce a red solution.

Dropwise addition of three equivalents of 4-biPhMgBr [0.34 mL, 1 M, 0.34 mmol] produces a bright yellow solution after one equivalent consistent with the preparation of **15**. Thereafter the solution darkens ultimately producing a black solution with a colourless precipitate of quarterphenyl. Quarterphenyl was then removed by filtration. The resulting filtrate is layered with hexanes and slow diffusion at -25 °C produced yellow crystals of **19** (trace) and colourless crystals of 2-(4'-Biphenyl)-8,9-benzo-1,7-dioxaspiro[4.4]nonane (no yield determined).

8.7.3 Isolation of $FeBr_2(\mu-Br)(\mu-acac)Mg(THF)_2$ (**19**) from **15**

An oven dried Schlenk was charged with **15** (200 mg, 0.34 mmol) and dissolved in 12 mL THF. Dropwise addition of one equivalent of PhMgBr (0.34 mL, 1 M, 0.34 mmol) produced a dark brown/ yellow solution. The resulting solution was layered with hexanes and slow diffusion at 4 °C produced bright yellow crystals of **19** (32 mg, 17 %*) and a precipitate of biphenyl.

* Remaining yield after selected crystals removed for crystallography.

8.7.4 Isolation of $[FeBr_4.Mg(THF)_6]$ (**19**)

An oven dried Schlenk was charged with $Fe(acac)_2$ (200 mg, 0.34 mmol) and 4-I-C₆H₄C₆H₄MgBr dissolved in 12 mL THF. Drop-wise addition of two equivalents of 4-biPhMgBr (0.68 mL, 1 M, 0.68 mmol) produced a dull brown/ yellow solution. The resulting solution was layered with hexanes and slow diffusion at 4 °C produced extremely pale-yellow crystals of **19** (trace).

8.7.5 Isolation of $FeBr_2(\mu-Br)(\mu-acac)Mg(THF)_2$ (**20**) from $Fe(acac)_2$ (**20**)

An oven dried Schlenk was charged with $Fe(acac)_2$ (200 mg, 0.34 mmol) and dissolved in 12 mL THF. Added drop-wise one equivalent of PhMgBr (0.68 mL, 1 M, 0.68 mmol) produced a dark brown solution. The resulting solution was then layered with hexanes and slow diffusion at 4 °C produced bright yellow crystals of **19** (trace) and a precipitate of biphenyl.

8.8 References

- (1) Guo, L.; Huang, Q.; Li, X.; Yang, S. *Phys. Chem. Chem. Phys.* **2001**, *3*, 1661.
- (2) Koltypin, Y.; Perkas, N.; Gedanken, A. *J. Mater. Chem.* **2004**, *14*, 2975..
- (3) Bedford, R. B.; Betham, M.; Bruce, D. W.; Davis, S. A; Frost, R. M.; Hird, M. *Chem. Comm.* **2006**, *13*, 1398.
- (4) Ranjan, J., Pathak, T.P., Sigman, M. S. *Chem. Rev.* **2011**, *111*, 1417.
- (5) Fürstner, A.; Leitner, A.; Mendez, M.; Krause, H. *J. Am. Chem. Soc.* **2002**, *124*, 13856.
- (6) Daifuku, S. L.; Al-afyouni, M. H.; Snyder, B. E. R.; Kneebone, J. L.; Neidig, M. L. *J. Am. Chem. Soc.* **2014**, *136*, 9132.
- (7) Daifuku, S. L.; Kneebone, J. L.; Snyder, B. E. R.; Neidig, M. L. *J. Am. Chem. Soc.* **2015**, *137*, 11432.
- (8) Kneebone, J. L.; Brennessel, W. W.; Neidig, M. L. *J. Am. Chem. Soc.* **2017**, *139*, 6988.
- (9) Daifuku, S. L.; Al-afyouni, M. H.; Snyder, B. E. R.; Kneebone, J. L.; Neidig, M. L. *J. Am. Chem. Soc.* **2014**, *136*, 9132.
- (10) Carpenter, S. H.; Neidig, M. L. *Isr. J. Chem.* **2017**, *57*, 1106.
- (11) Bedford, R. B. *Acc. Chem. Res.* **2015**, *48*, 1485.
- (12) Bedford, R. B.; Brenner, P. B.; Carter, E.; Cogswell, P. M.; Haddow, M. F.; Harvey, J. N.; Murphy, D. M.; Nunn, J.; Woodall, C. H. *Angew. Chem. Int. Ed.* **2014**, *53*, 1804.
- (13) Kauffmann, T. *Angew. Chem. Int. ed.* **1996**, *35*, 386.
- (14) Fürstner, A.; Krause, H.; Lehmann, C. W. *Angew. Chem. Int. Ed.* **2006**, *45*, 445.
- (15) Muñoz, S. B.; Daifuku, S. L.; Brennessel, W. W.; Neidig, M. L. *J. Am. Chem. Soc.* **2016**, *138*, 7492.

Chapter 9. Part Conclusion

9.1 Summary

Iron is an excellent candidate as an alternative metal in catalysis to Ni and Pd having major economic and environmental benefits. The previous limitations that limited the appeal of Fe catalysis were primarily a relatively narrow substrate scope and poor mechanistic understanding compared to the popular Pd systems. Major progress has been made in both areas in the last 20 years, but the mechanistic underpinning is still very much in its infancy.

The lability and range of accessible oxidation states in Fe means many competing active species can be observed in catalysis. Not only does the choice of substrate have a major influence on which species is kinetically dominant but ligand, solvent and temperature choices also appear to have a major influence. The most complete mechanistic studies to this authors knowledge are in the works of Neidig¹⁻⁸ and Bedford⁹⁻¹² employing the bulky bisphosphine ligands SciOPP but simple iron salts such as Fe(acac)₃ are much more common in catalysis. There is very little literature concerning the mechanistic studies of the use of Fe(acac)₃ and the attempts to deduce the structural identity of the active species by stoichiometric reactions were inconclusive.^{13,14}

Canonically the reduction of iron salts by Grignard reagents is agreed but there is no consensus on the ultimate oxidation state achieved nor the stoichiometry of this reaction. To this effect the stoichiometric reactions of Fe(acac)₃ with Grignard reagents were investigated.

In chapter 7 the reaction products of Fe(acac)₃ with one equivalent of Grignard reagent were identified unequivocally for the first time. Fe(acac)₃ undergoes a one electron reduction by RMgX producing half an equivalent each of homo-coupled Grignard (R-R), Mg(acac)₂ and two Fe(II) species; Fe(acac)₂ and FeX₂(μ-acac)₂Mg(THF)₂ X = Br, Cl or I (**15** – **17**). The same reaction mixture is produced regardless of the organic component of the Grignard; be it alkyl, allyl, alkyl or aryl and the halogen of the Grignard is incorporated into the intermetallic complex. The resultant Fe(II) complexes were characterised by ¹H NMR and IR spectroscopy, single-crystal XRD and Cyclic Voltammetry.

An alternate means to produce the intermetallic complexes **15** – **17** was established by reaction of ferrous salts, FeX_2 X = Br, Cl or I with $\text{Mg}(\text{acac})_2$. The simplicity of synthesizing $\text{Mg}(\text{diketone})_2$ derivatives provides an additional route to producing a diverse range of intermetallic complexes that can be studied for their catalytic activity to gain mechanistic insights.

The fact that two structurally distinct Fe(II) species are produced upon addition of the first equivalent of Grignard is unique in the literature to the authors knowledge and potentially enables the access to two competing catalytic cycles from the onset. This was investigated by employing the two Fe(II) salts as catalysts in a series of literature cross-coupling reactions in place of Fe(III). The activity of the three complexes was identical in all cases suggesting that each is ultimately converted to an identical catalytically active species.

In chapter 8 the reactivity of $\text{Fe}(\text{acac})_2$ and **15** with further equivalences of Grignard reagents was probed in an effort to identify this catalytically active species. The reaction of **15** with one or more equivalents of Grignard produces a paramagnetic species highly broadened in the ^1H NMR spectra precluded *in-situ* characterisation through this means. Several isolable species were characterised by single crystal XRD but were produced alongside amorphous insoluble black material, usually accounted to a further reduced species in the literature.^{15,16} The isolable complexes $\text{FeBr}(\text{I})(\mu\text{-Br})(\mu\text{-acac})_2\text{Mg}(\text{THF})_2$ (**18**) and $\text{FeBr}_2(\mu\text{-Br})(\mu\text{-acac})_2\text{Mg}(\text{THF})_2$ (**20**) provide some mechanistic insights, for instance that the catalytically active species is likely of similar structural composition. An Fe(II)/(III) redox couple is proposed akin to that described by Neidig *et al.* The generation of competing cycles is similarly expected based on the unidentified species in ^1H NMR spectroscopy, amorphous black material and unclear reaction stoichiometries. For instance, the isolation of $[\text{FeBr}_4][\text{Mg}(\text{THF})_2]$ (**19**) from the reaction of $\text{Fe}(\text{acac})_3$ with 3 equivalents of 4-biPhMgBr in the presence of an electrophile highlights the complexity of the system being investigated.

In the reaction of Fe(acac)₂ with Grignard reagents crystals of **20** can be isolated on crystallisation, the black amorphous material and a unidentified paramagnetic species are similarly observed but further supports a shared active species between the two Fe(II) complexes.

To ultimately determine if the catalytic cycles are divergent in future work we aim to turn to kinetic studies and to alternative spectroscopic techniques such as MCD and EPR that have proven effective in the literature.

9.2 References

- (1) Al-afyouni, M. H.; Fillman, K. L.; Brennessel, W. W.; Neidig, M. L. *J. Am. Chem. Soc.* **2014**, *136*, 15457.
- (2) Carpenter, S. H.; Neidig, M. L. *Isr. J. Chem.* **2017**, *57*, 1106
- (3) Bedford, R. B.; Brenner, P. B.; Carter, E.; Clifton, J.; Cogswell, P. M.; Gower, N. J.; Haddow, M. F.; Harvey, J. N.; Kehl, J. A.; Murphy, D. M.; Neeve, E. C.; Neidig, M. L.; Nunn, J.; Snyder, B. E. R.; Taylor, J. *Organometallics* **2014**, *33*, 5780.
- (4) Muñoz, S. B.; Daifuku, S. L.; Sears, J. D.; Baker, T. M.; Carpenter, S. H.; Brennessel, W. W.; Neidig, M. L. *Angew. Chem. Int. Ed.* **2018**, *57*, 6496.
- (5) Muñoz, S. B.; Daifuku, S. L.; Brennessel, W. W.; Neidig, M. L. *J. Am. Chem. Soc.* **2016**, *138*, 7492.
- (6) Daifuku, S. L.; Kneebone, J. L.; Snyder, B. E. R.; Neidig, M. L. *J. Am. Chem. Soc.* **2015**, *137*, 11432.
- (7) Daifuku, S. L.; Al-afyouni, M. H.; Snyder, B. E. R.; Kneebone, J. L.; Neidig, M. L. *J. Am. Chem. Soc.* **2014**, *136*, 9132.
- (8) Sears, J. D.; Neate, P. G. N.; Neidig, M. L. *J. Am. Chem. Soc.* **2018**, *140*, 11872
- (9) Bedford, R. B. *Acc. Chem. Res.* **2015**, *48*, 1485.
- (10) Bedford, R. B.; Brenner, P. B.; Carter, E.; Cogswell, P. M.; Haddow, M. F.; Harvey, J. N.; Murphy, D. M.; Nunn, J.; Woodall, C. H. *Angew. Chem. Int. Ed.* **2014**, *53*, 1804.

- (11) Adams, C.; Bedford, R. *J. Am. Chem. Soc.* **2012**, *134*, 10333.
- (12) Bedford, R. B.; Brenner, P. B.; Carter, E.; Carvell, T. W.; Cogswell, P. M.; Gallagher, T.; Harvey, J. N.; Murphy, D. M.; Neeve, E. C.; Nunn, J.; Pye, D. R. *Chem. Eur. J.* **2014**, *20*, 7935.
- (13) Lefèvre, G.; Jutand, A. *Chem. Eur. J.* **2014**, *20* (16), 4796.
- (14) Schoch, R.; Desens, W.; Werner, T.; Bauer, M. *Chem. Eur. J.* **2013**, *19*, 15816.
- (15) Fürstner, A.; Leitner, A. *Angew. Chem. Int. Ed.* **2002**, *41*, 609.
- (16) Aleandri, L. E.; Bogdanović, B.; Bons, P.; Durr, C.; Gaidies, A.; Hartwig, T.; Hockett, S. C.; Lagarden, M.; Wilczok, U.; Brand, R. A. *Chem. Mater.* **1995**, *7*, 1153.

Chapter 10. Closing Remarks

In Part 1 the use of di-molybdenum paddlewheel complexes as redox active moieties in mixed valence compounds was introduced. Mixed valence compounds are one of the most vital model complexes for investigating the fundamental properties of electron transfer that are useful in the development of future energy technologies.¹⁻³ A relatively new field where the MV state is stabilised by a hydrogen bonded bridge rather than a covalent bridge has emerged in the literature.⁴⁻¹² One potential mechanism for stabilisation for the mixed valence state in these systems known as Proton Coupled Mixed Valency (PCMV) is best described by the works of the Patmore group.¹³⁻¹⁵ Perhaps the most defining characteristic of this mechanism is the absence of an IVCT band in the near infra-red (NIR), which precludes direct electronic communication between the donor and acceptor. Our ongoing efforts to gain more fundamental insights into this mechanism are described in Chapters 2 - 4.

In Chapter 2 the synthesis of a new series of precursor paddlewheel complexes, $\text{Mo}_2(\text{DTolF})_{4-n}(\text{OAc})_n$ ($n = 1, 2$ *cis*- or *trans*-), complexes **3** – **5** respectively, was described. The generation of oligomeric and polymeric extended assemblies was attempted by the substitution of the labile acetate ligands for coordinating ligands capable of self-complimentary hydrogen bonds. There are limited studies of the MV state in analogous covalent systems¹⁶⁻¹⁹ but the extension to hydrogen bonded di-molybdenum assemblies would be a novel concept with potential application in functional materials.

The use of the DTolF ligand was anticipated to produce complexes being more soluble in solvents such as DCM required to stabilise the assembly through hydrogen bonding interactions. It instead produced complexes being generally less soluble in all solvents but the strongest donors such as DMSO that will disrupt the formation of a hydrogen bond and prevented clean isolation. The synthetic insights gained were however useful in the work described in subsequent chapters.

In chapter 3 the effects of substituting electron withdrawing and electron donating substituents into the H-bonding bridging was explored. In covalent systems such modifications are known to greatly influence the ligand π energy and thus the orbital mixing with the donor and acceptor.^{20,21} This was

the first study to understand how such modifications would impact stabilisation of the mixed valence state through the PCMV mechanism where there is no direct electronic communication between the donor and acceptor orbitals.

The series of complexes $\text{Mo}_2(\text{TiPB})_3(3\text{-R}',4\text{-R}''\text{-HDOP})$ where $\text{R}', \text{R}'' = \text{Cl, H (7), Br, H (8), H, H (9) Me, H (10) and Me, Me (11)}$ and also the fused ring system $\text{Mo}_2(\text{TiPB})_3(\text{HPhth})$ (**12**), where HPhth = phthalhydrazide were synthesized. Stabilisation of the MV state was quantified through cyclic voltammetry and seen to increase with increasing electron donating substituent of the bridging ligand. This is rationalised by considering the acceptor as a singly occupied molecular orbital that more readily accepts π -donation from the substituted DOP ligand than the donor. An electron donating substituent increase π -donation and produces a stabilisation of the acceptor localised charge and the observed thermodynamic stabilisation of the mixed valence state where an electron withdrawing substituent has the opposite effect.

In chapter 4 new examples of MV complexes stabilised by the PCMV mechanisms were reported. $\text{Mo}_2(\text{DAniF})_3\text{DSOP}$ (**13**) and $\text{Mo}_2(\text{DAniF})_3\text{SDOP}$ (**14**) were synthesized. Stabilisation of the mixed valence state was quantified by CV. The determined K_c values indicate that **14** is of the same order of magnitude determined for the most stable of the $\text{Mo}_2(\text{TiPB})_3(3\text{-R}',4\text{-R}''\text{-HDOP})$ series complex **11** but **13** showed a much greater stabilisation.

The UV-VIS NIR spectral response confirmed that these complexes are stabilised by the PCMV mechanism evident in the lack of an IVCT band in the NIR. However, complex **13** displayed a unique, IR centred transition that extended into the NIR. Because this transition is present and most intense in the doubly oxidised state (not MV) it is not an IVCT. But despite our efforts to model these systems through DFT the nature of this transition is still not well understood at this time. It is in some way related to the formation of the hydrogen-bonded dimer and generation of the MV state because it not observed when the UV-Vis spectroelectrochemistry is performed in THF were the hydrogen bond will be disrupted.

The results reported in part 1 are essential to the ongoing development of our understanding of the PCMV mechanism. The impact of structural changes in the bridging ligand upon stabilisation of the mixed valence state has been determined thus allowing us to tune the stabilisation of the mixed balance state. Potentially allowing us to design systems where the ET falls on the IR so the rate can be determined by IR spectral coalescence.²²⁻²⁴ The synthetic insights and increased familiarity with UV-Vis NIR and IR spectroscopic response of these compounds will also be useful in generating and understanding these new model systems.

In part 2 our efforts towards discerning the mechanisms of Fe(acac)₃ catalysed Kumada cross-coupling was described. Iron is an excellent candidate as an alternative to Pd the current most commonly employed metal in cross-coupling, having major advantages in terms economy, environmental impact and biocompatibility.^{25,26} A robust mechanistic understanding is essential to improve the utility and appeal of iron catalysis. The early mechanistic reports focused on the reactivity of iron halide salts and more modern studies on iron bisphosphine complexes.²⁷⁻³⁶ Iron salts such as Fe(acac)₃ are more prominent in synthetic reports in the literature but there are very few accompanying mechanistic studies.^{37,38}

In chapter 7 the reaction products of the equimolar reaction of Fe(acac)₃ with Grignard reagents was determined unequivocally for the first time. Two Fe(II) species are produced; Fe(acac)₂ and the novel intermetallic complex FeX₂(μ-acac)₂Mg(THF)₂ X = Br, Cl or I (**15** – **17**). The formation of the two Fe(II) species is identical regardless of the organic component of the Grignard reagent and the halogen incarnated into the intermetallic is identical to that in the Grignard reagent (RMgX, R – aryl, alkyl, allyl, propynyl X – Cl, Br or I).

The Fe(II) species were substituted in place of Fe(acac)₃ in a series of literature cross-coupling reactions. Identical isolated yields indicate preliminarily that each species is likely ultimately converted to the same catalytic species.

In chapter 8 the reaction beyond one equivalent was explored. $\text{Fe}(\text{acac})_3$, $\text{Fe}(\text{acac})_2$ and $\text{FeBr}_2(\mu\text{-acac})_2\text{Mg}(\text{THF})_2$ (**15**) were reacted with further equivalents of Grignard reagents and a number of isolable species were characterised structurally by single crystal x-ray diffraction. These species while off-cycle to perhaps give some mechanistic insights. Most importantly however the treatment of both **15** and $\text{Fe}(\text{acac})_2$ with one or two equivalents of Grignard reagent was shown to produce the same intermetallic species: $\text{Fe}(\text{Br})_2(\mu\text{-Br})(\mu\text{-acac})(\text{THF})_3$ (**19**) and further supports a shared active species for the two Fe(II) species.

There are numerous future studies required to better understand the complex nature of this chemistry. Firstly, to identify the paramagnetic species that is generated beyond one equivalent of Grignard reagents relative to the $\text{Fe}(\text{acac})_3$ substrate. Alternative spectroscopies such as EPR and MCD have proven effective in the literature in this regard.^{31,39} In combination with kinetic measurements via *in situ* IR spectroscopy to monitor product formation should be effective to confirm if the two Fe(II) pre-catalysts are ultimately converted to a common active species. Finally, the role of NMP in $\text{Fe}(\text{acac})_3$ catalysed reactions is to be investigated. Whether NMP has a simple solvent effect or plays a more intrinsic roll in iron speciation is debated in the literature.^{36,40-42}

The understanding of both the PCMV and catalytic mechanisms are still in ongoing development. Beyond the synthetic challenges of isolating new model complexes, we have previously faced the significant challenge of limited literature to which these results can be compared. The outlook is promising however as in recent years both fields appear to be gaining interest from groups applying novel approaches from which we can take inspiration.

The fundamental studies of described in this work are relatively niche but in a broader context of energy technologies and cross-coupling has major ramifications for application-based science. Future publication of this work should be in high impact journals. The results of chapter 7 have been published in part.⁴³ Manuscripts for a follow up publication of this work and the results of chapter 3 are also currently in preparation.

10.1 References

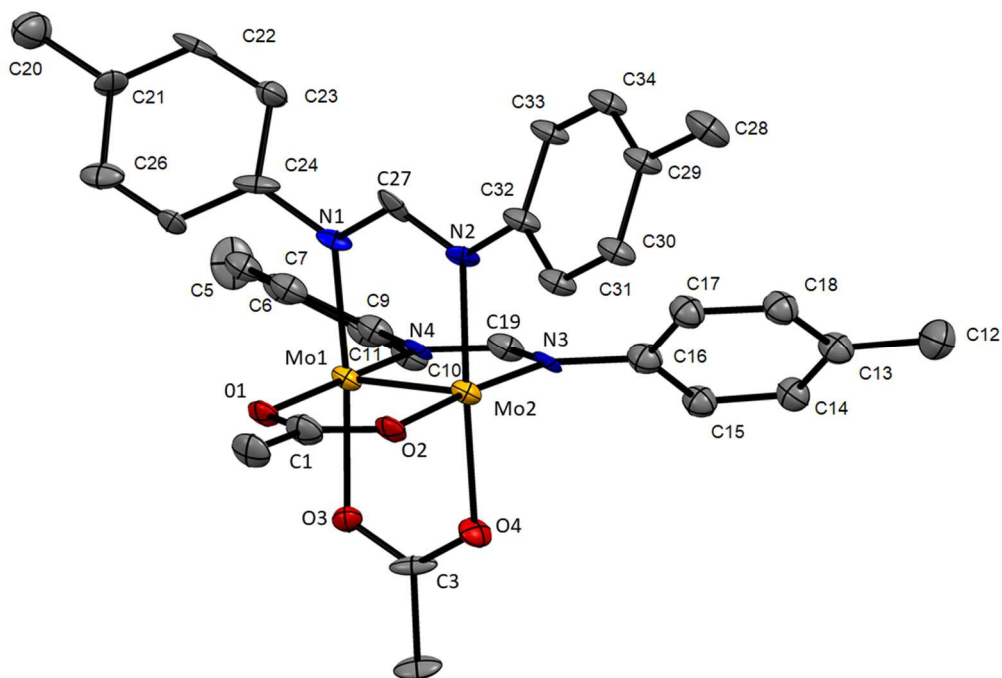
- (1) Tadokoro, M.; Hosoda, H.; Inoue, T.; Murayama, A.; Noguchi, K.; Iio, A.; Nishimura, R.; Itoh, M.; Sugaya, T.; Kamebuchi, H.; Haga, M. A. *Inorg. Chem.* **2017**, *56*, 8513–8526.
- (2) Schmuck, C.; Wienand, W. *Angew. Chem. Int. Ed.* **2001**, *40*, 4363–4369.
- (3) Sijbesma, R. P.; Beijer, F. H.; Brunsveld, L.; Folmer, B. J. B.; Hirschberg, J. H. K. K.; Lange, R. F. M.; Lowe, J. K. L.; Meijer, E. W. *Science*. **1997**, *278*, 1601–1604.
- (4) Wang, L.; Gong, Z.; Li, S.; Hong, W.; Zhong, Y.; Wang, D. *Angew. Chem. Int. Ed.* **2016**, *55*, 1.
- (5) Sun, H.; Steeb, J.; Kaifer, A. E. *J. Am. Chem. Soc.* **2006**, *128*, 2820.
- (6) Goeltz, J. C.; Kubiak, C. P. *J. Am. Chem. Soc.* **2010**, *132*, 17390.
- (7) Tadokoro, M.; Inoue, T.; Tamaki, S.; Fujii, K.; Isogai, K.; Nakazawa, H.; Takeda, S.; Isobe, K.; Koga, N.; Ichimura, A.; Nakasuji, K. *Angew. Chem. Int. Ed.* **2007**, *46*, 5938.
- (8) Jin-Long; Matsuda, Y.; Uemura, K.; Ebihara, M. *Inorg. Chem.* **2015**.
- (9) Cliff, S.; Kubiak, P.; Porter, T. M.; Heim, G. P.; Kubiak, C. P. *Chem. Sci.* **2017**, *8*, 7324.
- (10) Canzi, G.; Goeltz, J. C.; Henderson, J. S.; Park, R. E.; Maruggi, C.; Kubiak, C. P. *J. Am. Chem. Soc.* **2014**, *136*, 1710.
- (11) Sun, H.; Steeb, J.; Kaifer, A. E. *J. Am. Chem. Soc.* **2006**, *128*, 2820.
- (12) Wilkinson, L. A.; McNeill, L.; Meijer, A. J. H. M.; Patmore, N. J. *J. Am. Chem. Soc.* **2013**, *135*, 1723.
- (13) Wilkinson, L. A.; McNeill, L.; Scattergood, P. a.; Patmore, N. J. *Inorg. Chem.* **2013**, *52*, 9683.
- (14) Wilkinson, L. A.; Vincent, K. B.; Meijer, A. J. H. M.; Patmore, N. J. *Chem. Commun.* **2016**, *52*, 100.
- (15) Han, L. J.; Fan, L. Y.; Meng, M.; Wang, X.; Liu, C. Y. *Dalton. Trans.* **2011**, *40*, 12832.

- (16) Chisholm, M. H.; Macintosh, A. M. *Chem. Rev.* **2005**, *105*, 2949.
- (17) Köberl, M.; Cokoja, M.; Herrmann, W. a; Kühn, F. E. *Dalton Trans.* **2011**, *40*, 6834.
- (18) Chisholm, M. H.; Patmore, N. J.; Reed, C. R.; Singh, N. *Inorg. Chem.* **2010**, *49*, 7116.
- (19) Lambert, C.; Risko, C.; Coropceanu, V.; Schelter, J.; Amthor, S.; Gruhn, N. E.; Durivage, J. C.; Brédas, J.-L. *J. Am. Chem. Soc.* **2005**, *127*, 8508.
- (20) Fox, M. A.; Le Guennic, B.; Roberts, R. L.; Brue, D. A.; Yufit, D. S.; Howard, J. A. K.; Manca, G.; Halet, J. F.; Hartl, F.; Low, P. J. *J. Am. Chem. Soc.* **2011**, *133*, 18433.
- (21) Salsman, J. C.; Ronco, S.; Londergan, C. H.; Kubiak, C. P. *Inorg. Chem.* **2006**, *45*, 547.
- (22) Ito, T.; Hamaguchi, T.; Nagino, H.; Yamaguchi, T.; Kido, H.; Zavarine, I. S.; Richmond, T.; Washington, J.; Kubiak, C. P. *J. Am. Chem. Soc.* **1999**, *121*, 4625.
- (23) Londergan, C. H.; Kubiak, C. P. *Chem. Eur. J.* **2003**, *9*, 5962.
- (24) Fürstner, A. *ACS Cent. Sci.* **2016**, *2*, 778.
- (25) Johansson Seechurn, C. C. C.; Kitching, M. O.; Colacot, T. J.; Snieckus, V. *Angew. Chem. Int. Ed.* **2012**, *51*, 5062.
- (26) Bedford, R. B.; Betham, M.; Bruce, D. W.; Davis, S. a; Frost, R. M.; Hird, M. *Chem. Commun.* **2006**, *13*, 1398.
- (27) Bedford, R. B.; Brenner, P. B.; Carter, E.; Cogswell, P. M.; Haddow, M. F.; Harvey, J. N.; Murphy, D. M.; Nunn, J.; Woodall, C. H. *Angew. Chem. Int. Ed.* **2014**, *53*, 1804.
- (28) Bedford, R. B. *Acc. Chem. Res.* **2015**, *48*, 1485.
- (29) Al-afyouni, M. H.; Fillman, K. L.; Brennessel, W. W.; Neidig, M. L. *J. Am. Chem. Soc.* **2014**, *136*, 15457
- (30) Carpenter, S. H.; Neidig, M. L. *Isr. J. Chem.* **2017**, *57*, 1106.

- (31) Bedford, R. B.; Brenner, P. B.; Carter, E.; Clifton, J.; Cogswell, P. M.; Gower, N. J.; Haddow, M. F.; Harvey, J. N.; Kehl, J. a.; Murphy, D. M.; Neeve, E. C.; Neidig, M. L.; Nunn, J.; Snyder, B. E. R.; Taylor, J. *Organometallics* **2014**, *33*, 5767.
- (32) Muñoz, S. B.; Daifuku, S. L.; Sears, J. D.; Baker, T. M.; Carpenter, S. H.; Brennessel, W. W.; Neidig, M. L. *Angew. Chem. Int. Ed.* **2018**.
- (33) Muñoz, S. B.; Daifuku, S. L.; Brennessel, W. W.; Neidig, M. L. *J. Am. Chem. Soc.* **2016**, *138*, 7492.
- (34) Daifuku, S. L.; Kneebone, J. L.; Snyder, B. E. R.; Neidig, M. L. *J. Am. Chem. Soc.* **2015**, *137*, 11432.
- (35) Sears, J. D.; Neate, P. G. N.; Neidig, M. L. *J. Am. Chem. Soc.* **2018**, *140*, 11872.
- (36) Lefèvre, G.; Jutand, A. *Chem. Eur. J.* **2014**, *20*, 4796.
- (37) Schoch, R.; Desens, W.; Werner, T.; Bauer, M. *Chem. Eur. J.* **2013**, *19*, 15816.
- (38) Baker, T. M.; Mako, T. L.; Vasilopoulos, A.; Li, B.; Byers, J. A.; Neidig, M. L. *Organometallics* **2016**, *35*, 3692.
- (39) Mako, T. L.; Byers, J. A. *Inorg. Chem. Front.* **2016**, *3*, 766.
- (40) Ding, K.; Zannat, F.; Morris, J. C.; Brennessel, W. W.; Holland, P. L. *J. Organomet. Chem.* **2009**, *694*, 4204.
- (41) Muñoz, S. B.; Daifuku, S. L.; Sears, J. D.; Baker, T. M.; Carpenter, S. H.; Brennessel, W. W.; Neidig, M. L. *Angew. Chem. Int. Ed.* **2018**, *57*, 6496.
- (42) Adams, K.; Ball, A. K.; Birkett, J.; Brown, L.; Chappell, B.; Gill, D. M.; Lo, P. K. T.; Patmore, N. J.; Rice, C. R.; Ryan, J.; Raubo, P.; Sweeney, J. B. *Nat. Chem.* **2017**, *9*, 396.

11. Appendixes: X-ray Crystal Structure Data & Refinement Tables

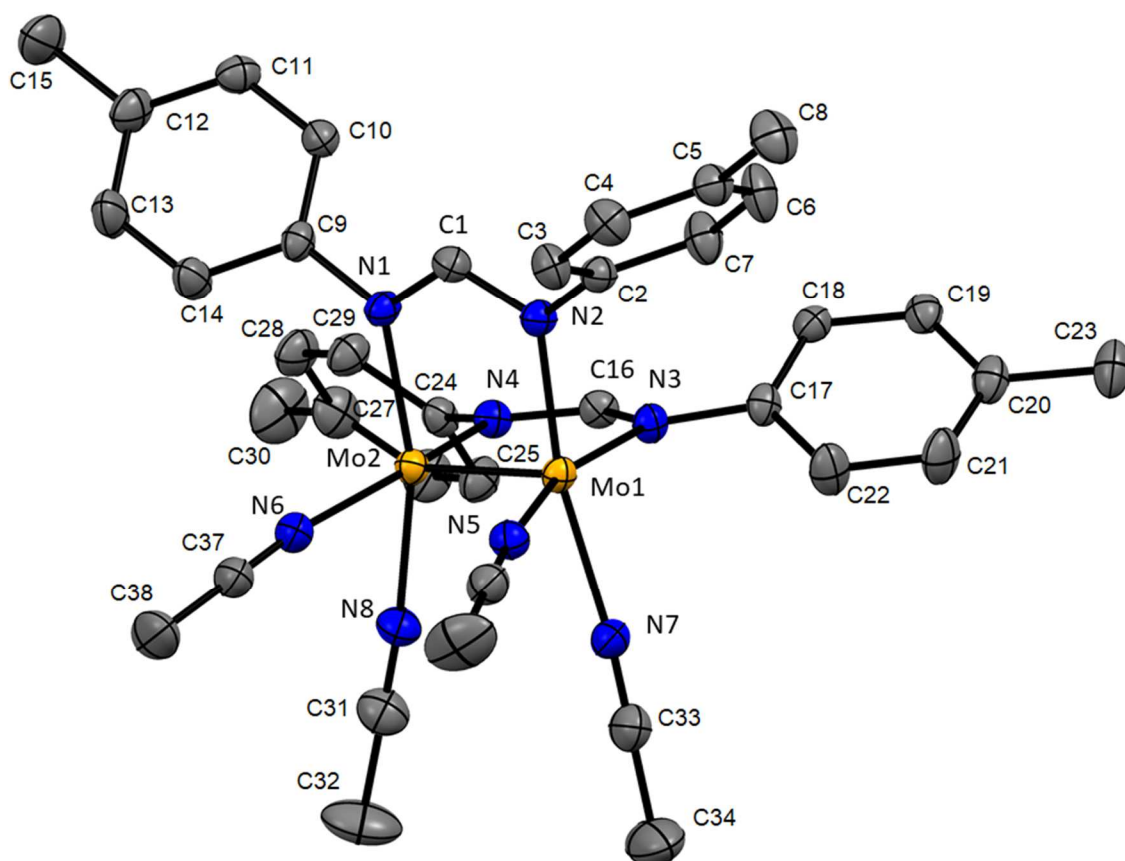
11.1 *cis*-Mo₂(DTolF)₂(OAc)₂ (5)



| | |
|---|---|
| Empirical Formula | C _{41.50} H ₄₉ B ₂ Cl ₇ F ₈ Mo ₂ N ₈ |
| Temperature (K) | 293(2) |
| Wavelength (Å) | 1.54178 |
| Crystal system, space group: | Triclinic, P-1 |
| <i>a</i> (Å) | 13.5517(4) |
| <i>b</i> (Å) | 14.5675(5) |
| <i>c</i> (Å) | 16.8834(5) |
| α (°) | 101.995(2) |
| β (°) | 92.379(2) |
| γ (°) | 98.471(2) |
| Volume (Å ³) | 3215.71(18) |
| Z, Calculated density (g cm ⁻³) | 4, 1.414 |
| F(000) | 1376 |
| θ range for data collection (°) | 2.683 to 68.432 |
| Limiting indices | -15 $\leq h \leq$ 16, -17 $\leq k \leq$ 17, -20 $\leq l \leq$ 13 |
| Reflections collected / unique: | 67000 / 16052 [<i>R</i> (int) = 0.0362] |
| Completeness to $\theta = 25.242$ | 99.9 % |
| Data/ restraints/ parameters | 10433 / 276 / 765 |

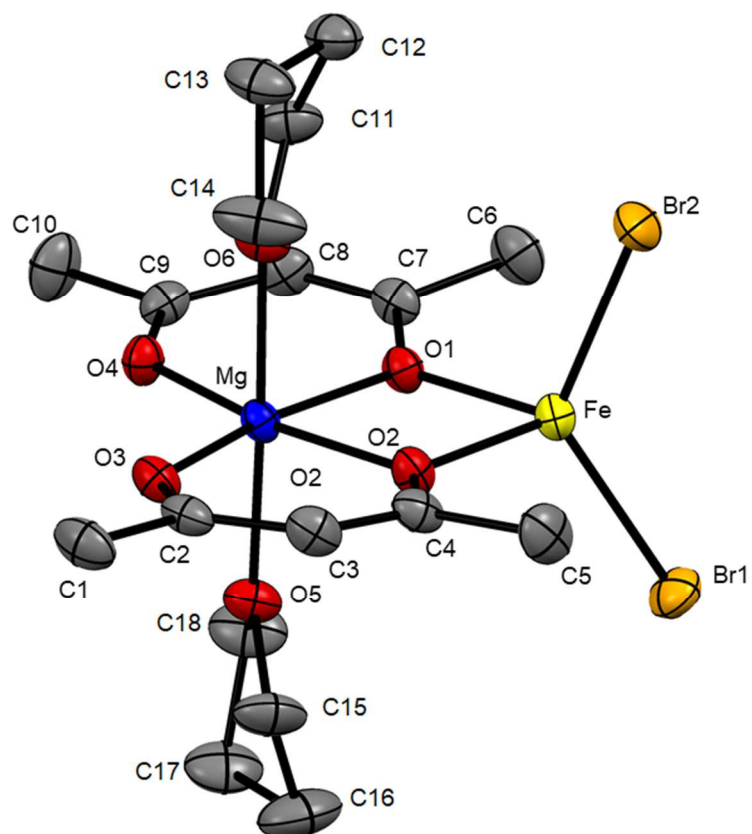
| | |
|--|----------------------------------|
| Goodness-of-fit F^2 | 1.125 |
| Final R indices [$I > 2\sigma(I)$]: | $R_1 = 0.1300$ $wR_2 = 0.2833$ |
| R indices all data | $R_1 = 0.1686$, $wR_2 = 0.3083$ |
| Largest diff. peak and hole ($e \text{ \AA}^{-3}$) | 2.140 and -1.856 |

11.3 *cis*-Mo₂(DTolF)₂(NCMe)₄·2BF₄·2CH₂Cl₂ (**6**)



| | |
|---|---|
| Empirical Formula | C _{41.50} H ₄₉ B ₂ Cl ₇ F ₈ Mo ₂ N ₈ |
| Temperature (K) | 150(2) |
| Wavelength (Å) | 0.71073 |
| Crystal system, space group: | Triclinic, P-1 |
| <i>a</i> (Å) | 11.5418(5) |
| <i>b</i> (Å) | 12.7088(6) |
| <i>c</i> (Å) | 19.6774(10) |
| α (°) | 78.1120(10) |
| β (°) | 78.2050(10) |
| γ (°) | 81.4560(10) |
| Volume (Å ³) | 2747.7(2) |
| Z, Calculated density (g cm ⁻³) | 2, 1.539 |

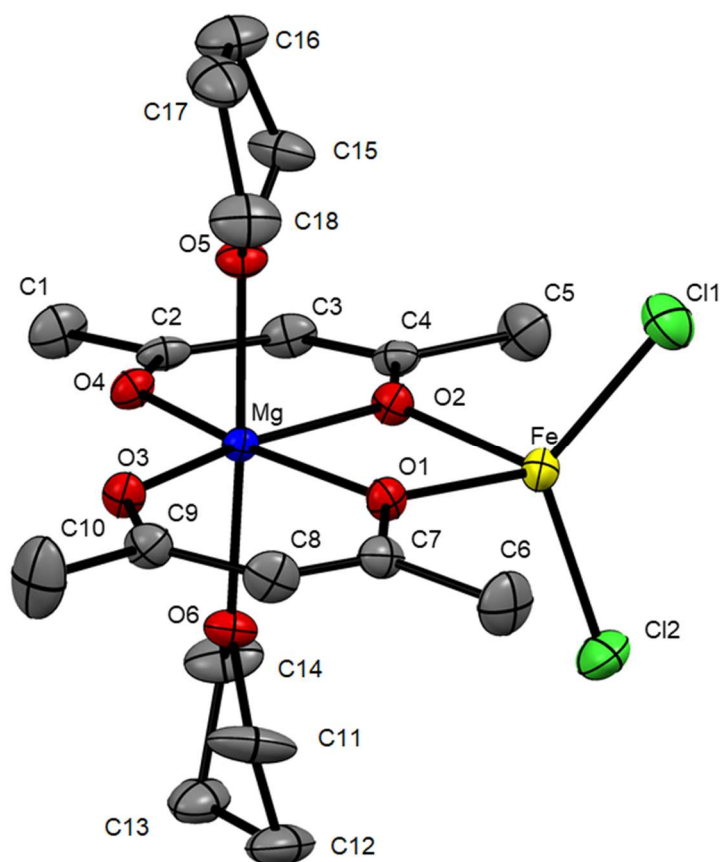
| | |
|---|--|
| F(000) | 1278 |
| θ range for data collection (°) | 2.388 to 30.030 |
| Limiting indices | $-16 \leq h \leq 16, -17 \leq k \leq 17, -27 \leq l \leq 27$ |
| Reflections collected / unique: | 67000 / 16052 [$R(\text{int}) = 0.0362$] |
| Completeness to $\theta = 25.242$ | 99.9 % |
| Data/ restraints/ parameters | 16052 / 102 / 725 |
| Goodness-of-fit F^2 | 1.040 |
| Final R indices [$I > 2\sigma(I)$]: | $R_1 = 0.0502, wR_2 = 0.1267$ |
| R indices all data | $R_1 = 0.0770, wR_2 = 0.1425$ |
| Largest diff. peak and hole ($\text{e} \text{ \AA}^{-3}$) | 1.708 and -1.215 |

11.4 FeBr₂(μ-acac)₂Mg(THF)₂ (15)

| | |
|---|--|
| Empirical Formula | C ₁₈ H ₃₀ Br ₂ FeMgO ₆ |
| Temperature (K) | 150(2) |
| Wavelength (Å) | 0.71073 |
| Crystal system, space group: | Monoclinic, P2 ₁ /c |
| <i>a</i> (Å) | 9.4901(5) |
| <i>b</i> (Å) | 14.9202(7) |
| <i>c</i> (Å) | 17.4333(9) |
| α (°) | 90 |
| β (°) | 101.940(2) |
| γ (°) | 90 |
| Volume (Å ³) | 2415.0(2) |
| Z, Calculated density (g cm ⁻³) | 4, 1.398 |
| F(000) | 1032 |
| θ range for data collection | 1.854 to 27.489 |
| Limiting indices | -13 $\leq h \leq$ 13, -18 $\leq k \leq$ 21, -24 $\leq l \leq$ 21 |

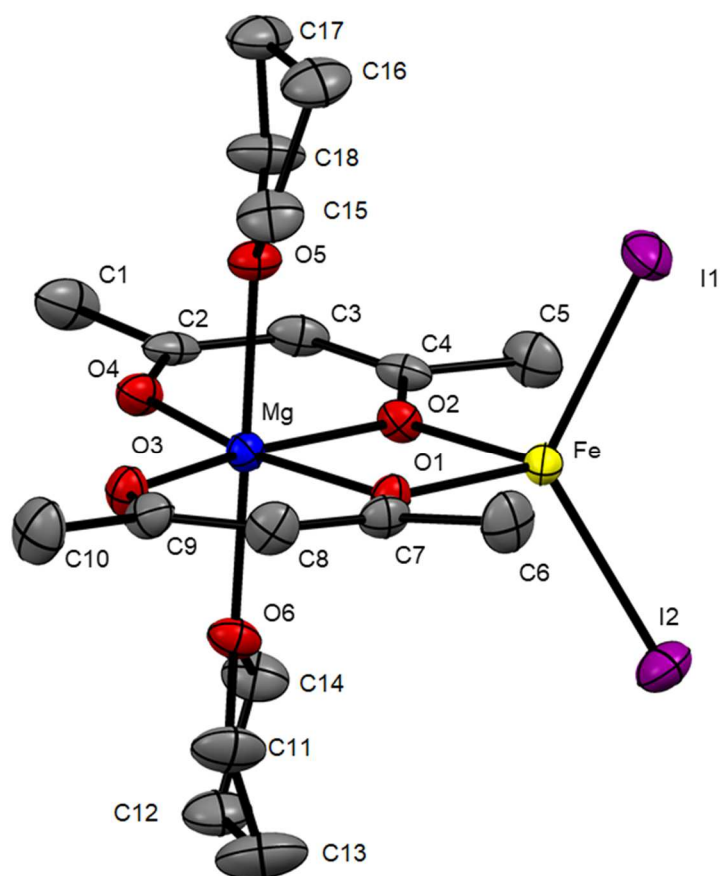
| | |
|--|---|
| Reflections collected / unique: | 23641 / 5384 [$R(\text{int}) = 0.0536$] |
| Completeness to $\theta = 25.242$ | 99.9 % |
| Data/ restraints/ parameters | 7054 / 81 / 277 |
| Goodness-of-fit F^2 | 1.045 |
| Final R indices [$I > 2\sigma(I)$]: | $R_1 = 0.0498$, $wR_2 = 0.1074$ |
| R indices all data | $R_1 = 0.0928$, $wR_2 = 0.1221$ |
| Largest diff. peak and hole ($e \text{ \AA}^{-3}$) | 1.896 and -0.591 |

11.5 FeCl₂(μ-acac)₂Mg(THF)₂ (16)



| | |
|------------------------------|--|
| Empirical Formula | C ₁₈ H ₃₀ Cl ₂ FeMgO ₆ |
| Temperature (K) | 150(2) |
| Wavelength (Å) | 0.71073 |
| Crystal system, space group: | orthorhombic, P2 ₁ 2 ₁ 2 ₁ |
| <i>a</i> (Å) | 9.5887(7) |
| <i>b</i> (Å) | 14.4312(13) |
| <i>c</i> (Å) | 16.9446(13) |
| α (°) | 90 |
| β (°) | 90 |
| γ (°) | 90 |
| Volume (Å ³) | 2344.7(3) |

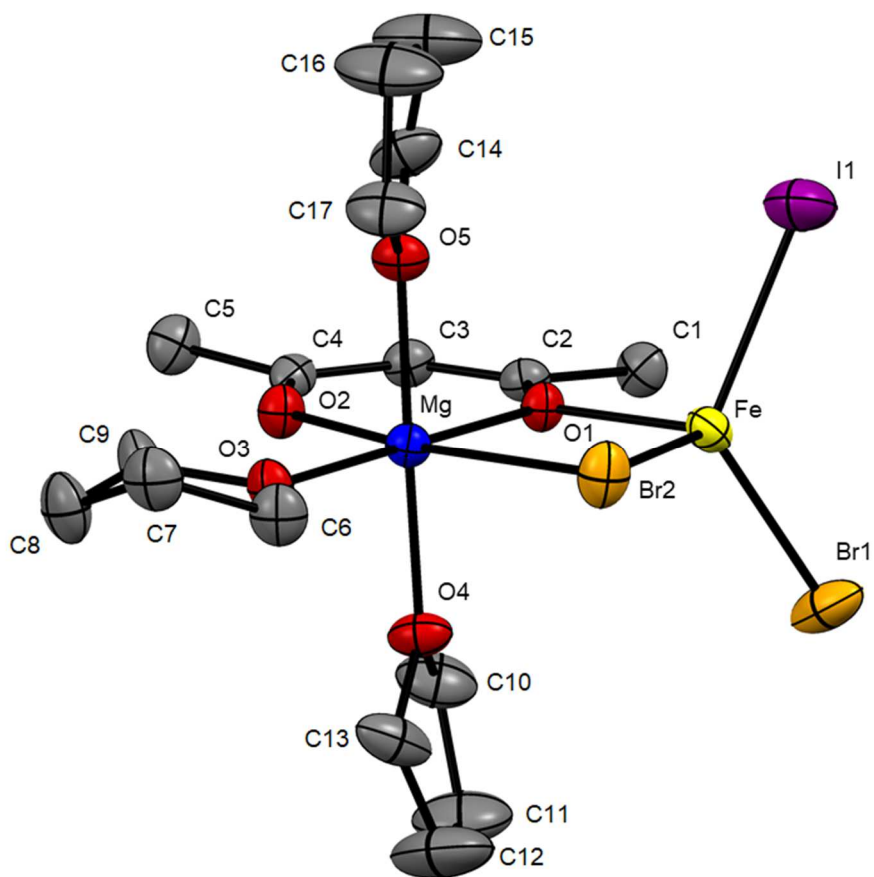
| | |
|--|--|
| Z, Calculated density (g cm ⁻³) | 4, 1.398 |
| F(000) | 1032 |
| θ range for data collection (°) | 1.854 to 27.489 |
| Limiting indices | $-12 \leq h \leq 12, -18 \leq k \leq 18, -21 \leq l \leq 22$ |
| Reflections collected / unique: | 37359 / 7054 [$R(\text{int}) = 0.0547$] |
| Completeness to $\theta = 25.242$ | 100.0 % |
| Data/ restraints/ parameters | 5384 / 79 / 273 |
| Goodness-of-fit F^2 | 1.021 |
| Final R indices [$I > 2\sigma(I)$]: | $R_1 = 0.0392, wR_2 = 0.0860$ |
| R indices all data | $R_1 = 0.0536, wR_2 = 0.0916$ |
| Largest diff. peak and hole (e Å ⁻³) | 0.436 and -0.416 |

11.6 FeI₂(μ-acac)₂Mg(THF)₂ (17)

| | |
|---|---|
| Empirical Formula | C ₁₈ H ₃₀ FeI ₂ MgO ₆ |
| Temperature (K) | 150(2) |
| Wavelength (Å) | 0.71073 |
| Crystal system, space group: | Monoclinic, P2 ₁ /c |
| <i>a</i> (Å) | 9.5399(6) |
| <i>b</i> (Å) | 15.0987(11) |
| <i>c</i> (Å) | 17.9645(13) |
| α (°) | 90 |
| β (°) | 100.352(2) |
| γ (°) | 90 |
| Volume (Å ³) | 2545.5(3) |
| Z, Calculated density (g cm ⁻³) | 4, 1.765 |
| F(000) | 1320 |

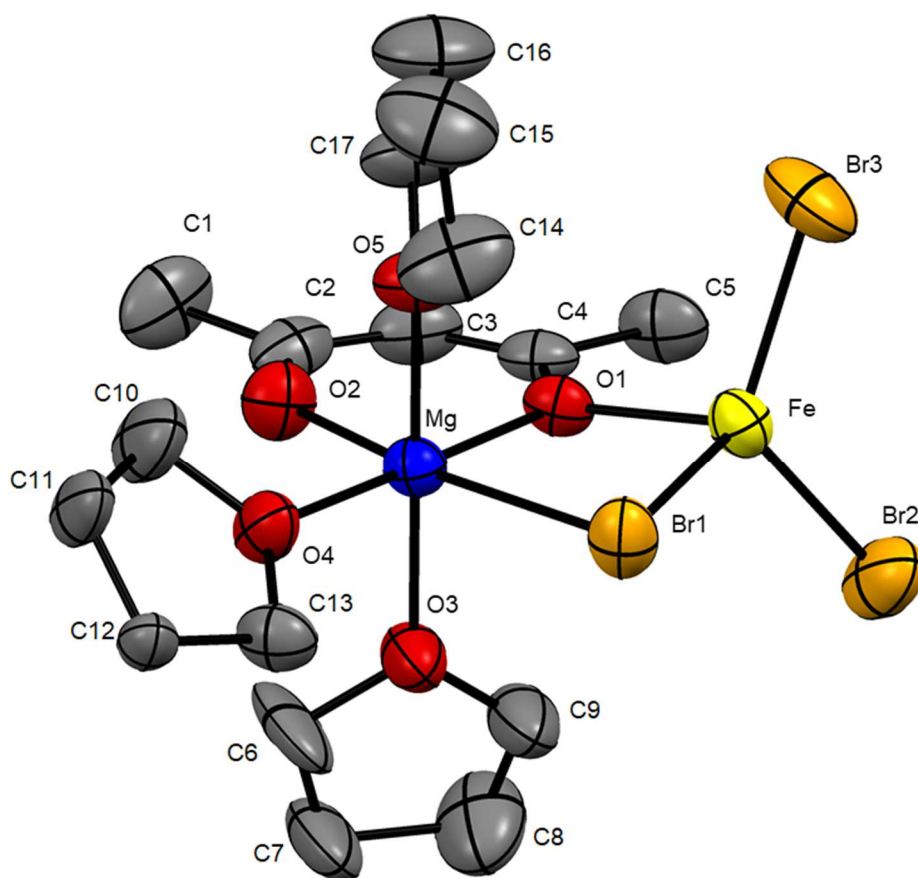
| | |
|--|--|
| θ range for data collection | 2.170 to 27.530 |
| Limiting indices | $-11 \leq h \leq 12, -19 \leq k \leq 16, -23 \leq l \leq 23$ |
| Reflections collected / unique: | 41040 / 5861 [$R(\text{int}) = 0.0418$] |
| Completeness to $\theta = 25.242$ | 99.9 % |
| Data/ restraints/ parameters | 5861 / 60 / 272 |
| Goodness-of-fit F^2 | 1.039 |
| Final R indices [$I > 2\sigma(I)$]: | $R_1 = 0.0281, wR_2 = 0.0537$ |
| R indices all data | $R_1 = 0.0436, wR_2 = 0.0575$ |
| Largest diff. peak and hole ($e \text{ \AA}^{-3}$) | 0.606 and -0.779 |

11.7 FeBr(I)(μ -Br)(μ -acac)Mg(THF)₃ (**18**)



| | |
|------------------------------|---|
| Empirical Formula | C ₁₇ H ₃₁ Br ₂ FeIMgO ₅ |
| Temperature (K) | 150(2) |
| Wavelength (Å) | 0.71073 |
| Crystal system, space group: | Monoclinic, P2 ₁ n |
| <i>a</i> (Å) | 11.6677(6) |
| <i>b</i> (Å) | 17.1186(9) |
| <i>c</i> (Å) | 12.3654(6) |
| α (°) | 90 |
| β (°) | 90.891(2) |
| γ (°) | 90 |
| Volume (Å ³) | 2456.8(2) |

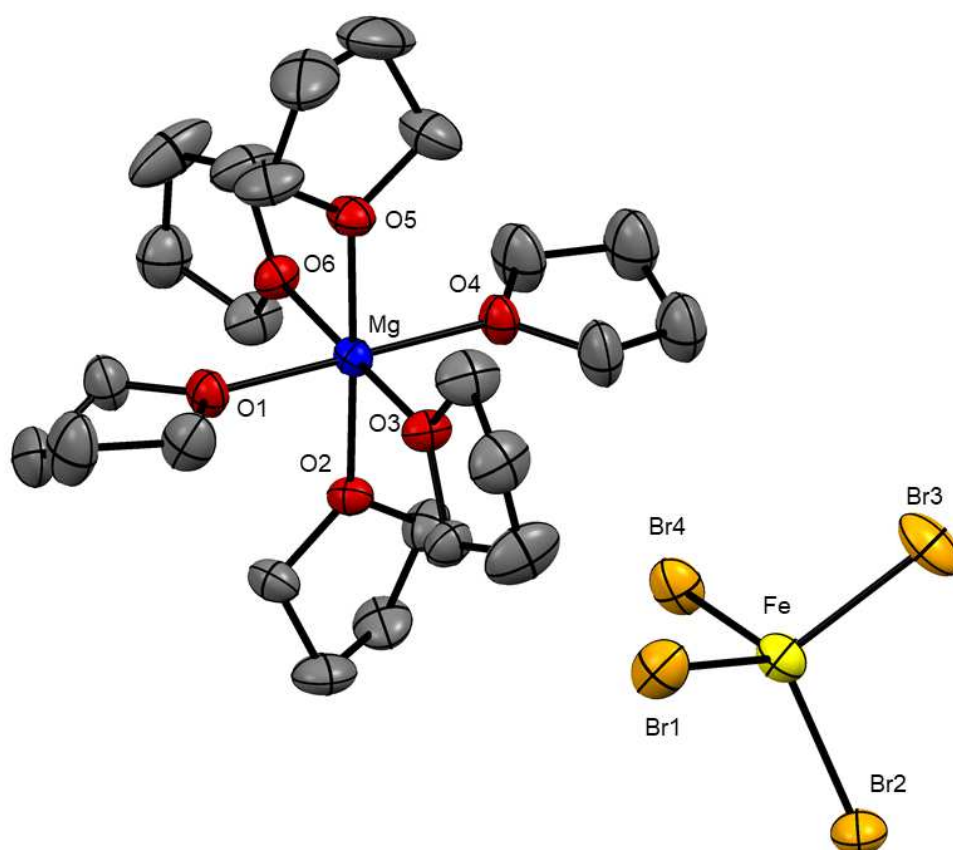
| | |
|--|--|
| Z, Calculated density (g cm ⁻³) | 4, 1.602 |
| F(000) | 1176 |
| θ range for data collection | 2.388 |
| Limiting indices | $-13 \leq h \leq 13, -18 \leq k \leq 21, -24 \leq l \leq 21$ |
| Reflections collected / unique: | 37359 / 7054 [$R(\text{int}) = 0.0547$] |
| Completeness to $\theta = 25.242$ | 99.9 % |
| Final R indices [$I > 2\sigma(I)$]: | $R_1 = 0.0498, wR_2 = 0.1074$ |
| R indices all data | $R_1 = 0.0928, wR_2 = 0.1221$ |
| Largest diff. peak and hole (e \AA^{-3}) | 1.896 and -0.591 |

11.8 FeBr₂(μ-Br)(μ-acac)Mg(THF)₃ (19)

| | |
|---|--|
| Empirical Formula | C ₁₇ H ₃₁ Br ₃ FeMgO ₅ |
| Temperature (K) | 250(2) |
| Wavelength (Å) | 0.71073 |
| Crystal system, space group: | Orthorhombic, P2 ₁ n |
| <i>a</i> (Å) | 11.8173(7) |
| <i>b</i> (Å) | 16.7768(11) |
| <i>c</i> (Å) | 12.9488(8) |
| α (°) | 90 |
| β (°) | 99.127(2) |
| γ (°) | 90 |
| Volume (Å ³) | 2534.7(3) |
| Z, Calculated density (g cm ⁻³) | 4, 1.665 |
| F(000) | 1264 |

| | |
|--|--|
| θ range for data collection ($^{\circ}$) | 2.126 to 30.030 |
| Limiting indices | $-16 \leq h \leq 15$, $-18 \leq k \leq 23$, $-18 \leq l \leq 13$ |
| Reflections collected / unique: | 26777 / 7409 [$R(\text{int}) = 0.0885$] |
| Completeness to $\theta = 25.242$ | 99.9 % |
| Data/ restraints/ parameters | 5384 / 79 / 273 |
| Goodness-of-fit F^2 | 1.006 |
| Final R indices [$I > 2\sigma(I)$]: | $R_1 = 0.0640$, $wR_2 = 0.1235$ |
| R indices all data | $R_1 = 0.1726$, $wR_2 = 0.1595$ |
| Largest diff. peak and hole ($e \text{ \AA}^{-3}$) | 0.821 and -0.851 |

11.9 FeBr₄.Mg(THF)₆ (20)



| | |
|-------------------|--|
| Empirical Formula | C ₄₈ H ₉₆ Br ₈ FeMgO ₆ |
| Temperature (K) | 150(2) |

| | |
|--|--|
| Wavelength (Å) | 0.71073 |
| Crystal system, space group: | Monoclinic, $P2_1/c$ |
| a (Å) | 18.6556(17) |
| b (Å) | 10.0287(9) |
| c (Å) | 35.224(3) |
| α (°) | 90 |
| β (°) | 101.940(2) |
| γ (°) | 90 |
| Volume (Å ³) | 6512.2(10) |
| Z, Calculated density (g cm ⁻³) | 4, 1.698 |
| F(000) | 3344 |
| θ range for data collection | 2.113 to 26.431 |
| Limiting indices | $-23 \leq h \leq 23$, $-12 \leq k \leq 11$, $-44 \leq l \leq 44$ |
| Reflections collected / unique: | 100348 / 13354 [$R(\text{int}) = 0.0699$] |
| Completeness to $\theta = 25.242$ | 99.9 % |
| Data/ restraints/ parameters | 13354 / 537 / 837 |
| Goodness-of-fit F^2 | 1.046 |
| Final R indices [$I > 2\sigma(I)$]: | $R_1 = 0.0671$, $wR_2 = 0.1574$ |
| R indices all data | $R_1 = 0.1099$, $wR_2 = 0.1779$ |
| Largest diff. peak and hole (e Å ⁻³) | 1.837 and -1.472 |